CONSEJO SUPERIOR DE INVESTIGACIONES CIENTIFICAS

UNIVERSIDAD AUTONOMA DE MADRID

INORGANIC MULTIFUNCTIONAL NANOSTRUCTURES BASED ON IRON OXIDE

A thesis submitted in fulfillment of the requirements for the degree of Doctor of Philosophy to the Departamento de Física Aplicada of the Universidad Autónoma de Madrid

YURENA LUENGO MORATO

Supervisor: Dr. Sabino Veintemillas-Verdaguer

Tutor: Oscar Bomatí-Miguel

Instituto de Ciencia de Materiales de Madrid

Madrid 2017

NANOESTRUCTURAS MULTIFUNCIONALES INORGANICAS BASADAS EN OXIDO DE HIERRO

Memoria presentada para optar al grado de

DOCTOR EN MATERIALES AVANZADOS Y NANOTECNOLOGÍA

YURENA LUENGO MORATO

Director: Dr. Sabino Veintemillas-Verdaguer

Tutor: Oscar Bomatí-Miguel

Instituto de Ciencia de Materiales de Madrid

Madrid 2017

Agradecimientos

Cuando empecé en el ICMM no conseguía imaginar el día que me tocara escribir los agradecimientos de la tesis y, sin embargo, el tiempo vuelta y toca cerrar una etapa en la que he tenido la suerte de contar con la ayuda, el apoyo y el cariño de mucha gente. Por ello, quiero dedicar estas líneas a todas las personas que han ayudado directa o indirectamente en la realización de este trabajo (espero no olvidarme de nadie).

En primer lugar quiero agradecer al Dr. Sabino Veintemillas-Verdaguer por la dirección de esta tesis, por su apoyo y su ilimitada capacidad de trabajo. Gracias también a la Dra. M. Puerto Morales por darme la posibilidad (allá por 2010) de realizar unas prácticas en este grupo y conseguir que "me picara el gusanillo" de la investigación. Sin vuestra paciencia, esfuerzo y dedicación esta tesis no habría sido posible. Hago extensivo este agradecimiento a la Dra. Teresita Gonzalez-Carreño, al Prof. Dr. Carlos J. Serna (estos años no habrían sido lo mismo sin los pinchitos en la mesa de la esquina) y a todos mis compañeros que forman o han formado parte del grupo "Nanocristales y Química": Marzia, Helena, María, Juan, Rocío, Carmenchurri, Amalia, Lucia, Vero, Gorka, Carlos, Watson, Gustavo,… Muchas gracias por amenizar las largas jornadas en el laboratorio, por vuestra ayuda y consejos con experimentos que se resistían a salir, por las alegrías compartidas cuando por fin salían y por todos esos buenos momentos fuera del laboratorio compartiendo comidas, cervezas, viajes…

Me gustaría agradecer a la Dra. María Varela y al Dr. Manuel Roldán su dedicación, paciencia y horas de trabajo para conseguir fotos bonitas durante mi estancia en Oak Ridge National Laboratory en 2014. Gracias a Lidia (por acogerme como si fuera de su familia, por las tardes de compras y zumba y por enseñarme algunos de los platos de la gastronomía peruana), a Leo (por ser el mejor room-mate que se puede tener, a pesar de nuestras diferencias, gracias por las excursiones, los conciertos, las conversaciones

nocturnas en la terraza y por enseñarme cosas de mi misma que no sabía) y a Mariona, Gabriel y Jaume (que llegaron desde España con aire fresco cuando más lo necesitaba). I would like to thank Dr. Matthew F. Chisholm for receiving me in the Electron Microscopy Group, and all the nice people that I met there (Andrés, Valeri, Charles, Juan Carlos, Juan, Anas, Ritesh, Rohan, Jordan, Ana, Janie, Qian, Bethany, Junhao, Mark, Chen, Amy, Jon, Qiao, Kuibo…). Thank you very much for making my stay in Knoxville an unforgettable experience.

También quiero darle las gracias a los técnicos del ICMM (Jose, Mª Carmen, Carolina, Pedro, Andrés y Javier) por su ayuda, accesibilidad y facilidades cuando lo he necesitado. A Paco por sus conversaciones, sus ánimos y sus enseñanzas sobre el microscopio de La Paz (da gusto como lo cuidas!). A la Dr. Patricia de la Presa por las medidas de magnetismo, a la Dr. María C. Serrano por todo el trabajo con células y a los investigadores de la Unidad de Imagen Avanzada del CNIC (Fernando, Bea, Juan y Marco) porque sin vosotros las tediosas jornadas de medidas de r_1 y r_2 hubieran sido insufribles. No quiero dejar de agradecer la buena acogida que me han dado en el grupo de Nanotecnología y Apoptosis del INCA en las excursiones fugaces que he realizado en estos últimos meses (especialmente a Lucia, Laura y Vanesa, gracias por vuestra ayuda con las medidas de hipertermia) así como a los técnicos del Laboratorio de Microscopia Avanzada (Rodrigo y Alfonso) por vuestra paciencia respondiendo todas nuestras dudas.

Desde un punto de vista más personal, hay mucha gente en el ICMM a la que dar las gracias:

- A mis compis del 268 (Juanmi, Hugo, Marzia, Sariña y María) gracias por vuestra paciencia infinita, por aguantar mis desvaríos y por compartir dudas y confidencias a partes iguales.
- A la gente de los desayunos (Sandra, Isabel, Virginia, María, Puerto, Wilmer, Vero, Kamel, Amalia y Luis) porque el café del CNB sabe mucho mejor y despierta mucho más cuando se toma a vuestro lado.
- Al grupo "los más chachi del ICMM" (Iván, Gelines, Bea, Violeta, Vanesa, Pau, Loreto, Gonzalo y Fede) con los que he tenido el placer de compartir comidas,

cervezas, salidas nocturnas y diurnas, desayunos post-Héroes… Gracias por todos los buenos ratos y por vuestro apoyo en este último tramo de la tesis… y que nos quiten lo bailao!

- A los teatreros y salseros (Jorge, Rafa, Nacho, Javi, Álvaro, Julián, Rafa J, Ramón, Harvey, Carmen, Armando, Bego, Elena, Fran, Eva, Celia, Pablo, Paloma, Sonia… y todos los demás que han participado en alguna de las hilarantes obras) gracias por hacerme reír a carcajadas, por quitarme la vergüenza, por conseguir que sienta que estoy en el sitio justo en el momento adecuado y por hacer que cada Navidad sea especial y diferente (porque el teatro es al IKKM como Cortilandia es a la Navidad o como el posado de Ana Obregón es al verano).

- Gracias a todas las personas que, aunque no han contribuido directamente en esta tesis, me han hecho la vida mucho más fácil en el ICMM (Pedro, Rocío, Cayetana, Paqui) y especialmente a Marisa por todas esas conversaciones que me han ayudado a despejarme por las tardes, pero sobre todo gracias por tus consejos sobre la vida, la tesis y los gatos.

- Y finalmente, a todos los que han pasado por el ICMM y que, aunque por diversas razones ya no están aquí, me han aportado grandes cosas y no solo a nivel científico (Rafa, WikIvan, Carmenchurri, Oscar, Hugo, Juanmi, Carlos, Ramón, Ricardo, Juan, Juanma…).

A los amigos que me llevan aguantando desde hace un puñado de años: Julián (eres un pilar muy importante en mi vida, has estado en mis mejores y en mis peores momentos y por eso me conoces como pocos, te quiero mucho y lo sabes!), Perce (químico y farandulero, gracias por las risas, los consejos y todos los buenos momentos que hemos compartido), Pe (siempre estás ahí aportándome calma, un punto de frikismo y haciéndome las preguntas adecuadas), Jessy (la alegría y el positivismo personificados, siempre dispuesta para charlar, eso sí con una cervecita fría en la mano), Alberto (eres una de las mejores personas que conozco, te deseo todo lo mejor de corazón), Belén y Cris (aunque nos vemos menos de lo que nos gustaría, nuestros reencuentros me trasladan directamente de vuelta a los años de la universidad).

A dos grandes mujeres a las que, aunque he conocido más recientemente, se han convertido en partes muy importantes de mi vida: Marzia (mi hermana mayor, mi mejor confidente, un apoyo incondicional, gracias por ayudarme a crecer día a día, espero poder seguir contando contigo siempre) y Rocío (gracias por recordarme que aún existen personas buenas, íntegras y nobles, me faltan palabras para agradecerte lo bien que te has portado siempre conmigo y lo que me has ayudado, espero poder hacerlo con hechos). Estoy muy orgullosa de vosotras y os admiro mucho. Gracias a las dos (y por supuesto a Marco y a Javi) por haberme dado la posibilidad de ser tía, no de sangre pero sí de corazón.

A otros compis de charlas, copas y risas que también han aportado su granito de arena durante estos cuatro años: Rebe (muchas gracias por tus sabios consejos, por los momentos de farra y cachondeo y por el diseño de la portada de esta tesis), Oscar (gracias por tu positividad, por tu buen rollo y por presentarme al cartuli de tu amigo; eres un buen guía de Montreal y mejor persona, si algún día tengo que hacer una mudanza ya sé a quién llamar), Charli (contigo he aprendido que los cambios, aunque parezcan duros al principio, pueden llegar a ser maravillosos, y sino… siempre nos quedará Benasque) y Ali (gracias por tu apoyo cuando lo he necesitado y por esas veladas de charlas filosóficas y juegos de mesa).

No quiero dejar de dar las gracias a mi equipo de Resakosas, que con los entrenamientos, partidos, post-partidos, cenas, karaokes y demás, me habéis ayudado a desconectar muchísimo del trabajo y de la tesis en estos dos últimos años.

A mi compañero de viaje, Miguel, gracias por tu apoyo, por conseguir sacarme siempre una sonrisa en los malos momentos y por hacer más felices los buenos. Te ha tocado aguantarme en la peor etapa de la tesis, gracias por tu infinita paciencia y por conseguir contagiarme con tu alegría. Es un placer poder compartir mi día a día contigo (y con nuestra Gordita).

Por último, quiero dar las gracias a las personas más importantes de mi vida, mis padres, que siempre han luchado para que sea feliz y pueda elegir mi propio camino, que han hecho posible que pueda estudiar y trabajar en lo que me gusta, que siempre me han

apoyado en todo… Sin vosotros esto no habría sido posible. No tengo palabras para expresar todo lo que os lo agradezco y lo que os quiero. Todo el mundo cree que sus padres son los mejores pero eso es, sin duda, porque no os conocen.

En fin, por todo lo que me habéis enseñado, por lo que me habéis aguantado, porque en mayor o menor medida habéis influido en mi vida y en mi carácter, por vuestro tiempo, por todo esto y mucho más… MILLONES DE GRACIAS A TODOS.

A mis padres

"Siempre se llega a alguna parte si se camina lo bastante"

Lewis Carroll, Alicia en el país de las maravillas

Contents

Resumen

Summary

List of abbreviations

Sample nomenclature

Resumen

Los sistemas coloidales constituidos por nanopartículas magnéticas constituyen en la actualidad uno de los sistemas más estudiados debido a su gran potencial en el campo de la biotecnología. El presente trabajo estudia comparativamente la síntesis y la caracterización química, estructural y magnética tanto de nanopartículas de tamaños menores de 15 nm obtenidas por la técnica estándar de coprecipitación, como de nanocristales magnéticos de óxido de hierro de mayor tamaño (30-100 nm) obtenidos por precipitación oxidante (capítulos 2-4).

Además, debido a la necesidad de aportar nuevas funcionalidades a las partículas para ampliar su campo de aplicación, se han sintetizado nuevos nanocristales bimetálicos adaptando la precipitación oxidante a este fin (capítulo 5).

Las muestras con mejores características se han dispersado y recubierto con diferentes moléculas para obtener suspensiones coloidales estables. Estas moléculas, además, presentan grupos terminales activos lo que permitiría una funcionalización posterior de las partículas con biomoléculas que proporcionen características especiales (capítulo 6).

Por último, debido a las propiedades que presentan las nanopartículas magnéticas relacionadas con el tratamiento y diagnóstico del cáncer, las muestras seleccionadas y estabilizadas se han evaluado para su utilización en tratamientos de hipertermia magnética y como agentes de contraste para resonancia magnética de imagen. También se han llevado a cabo estudios preliminares de toxicidad que han consistido en el análisis de la interacción de las nanopartículas con el medio celular y con diferentes líneas celulares (capítulo7).

Summary

Colloidal systems consisting of magnetic nanoparticles are currently one of the most studied systems due to their great potential in the biotechnology field. The present work comparatively studies the synthesis and the chemical and structural characterization of both, nanoparticles of sizes smaller than 15 nm obtained by the standard coprecipitation technique, and of larger iron oxide magnetic nanocrystals (30-100 nm) obtained by oxidizing precipitation (Chapters 2-4).

In addition, because of the need to provide new particle functionalities to expand their application field, new bimetallic nanocrystals have been synthesized by adapting the oxidant precipitation synthesis (Chapter 5).

Selected samples with the best characteristics have been dispersed and coated with different molecules to obtain stable colloidal suspensions. These molecules also present active terminal groups which would allow further particle functionalization with biomolecules that provide special characteristics for specific applications (chapter 6).

Finally, due to the properties of magnetic nanoparticles related to the treatment and diagnosis of cancer, selected and stabilized samples have been evaluated for use in magnetic hyperthermia treatments and as contrast agents for magnetic resonance imaging. Preliminary toxicity studies have been carried out by analyzing the nanoparticle interactions with cell media and different cell lines (Chapter 7).

List of abbreviations

AAN: Agglomerated average number

AC: Alternating current

APS: (3-Aminopropil)trietoxysilane

B: Hofmeister parameter

CT: Computed tomography

$D_{average}$: TEM mean value of caliper diameter

DEX: Dextran

DEMEM: Dulbecco's Modified Eagle's Medium

DMSA: Dimercaptusuccinic acid

DNA: Deoxyribonucleic acid

DTA: Differential thermal analysis

EELS: Electron energy loss spectroscopy

EGM-2: Endothelial growth media 2

EDX: Energy Dispersive X-ray spectroscopy

FCC: Face-centered cubic structure

FDA: Food and drug administration

FTIR: Fourier transform infrared

Hc: Coercivity

HAADF: High-angle annular dark-field imaging

HCP: Hexagonal close-packed structure

ICP-OES: Inductively Coupled Plasma – Optical Emission Spectrometry

IEP: Isoelectric point

ILP: Intrinsic loss power

JCPDS: Joint Committee on Powder Diffraction Standards

K: intrinsic magnetocrystalline anisotropy

k_B: Boltzmann constant

K_{eff}: Effective magnetic anisotropy

LRT: Linear response theory

MRI: Magnetic resonance imaging

Ms: Saturation magnetization

NIR: Near infrared absorption

NC: Nanocrystal

NP: Nanoparticle

OA: Oleic acid

P: Loss power density

PDI: Polydispersity index (defined as STD/$D_{average}$)

QD: Quantum dots

RCF: Relative centrifugal force

RT: Room temperature

SAR: Specific absorption rate

SP: Surface plasmon

STD: Standard deviation

STEM: Scanning transmission electron microscopy

T_1: Longitudinal relaxation time

T_2: Transversal relaxation time

T_B: Blocking temperature

TEM: Transmission electron microscopy

TGA: Thermogravimetric analysis (weight loss)

UV-VIS: Ultraviolet–visible spectroscopy

XRD: X-ray diffraction

ZFC-FC: Zero field cooling-Field cooling

Sample nomenclature

Nanocrystal samples were named by the following nomenclature:

MxAByC-D

- M: Secondary metal (Bi, Gd, Co, Au)
- x: Secondary metal proportion (%at)
- A: Anion (Cl^- = C, SO_4^{2-} = S, Br^- = B)
- B: Cation (Na^+ = N, K^+ = K)
- y: Ethanol proportion (0, 25, 50%)
- C: Fe (only in case of Fe excess)
- D: Coating molecules (APS, DMSA, DEX, OA)

1

Introduction

1. STATE OF THE ART

Nanoparticles are a special case of particles that possess at least one dimension in the nanometer range. What is interesting about nanoparticles is that they often possess unique physical properties, which are shape or size dependent and they can be controlled by varying the dimensions of the nanomaterial. This is not the case for bulk materials, whose intrinsic properties usually remain fixed, regardless of their dimensions. Magnetic materials in the nanometer scale exhibit fascinating properties such as giant magnetoresistance (Batlle, 2002; Levy, 2006), superparamagnetism (Faraudo, 2013), large coercivities and quantum tunneling of the magnetization (Hernandez-Minguez, 2005), which are due to finite-size and surface effects together with collective phenomena arising from interparticle interaction (Batlle, 2002). In addition and because of the unique combination of small size and exotic properties, magnetic nanoparticles (NPs) can be used for technological applications such as data recording, magnetic sealing in motors, magnetic inks for bank checks or bar codes, magneto-optical and biotechnology applications (Moser, 2002; Tartaj, 2006).

Nanoparticles of metal oxides, such as iron oxides, are particularly useful in several biological applications, for instance, magnetic resonance imaging (MRI), drug delivery, cell labelling, gene therapy and magnetic hyperthermia (selective destruction of cancer cells by the combination of AC fields and magnetic NPs). Iron oxides have many different compositions and multiple crystal structures (Ross, 2001). The most frequently encountered iron oxides are FeO, γ-Fe_2O_3, and Fe_3O_4, which have remarkably different magnetic properties. The wüstite-type FeO is paramagnetic at room temperature. Magnetite (Fe_3O_4) is ferromagnetic with a half metallic structure and its conductivity results from the electron exchange between Fe^{2+} and Fe^{3+}. The cubic maghemite (γ-Fe_2O_3) obtained by oxidation of magnetite has the same structure with iron (III) vacancies, is also ferromagnetic and commonly used in recording tapes (Jeong, 2007). Magnetic iron oxides are popular materials for biomedical applications because of their biocompatibility and good magnetic properties. However, to improve the magnetic properties, other metal ions such as manganese, zinc and cobalt can be chosen to dope

them (Lee, 2007b). The magnetization of Fe_3O_4 arises from antiferromagnetic coupling (superexchange through oxygens) between the Fe^{3+} ions in octahedral and tetrahedral interstices, leaving the magnetic moments of the Fe^{2+} ions (in octahedral positions) responsible for the magnetization of the unit cell (Reddy, 2012). The solid solution magnetite/maghemite present the same typical spinel crystal structure, with oxygen ions forming a close-packed cubic lattice, with iron ions located at the interstices and some vacancies to balance the partial oxidation of Fe^{2+} leading to a partial reduction of the magnetization with respect to pure magnetite.

The magnetic behavior of magnetite-maghemite nanoparticles is controlled by the oxidation degree and the particle size that originate its superparamagnetic character (thermal fluctuation of particle spins at room temperature). Superparamagnetic particles have the peculiar property to orient their magnetic moments in the presence of an external magnetic field and become random when it is removed. This is useful for in vivo applications because enable the preparation of stable colloids in absence of magnetic field. These colloids could be intravenously injected and fixed to the target zone by an external magnet. After the therapeutic effect is completed (by the drug contained in the coating for example) the external magnet could be removed and the nanoparticles that no longer show a magnetic moment can be resuspended in the blood and eliminated (Mahmoudi, 2011).

The chemical synthesis of magnetic NPs is an emergent and diverse area of research, driven by the need to understand the relationship between a particle's size and morphology and its physical properties. Understanding this often complicated relationship enables researchers to tailor the properties of particles for a specific application. This will require the non-trivial task of synthesizing homogeneous 'high quality' NPs; that is, particles which have a narrow size distribution, well-controlled shape and high crystallinity throughout the sample. Wide size distributions are undesirable, as many NP properties are size dependent and hence products with wide size distributions will have ill-defined physical properties.

1.1. Nanoparticles versus nanocrystals

Nanocrystals (NCs) are a special class of nanoparticles with improved crystallinity and the term is commonly applied to nanoparticles of metals, oxides, nitrides and chalcogenides that are often single crystals (figure 1.1) (Rao, 2007). Besides the desired properties of NPs related with quantum effects and high specific surface, other important properties suffer a significant damage when the particle size is extremely low. This is the case of the magnetic properties and in particular the saturation magnetization that for particles below 5 nm is extremely low and they need large saturating fields (Morales, 1999). In contrast to that, magnetic nanocrystals with particle sizes of 12 – 34 nm combine the superparamagnetic behavior (Coey, 2010) with a saturation magnetization close to the bulk value and smaller saturating fields (Veintemillas-Verdaguer, 2014).

NANOCRYSTALS

NANOPARTICLES

MORE ORDERED

High surface energy
Round shapes

Lower surface energy
Less rounded shapes
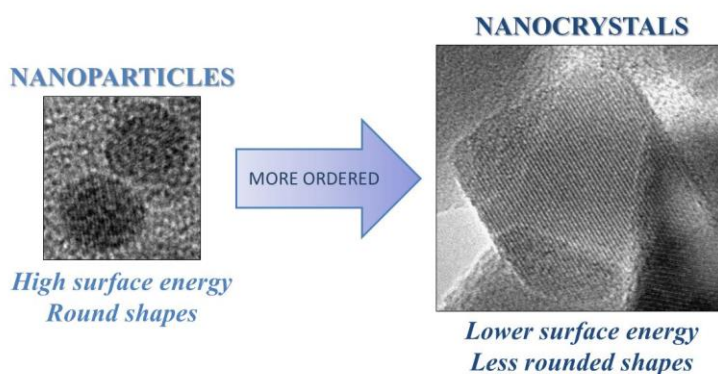
Figure 1.1. *Differences between nanoparticles and nanocrystals.*

Therefore, the main difference between NCs and NPs is that the former have less rounded shapes and larger sizes and present magnetic susceptibility values and saturation magnetization higher than the NPs. Such materials have been investigated in lesser extent than NPs, whose maximum size is around 12 nm, in reference to their efficiency in biomedical applications (Jun, 2005). Recently NCs of around 30 nm, near the multidomain limit, have been evaluated as contrast agents for MRI and magnetothermia heaters, showing very promising results in spite of the difficulties of their colloidal stabilization

(Gonzalez-Fernandez, 2009; Salas, 2012; Marciello, 2013). However, in the literature many authors use indistinctly the terms nanoparticle and nanocrystal to refer to nanoparticulate systems with sizes smaller than 1 micron.

1.2. Multifunctional magnetic colloids

Magnetic NPs and NCs are usually used in the form of colloids. A magnetic colloid is a suspension of nanometric ferromagnetic or ferrimagnetic particles (magnetic phase) in a carrier liquid (non-magnetic phase). Such systems are highly susceptible to magnetic fields (Williams, 1993). Colloidal NCs or NPs are among the most modular and versatile nanoscale materials, due to both their compositional and morphological tunability and their "free" (unsupported) colloidal state that allows their deposition onto various surfaces or integration into various matrices. Beginning in the 2000s and until now, a multitude of metals, metal oxides, and semiconductors have been developed in the form of isotropic and anisotropic nanocrystals colloids (Kovalenko, 2015).

Magnetic colloids have found widespread use in many traditional areas including magnetic data storage, ferrofluids technology, magnetorheological polishing, and energy storage; they also hold great potential for many other applications related to biomedical research (Bulte, 2001; Spaldin, 2003; Gupta, 2005). To this end, superparamagnetic colloids have been exploited for labeling and separation of DNAs, proteins, bacteria, and various biological species, as well as applied to magnetic resonance imaging (MRI), guided drug delivery, and hyperthermia treatment of cancer (Jeong, 2007).

Typically, magnetic colloids for biomedical applications are composed of a magnetic core, usually a ferrite and most probably iron oxide, modified by a biocompatible material (Ling, 2015; Marciello, 2016). The coating acts not only as a hydrophilic layer to render colloidal stability, avoid aggregation and prevent any change of the original structure or biodegradation of the nanoparticles, but also as a platform for functionalization for specific applications within the biomedical area. Thus, the surface modification of magnetic NPs in aqueous media is crucial to obtain magnetic colloidal

ferrofluids that are stable against aggregation in a biological medium and under the action of external magnetic fields (Pankhurst, 2003; Sun, 2008; Na, 2009; Kumar, 2011).

For bioapplications, magnetic colloids should show these important features: (1) biocompatibility and no toxicity, (2) colloidal stability under physiological conditions, (3) proper particle size, (4) adequate magnetic properties, (5) suitable coating to avoid aggregation and to protect the magnetic core against degradation, and (6) opportune surface modification (Marciello, 2016).

Colloidal NPs and NCs with increasingly chemical and structural complexities and high level of sophistication are being widely studied nowadays. This evolution toward more complex nanosystems, responds to the growing demand not only for optimized their characteristics and properties, but also for obtaining multifunctional platforms that can be used in different applications. To this end, compositional modulation, electronic doping and tailored surface chemistries are now feasible for a broad range of inorganic compounds (Kovalenko, 2015). In particular important efforts are devoted to the combination of medical imaging and therapeutic functionalities in the same particle with the aim of developing theranostic agents, able to treat the illness and monitor the response to the therapy in real time (Cole, 2011; Singh, 2014). Currently, there are two strategies to fabricate magnetic nanoparticle-based multifunctional nanostructures. The first, molecular functionalization, involves attaching antibodies, proteins, and dyes to the magnetic nanoparticles. The other method integrates magnetic nanoparticles with other functional nanocomponents, such as quantum dots (QDs) or metallic nanoparticles (Au, Ag). Because they can exhibit several features synergistically and deliver more than one function simultaneously, such multifunctional magnetic nanoparticles could have unique advantages in biomedical applications (figure 1.2) (Gao, 2009).
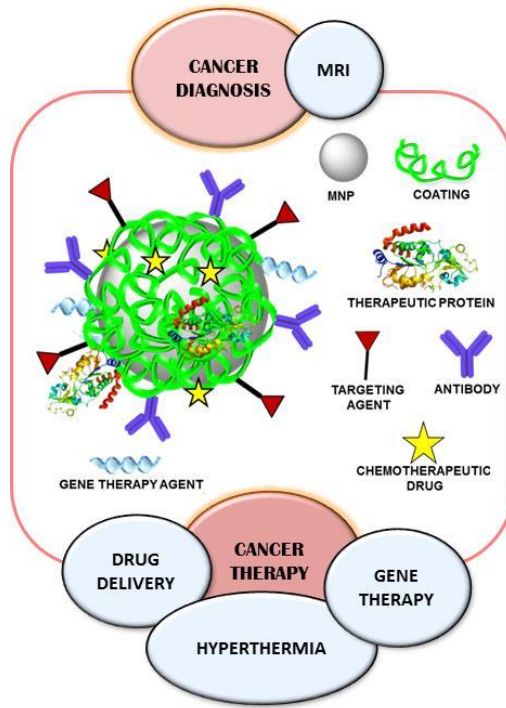
Figure 1.2. *Scheme of therapeutic multifunctional iron oxide nanoparticles and their application in biomedicine (Marciello, 2016).*

From the materials point of view, NCs due to its bigger size and predictable physical properties have good potentiality to develop multifunctional colloids (Rivera-Gil, 2013). Thus, even when the inorganic NC cores act only as passive carriers, the possibility to link different functional molecules to their surface enables multifunctionality straightforwardly. Functional molecules may involve ligands for specific targeting, for reducing interactions with the immune system, and for providing contrast for imaging, etc. However, the NC cores may also introduce functionality, such as fluorescence, superparamagnetism, or plasmon resonance absorption. Therefore, with inorganic cores and organic shells together, NCs are suitable for combining different functionalities. For example, by combining fluorescent, magnetic, or radioactive cores with fluorescent, magnetic, or radioactive shells, NCs can be detected with several imaging modalities such as fluorescence microscopy, magnetic resonance imaging (MRI), or single-photon emission computed tomography (Ali, 2011; Jing, 2014; Kovalenko, 2015).

In addition, NCs fulfill theranostic purposes, first, by helping to diagnose tumor tissue by providing contrast in MRI to visualize it (Yu, 2011) and, second, by facilitating therapy (i.e., tumor ablation) by local hyperthermia (Lartigue, 2012; Kovalenko, 2015) (figure 1.3). Moreover, hyperthermia generated by an external magnet can trigger the release of chemotherapeutics (Raju, 2015). Efforts in the increase of heat power at low dose to reduce toxic side effects are currently done. In this context, successful approaches have been demonstrated in terms of exchange-coupled core shell architectures (Lee, 2011) and optimized shapes (Alphandery, 2011; Guardia, 2012).
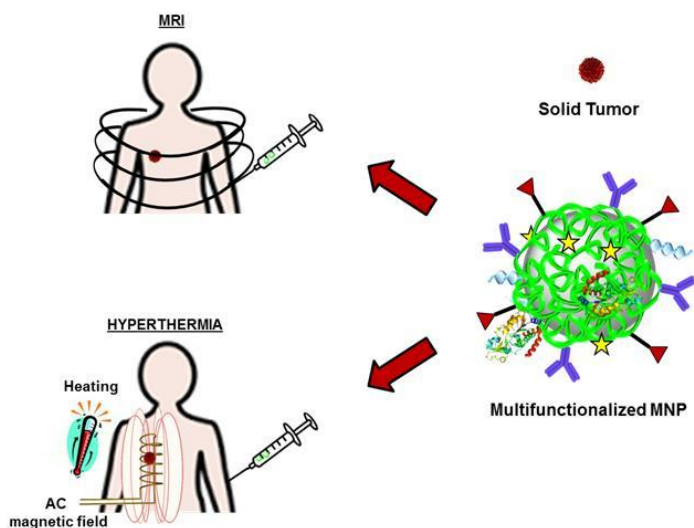
Figure 1.3. Schematic representation of NPs application in diagnosis and therapy (Marciello, 2016).

To integrate functional materials into one entity, several types of iron oxide-based nanoarchitectures including core/shell (Mukh-Qasem, 2005), Janus (Wu, 2009) and satellite nanostructures (Mornet, 2004; Santra, 2005) have been developed (figure 1.4). The resulting heteronanocomposites could exhibit superior properties due to the synergistically combinations of magnetic, optical, electrical, and other properties of each entity, and have

shown great potential for biomedical applications (Sun, 2008). However, the main problem is that sometimes different components in multifunctional NPs interact negatively with each other, which will weaken or reduce the functionality of each unit (Zhang, 2013a).

Core-shell nanoparticles   **Magnetic Janus nanoparticles**   **Core-satellite nanoparticles**
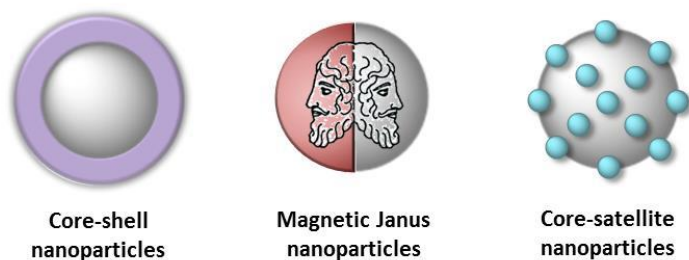
Figure 1.4. *Scheme of different iron oxide-based nanoarchitectures.*

Core/shell structure is the most common type of multifunctional NPs. This kind of nanoarchitecture is usually a magnetic core surrounded by other component that may be fluorescent molecules, metal nanoparticles or semiconductor nanocrystals, polymers, etc. (Wang, 2004; Ding, 2012; Zhang, 2012). Magnetic Janus NPs consist of an iron oxide particle linked to other particle of a material with different physicochemical properties on opposite sides. These anisotropic/asymmetric particles present reduced contact of the combined individual components in contrast with a core/shell structure (Glotzer, 2007), so that their fingerprint optical, magnetic, and electronic properties are not often interfered with or completely lost (Mokari, 2004; Jin, 2009). Core-satellite NPs, another interesting model of multifunctional NPs, possess one single core with the attachment of various smaller particles through electrostatic interactions or covalent bonds. The most common core-satellite particle is Fe_3O_4-noble metal composite (Wang, 2008; Xuan, 2009). Usually this kind of particle is the intermediate state previous to the formation of the core/shell NPs. However, core-satellite NPs have the advantage of the presence of uncovered core surface eligible for further functionalization and a high surface area of satellite material for specific functions. Moreover, this structure can reduce the interference of two individual components (Zhang, 2013a).

2. MOTIVATION

It is well known that the large variability of magnetic properties observed in NPs bigger than a few nanometers are related to extrinsic structural features rather than being originated form intrinsic size dependent properties (Hernandez-Minguez, 2005; Levy, 2006; Faraudo, 2013). These structural features, such as shape, size, size distribution, crystallographic defects, polycrystalline nature of the NPs, lack of crystallinity at the particle surface, etc., are a consequence of subtle differences in the synthesis method. Therefore, for most applications and fundamentally in the case of biomedical applications where the requirements are highly demanding (size, uniformity, and crystallinity of the nanoparticles are critical to reduce the therapeutic dose and eventual collateral effects), the choice of a suitable synthesis method is of key importance to obtain monodisperse NPs of high-crystalline quality.

In this thesis we focused on synthesis routes in aqueous media, which can be considered as green routes due to the high availability and low cost of its reagents, relatively low temperature and the overall ease of scaling-up the process. We have used two approaches: the first based on the precipitation of a mixed Fe^{2+}/Fe^{3+} solution, the so-called coprecipitation route, commonly used for the industrial production of magnetic NPs up to 15 nm (used as a reference), and the second based on the partial oxidation of a Fe^{2+} salt, the so-called oxidative precipitation that is less studied and enable to obtain bigger nanoparticles that due to their shape and magnetic performance will be called nanocrystals. **The first hypothesis to be tested in this thesis is the fact that nanocrystal sizes are influenced by counterions and cosolvents in addition to the basic synthetic parameters such as temperature, iron concentration and nature of the oxidant.** For this purpose we have studied the formation mechanism of NCs in the presence of different anions and cations. The colloidal and magnetic properties were compared with those for NPs.

It is known the possibility of partial substitution of iron with other transition metal in the coprecipitation approach, which results in ferrite nanoparticles (Spaldin, 2003; Lee, 2007b). The ferrites may display enhanced properties, such as higher magnetic

permeability or electrical resistivity than those of magnetite (Jeong, 2007). The capability of oxidative precipitation to exploit this procedure in the production of core shell, solid solutions or other nanostructures is yet unexplored in spite of the promising results attained in the case of the partial substitution of iron by bismuth (Veintemillas-Verdaguer, 2015). **The second hypothesis to be tested in this thesis is concerned with whether the oxidative precipitation is able to produce bimetallic nanostructures and ferrite solid solutions when part of the iron is substituted by a second metal.**

We have prepared Co bimetallic magnetite NCs ($Co_xFe_{3-x}O_4$) in the search of high values of magnetic anisotropy induced by a modification of the electronic density, and defects and vacancies in the crystal structure, which make them potential candidates for future highly sensitive magnetic nanodevices in similar way than Co-ferrites NPs do (Schwertmann, 2008; Cullity, 2011). On the other hand, we have chosen other transition metals and rare earth elements (Au, Bi, Gd) to obtain nanocrystals that could exhibit several features synergistically and could be followed by other imaging techniques such as optical, computed tomography (CT) or MRI (Gao, 2009). The exploration of both hypothesis will lead to a deeper understanding of the possibilities of the oxidative precipitation to produce tailor made magnetite nanocrystals and multifunctional magnetic nanoplatforms in a single step.

3. OBJECTIVES

The main objectives of this research are:

1. Production of magnetic nanoparticles and nanocrystals and comparison of their physical properties by coprecipitation and oxidative precipitation in aqueous medium.

    (i)   Preparation of standard magnetic nanoparticles by coprecipitation

    (ii) Study of the effect of counterions and ethanol on the size, shape and nature of the nanocrystals produced by oxidative precipitation.

(iii) Study of the reaction mechanism involved in the synthesis of nanocrystals by oxidative precipitation.

(iv) Characterization and comparison of the magnetic properties of the synthesized nanoparticles and nanocrystals.

2. Production of bimetallic nanocrystals and characterization of their nanostructures, containing the following secondary metals:

    (i) Bismuth

    (ii) Gadolinium

    (iii) Cobalt

    (iv) Gold

3. Coating of nanoparticles and nanocrystals to obtain stable magnetic colloidal systems by standard methods.

4. Evaluation of the nanoparticles, nanocrystals, cobalt and gadolinium magnetite bimetallic nanocrystals for hyperthermia.

5. Evaluation of the nanoparticles, nanocrystals, cobalt and gadolinium magnetite bimetallic nanocrystals as contrast agents for MRI.

6. Preliminary study of the nanoparticle toxicity by analyzing its interaction with cell media and different cell lines.

2

Magnetic nanoparticles

1. INTRODUCTION

Magnetic NPs were used in this work as reference and synthesized by a traditional method as it is the coprecipitation. This process in aqueous solution is perhaps the simplest and the most cost efficient chemical pathway to synthesize superparamagnetic iron oxide NPs (average diameters are typically below 20 nm) (Massart, 1981). Nowadays, most of the commercially available iron oxide nanoparticles are prepared by this method.

The method is based on the chemical reactions carried out in aqueous solution, allowing both the nucleation and growth of iron hydroxide nuclei to be controlled (Colombo, 2012). The synthesis procedure consists in the mixture of aqueous Fe^{2+}/Fe^{3+} salt solutions with a base (equation 2.1). Under these conditions, magnetite NPs are formed by aggregation of primary particles within a $Fe(OH)_2$ gel. Then, the precipitate is isolated by magnetic decantation or centrifugation, and treated with concentrated base or weakly acid solutions to obtain a ferrofluid electrostatically stabilized. Alternatively, the iron hydroxide precipitate can be sterically stabilized to the resulting Fe_3O_4 or other ferrites by heating in the presence of a suitable surfactant.

$$Fe^{2+} + 2Fe^{3+} + 8OH^- \rightarrow Fe_3O_4 + 4H_2O \qquad (2.1)$$
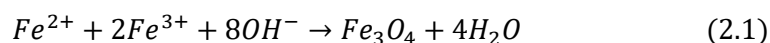
Depending on the mixing rate and proportion of ferrous and ferric salts in the aqueous medium and on other experimental conditions (ionic strength and pH of the medium, stirring rate, presence of oxygen, nature of the salts, temperature, nature and concentration of the alkali medium, or nature of the surfactant) a variety of iron oxide particles with suitable diameter and relatively narrow particle size distribution, magnetic responsiveness, and surface properties can be obtained (Si, 2004; Lee, 2007a). The coprecipitation approach offers a wide range of advantages including: the use of cheap chemicals and mild reaction conditions; the possibility to perform direct synthesis in water; the ease scale up, the production of highly concentrated ferrofluids thanks to the high density of surface hydroxyls able to be charged under non neutral pH conditions.

Nucleation and crystal growth are the two underlying fundamental processes in nanoparticle synthesis. Taking into consideration the classical model of crystallization

proposed by LaMer and Dinegar (LaMer, 1950), monodispersed nanoparticles can be produced by a single short burst of nucleation, which occurs when a solution reaches its critical supersaturation concentration (figure 2.1). The obtained nuclei undergo a growth as a result of solute/ions diffusion from the solution to the nuclei surface, until a suitable size is reached. To achieve monodispersity, it is important to ensure that secondary nucleation does not occur during crystal growth phase.
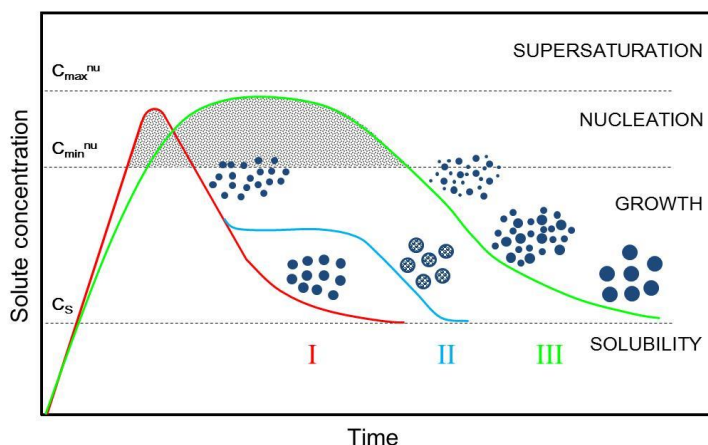
Figure 2.1. *Formation mechanism of uniform particles in solution: curve I (red): single nucleation and uniform growth by diffusion (classical model of LaMer and Dinegar); curve II (blue): nucleation, growth and aggregation of smaller subunits; curve III (green): multiple nucleation events and Ostwald ripening growth (Marciello, 2016).*

Particulate nanophases have high energy and secondary processes can happen after the primary nucleation during formation of uniformly dispersed nanoparticles. The best known is Ostwald ripening, a self-reforming process whereby small nuclei crystals formed get re-dissolved and deposited onto larger nuclei, forming large uniform crystals. More recently aggregation of smaller units has been reported to result in uniform-sized nanoparticles when it takes place under control (Morales, 1992; Schladt, 2011; Wahajuddin, 2012).

To prepare the as synthesized magnetic NPs for coating an acid treatment is carried out in the pharmaceutical industry, for example for the production of commercial contrast agents for MRI (Port, 2009). This acid treatment is a careful oxidation and partial

dissolution process that takes place under acid media (Tourinho, 1990; Bee, 1995; van Ewijk, 1999; Gomes, 2008). When properly optimized it leads to the improvement of magnetic properties and colloidal stability of the magnetic NPs (Costo, 2012). During the process there is a rearrangement and recrystallization of the disordered surface shell. The recrystallization of the surface increases the size of the magnetic crystalline core with no increase in the particle size. Thus, magnetic quality parameters as the saturation magnetization and the low field susceptibility are significantly improved. Moreover, the treatment seems to reduce the interparticle interactions. Most importantly, the acid treatment modifies the particle surface so that it becomes a highly hydrated shell. This increase in the hydration degree increases the surface charge density and thus, enhances the colloidal stability of the sample. Finally, the treatment likewise allows activating the particle surface for further coating. As a bonus, this procedure also allows the complete oxidation of magnetite (contains both divalent and trivalent ions) to maghemite (with all Fe in the trivalent state), which is required to obtain a safer and more stable iron oxide NPs.

2. EXPERIMENTAL SECTION

Maghemite nanoparticles were obtained following the Massart coprecipitation protocol (Massart, 1981). Some modifications were introduced to control particle size between 6, 8, 11, 13, and 14 nm and to reduce size distribution below polydispersity degree of 0.2 (standard deviation/mean size) (Costo, 2012).

2.1. Nanoparticle synthesis by coprecipitation

Magnetite (Fe_3O_4) nanoparticles were synthesized by coprecipitation of 425 ml of a mixture of $FeCl_3·6H_2O$ (0.09 mol) and $FeCl_2·4H_2O$ (0.054 mol) in 75 mL of alkaline medium (figure 2.2). The particles size can be tuned by the nature of the basis used in the coprecipitation, the addition rate, and the aging time (Morales, 1999). Thus, for the synthesis of the smallest particles fast addition rates (40 ml/s) and KOH (25%) and

NH$_4$OH (25%) as alkaline solutions were used to produce the 6 and 8 nm particles, respectively. Slow addition rates (0.2 ml/s) and NH$_4$OH solutions were used to synthesize all the other samples (11, 13, and 14 nm). The largest particles, 13 and 14 nm, were obtained by subjecting the 11 nm particles to a heating process at 90 °C for 1 and 3 h, respectively. After every synthesis the particles were washed three times with distilled water and the help of a 55 mm diameter 25 mm high 0.5 T NdFeB magnet for magnetic decantation (de la Presa, 2012).
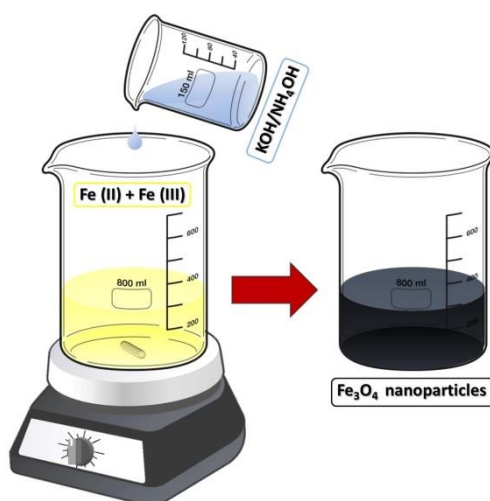
Figure 2.2. *Scheme of the experimental conditions for the coprecipitation synthesis.*

2.2. Acid treatment

A standard protocol was used (Gazeau, 2008; Costo, 2012) consisting of adding 300 ml of HNO$_3$ (2 M) to the particle suspension, and the mixture was stirred for 15 min. Then, nitric acid was removed by magnetic decantation, and 75 ml of Fe(NO$_3$)$_3$ (1 M) and 130 ml of water were added to the particles. The mixture was heated up to boiling temperature and stirred for 30 min (van Ewijk, 1999; Costo, 2012). The particles were then cooled down to room temperature, and by magnetic decantation the supernatant was substituted by 300 ml of HNO$_3$ (2 M) and stirred for 15 min (figure 2.3). Finally, the

particles were washed three times with acetone and redispersed in water. A rotary evaporator was used to remove any acetone waste and concentrate the sample.
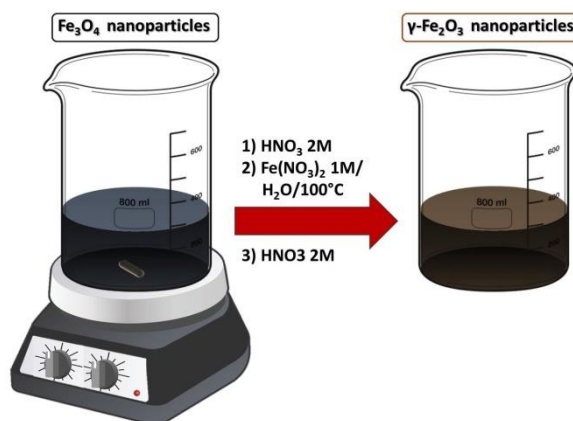
Figure 2.3. *Scheme of the experimental conditions for the acid treatment of the samples prepared by the coprecipitation process.*

Suspensions at high Fe concentration (over 200 mg Fe/ml) were obtained following the previous procedures in a reproducible way (it was obtained approximately 4 g of sample per batch) and it was used thorough this thesis as reference materials.

3. SAMPLES CHARACTERIZATION

3.1. Structural and morphological characterization

Figure 2.4 shows the X-ray diffractograms for the different uncoated iron oxide nanoparticles obtained. X-ray diffraction (XRD) has been used both to identify the nature of the material and to determine the particle size. All the peaks are ascribed to a spinel structure, most probably maghemite (γ-Fe$_2$O$_3$ JCPDS 39-1346).

The width of the peaks in the diffractogram is related to the nanoparticle crystal size, so that the smaller the peak width the larger the crystal size. Therefore, it can be seen that the diffraction peaks become broader as the NP size decreases. Using the Scherrer

equation for the width values obtained from the main (311) peaks for samples C6, C8, C11, C13 and C14, crystal sizes of 5.7 nm, 8.0 nm, 10.6 nm, 12.3 nm and 13.0 nm are obtained for the samples C6, C8, C11, C13 and C14, respectively.
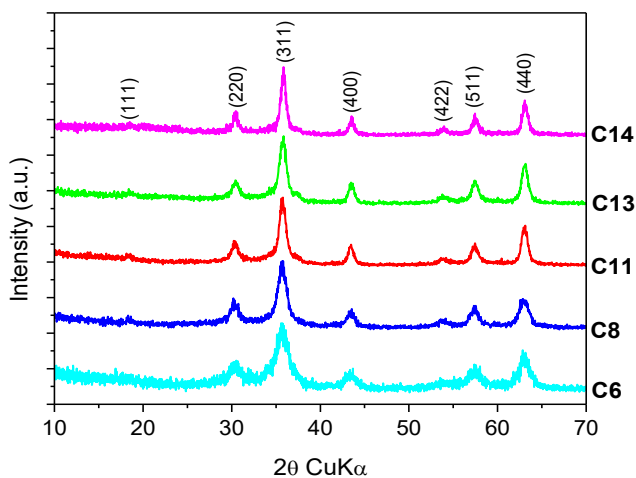
Figure 2.4. *XRD patterns for samples C6 to C14 prepared by the coprecipitation process. (hkl) indices are included for peak identification.*

Transmission electron microscopy (TEM) images were used to observe the nanoparticle morphology (size and shape) as well as the particle size distribution. Figure 2.5 shows nearly spherical uniform nanoparticles. Also, a gradual increase in the particle size can be observed from samples C6 to C14, which is consistent with observations from the X-ray diffractograms.

Statistical analysis of the particle size data obtained from TEM micrographs was carried out. The average particle size and distribution were evaluated by measuring the largest internal dimension of at least 300 particles for each sample, in order to have enough statistical validity. The different size populations were organized in a histogram and were adjusted to a log-normal function (O'Grady, 1983), as described above for other nanoparticle systems (Blanco-Mantecón, 1999).
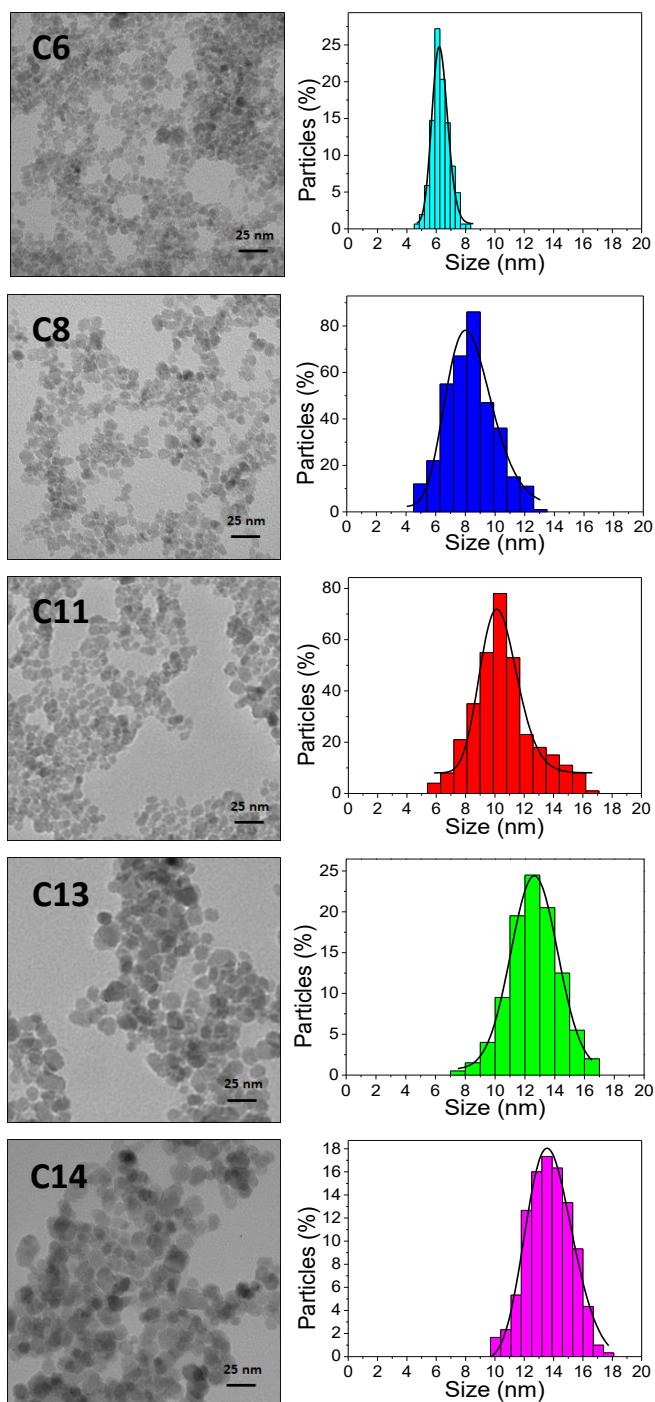
Figure 2.5. TEM *micrographs of the samples prepared by the coprecipitation process (left) and histograms of the particle size distribution (right).*

Table 2.1 shows the size and size distribution obtained for each sample by X-ray diffraction and transmission electron microscopy.

Sample	D_{XRD} (nm)	D_{TEM} (nm)	STD
C6	5.7	6	0.22
C8	8.0	8	0.24
C11	10.1	11	0.23
C13	12.3	13	0.21
C14	13.0	14	0.25

Table 2.1. *DRX and TEM sizes obtained for different samples prepared by the coprecipitation process.*

The similitude of XRD and TEM size confirms the monocrystalline nature of the samples. It should be noticed that the size calculated by XRD gives lower values than those observed by TEM. This is because the Scherrer equation measures crystallite size while from the micrographs what is determined is the particle size. The particle size includes the amorphous surface layer always present in NPs that do not contribute to the X-Ray diffraction. In any case the small differences could be within the experimental error of the evaluation of the TEM micrographs.

3.2. Chemical characterization

Fourier transform infrared (FTIR) spectra of uncoated samples were obtained in the range between 1750 and 400 cm^{-1} (figure 2.6). The observed bands are compared with bibliographic data and properly assigned. The small shifts in some of the IR absorption bands are induced by the degree of crystallinity and by the appearance of adsorbed impurities which are characteristics of the synthesis method.

In the high frequency region, a band at 1625 cm^{-1} was observed and corresponds to deformation (δOH) water vibrations. The band at 1383 cm^{-1} is characteristic of nitrates, which appears because of the use of nitric acid during the acid treatment.
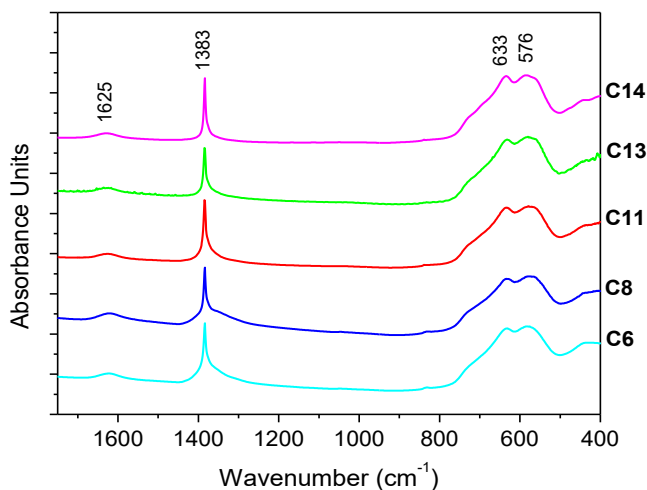
Figure 2.6. *Infrared spectra of the samples synthesized by the coprecipitation process.*

In the low frequency region, the bands between 700 and 300 cm^{-1} are associated with the vibration modes of the iron oxide, specifically Fe-O stretching. The bands around 633 cm^{-1} and 397 cm^{-1} correspond to symmetric and antisymmetric vibration of the Fe-O, respectively. The intensity and position of the bands are typical of maghemite (Cornell, 2006). It is noteworthy that the degree of order in the nanoparticle structure depends on the synthesis method and the particle size. The smaller the particle, the higher the disorder and the width of these absorption bands (Morales, 1994).

Thermogravimetric analyses (TGA) of all samples were carried out from room temperature up to 900 °C in air atmosphere and allowed obtaining information about de loss weight with the temperature (figure 2.7). Samples show a higher weight loss when the particle size decreases, about 5 % to 10 % for samples from 14 nm to 6 nm, respectively, due to an increase of the NPs specific surface area and its high water content. In the differential thermal analysis (DTA) of the samples a small endothermic peak can be observed in all cases at about 50 °C, which is associated with weight loss (TGA) and it is caused by desorption of water molecules. Moreover, in all samples an exothermic peak appears between 400 and 600 °C, which is not associated with weight loss, and it is related to the structural phase transition of maghemite to hematite (Cornell, 2006). Maghemite (γ-

Fe$_2$O$_3$) has the oxygen atoms arranged in a face-centered cubic structure (FCC) as an inverse spinel phase. When the temperature rises above a certain value (260 °C for bulk materials), the nanocrystalline structure of metastable γ-Fe$_2$O$_3$ becomes stable hematite (α-Fe$_2$O$_3$), in which the oxygen atoms are arranged in a hexagonal close-packed structure (HCP).
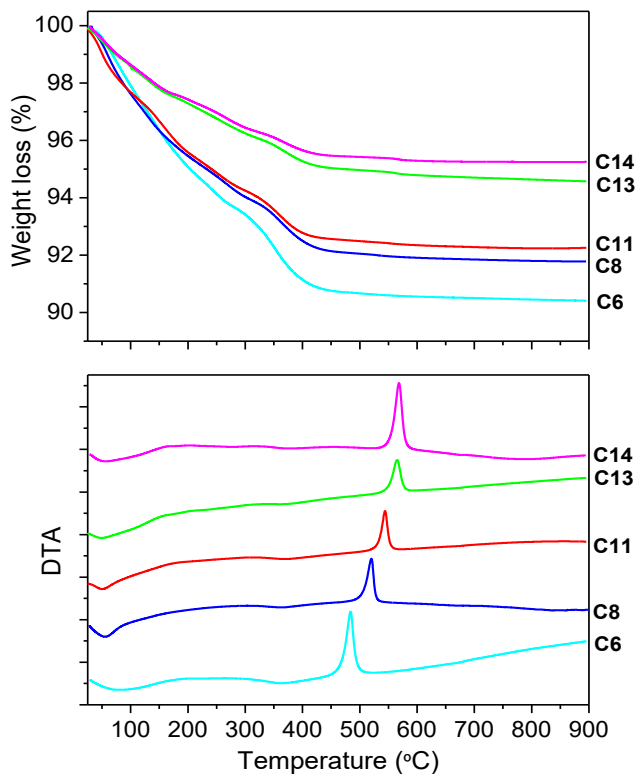
Figure 2.7. *Results of DTA-TGA of samples synthesized by the coprecipitation process.*

Differences in peak intensity are simply related with differences in the amount of sample analyzed in each case and are not relevant. On the contrary, the transition temperature has been related to the particle size, the smallest ones being transformed at lower temperatures (Feitknecht, 1967). This is because the increase in surface-to-volume ratio at reduced dimensions decreases the activation energy of the system, facilitating phase transitions (Gnanaprakash, 2006).

3.3. Magnetic characterization

The study of the magnetic properties of the samples shows not only the magnetic behavior of the samples as a function of field and temperature but also it can help to get a better understanding of the nanoparticles structure. For this reason, magnetization curves and zero field cooling-field cooling curves were measured.

A large amount of information can be obtained on the magnetic properties of a material by studying its magnetization curve or hysteresis loop. These measurements show the relationship between the induced magnetization and the applied field. The loop is generated by measuring the magnetic moments of the nanoparticles while a static magnetic field is applied. The higher the value of the applied field, the stronger the magnetization is. There is a sufficiently high field where almost all of the magnetic moments are aligned and where a small additional increase in the magnetizing force will produce a very little increase in the total magnetization. At this point, the material has reached magnetic saturation (M_S). If the material is superparamagnetic, the magnetization will return to zero when the applied field is removed. At this instant, all the magnetic moments are no longer aligned and the total magnetization is zero. We can say then that the material shows reversible magnetic behavior at that temperature.

Magnetization curves of C8, C11 and C13 samples (considered as representative of the whole set of samples) were measured at room temperature and 10 K (Figure 2.8). C6 and C14 samples are not included in this study because, C6 particles have a very low magnetic response, and C14 particles are similar to C13 sample, but their polydispersity is larger.

Hysteresis loops measured at 250 K for all samples in the form of aqueous suspensions showed nearly superparamagnetic behavior with negligible coercivity (<0.8 kA/m) and remanent magnetization. At 10 K and 4000 kA/m, the magnetic saturation is 68-70 Am^2/Kg for magnetic NPs sizes larger than 8 nm. At low temperature, the coercivity increases with size: 8, 16 and 24 kA/m for the 8, 11 and 13 NPs sizes, respectively.
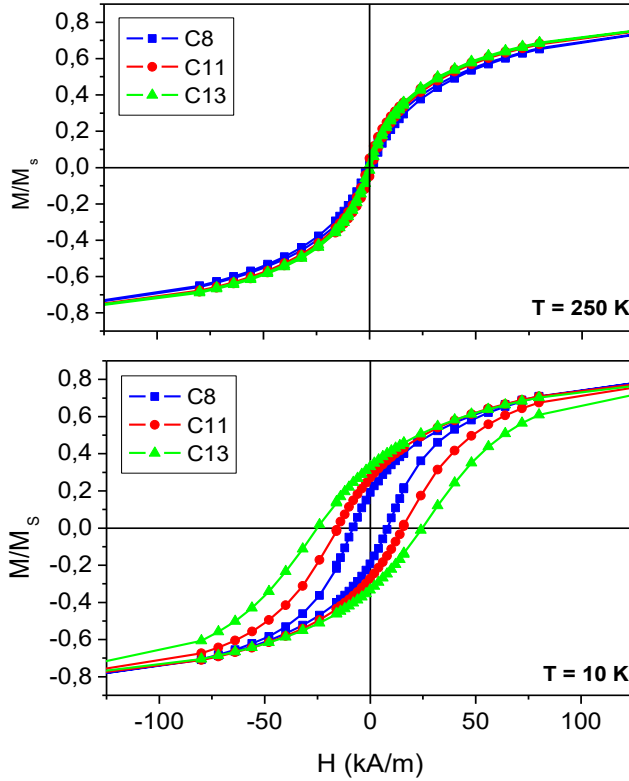
Figure 2.8. *Hysteresis loops for 8, 11 and 13 nm nanoparticles synthesized by the coprecipitation process. Normalized hysteresis curves at 10 and 250 K.*

Due to the small NPs sizes, the magnetic behavior is in the single domain regime; therefore, the coercive field depends on effective magnetic anisotropy K_{eff}, saturation magnetization M_S, particle volume V, and absolute temperature T as shown in equation 2.2 (Hernando, 1995).

$$H_C = \left(\frac{2K_{eff}}{\mu_0 M_S}\right)\left(1 - \left(\frac{25 k_B T}{K_{eff} V}\right)\right) \tag{2.2}$$

If M_S and K_{eff} are volume-independent, then the coercive field decreases with size as observed for our samples. However, it has been reported that for small magnetic NPs the coercivity increases with size due to surface anisotropy contribution that increases K_{eff} to much larger values than those expected for the bulk magnetocrystalline anisotropy (Del

Bianco, 1998; Morales, 1999; de la Presa, 2008). As in our samples M_S is almost the same for the three sizes, then the size dependence of the coercivity observed here (decrease of the coercivity with decreasing size) reflects the high degree of crystallinity of these particles and small surface anisotropy coherent with a K_{eff} nearly volume-independent.

Zero Field Cooling-Field Cooling (ZFC-FC) curves were carried out to determine the magnetic sizes profile of the samples as well as to confirm the superparamagnetic nature of the samples at room temperature. Prior to the description of the measured ZFC-FC curves, we will briefly explain the basic physical significance of these curves.

- ZFC: At room temperature, the moments are randomly aligned. After zero-field cooling down to 10 K, the randomly aligned moments become blocked. Then, a small field of 4 kA/m is applied. As the temperature is increased, the smallest particles become unblocked and align with the applied field, increasing the magnetization. As the temperature is further increased, more particles unblock and the magnetization continues to increase. However, there is a critical temperature where thermal activation is too high, particles become superparamagnetic and their magnetization decreases according to the Langevin function. The combination of these two effects causes the peak in the ZFC magnetization.

- FC: FC measurements were made after cooling the sample down to 10 K under an applied field of 4 kA/m. In this way, the magnetic moments were partially aligned in the field direction. Then, similar to the ZFC curve, keeping the field applied, the magnetization was measured while increasing the temperature. As it happens in the ZFC curve, the magnetization decreases due to thermal activation.

The ZFC and FC curves converge when all the magnetic moments have been unblocked. Beyond this point, where the superparamagnetic regime is reached, a segment of the curve follows the Langevin law.

The ZFC-FC curves show an increase in blocking temperature (T_B) as size increases. T_B varies from 70 to 130 K for the 8 and 11 nm NPs, whereas for the 13 nm it

is around 250 K. The behavior is related to the increase of the magnetocrystalline energy due to the increasing particle volume (Figure 2.9) and agrees well with reported data (Goya, 2003; Jeong, 2005).
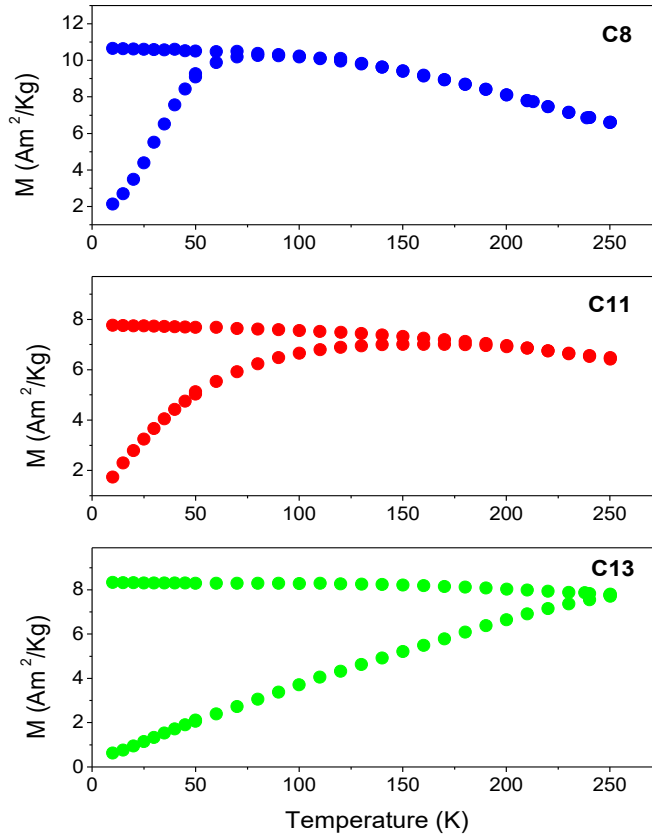
Figure 2.9. *ZFC-FC curves at 4 kA/m applied field for 8, 11 and 13nm sizes nanoparticles synthesized by the coprecipitation process.*

4. CONCLUSIONS

A synthesis method of uniform and biocompatible magnetic nanoparticles for biomedical applications has been optimized. The method is cheap, fast, simple and reproducible, uses no toxic reagents or additives (just inorganic salts and water) and allows obtaining large amounts of sample (4 g of sample per batch, approximately). In addition,

the nanoparticles synthesized in this work can be concentrated above 200 mg/ml at acid pH and its colloidal stability can last for months.

With this synthesis method rounded NPs are obtained, with different size (6±2, 8±3, 11±5, 13±4 and 14±4 nm). Samples consisting of 8, 11 and 13 nm particles were selected for further work and used as reference in this thesis.

3

Magnetic nanocrystals

1. INTRODUCTION

For particles of a given composition and at a given temperature, size is probably the most important parameter among those that rule their behavior, as well as the behavior of colloidal fluids prepared with them. First, when particles are dispersed in a liquid, size will determine their facility to diffuse and to sediment. Secondly, particle size will determine if the particle behaves as a single magnetic domain or as a multiple domain or if it is superparamagnetic or blocked at a certain temperature. This, in turn, will affect the magnetization curve of the particles, and for instance, the magnitude of the thermal losses when they are exposed to an alternating magnetic field. Finally, the dipolar interaction between particles also has strong volume dependence so that particle size will determine the extent of the response of the magnetic fluid to an external magnetic field, including the formation of chains, loops, etc. (Vereda, 2008).

There are several works in the literature that have succeeded in obtaining uniform particles larger than 30 nm and with different morphologies using the oxidative precipitation of iron (II) salts (Domingo, 1991; Domingo, 1994; Ma, 2004; Yang, 2004; Zhang, 2007). However, the main difficulty that it presents is the reduction of particle size below 30 nm maintaining a narrow particle size distribution. The oxidative precipitation of iron (II) salts induced by nitrate as soft oxidant in strong alkaline media is the most convenient medium for obtaining aqueous dispersions of monodisperse magnetite nanocrystals in a size range neatly superior than NPs and close to the superparamagnetic-ferrimagnetic limit (Nishio, 2007; Andrés-Vergés, 2008; Vereda, 2008; Aphesteguy, 2015). It should be mentioned that particles greater than 15 nm (to neglect surface effects) and smaller than 30 nm (to avoid the multidomain formation) have been proved to be the best choice for biomedical applications such as magnetothermia and magnetically guided drug delivery (Gonzalez-Fernandez, 2009; Salas, 2012; Marciello, 2013; Salas, 2013).

This synthesis method proved to be suitable for the fabrication of not only spinel iron oxides, such as magnetite, but also a variety of ferrites (Tamura, 1982; Regazzoni, 1983) and even iron hydroxides (Domingo, 1994). Furthermore, the process has been scaled up to obtain grams quantity preserving high crystallinity and high heating capacities.

This procedure is easier, cleaner and more cost effective than methods in non-aqueous medium, i.e., it does not need high temperatures, expensive organic solvents and a cumbersome purification step after the synthesis.

The oxidative precipitation as most of the synthesis procedures starting from iron (II) salts is very sensitive to the interplay of a number of experimental factors such as: nature of the oxidant, the base and the iron (II) salt, pH, temperature and additives. Unfortunately often two iron oxide phases are formed simultaneously if the conditions are not properly chosen (Cornell, 2006). The problem is more acute if we are interested in obtaining samples of magnetite nanocrystals with high degree of homogeneity in a relatively narrow size range and in a reproducible way. Even that the control of the main parameters of the process (the oxidant, pH and the temperature) following the guidelines stated by Sugimoto and Matijević (Sugimoto, 1980) enables the reproducible synthesis of magnetite nanocrystals without any secondary goethite, the need of tuning the particle size requires an exploration of the secondary variables of the process, such as the counterions and the use of mixed solvents. This is especially relevant in this case because the particle sizes obtained are often close to the superparamagnetic-ferrimagnetic limit and if a proportion of the population is magnetically blocked at room temperature this will affect deeply the magnetic properties of the ensemble.

The influence of counterions (the ions that accompanies the reactant ion in order to maintain electric neutrality) on the synthetic procedures in water solutions has been often considered secondary. However, it has been reported that they influence the colloidal properties of the products by adsorption (Hu, 2003; Bishop, 2009), stabilize unstable polyoxometalates (Sadeghi, 2015) and influence their packing into supracrystals (Yao, 2015), that is processes in which surfaces are relevant such as the precipitation. Other authors have been studied the influence of counterions in the precipitation of hydroxides such as $Mg(OH)_2$ (Giorgi, 2005) and akaganeite (Yue, 2011). In both cases the particle size was related to the hydration capacity of the counterions.

On the other hand, the influence of ethanol on the nanoparticle precipitation due to the interplay of hydrogen-bonding and hydrophobic interactions in water/ethanol

mixtures has been the object of fundamental studies (Ivanov, 2012; Chen, 2013). From the point of view of the materials preparation they have been used often to ease the preparation of anhydrous phases under hydrothermal conditions. Also, the presence of ethanol in the medium has been related to a reduction of particle size (Andrés-Vergés, 2008).

2. EXPERIMENTAL SECTION

Magnetite nanocrystals were prepared by oxidative precipitation in aqueous media following the work by Sugimoto and Matijević with some modifications to obtain different particle size (from 21 to 605 nm), shapes (cubes or spheres) and control the size distribution (Sugimoto, 1980).

2.1. Nanocrystal synthesis by oxidative precipitation

Briefly, the precipitation of an iron (II) salt ($FeSO_4$, $FeCl_2$ or $FeBr_2$) was carried out in a basic media (NaOH or KOH) and in the presence of a mild oxidant ($NaNO_3$ or KNO_3) under stirring in an oxygen free atmosphere (glove box under nitrogen) (Andrés-Vergés, 2008). The reaction was carried out in a 500 ml or 2000 ml double-walled reactor heated by means of a fluid set to 90 °C using a thermostat recirculating bath (figure 3.1).

In a typical experiment, two solutions were prepared independently before the precipitation:

(a) 200 ml of water containing OH^- and NO_3^- to obtain de final concentration of 0.2 M OH^- and 0.02 M or -0.04M OH^- excess. The excess hydroxyl ion concentration was calculated by applying the equation 3.1 (Sugimoto, 1980).

$$[OH^-]_{excess} = [OH^-] - 2[Fe^{2+}] - n[H^+] \qquad (3.1)$$

where n is 1 or 2 depending on the monoprotic or diprotic character of the acid used to dissolve the iron salt.

(b) 50 ml of Fe^{2+} in 10^{-2} M of acid solution (H_2SO_4, HCl or HNO_3 depending on the iron salt) to obtain a final concentration value of 0.2 M. The dissolution of Fe^{2+} was carried out in acid medium immediately before its use to prevent uncontrolled hydrolysis. The iron salt concentration was selected on the basis of previous results (Sugimoto, 1980; Andrés-Vergés, 2008; Marciello, 2013).

The iron (II) solution was quickly added to the basic solution under stirring, obtaining a final volume of 250 ml. When the addition was completed the green rust formed initially was overhead stirred for 15 min. After this time, this reaction intermediate was aged at 90 ºC for 24 h without agitation to obtain magnetite nanocrystals (figure 3.1). Ageing time was fixed at 24 h in order to reach conditions near equilibrium. At the end of the synthesis the system was left to cool and the nanocrystals were separated by magnetic decantation followed by several washings with distilled water.
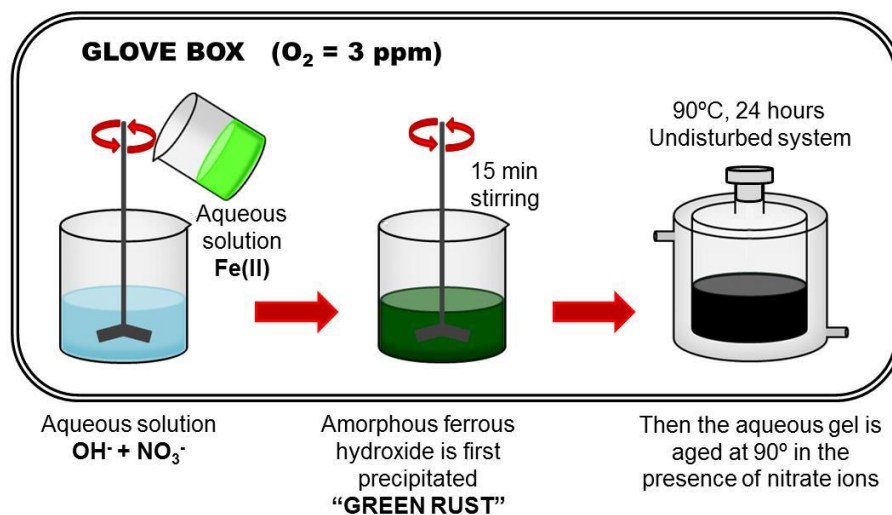
Figure 3.1. *Scheme of the experimental synthesis of magnetite nanocrystals prepared by oxidative precipitation.*

2.2. Effect of experimental parameters

The oxidation rate and, therefore, the average particle size, is controlled by changing the reaction conditions, such as the iron salt concentration, the nature of the iron, base and nitrate salts and the used of mixed solvents.

2.2.1. Counterions

The effect of the chemical nature of the reactants employed in the oxidative precipitation of magnetite was explored. For that we used $FeSO_4$, $FeCl_2$ and $FeBr_2$ (counteranions SO_4^{2-}, Cl^-, Br^-) as iron (II) precursors, $NaNO_3$ and KNO_3 as oxidants and NaOH and KOH to promote the hydrolysis (countercations Na^+, K^+) in water.

The main difference in the experimental procedure is the acid used to dissolve the iron salt in each case. When $FeSO_4$ is used as precursor, it is dissolved in H_2SO_4 while in the case of used $FeCl_2$ it is dissolved in HCl, in order to not add extra anions to the system. Moreover, the $FeBr_2$ was dissolved in HNO_3 due to de high reactivity of hydrobromic acid that easily oxidizes to bromine gas.

The experimental conditions used to evaluate the effect of different counterions in the reaction are summarized in table 3.1.

Sample	Counterions	Iron salt	Acid media (10^{-2} M)	Base salt	[OH-] (M)	Oxidant salt
CN0	Na^+, Cl^-	$FeCl_2$	HCl	NaOH	0.422	$NaNO_3$
BN0	Na^+, Br^-	$FeBr_2$	HNO_3	NaOH	0.422	$NaNO_3$
SN0	Na^+, SO_4^{2-}	$FeSO_4$	H_2SO_4	NaOH	0.424	$NaNO_3$
CK0	K^+, Cl^-	$FeCl_2$	HCl	KOH	0.421	KNO_3
BK0	K^+, Br^-	$FeBr_2$	HNO_3	KOH	0.421	KNO_3
SK0	K^+, SO_4^{2-}	$FeSO_4$	H_2SO_4	KOH	0.422	KNO_3

Table 3.1. *Experimental conditions for the synthesis of magnetite nanocrystals by oxidative precipitation with different counterions.*

The iron concentration and the nitrate concentration are 0.2 M in all cases. The excess of OH$^-$ is 0.02 M.

2.2.2. Ethanol addition

To evaluate the effect of the presence of alcohol in the media, the same reactions previously described were carried out in hydroalcoholic solutions with 25% and 50% of ethanol content (the final volume was kept constant, so we substituted the corresponding volume of water by ethanol).

The experimental conditions used to evaluate the effect of the presence of different ethanol proportion in the reaction are summarized in table 3.2.

Sample	Ethanol (%)	Counterions	Iron salt	Acid media (10^{-2} M)	Base salt	OH$^-$ (M)	Oxidant salt
CN25	25	Na$^+$, Cl$^-$	FeCl$_2$	HCl	NaOH	0.422	NaNO$_3$
CN50	50	Na$^+$, Cl$^-$	FeCl$_2$	HCl	NaOH	0.422	NaNO$_3$
BN25	25	Na$^+$, Br$^-$	FeBr$_2$	HNO$_3$	NaOH	0.422	NaNO$_3$
BN50	50	Na$^+$, Br$^-$	FeBr$_2$	HNO$_3$	NaOH	0.422	NaNO$_3$
SN25	25	Na$^+$, SO$_4^{2-}$	FeSO$_4$	H$_2$SO$_4$	NaOH	0.424	NaNO$_3$
SN50	50	Na$^+$, SO$_4^{2-}$	FeSO$_4$	H$_2$SO$_4$	NaOH	0.424	NaNO$_3$

Table 3.2. *Experimental conditions for the synthesis of magnetite nanocrystals by oxidative precipitation with different counterions and ethanol proportion.*

2.2.3. Base excess

To evaluate the effect of the base concentration the same reactions previously described for the K$^+$ counterions were carry out, but in this case the base excess was set at -0.04 M, which means that there is an iron excess (0.02 M) in the reaction determined by equation 3.2 (Sugimoto, 1980).

$$[Fe^{2+}]_{excess} = [Fe^{2+}] - \frac{[OH^-]}{2} - n[H^+] \tag{3.2}$$

The experimental conditions used to evaluate the effect of different base concentration in the reaction are summarized in table 3.3.

Sample	Ethanol (%)	Counterions	Iron salt	Acid media (10^{-2} M)	Base salt	OH⁻ (M)	Oxidant salt
CK0Fe	0	K^+, Cl^-	$FeCl_2$	HCl	KOH	0.359	KNO_3
CK25Fe	25	K^+, Cl^-	$FeCl_2$	HCl	KOH	0.359	KNO_3
CK50Fe	50	K^+, Cl^-	$FeCl_2$	HCl	KOH	0.359	KNO_3
BK0Fe	0	K^+, Br^-	$FeBr_2$	HNO_3	KOH	0.359	KNO_3
BK25Fe	25	K^+, Br^-	$FeBr_2$	HNO_3	KOH	0.359	KNO_3
BK50Fe	50	K^+, Br^-	$FeBr_2$	HNO_3	KOH	0.359	KNO_3
SK0Fe	0	K^+, SO_4^{2-}	$FeSO_4$	H_2SO_4	KOH	0.361	KNO_3
SK25Fe	25	K^+, SO_4^{2-}	$FeSO_4$	H_2SO_4	KOH	0.361	KNO_3
SK50Fe	50	K^+, SO_4^{2-}	$FeSO_4$	H_2SO_4	KOH	0.361	KNO_3

Table 3.3. *Experimental conditions for the synthesis of magnetite nanocrystals by oxidative precipitation with different base concentration and ethanol proportion.*

2.2.4. Scaled up process

The process has been scaled up by 2 and 8 times (final volume of 500 ml and 2000 ml, respectively) with respect to the quantity of reactants mentioned above. In this case, the syntheses were carried out using the same concentrations previously described of $FeSO_4$, NaOH, $NaNO_3$ and 50% ethanol.

Before carrying out the scaling process, a test was conducted in each of the reactors with the equivalent amount of distilled water to determine the heating rate in each case.

3. SAMPLES CHARACTERIZATION

3.1. Effect of different counterions

Highly crystalline magnetic nanocrystals with TEM sizes between 37 and 66 nm have been obtained in aqueous media using different iron salts and keeping constant the final reactant concentrations. Figure 3.2 presents the TEM micrographs of the magnetite nanoparticles obtained in water from the sodium and the potassium salts and the particle size distribution.
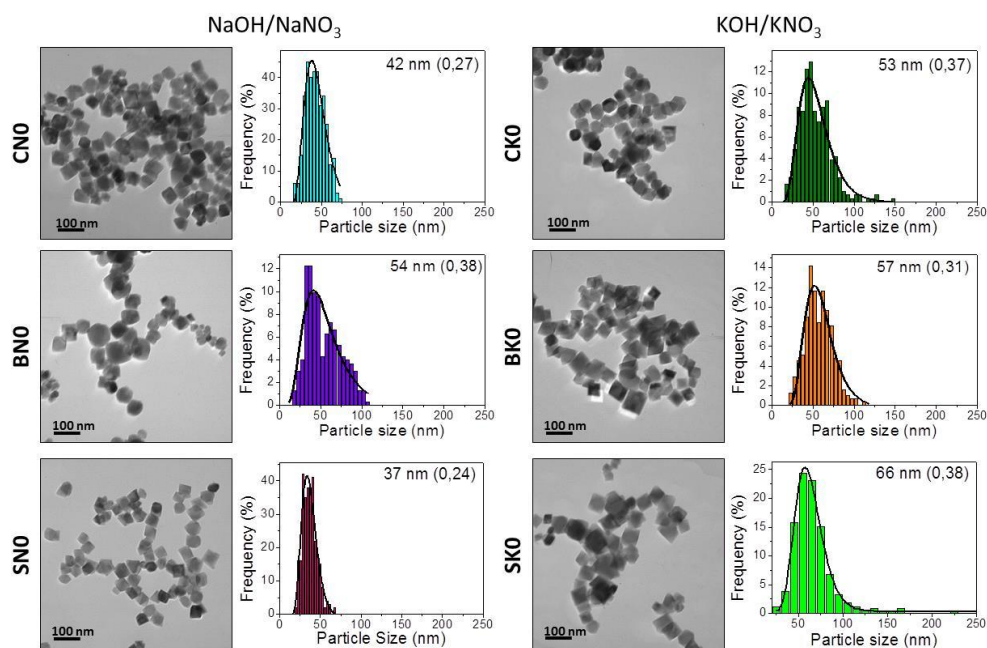
Figure 3.2. *TEM micrographs and size distribution (log-normal fit) of nanocrystals synthesized by oxidative precipitation with different salts in water. In the inset it is shown the mean size ($D_{average}$) and in parentheses it is shown the polydispersity index (PDI) defined as Standard deviation/$D_{average}$.*

It can be observed that the particle size is bigger for the samples prepared with potassium salt than the correspondent samples prepared with sodium salts. In the case of samples prepared using NaOH and $NaNO_3$ particle size increases going from $FeSO_4$ to

FeCl$_2$ and FeBr$_2$; likewise, the size distribution becomes wider with increasing particle size. However, for the samples prepared using KOH and KNO$_3$ the particle size evolves oppositely being bigger for FeSO$_4$ and smaller for the FeCl$_2$.

The formation of crystalline magnetite nanoparticles independently on the iron salt precursor was confirmed by X-ray analysis (figure 3.3). All peaks were assigned to a spinel structure similar to magnetite (JCPDS 89-0691). Crystal sizes were calculated from the (311) peak broadening. Table 3.4 shows both the particle size obtained by TEM and crystal size obtained by X-Ray.
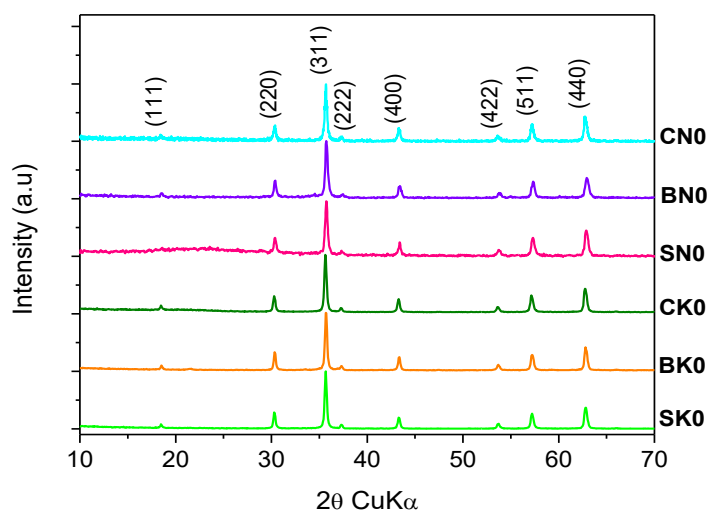
Figure 3.3. *X-ray diffraction patterns for magnetite nanocrystals synthesized from different salts in water.*

TGA and DTA results are shown in figure 3.4 and table 3.4. The most striking feature of the TGA/DTA curves is the increase of weight and the exothermic peak at temperatures from the ambient to 250ºC due to the oxidation of the iron (II) from magnetite to maghemite. This process is superimposed to desorption of physically adsorbed water molecules. Finally, very small weight loss of less than 1% was observed when heating from room temperature up to 900 ºC, as expected for magnetite particles of these sizes due to desorption of structural OH$^-$ (figure 3.4).

Sample	TEM size (nm)	XRD size (nm)	Water loss (%)	Weight increase (%)	Trans. temp. to αFe_2O_3 (ºC)
CN0	42	41.7	0.5	1.9	732
BN0	54	47.2	0.5	0.9	814
SN0	37	42.4	0.4	1.5	677
CK0	53	53.5	0.4	1.7	769
BK0	57	56.8	0.4	1.5	769
SK0	66	67.8	0.4	1.9	738

Table 3.4. *XRD and TEM sizes and TGA data obtained for different magnetite nanocrystals synthesized from different salts in water.*
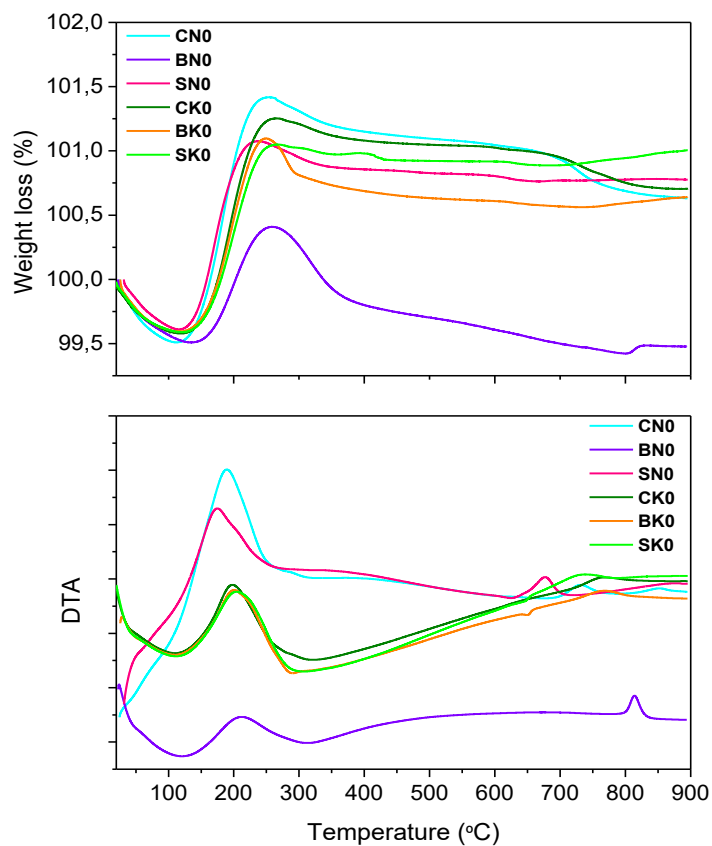
Figure 3.4. *TGA and DTA of magnetite nanocrystals synthesized from different salts in water.*

In the DTA curves, an exothermic peak between 677 and 814 °C is detected for the different samples due to the maghemite-hematite transformation (figure 3.4). This is in agreement with the fact that for nanoparticles a sintering process has to take place before the transformation of a high symmetry phase into other with lower symmetry (Ye, 1998). It has been shown that transition temperature decreases with decreasing particle size due to the reduced activation energy of the system (Hamada, 1981) which agrees with the results for our samples. It should be remembered that this transition takes place at 400-600 °C for the nanoparticles (6-14 nm) analyzed in the previous chapter.

Infrared spectra for magnetic nanocrystals prepared using the same reactant concentrations but from different salts (figure 3.5) show similar features: two main peaks at low frequency due to Fe-O bonds in magnetite (around 400 and 600 cm^{-1}) (Cornell, 2006), a broad peak at around 1000 cm^{-1} due to surface impurities, and a broad band at 1630 cm^{-1} due to the bending HOH of water.
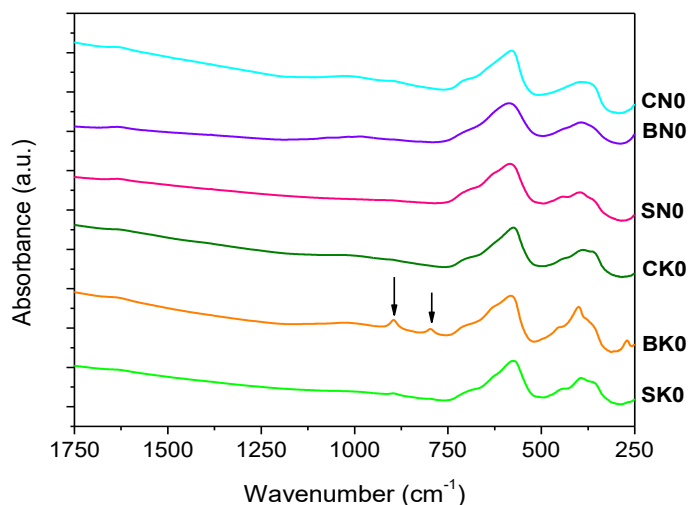
Figure 3.5. *Infrared spectra of magnetite nanocrystals synthesized from different salts in water.*

With respect to the characteristic bands of iron oxide structure, the higher frequency absorption band lies around 600 cm^{-1} and is assigned to the intrinsic vibration of the tetrahedral metal oxygen coordination, and the lower frequency absorption band

lies around 400 cm⁻¹ and is assigned to the intrinsic vibration of the octahedral metal oxygen coordination (Waldron, 1955). Sample BK0 (prepared from $FeBr_2$, KOH and KNO_3) presents two peaks at 896 and 798 cm⁻¹ attributable to a secondary phase formed during the synthesis process. This secondary phase is observable by TEM (not shown) but not by DRX, which suggests an amorphous structure or a low proportion.

The magnetic behavior of these nanocrystals in powder form was investigated at room temperature (RT). Hysteresis parameters for magnetite nanocrystals of different sizes are listed in table 3.6 and the corresponding curves are presented in figure 3.5.
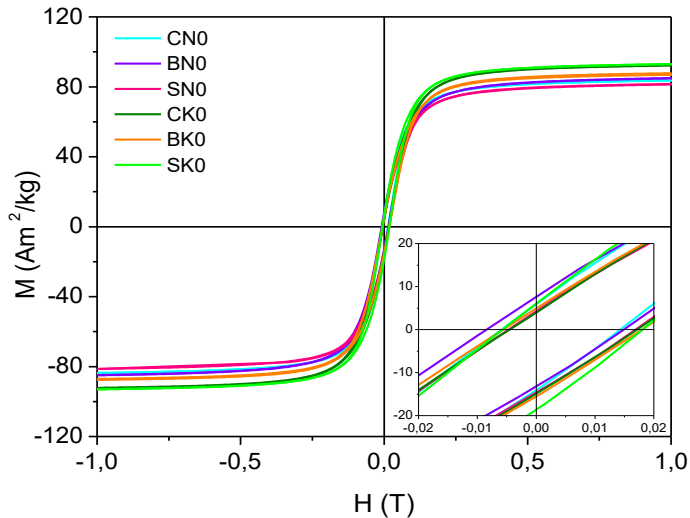
Figure 3.5. *Magnetization curves at room temperature for magnetite nanocrystals with different sizes synthesized in water. The inset shows the central area of the loop at higher magnification.*

All the samples present a ferromagnetic behavior. In general, the saturation magnetization and coercivity values decrease as the particle size decreases. Thus, M_S values vary between 96 and 85 Am²/kg, close to the theoretical values reported for bulk magnetite at room temperature, 94 Am²/kg (Cullity, 2011), and the coercivity values decreases from 9.56 to 8.05 kA/m, approaching the reported value for magnetite due to magnetocrystalline anisotropy (6 kA/m). It should be remembered that Ms values are in the range between 68 and 70 Am²/kg for NPs (6-14 nm) analyzed in the previous chapter.

Sample	TEM size (nm)	M_S (Am²/kg)	H_C (kA/m)
CN0	42	87	8
BN0	54	89	9
SN0	37	85	9
CK0	53	96	9
BK0	57	90	9
SK0	66	96	10

Table 3.5. *Hysteretic parameters at RT for magnetite nanocrystals synthesized from different salts in water.*

3.2. Reduction of particle size by ethanol addition

Further reduction in particle size approaching the superparamagnetic-ferromagnetic limit was investigated by addition of ethanol to the reaction medium. We chose the counterions conditions that result in the smallest particle sizes, that is with NaOH and NaNO₃ using $FeSO_4$, $FeCl_2$ and $FeBr_2$ as iron (II) precursors and 25 and 50% proportions of ethanol for each case. As a result high crystalline magnetic nanocrystals with TEM sizes between 21 and 46 nm were obtained.

Figure 3.7 presents the TEM micrographs and particle size distribution of the magnetite nanocrystals obtained using 25% and 50% of ethanol and sodium salts. It can be observed that the particle size is reduced by ethanol addition with respect the same sample prepared in water. The smallest nanocrystal size is obtained from $FeSO_4$ and 25% of ethanol. The addition of 50% of ethanol leads in general to a slight decrease of size with respect to the obtained at 25% but with higher polydispersity and, in addition, in the case of using $FeBr_2$ as iron precursor (sample BN50), a secondary phase of iron oxide is formed (not observed by XRD).
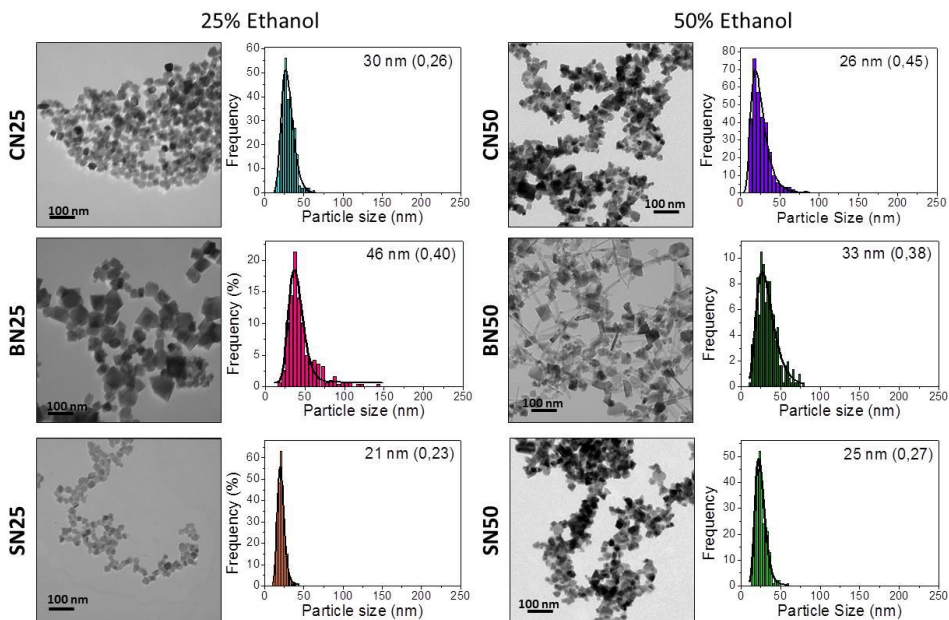
Figure 3.7. *TEM micrographs and size distribution (log-normal fit) of magnetite nanocrystals synthesized with different salts in water/ethanol media. In the inset it is shown the mean size (D$_{average}$) and in parentheses the polydispersity index (PDI) defined as Standard deviation/D$_{average}$.*
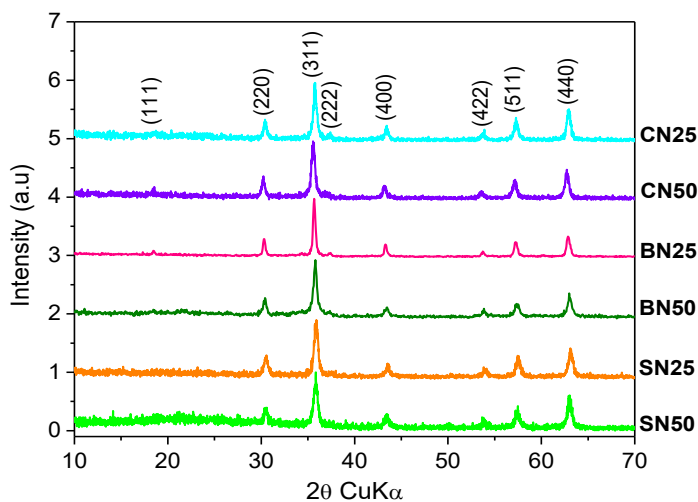
Figure 3.8. *X-ray diffraction patterns for magnetite nanocrystals synthesized in water/ethanol media.*

X-ray diffractograms for the samples prepared in water/ethanol media are shown in figure 3.8. All peaks were assigned to a spinel structure similar to magnetite and there were not found any secondary phase peaks. Crystal sizes were calculated from the (311) peak broadening. Table 3.6 shows both the particle size obtained by TEM and crystal size obtained by X-Ray.

TGA and DTA results of the samples prepared in water/ethanol medium (figure 3.9 and table 3.6) are very similar to those of the samples prepared in water. In this case, it can be observed a slightly higher weight loss (up to 1.6%) which may be due to a greater amount of water molecules adsorbed on the nanocrystal surface due to the increase of specific surface due to the size decrease with respect with the equivalent synthesis in water (figure 3.4). The next feature is the weight increase due to the oxidation. In the DTA curves, the exothermic peak between 696 and 811 ºC is also present for the different samples due to the maghemite-hematite transformation (figure 3.9) in the same range of temperature than the water samples.

Sample	%EtOH	TEM size (nm)	XRD size (nm)	Water loss (%)	Weight increase (%)	Trans. temp. to αFe_2O_3 (ºC)
CN25	25	30	24.4	0.6	1.7	725
CN50	50	26	25.9	0.9	1.8	780
BN25	25	46	44.2	0.5	1.1	811
BN50	50	33	25.8	1.3	0.5	791
SN25	25	21	21.4	1.6	0.2	696
SN50	50	25	21.3	1.0	0.8	709

Table 3.6. *XRD and TEM sizes and TGA data obtained for different samples synthesized in water/ethanol media.*
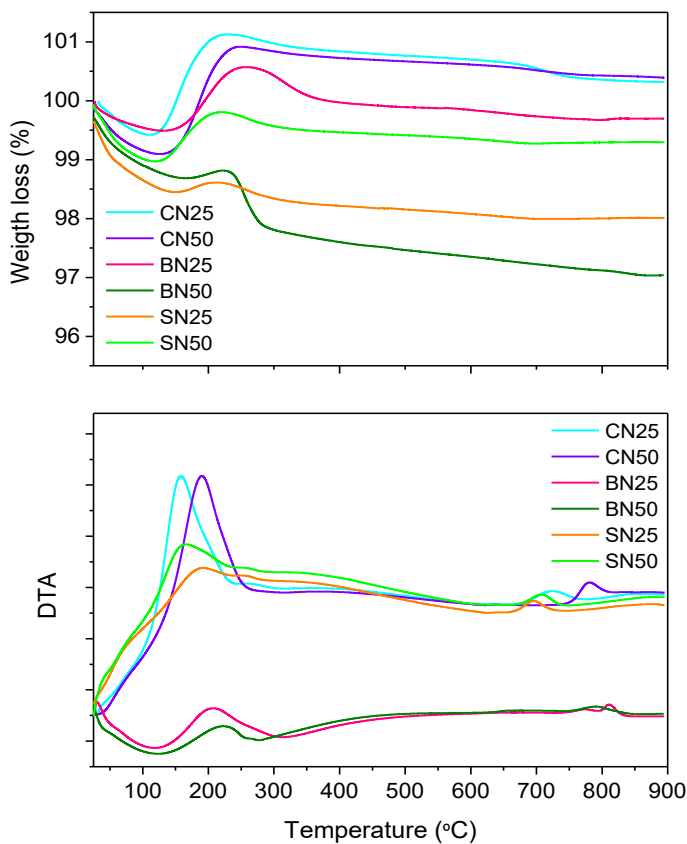
Figure 3.9. *TGA and DTA of magnetite nanocrystals synthesized in water/ethanol medium.*

Infrared spectra for magnetic nanocrystals prepared in water/ethanol medium (figure 3.10) show similar features with respect to those prepared in water. Likewise, the sample BN50 presents two peaks between 800 and 900 cm^{-1} which are not observed in the other spectra and they could be due to the secondary iron oxide phase observed in TEM micrographs.
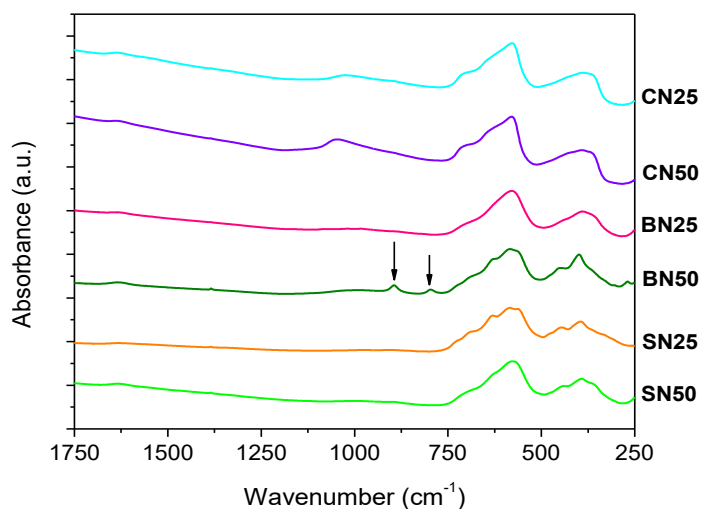
Figure 3.10. *Infrared spectra of magnetite nanocrystals synthesized in water/ethanol medium.*

The magnetic behavior of these nanocrystals in powder form was investigated at room temperature (RT). Hysteresis parameters for magnetite nanocrystals of different sizes are listed in table 3.7 and the corresponding curves are presented in figure 3.11. The largest nanocrystals (46 nm) showed a saturation magnetization value of 90 Am^2/kg and a coercivity value of 9 kA/m, which agrees well with the theoretical values reported for bulk magnetite (Cullity, 2011).

Sample	%EtOH	TEM size (nm)	Ms (Am^2/kg)	Hc (kA/m)
CN25	25	30	86	6
CN50	50	26	81	7
BN25	25	46	90	9
BN50	50	33	66	12
SN25	25	21	78	7
SN50	50	25	81	6

Table 3.7. *Hysteretic parameters at room temperature for magnetite nanocrystals in water/ethanol media.*
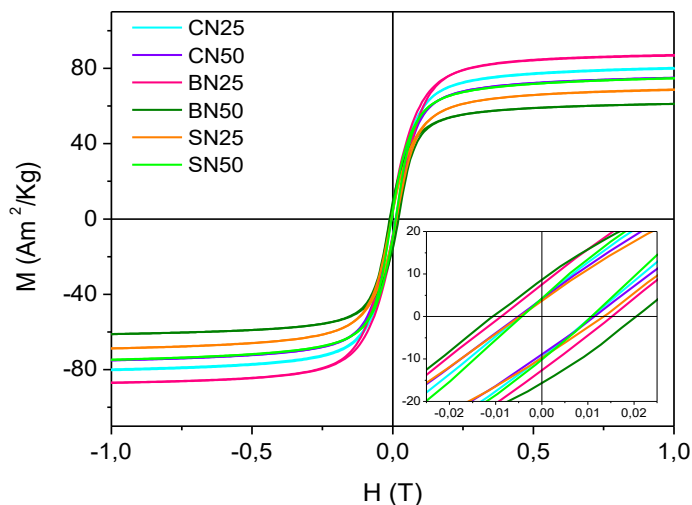
Figure 3.11. *Magnetization curves at room temperature for magnetite nanocrystals with different sizes synthesized in water/ethanol media. The inset shows the central area of the loop at higher magnification.*

As particle size decreases down to 21 nm, the saturation magnetization value decreases to 78 Am^2/kg, probably as a consequence of surface spin canting. Coercivity also decreases for smaller nanocrystals, approaching zero (the superparamagnetic limit). The lowest saturation magnetization value (66 Am^2/kg) corresponds to the sample containing a secondary phase (sample prepared from $FeBr_2$ and 50% ethanol), which is probably a non-magnetic oxihydroxide.

3.3. Morphology modification by changing the base excess

Experiments reducing the base excess or what is the same, according to equation 3.2, increasing iron excess, have been carried out in water and water/ethanol solvents. $FeCl_2$ and $FeSO_4$ have been used as iron precursors ($FeBr_2$ has been ruled out because previous experiments have proved that this salt produces more polydisperse particles) and KOH and KNO_3 as base and oxidant, respectively.

Surprisingly, magnetic nanocrystals with TEM sizes between 22 and 605 nm (the latter could be considered submicronic more than nanometric) have been obtained in water and water/ethanol media keeping constant the base excess. Figure 3.12 presents the

TEM micrographs of the magnetite nanocrystals obtained in water and water/ethanol from potassium salt and the particle size distribution.
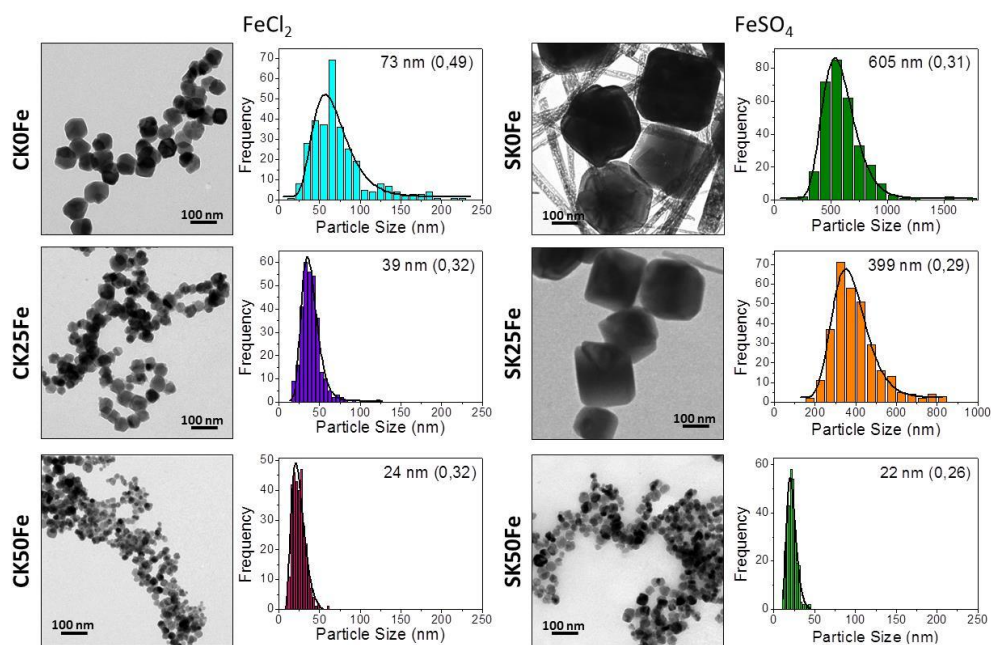
Figure 3.12. *TEM micrographs and size distribution (log-normal fit) of nanocrystals synthesized with iron excess in water and water/ethanol medium. In parentheses it is shown the polydispersity index (PDI) defined as $STD/D_{average}$.*

It can be observed that the crystal size is bigger for the samples prepared with $FeSO_4$ in water and in 25% ethanol than the correspondent samples prepared with $FeCl_2$. However, the sample prepared with $FeSO_4$ in 50% is smaller than the correspondent sample prepared with $FeCl_2$. In both cases (with $FeCl_2$ and with $FeSO_4$) particle size decreases as the amount of ethanol in the reaction medium increases. The width of the size distribution also decreases in the same direction. Moreover, it can be seen that the size of the nanocrystals of the samples prepared in water and Fe^{2+} excess (CK0Fe and SK0Fe) is larger than the corresponding samples prepared in water and OH^- excess (CK0 and SK0). This effect is more pronounced for samples prepared using $FeSO_4$. For larger samples SK0Fe and SK25Fe ($FeSO_4$ in water and 25% ethanol, respectively), it can be

seen that a secondary phase appears during synthesis (needle shape crystals), which is not observed when 50% ethanol is added to the reaction medium. Comparing these samples prepared in Fe excess with samples prepared in OH$^-$ excess (figures 3.2 and 3.7), it can be noted that the particle morphology changes from cubes to spheres. Similar trend was already reported showing that large spherical particles of 500 nm in diameter are obtained in Fe^{2+} excess but when the OH$^-$ is in excess, the particles become cubic and the size decreases. A sharp pH change associated with the Fe^{2+} concentration is the origin of these results, which affects the formation mechanism of the particles (Sugimoto, 1980). In excess of Fe^{2+}, ferrous hydroxide is first formed at pH 6-7 and the pH decreases as the reaction proceeds down to pH 5. However, in the case of OH$^-$ excess, the pH of the dispersion is around 12 and it stays approximately constant during the reaction. Particle aggregation mechanism seems to be involved in the formation of the spheres, what agrees well with a faster growth under small electrostatic repulsion forces at pH 6-7 (IEP of magnetite) (Garcell, 1998). An increase in pH above the isoelectric point causes charging of the primary particles and prevents their aggregation. The resulting cubic morphology suggests a direct growth mechanism slower than the previous one which leads to smaller particles with a well-defined habit (Andrés-Vergés, 2008).

Likewise, we can observe a variation in particle shape from octahedral to spherical as particle size decreases, which has previously been observed for magnetite nanoparticles prepared by different methods (Salas, 2012). It has been reported that in general for a given material, the resulting crystal morphology depends upon the supersaturation (Cornell, 2006). At low supersaturation levels, polyhedral crystals are favored due to the low driving force and extended growth that lead to well-ordered crystallographic (100) and (111) faces. At high supersaturation levels there is abundant nucleation and the rate of growth is limited by the rate of diffusion of new material to the crystal surface; the growing surface tends to become rougher and the particles become spherical (Marciello, 2013).

X-ray diffractograms for the samples prepared in water and water/ethanol media are shown in figure 3.13. All peaks were assigned to a spinel structure similar to magnetite. However, for the samples that present a secondary phase (SK0Fe and SK25Fe), an extra

small peak in the X-ray diffractograms is observed, which corresponds to (101) peak of goethite (JCPDS 01-0401). Crystal sizes were calculated from the (311) peak broadening. Table 3.8 shows both the particle size obtained by TEM and crystal size obtained by X-Ray.
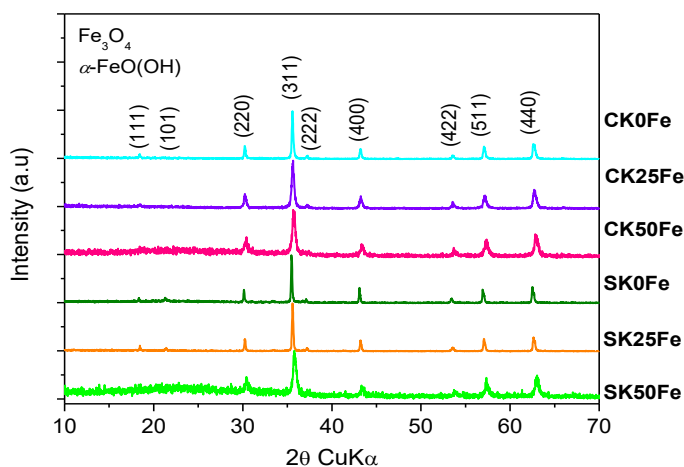
Figure 3.13. *X-ray diffraction patterns for magnetite nanocrystals synthesized with iron excess in water and water/ethanol media.*

Sample	%EtOH	TEM size (nm)	XRD size (nm)	Water loss (%)	Weight increase (%)	Trans. temp. to αFe_2O_3 (ºC)
CK0Fe	0	73	105.6	0.2	2.0	650
CK25Fe	25	39	38.6	0.3	1.1	749
CK50Fe	50	24	26.5	0.7	0.8	661
SK0Fe	0	605	---	0.2	0.9	636
SK25Fe	25	399	397.3	0.1	1.3	614
SK50Fe	50	22	27.7	0.6	0.8	710

Table 3.8. *XRD and TEM sizes and TGA data obtained for different samples under Fe^{2+} excess in water and ethanol/water media.*

TGA and DTA results are shown in figure 3.16 and table 3.8. A very small loss of less than 1% was observed when heating from room temperature up to 900 °C, as expected for magnetite particles of these sizes. First, physically adsorbed water molecules were eliminated at 120 °C, leading to a small weight loss and then the weight increased in TGA curves as a consequence of the oxidation of magnetite into maghemite (figure 3.4).
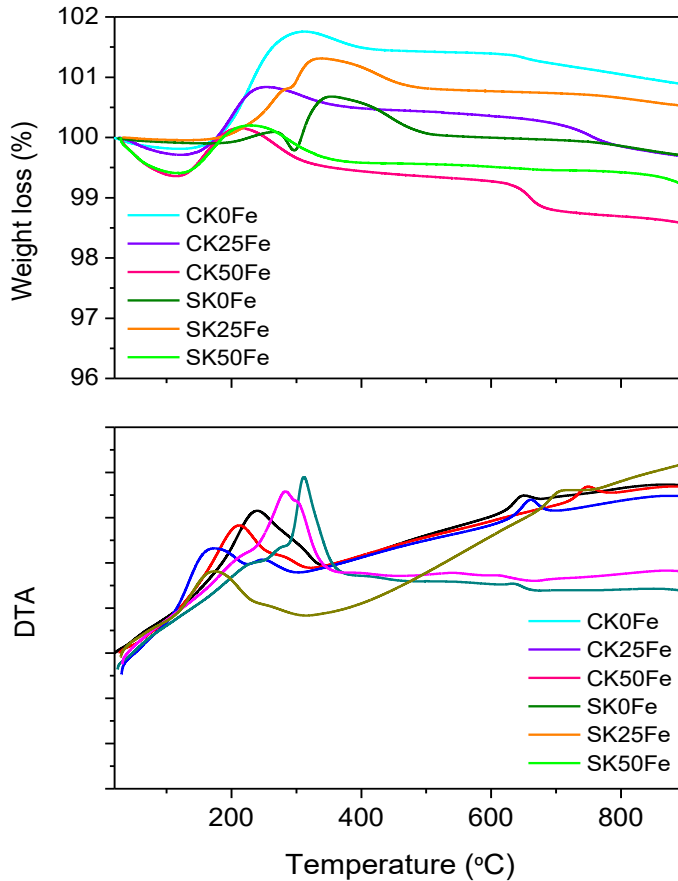
Figure 3.14. *TGA and DTA of magnetite nanocrystals synthesized with iron excess in water and water/ethanol medium.*

As in all this study the exothermic peak between 614 and 749 °C detected for the different samples due to the maghemite-hematite transformation depends on the particle size (figure 3.14). This is in agreement with the fact that for nanoparticles a sintering

process has to take place before the transformation of a high symmetry phase into other with lower symmetry as previously mentioned (Ye, 1998). For samples SK0Fe and SK25Fe having the largest nanocrystals, an extra exothermic peak at around 300°C is observed probably due to the secondary phase present in these samples.

Infrared spectra for magnetic nanocrystals prepared with iron excess in water and water/ethanol medium (figure 3.15) show similar features with respect to those prepared with OH$^-$ excess.
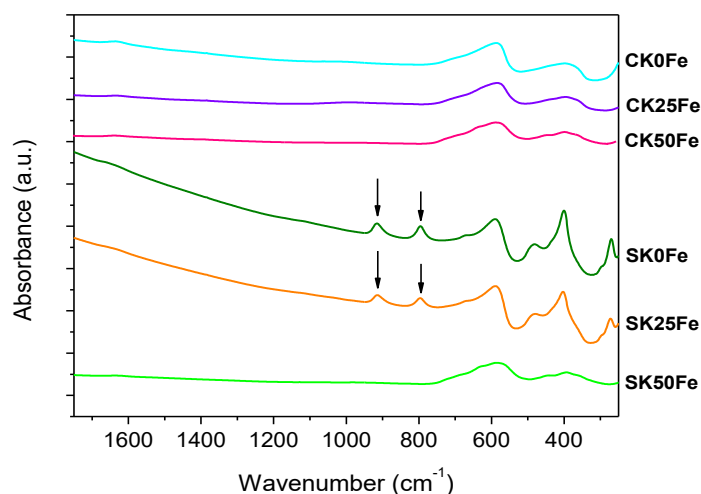
Figure 3.15. *Infrared spectra of magnetite nanocrystals synthesized with iron excess in water and water/ethanol medium.*

Likewise, samples SK0Fe and SK25Fe present two peaks between 800 and 900 cm^{-1} which are not observed in the other spectra and they could be due to the secondary phase observed in TEM micrographs and X-ray diffractograms.

The magnetic behavior of these nanocrystals in powder form was investigated at room temperature (RT). Hysteresis parameters for magnetite nanocrystals of different sizes are listed in table 3.9 and the corresponding curves are presented in figure 3.16. The largest nanocrystals (605 nm) showed a saturation magnetization value of 96 Am²/kg and coercivity value of 4 kA/m. As particle size decreases down to 22 nm, the saturation

magnetization value decreases to 87 Am²/kg, as expected for nanocrystals close to the superparamagnetic limit.
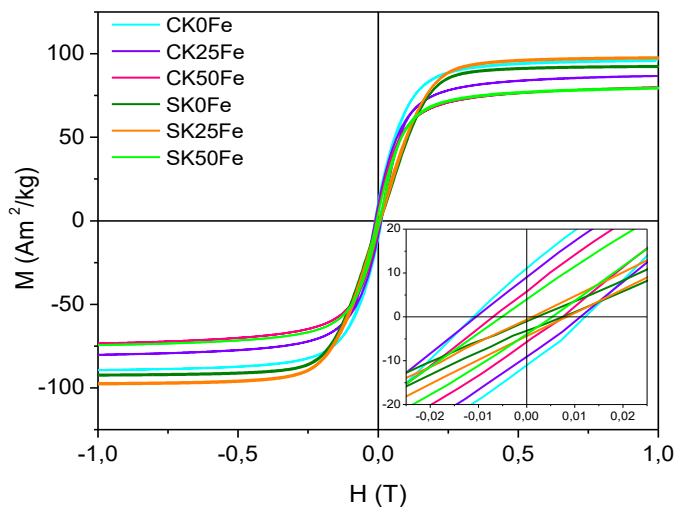
Figure 3.16. *Magnetization curves at room temperature for magnetite nanocrystals with different sizes synthesized in water and ethanol under conditions of iron excess. The inset shows the central area of the loop at higher magnification.*

Sample	%EtOH	TEM size (nm)	Ms (Am²/kg)	Hc (kA/m)
CK0Fe	0	73	98	9
CK25Fe	25	39	90	9
CK50Fe	50	24	84	6
SK0Fe	0	605	96	4
SK25Fe	25	399	103	4
SK50Fe	50	22	87	4

Table 3.9. *Hysteretic parameters at room temperature for magnetite nanocrystals with different sizes.*

3.4. Effect of the scaled up process

The method was reproducible for a given volume and a mass production of 30 g of magnetic nanocrystals in one batch was achieved by using a 2000 ml reactor and 0.2 M iron (II) salt. Figure 3.17 shows the TEM micrographs of the magnetite nanocrystals obtained from $FeSO_4$, NaOH and $NaNO_3$ in water with two different reaction volumes.

Figure 3.17. *TEM micrographs for magnetite nanocrystals prepared in 500 ml and 2000 ml reactors.*

The size distribution presented in figure 3.18 shows that an increase in the reaction volume leads to an increase in the particle size and polydispersity.
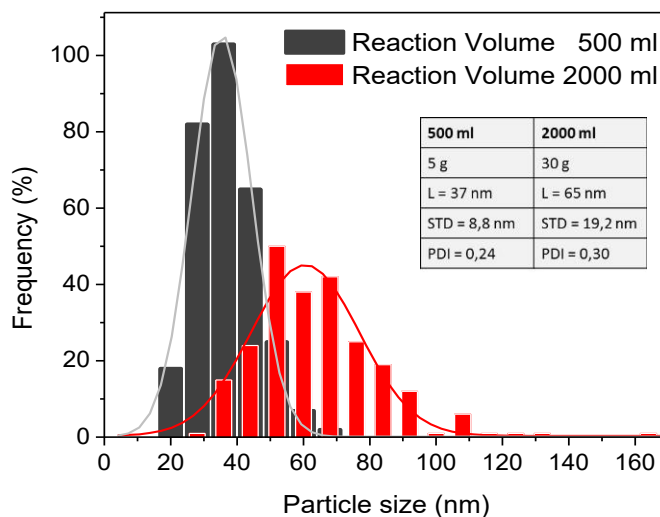
Figure 3.18. *Size distribution of magnetite nanocrystals prepared in 500 ml and 2000 ml reactors.*

As expected, it can be seen in figure 3.19 that the heating rate for the 500 ml reactor is faster than for the 2000 ml reactor, reacting in 20 min in the first case and in 40 min in the second one. In the first case, a burst nucleation takes place generating a larger number of nuclei that will further growth. For the larger reactor, a smaller amount of nuclei seems to be formed leading to larger particles.
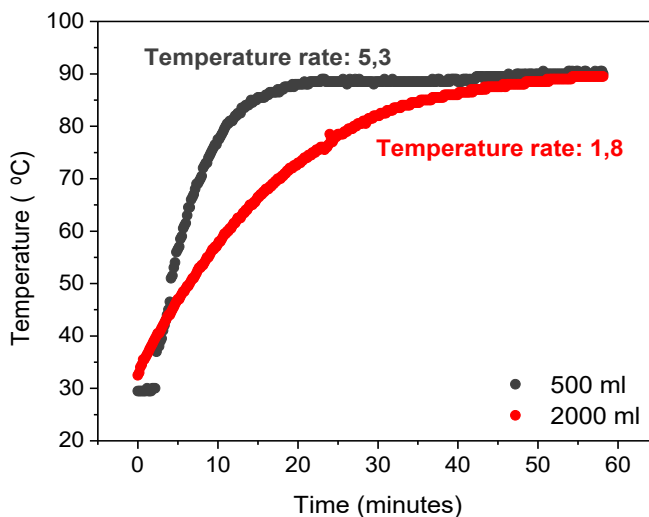
Figure 3.19. *Heating rate for the 500 ml and 2000 ml reactors.*

Therefore, the heating rate directly affects the size and polydispersity of the nanocrystals. The faster the reaction mixture reaches 90 °C, the smaller and more homogenous nanocrystals are obtained.

3.5. Secondary phases

As we have seen above, there are some synthesis conditions that give rise to the formation of needle-shaped crystals as a secondary phase. To identify this phase, the SK0Fe sample was chosen and electron diffraction was performed (figure 3.20).
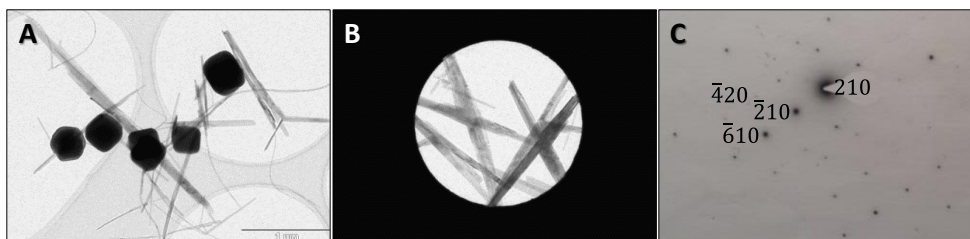
Figure 3.20. *(a) TEM micrograph of sample SK0Fe, (b) selected area to carried out the electron diffraction, (c) electron diffraction pattern.*

From the planes indexed in the electron diffraction pattern, it can be determined that the needle-shaped crystals correspond to goethite (α-FeO(OH)), which agrees well the morphology observed by TEM and the position of the small peak in XRD. The formation of this ferric oxyhydroxides with an orthorhombic crystal structure is marked by the oxidation state change of Fe^{2+} to Fe^{3+}, which is precisely what happens in our system. Goethite is an antiferromagnetic material, so its presence in samples as a secondary phase can affect the magnetic properties of the magnetite nanocrystals obtained, mainly by lowering the saturation magnetization.

In addition to the sample SK0Fe, the other samples with secondary phases are: BK0, SK0, BN50 and SK25Fe. In all of them, the secondary phase has the same appearance in the TEM micrographs, so it is most probably goethite.

4. DISCUSSION

Values of saturation magnetization (Ms) and coercivity (Hc) as a function of particle size are given in figure 3.21. It can be seen that in general, as particle size decreases, the saturation magnetization decreases as a consequence of the increase in surface area and the presence of spin canting. However, Ms values are always larger (~80 Am²/kg) than those for nanoparticles (~60 Am²/kg) as showed in the previous chapter. This is an important advantage of nanocrystals against nanoparticles.
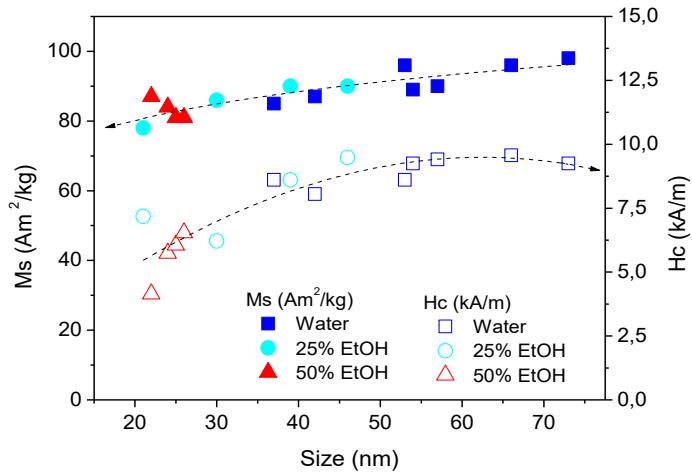
Figure 3.21. *Saturation magnetization and coercivity values at room temperature for nanocrystals prepared in water, 25% ethanol and 50% ethanol with different sizes.*

Coercivity also decreases with nanocrystal size, indicating that thermal energy is affecting the magnetization reversal for the smallest nanocrystals, which means that they are close to the superparamagnetic limit. This magnetic behavior agrees with the reported in the literature (Andrés-Vergés, 2008; Marciello, 2013).

The dispersion observed in the Ms and Hc data may be due to several factors. On the one hand, the polydispersity present in the samples, which is always around 25%. On the other hand, the oxidation degree of the magnetite nanocrystals to maghemite, which is inversely related to the nanocrystal size and the weight gain observed in the TGA graphs (figures 3.4, 3.9 and 3.14) (Bomati, 2008). Assuming that the cubic NCs are approximated by a core/shell structure with a reduced magnetite core and a full oxidized maghemite shell, a theoretical relation among the weight increase and the particle size could be written for each possible thickness of the oxidized layer (Appendix II). Figure 3.22 shows the plot of such relations with the experimental points corresponding to our samples superposed. The conclusion obtained of this figure is that the thickness of the oxidized layer is for the majority of the samples among 3 and 5 nm independently of the particle size and the minimum was 2 nm thicknesses.
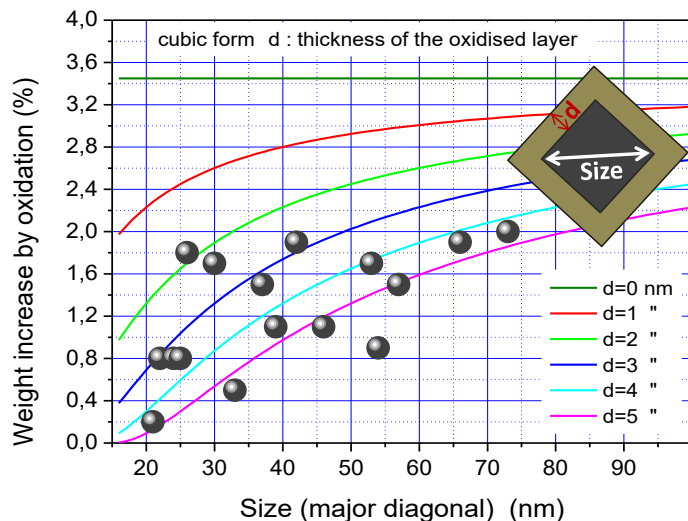
Figure 3.22. *Dependence of the weight increase by oxidation with the crystal size and the thickness of the oxidized layer. The inset shows a scheme of a cubic magnetite nanocrystal with an oxidized maghemite layer.*

5. CONCLUSIONS

An efficient and large-scale method to obtain high-quality magnetite nanocrystals with core sizes in a wide range via green chemistry is described. Reproducible scale-up of the synthesis up to 20 g per batch was successfully achieved.

The results obtained are of interest in the fine tuning of the particle size of magnetite nanocrystals by oxidative precipitation through the manipulation of some reaction parameters, such as the iron salt concentration, the nature of the iron, base and nitrate salts and the used of mixed solvents. The average particle sizes and polydispersity of the magnetite nanocrystals obtained by oxidative precipitation are strongly influenced by the nature of the counterions present. This effect is more pronounced in water-ethanol mixtures than in pure water.

The synthesized iron oxide nanocrystals, some of them with core sizes in the region close to the superparamagnetic-ferromagnetic transition, present crystalline structure and high saturation magnetization.

All the magnetite samples present a surface maghemite layer of 3-5 nm of thickness independently of their size. This could help understanding the decrease in saturation magnetization with size decrease of magnetite NCs being due to not only surface spin canting but also to partial oxidation to maghemite with lower saturation magnetization than magnetite.

4

Study of the reaction mechanism to form nanocrystals

1. INTRODUCTION

Understanding the mechanisms of NCs synthesis allows designing NCs materials with controlled size, shape, and composition. Concerning the synthesis of NCs the in situ observation of its formation at the nucleation stage and at a very early stage of growth, which is critical for understanding the process, remains to be done (Kovalenko, 2015).

The reaction mechanism that occurs during oxidative precipitation is presumably complex, because it takes place through a gelatinous intermediate (a partially oxidized ferrous hydroxide called green rust immediately formed) that can evolve to magnetite through a second intermediate phase such as goethite (sometimes detected in our experiments) that finally reacts with Fe^{2+} in solution to form magnetite (Tamaura, 1981) or directly by reaction with Fe^{2+} in solution (Sugimoto, 1980), depending mostly on the oxidation rate. Green rust (GR) is a generic name for various green crystalline chemical compounds containing iron (II) and iron (III) cations, the hydroxide (HO^-) anion, and another anion such as carbonate (CO_3^{2-}), chloride (Cl^-), or sulfate (SO_4^{2-}), in a layered double hydroxide structure. The most studied GR varieties are carbonate ($[Fe^{2+}_4Fe^{3+}_2(HO^-)_{12}]^{2+} \cdot [CO^{2-}_3 \cdot 2H_2O]^{2-}$), chloride ($[Fe^{2+}_3Fe^{3+}(HO^-)_8]^+ \cdot [Cl^- \cdot nH_2O]^-$) and sulfate ($Fe^{2+}4Fe^{3+}2(HO^-)_{12}]^{2+} \cdot [SO^{2-}_4 \cdot 2H_2O]^{2-}$) (Bernal, 1959; Génin, 1998).

The influence of the anion on the formation of iron oxides, either starting from Fe(III) or Fe(II) salts, it is well known. When starting from the hydrolysis of Fe(III) salts, it has been reported that the formation of β-FeOOH (akaganeite) is induced by chloride instead of α-FeOOH (goethite), favored in the presence of nitrate (Bernal, 1959). In the case of oxidative precipitation of iron (II) salts by oxygen at neutral pH, it has been reported that F^-, $H_2PO_4^-$ and HPO_4^{2-} accelerate the oxidation of Fe^{2+} whereas most anions slow it down in the order $ClO_4^- > NO_3^- > Cl^- = H_3SiO_4^- > Br^- = I^- = SO_4^{2-}$ (Tamura, 1976); it means that we could expect that counterions influence on the oxidation rate of Fe^{2+}. This effect was explained by the different oxidation rates of ferrous complex with the counteranion FeX^- and $FeOH^-$. The effect is relevant because magnetite formation needs the complete dihydroxylation of the green rust precursor prior to complete oxidation and this is only possible if sufficient time is available. However, if complete

oxidation is fast and precedes dihydroxylation, Fe(III) oxohydroxides like lepidocrocite forms instead of magnetite (Schwertmann, 1989).

Among the factors that influence the oxidation rate of green rust, the counteranions are presumably relevant because they affect green rust's structure, which consists in positively charged octahedral brucite-type Fe(II)-Fe(III) hydroxy layers linked by interlayer anions (our counteranions). The green rust stability depends on such interlayer composition in the following trend: $CO_3^{2-} > SO_4^{2-} > Cl^-$ (Taylor, 1980). Given to the fact that this phase need to dissolve prior to the formation of magnetite, those differences in stability could have influence in the process. In short, the counterions could influence the solubility/reactivity of the green rust. The effects of cations and anions on the solubility of proteins were discovered by Franz Hofmeister in 1888 (Hofmeister, 1891). The Hofmeister series or lyotropic series (figure 4.1) is a classification of ions in order of their ability to salt out or salt in proteins (salting-out is the effect when adding a salt to a solvent containing an organic solute reduces the solubility of that solute, from Collins *English* Dictionary). This behavior was also observed with some other colloidal suspensions and it is relevant to a broad range of fields, especially in colloidal science and biochemistry. (Lyklema, 2009; Parsons, 2011; Lo Nostro, 2012; Salis, 2014).

For ANIONS:

$Citrate^- > SO_4^{2-} > PO_4H^{2-} > F^- > CH_3COO^- > Cl^- > Br^- > I^- > NO_3^- > ClO_4^- > SCN^-$

Kosmotropic — Chaotropic

For CATIONS:

$N(CH3)4^+ > NH_4^+ > Cs^+ > Rb^+ > K^+ > Na^+ > H^+ > Ca^{2+} > Mg^{2+}$

Chaotropic — Kosmotropic
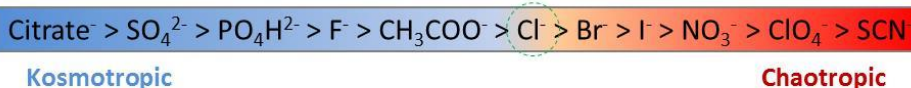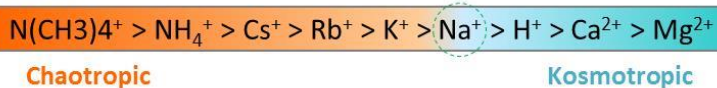
Figure 4.1. *Scheme of Hofmeister series for different anions and cations.*

Anions have a larger effect than cations, and therefore the Hofmeister series are divided into anionic and cationic series. Both series contains monovalent and divalent ions and monatomic and polyatomic ions. Most of the positions in the series correspond

to the degree of hydration of the ions, i.e. Na^+ hydrates more than K^+ and SO_4^{2-} more than Cl^- (Zavitsas, 2001). Originally, it was thought that an ion's influence on macromolecular properties was caused at least in part by "making" or "breaking" bulk water structure. However, ions not only change the hydrogen bond network and the orientation of water molecules in the bulk, they also disturb the arrangement of water molecules close to interfaces. Due to the reduced density of water molecules and the accumulation of ions near the interface, the effect is enhanced at interfaces. Chaotropic ions are known as "water structure breakers" (weakly hydrated, have weaker interactions with water than water itself) destabilize the "polymeric" water structure, increase the solvation capacity of water molecules in the liquid water that result in the salting-in effect observed on proteins and macromolecules. On the contrary, kosmotropic ions were believed to be "water structure makers" (having the opposite effect, exhibiting strong interactions with water molecules). They are strongly hydrated and have stabilizing effect on the water structure and consequently salting-out behavior on macromolecules (Zhang, 2006b).

Studies on the gelation kinetics of silica nanoparticles showed that gelation times are increased by over 4 orders of magnitude simply changing the monovalent salt species of the background electrolyte from CsCl to LiCl, which is consistent with the Hofmeister series (van der Linden, 2015). Moreover, the experimental study carried out by Merk et al. gives evidence of ion-specific effects on ligand-free gold nanoparticles prepared by laser ablation in aqueous saline solutions (Merk, 2014). The colloidal stability of gold nanoparticles prepared in highly dilute electrolytes seems to follow a Hofmeister series: kosmotropes (F^-, SO_4^{2-}) act as coagulants, chaotropes (Br^-, I^-, SCN^-) lead to enhanced colloidal stability and others (Cl^- and NO_3^-) present an intermediate effect. Interestingly, these effects predominantly occur when anions are present during the particle formation process; hence Hofmeister effects were shown to affect the dynamics of particle formation (Merk, 2014). Finally, Vereda and co-workers studied the ion specific phenomena in aqueous colloidal suspensions of positively charged, bare magnetite nanoparticles. Concretely, the electrophoretic mobility of the magnetite particles in the presence of increasing concentrations of different anions showed that anions regarded as

kosmotropic are more efficient in decreasing, and even reversing, the mobility of the particles (Vereda, 2015). However, no study has been found on the effect of the presence of different ions during the synthesis of magnetic nanoparticles in aqueous media.

On the other hand, it has been demonstrated that Hofmeister effect can be amplified by the addition of alcohols to the aqueous solutions revealing that this effect is determined by the stability of the newly formed water/alcohol complex, which is strongly dependent on the chemical structure of alcohols. The more stable solvent complex is formed via stronger hydrogen bonds can more effectively differentiate the anions through the anion-solvent complex interactions, resulting in a stronger amplification of Hofmeister effect (Xu, 2014). In the case of iron, it was shown that the effect of mixed ethanol-water solvents promotes the hydrolysis and complexation of iron. For example, it has been reported that the formation of hematite nanocubes (Hamada, 1982) and akaganeite (Matijević, 1987) is accelerated when $FeCl_3$ solutions are heated in ethanol-water or ethylene glycol-water solutions.

2.   EXPERIMENTAL SECTION

In this study, the evolution of the system during the formation of magnetite NCs was followed measuring the temperature, the pH (temperature compensated) and the amount of remnant iron II hydroxide analyzed using the procedure described by Wang et al. (Wang, 2005a). This procedure exploits the selective solubility of $Fe(OH)_2$ at pH 4.5 in presence of insoluble ferric hydroxides and magnetite. In brief, samples of 1 ml of the suspension were taken at regular time intervals from the slurry during the formation of the green rust and the subsequent heating process and added to 25 ml of buffer acetic acid sodium acetate (molar ratio 1:0.285, pH 4.5, 0.05 M) in the glove box (figure 4.2).
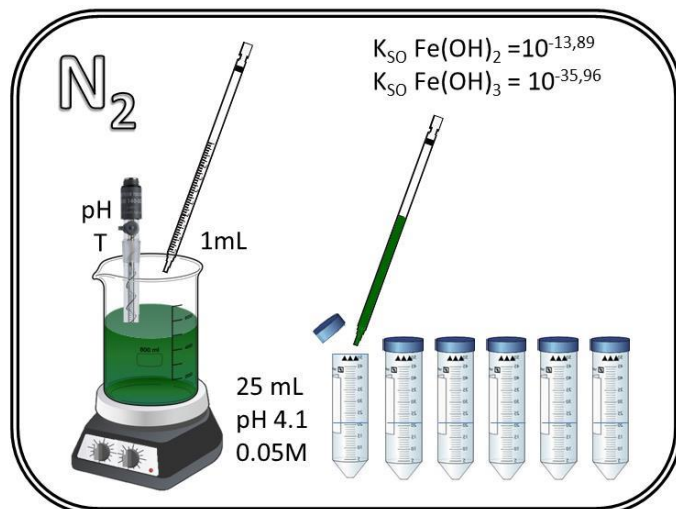
Figure 4.2. *Scheme of the experimental procedure for the study of the evolution of the system.*

After shaking, the suspension color changed from dark green to yellow due to the selective redissolution of Fe^{2+}. Tubes were then centrifuged (RCF=6535 and 30 min) (figure 4.3), 5 ml of supernatant was diluted to 50 ml in HCl 3M and it was analyzed for iron by standard ICP-OES technique.
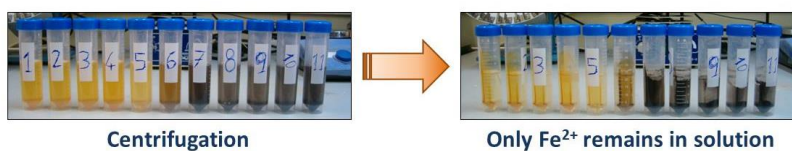
Figure 4.3. *Tubes obtained for studying the evolution of the system.*

This procedure studying the evolution of the system was carried out for the samples shown in table 4.1. The OH⁻ excess was maintained at 0.02 M and the iron concentration at 0.2 M. The results will be interpreted in terms of differences in the oxidation rates of iron (II), hydrolysis rate, green rust stability and the Hofmeister character of the counterions present in each case.

Sample	Counterions	Solvent	Iron salt	Acid media (10^{-2} M)	Base salt	OH⁻ (M)	Oxidant salt
CN0	Na^+, Cl^-	w	$FeCl_2$	HCl	NaOH	0.422	$NaNO_3$
BN0	Na^+, Br^-	w	$FeBr_2$	HNO_3	NaOH	0.422	$NaNO_3$
SN0	Na^+, SO_4^{2-}	w	$FeSO_4$	H_2SO_4	NaOH	0.424	$NaNO_3$
CK0	K^+, Cl^-	w	$FeCl_2$	HCl	KOH	0.421	KNO_3
BK0	K^+, Br^-	w	$FeBr_2$	HNO_3	KOH	0.421	KNO_3
SK0	K^+, SO_4^{2-}	w	$FeSO_4$	H_2SO_4	KOH	0.422	KNO_3
CN25	Na^+, Cl^-	w/et	$FeCl_2$	HCl	NaOH	0.422	$NaNO_3$
BN25	Na^+, Br^-	w/et	$FeBr_2$	HNO_3	NaOH	0.422	$NaNO_3$
SN25	Na^+, SO_4^{2-}	w/et	$FeSO_4$	H_2SO_4	NaOH	0.424	$NaNO_3$
CK25	K^+, Cl^-	w/et	$FeCl_2$	HCl	KOH	0.421	KNO_3
BK25	K^+, Br^-	w/et	$FeBr_2$	HNO_3	KOH	0.421	KNO_3
SK25	K^+, SO_4^{2-}	w/et	$FeSO_4$	H_2SO_4	KOH	0.422	KNO_3

__Table 4.1.__ Experimental conditions for the synthesis of magnetite nanocrystals with different counterions in water and water-ethanol (25%) medium.

3. RESULTS

The onset of nucleation of magnetite takes place at 22 ± 1 min (52 ± 5 °C) for sodium salts and 26 ± 1 min (62 ± 4 °C) for potassium salts in water or ethanol 25% and at pH values around 11. The impression that sodium and potassium salts behave differently is confirmed in figure 4.4 where the evolution of iron (II) concentration with time for all the counterions studied in water and ethanol mixtures is presented. The conclusion is that potassium salts resist more the oxidation than the sodium salts (and consequently the crystallization of magnetite take place at higher temperatures), and that the differences increase in the presence of ethanol. The pH evolution also shows that the potassium salts neatly separate from the sodium ones (figure 4.5). These results have to be correlated with the fact that potassium salts generate bigger crystallite sizes than sodium salts and the general influence of ethanol reducing nanocrystal sizes.
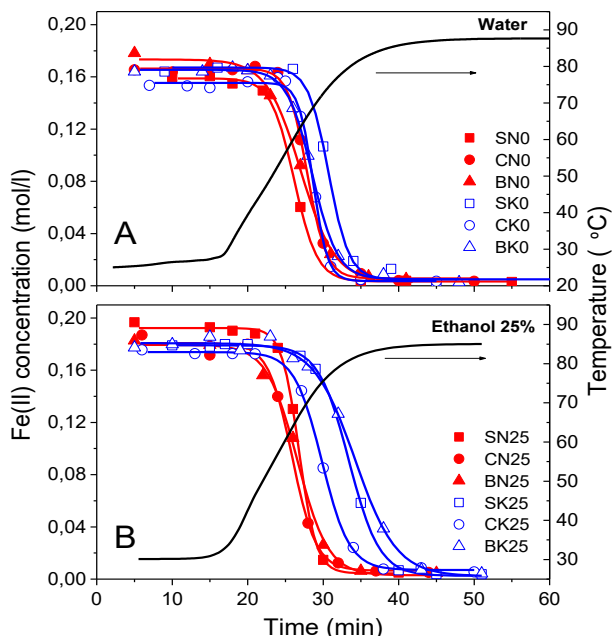
Figure 4.4. *Evolution of the concentration of soluble iron (II) with time during the synthesis of magnetite nanocrystals in the presence of different counterions in water (A) and in ethanol 25% (B).*
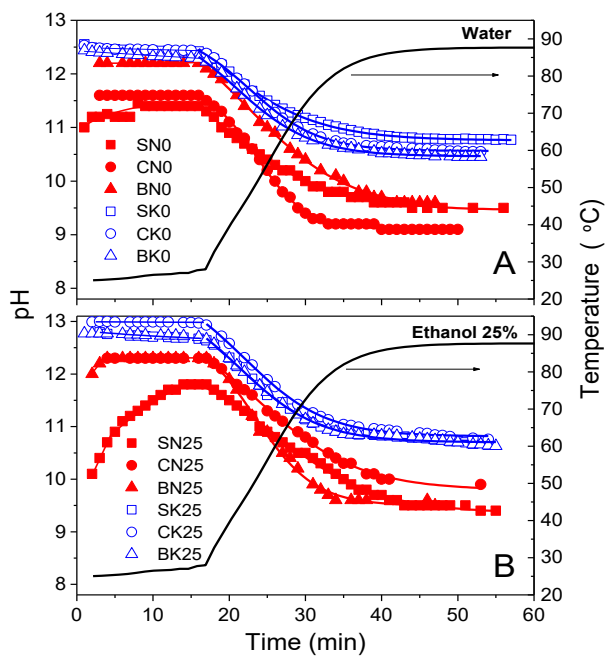

Figure 4.5. *Evolution of the pH with time during the synthesis of magnetite nanocrystals in the presence of different counterions in water (A) and in ethanol 25% (B).*

4. DISCUSSION

The formation of magnetite nanocrystals by oxidative precipitation is a complex phenomenon that was described long ago using air as oxidant (Kiyama, 1974). The process proceed as follows: after the initial formation of green rust, the ferrous ions remaining in the alkaline suspension are in the form of $FeOH^+$ forming a dense layer surrounding the negatively charged green rust particles (Guilbaud, 2013). Then, Fe_3O_4 nanoparticles begin to grow in this layer at pH 9-10 by the slow coprecipitation of $FeOH^+$ with ferric hydroxocomplexes formed by oxidation in solution. In general terms, the formation of magnetite via the green rust is a coupled oxidation-dehydration process. The particle sizes attained should be inversely proportional to the speed of the overall process. The effect of the counterions and the ethanol on the final particle size had to be understood through their influence on the underlying kinetics of dehydration and/or oxidation processes and the stability of the green rust precursor.

4.1. Dehydration: The Hofmeister approach.

In order to apply the Hofmeister concept to our case, we evaluated the water affinity of all the counterions pairs by means of their linear coefficient (B) in the Jones Dole equation for the relative viscosity ($\eta/\eta^0 = 1 + A\sqrt{c} + Bc$) calculated by adding the cation and anion contribution (Table 4.2) (Collins, 2006). This value (called in this work the Hofmeister parameter) is considered a measure of the strength of the ion-water interactions normalized to the strength of water-water interactions.

Ions that are weakly hydrated exhibit a smaller change in viscosity with concentration, having negative B coefficients (chaotropes). The opposite effect is presented by the strongly hydrated ions that have positive B coefficients (kosmotropes). It means that the higher this parameter is, the higher cosmotropicity and salting out capacity of the solutions are. Figure 4.6 presents the plots of the nanocrystal TEM sizes as a function of the Hofmeister parameter for water and water/alcohol mixtures.

Counterions electrolyte	B (cation)	B (anion)	Hofmeister parameter
Na$_2$SO$_4$	0.086	0.208	0.380
K$_2$SO$_4$	-0.007	0.208	0.194
NaCl	0.086	-0.007	0.079
NaBr	0.086	-0.032	0.054
KCl	-0.007	-0.007	-0.014
KBr	-0.007	-0.032	-0.039

Table 4.2. *Evaluation of the Hofmeister parameters of the electrolyte formed by the counterion pairs from the B coefficients of the ions (Collins, 2006).*
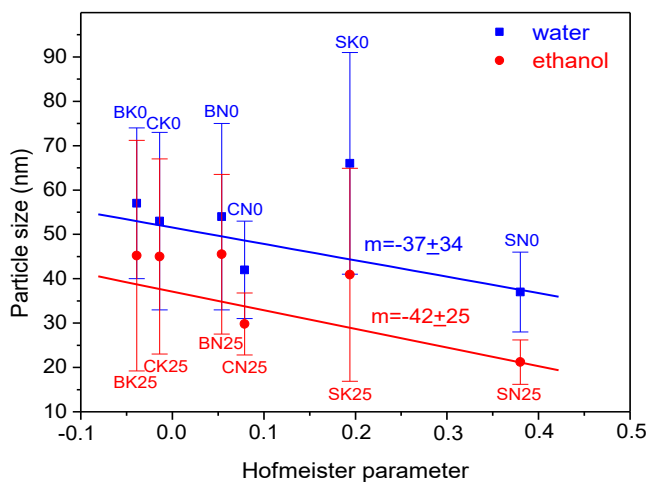
Figure 4.6. *Particle sizes of magnetite nanocrystals produced by oxidative precipitation as a function of the Hofmeister parameter (the error bars represent the width of the particle size distribution and m stands for the slope).*

It appears to be a weak negative dependence of the size with this parameter in the case of water solutions that becomes more defined in the case of ethanol 25% solvent. The necessary conclusion is that the increase in cosmotropicity leads to a decrease in particle size. This is because of the cosmotropic anions have the capacity to structure the solvent molecules around them. More structuration implies more salting out effect, intensive nucleation and smaller particle sizes. Therefore, particle sizes correlation with the

Hofmeister series reflects the influence of the cosmotropic or caotropic hydration of the counterions. The Hofmeister effect operates on the reactivity of the intermediate green rust from which magnetite is produced (Luengo, 2016). This dependence was mentioned in previous works for different materials such as $Mg(OH)_2$ (Giorgi, 2005) and akaganeite (Yue, 2011).

4.2. Influence of counterions and ethanol on green rust

The first solid to appear after mixing all the reagents for the synthesis of magnetite nanocrystals by oxidative precipitation is the GR. Assuming that its particle size and solubility should influence the final product any factor that influence the GR will influence the NCs size. It has been determined that green rust incorporates to its structure not only anions but also cations present in the solution (Christiansen, 2009), so it is expected that both the counteranions and countercations influence its stability. Thermodynamic data compiled by Rickard D. and Luther G.W. gave the log K's values of the dissociation of chloride and sulphate green rusts (equations 4.1 and 4.2), i.e. 28.3 and 3.9, respectively (Rickard, 2007).

$$Fe_4(OH)_8Cl + 8H^+ \leftrightarrow 3Fe^{2+} + Fe^{3+} + Cl^- + 8H_2O \qquad (4.1)$$

$$Fe_6(OH)_{12}SO_4 + 12H^+ \leftrightarrow 4Fe^{2+} + 2Fe^{3+} + SO_4^{2-} + 12H_2O \qquad (4.2)$$
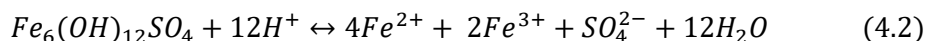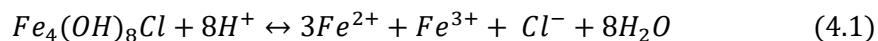
Unfortunately there are no thermodynamic data for the bromide green rust, but we could assume that the bromide bearing green rust will be less stable than the chloride one due to the increase in interlayer distance from Cl- (0.795) to Br- (0.806) (Cornell, 2006). Consequently an increase in stability of the green rust is expected as follows:

$$KBr \approx NaBr < KCl \approx NaCl < K_2SO_4 \approx Na_2SO_4$$

So for any given condition, the supersaturation for the green rust formation should be higher in the sulphate case and lower in the bromide case, and for these reason we expect a green rust formed by smaller particles in the sulphate case. The salting out generated by the presence of ethanol enhanced the differences observed in water, leading

to a massive green rust precipitation. In the most extreme case (sodium sulphate and ethanol) a thick suspension was formed whose pH evolved the slowest figure 4.5B.

The important effect of ethanol reducing the particle size has been related to the improvement of dispersability/dehydration of iron hydroxides (Starowicz, 2011), and enhancement of hydrolysis (Hamada, 1982) and decrease of dielectric constant that lowered the solubility of ferrites easing the crystallization (Ding, 2015).

4.3. Oxidation

We expect magnetite particle size to be governed by the oxidation rate, modified by the counter anions present in solution, and the competitive nuclei growth, according to previous studies (Tamura, 1976; Wang, 2005a). Following this approach, it can be concluded that the faster the oxidation takes place, the smaller particles are obtained.
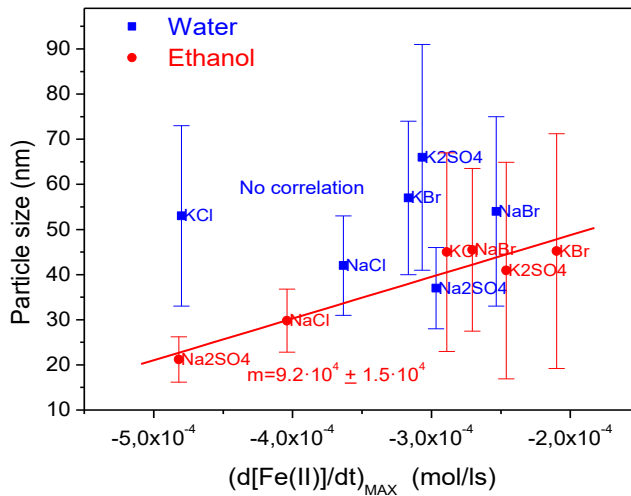

Figure 4.6. Variation of magnetite nanocrystal size as a function of the oxidation rate.

This correlation among the oxidation rate of Fe(II) (represented by the maximum slope of the [Fe(II)] decrease with time) and particle size is only observed when ethanol is

present in the reaction media (Figure 4.7). In water there appears no dependence of particle size on oxidation rate.

Oxidation proceeds with a pH decrease following a combination of oxidation pathways:

$$Fe_6(OH)_{12}SO_4 + NaNO_3 + NaOH \rightarrow 2Fe_3O_4 + HNO_2 + Na_2SO_4 + 6H_2O$$

$$Fe_6(OH)_{12}SO_4 + \frac{2}{3}NaNO_3 + \frac{4}{3}NaOH \rightarrow 2Fe_3O_4 + \frac{2}{3}NO + Na_2SO_4 + \frac{20}{3}H_2O$$

$$Fe_6(OH)_{12}SO_4 + \frac{1}{4}NaNO_3 + \frac{7}{4}NaOH \rightarrow 2Fe_3O_4 + \frac{1}{4}NH_4OH + Na_2SO_4 + \frac{25}{4}H_2O$$
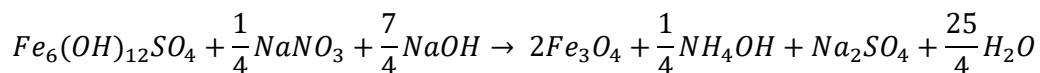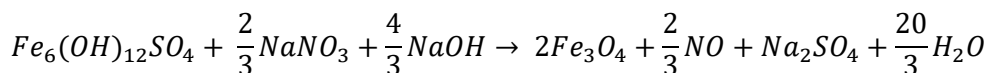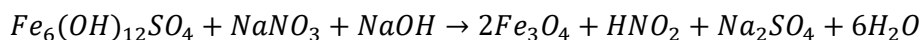
The rate of pH decrease depends on the proportion of the three processes that take place subsequently. In most cases, the pH decreases at a rate of -0.119 ± 0.008 min^{-1} revealing a common pathway. Only NaBr in ethanol and NaCl in water decrease significantly faster at -0.181 and -0.175 min^{-1} respectively. Being a consequence of the overall process, the pH evolution during the precipitation could not be related with the oxidation rate, particle size, polydispersity or the Hofmeister parameter in this study.

5. CONCLUSIONS

The main factors that influence the final particle size of the magnetite nanocrystals are: dehydration of hydroxylated iron species, stability of the intermediate green rust and oxidation rates of iron (II). These three factors accelerate the process and favour smaller magnetite particle sizes, but its influence largely depends on the solvent. In water, dehydration and oxidation rates seem to have less influence than the differences in the stability of green rust. In ethanol solutions, the decrease of available water enhances directly the dehydration factor and indirectly the oxidation. The link among both processes is illustrated by the differences in oxidation rates with K$^+$ (caotropic-less hydrated-slower oxidation) and Na$^+$ (cosmotropic-more hydrated-faster oxidation). In the presence of ethanol 25%, the three factors point in the same direction enhancing the counterions effects.

5

Bimetallic nanocrystals

1. INTRODUCTION

The combination of materials with different physical properties in one single structure is a common approach for the creation of novel systems with improved functionalities (Cheon, 2008; Lee, 2013; Tan, 2016). Among them, the synthesis of bimetallic nanoparticles has attracted much attention due to the potential to explore the special functions of two or even more metal elements (Sun, 2004; Figuerola, 2010; Deepak, 2015; Prodi, 2015). Depending on the materials and synthesis method, different structures may appear like solid solutions, doped oxides, core/shell or pudding-like particles, etc.
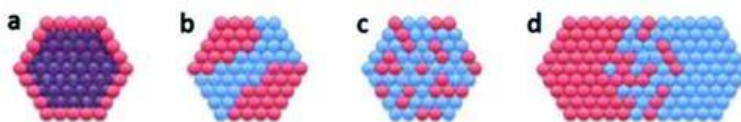
Figure 5.1. *Schematics showing different types of bimetallic nanoparticles: (a) core/shell, (b) phase-segregated, (c) solid solution and (d) coalesced nanoparticles (Tan, 2016).*

Different inorganic hybrid nanostructures based on iron oxide have been synthesized to improve their magnetic performance and to obtain more efficient systems (Figuerola, 2010). The main interest in these nanostructures is that each of the components should be able in principle to accomplish a specific task, which can be performed simultaneously without damaging each other.

Doping, which involves the intentional addition of appropriate atoms or ions into the host materials, is one of the effective ways of improving the physical/chemical characteristics of the parent materials and imparting desirable properties to the host materials (Park, 2016). Particles of various spinel ferrites can now be routinely prepared using the coprecipitation method by partial or complete replacement of Fe^{2+} ions in magnetite (Fe_3O_4) nanocrystals with other divalent transition metal ions (Co^{2+}, Ni^{2+}, Mn^{2+}) (Sun, 2004; Schultz-Sikma, 2011; Sytnyk, 2013; Sathya, 2016). Among the various spinel ferrites, cobalt ferrite exhibits a cubic spinel structure with a ferromagnetic nature

(Grigorova, 1998; Cui, 2013) and has been attracting attention in the last years because of its interesting electronic, magnetic, optic and catalytic properties (Kumbhar, 2012; Houshiar, 2014; Lopes-Moriyama, 2014; Avazpour, 2015). $CoFe_2O_4$ stands out as particularly appealing material: despite its bulk Ms (80 Am²/kg) lower than that of Fe_3O_4 (92 Am²/kg) at room temperature (Cullity, 2011), this material is characterized by a high intrinsic magnetocrystalline anisotropy (K) of nearly $2 \cdot 10^5$ J/m³. This value is almost one order of magnitude higher than that of Fe_3O_4, and it is responsible for the large coercivity of $CoFe_2O_4$ (Cullity, 2011). In $CoFe_2O_4$ nanocrystals, such large coercivity values should provide hysteresis loops that are wider than those of other spinel ferrite nanocrystals of similar size, and would originate higher heat dissipation under an alternate magnetic field (Sathya, 2016). $CoFe_2O_4$ magnetic nanoparticles have also been studied for the fabrication of biosensors because of their biocompatibility and relatively low toxicity (Yardımcı, 2012).

Recently, magnetic NPs engineered by lanthanide doping have attracted considerable attention due to their wide applications in biology, catalysis and solar cells (Wang, 2011a; Prodi, 2015). Among de lanthanide elements, the interest in gadolinium (Gd) has increased because of its intriguing properties (Park, 2016). First, this element has a strong paramagnetic character due to its seven unpaired 4f electrons (Gd^{3+}), which can be advantageously exploited for MRI (Caravan, 1999; Bottrill, 2006). Recently, T_1-T_2 dual modal magnetic resonance imaging (MRI) contrast agents were produced by conjugating Gd complexes on the surface of T_2 contrast agents (Bae, 2010) or by grafting Gd oxide nanocrystals onto the shell of core-sell structured nanomaterials (Choi, 2010). Gd-doped iron oxide NPs may provide an effective route for the fabrication of T_1-T_2 dual modal MRI contrast agents (Zhou, 2012; Xiao, 2014). Gd doping or labelling has been shown to improve the MRI contrast of iron oxide NPs via T_1 enhancement (Bae, 2010; Wang, 2013; Zhou, 2013; Xiao, 2014; Shin, 2015), whereas the magnetic hyperthermia properties of gadolinium-doped magnetite have received much less attention (Drake, 2007; Douglas, 2016).

Secondly, given the strong propensity of the Gd element to absorb X-ray photons (owing to the relatively high atomic number of 57) and the high neutron capture cross-

section of two gadolinium isotopes (^{155,157}Gd) (Shih, 1992; De Stasio, 2001) render Gd^{3+}-based compounds very attractive, since they can combine medical imaging (MRI) and two different therapeutic protocols to fight cancer (radiotherapy and neutron-capture therapy) (Roux, 2010).

Core/shell nanostructures with modulated composition and size are an efficient way to construct multicomponent structures that combine various properties of constituent materials in a single system (Xu, 2007; Schartl, 2010; Wang, 2015; Khan, 2016; Nairan, 2016). Interesting features might arise from the interfaces between components, which might be translated into new applications. It has been recently shown that a significant increase in the magnetic thermal induction by nanoparticles can be achieved by core/shell particles growth by a multistep seed-mediated particle process (Lee, 2011). However, it should be noted that most of the preparation methods leading to these multipurpose nanostructures convey a high level of complexity. Two heavy elements have been chosen in this work to produce multifunctional particles, bismuth and gold with high X-ray absorption coefficients, which makes them interesting for computed tomography (Kalender, 2006; Pan, 2008; Lee, 2013).

Core/shell magnetic nanoparticles based on magnetite/bismuth oxide showed great potential in cancer therapy since they combine the ability to image a specific tumor area by two different techniques, MRI and tomography (CT), and the ability to target it under the influence of a magnetic field and destroy the tumor with heat (Andrés-Vergés, 2012; Laguna-Marco, 2014; Veintemillas-Verdaguer, 2015).

On the other hand, gold nanoparticles can be used as X-ray contrast agents with properties that overcome some significant limitations of iodine-based agents. Gold has higher absorption than iodine with less bone and tissue interference achieving better contrast with lower X-ray dose. Nanoparticles clear the blood more slowly than iodine agents, permitting longer imaging times. Ideally, gold nanoshells on magnetic nanoparticles should be thin enough to induce minimal alteration of the magnetic properties of the magnetite core. Gold-coated NPs can provide a number of additional

advantages, such as near-infrared (NIR) absorption, photon scattering, and the preservation of the core magnetic properties (Shah, 2013).

Bimetallic core/shell magnetite/Au NPs are promising candidates as dual-mode contrast agents for MRI and CT imaging (Narayanan, 2012). However, the magnetization and X-ray attenuation of hybrids appears to have opposing effects (Zhang, 2013b). A thick gold nanoshell layer improves the X-ray absorption ability but reduces the saturation magnetization of the hybrids (Lyon, 2004; Guo, 2010). Gold nanoshells have also been reported to exhibit photothermal properties. Laser illumination of gold nanoshell can be used for increasing the local temperature around tumor thus helping in their heat destruction. This property helps gold shell to act as a potent material for hyperthermia treatment (Hirsch, 2003; Pissuwan, 2006; Ke, 2011).

Several papers have reported the synthesis of core-shell Fe_3O_4@Au nanocomposites, but in most cases, the coating of individual magnetite nanoparticles and the tenability of the shell thickness still remain unresolved (Lyon, 2004; Mikhaylova, 2004). This synthesis involves two main processes: the magnetite nanoparticle core synthesis and the subsequent coating with a layer of gold (Goon, 2009; Sood, 2016). Methods for obtaining gold-coated magnetite can be categorized according to the variations in each of the two processes: use of reverse micelles (Mikhaylova, 2004; Mandal, 2005), both synthesis and coating in aqueous phase (Lyon, 2004; Lo, 2007), both synthesis and coating in organic phase (Wang, 2005b) and a combination of organic synthesis of magnetite cores followed by gold coating of particles in an aqueous environment (Xu, 2007; Lim, 2008). Another class of gold-magnetite composites has also been reported involving the attachment of discrete gold nanoparticles onto magnetite without forming a full coating (Caruntu, 2005; Bao, 2007). Such composites may be useful in applications such as protein separation, optical imaging or catalysis, where a full coating is not necessarily required and has the advantage of having not only the gold surface but also the iron oxide surface partially available for further functionalization.

2. EXPERIMENTAL SECTION

2.1. Preliminary results: synthesis of bimetallic nanocrystals by varying the iron concentration

To obtain the bimetallic nanocrystals the same experimental procedure described by Andrés-Verges et al. (Andrés-Vergés, 2012) has been followed. In this paper the synthesis is carried out by coprecipitation of iron (II) sulfate and bismuth nitrate and subsequent aging, as explained in Chapter 3 for pure magnetite nanocrystals. To study the effect of the Bi, Bi/Fe atomic ratio was changed substituting iron by bismuth.

We performed the same study using Co and Gd as well as Bi for reference. The idea is to obtain nanoparticles with new or improved properties derived from secondary metals that are substituting iron. In the previous work, Bi/Fe atomic ratio (($Bi/Fe)_{at}$ x 100) has varied from 5 to 20% resulting a reduction in the nanocrystal size as the Bi amount increases (Andrés-Vergés, 2012). However, here we observed that by varying the ratio of both Co and Gd (from 2 to 20 %) opposite effect is observed, i.e., the crystal size increases as the amount of these metals increases (Table 5.1, Appendix III).

The salts used as metal precursors were $Bi(NO_3)_3$, $Gd(NO_3)_3$ and $Co(NO_3)_2$, respectively, and the concentration of metal was set at $5 \cdot 10^{-4}$ M for all cases. The concentration of $NaNO_3$ and the OH^- excess also remained constant (0.05 M and 0.02 M, respectively). All syntheses were carried out in a mixture 50% H_2O/ethanol.

In all cases, the proportion of secondary metal determined by ICP in the samples closely follows the preexistent in the reactant mixture, indicating that both iron and secondary metal are precipitated during the reaction process.

The presence of bismuth reduces dramatically the nanocrystal size because it acts as a coating, being accumulated at the nanoparticle surface and limiting the particle growth (Andrés-Vergés, 2012). However, the effect of the presence of Gd and Co is less clear, since the increased particle size may be due not only to the presence of these metals, but

also to the reduction of the iron concentration as reported before in Verges et al. (Andrés-Vergés, 2012).

Sample	$\%_{at}$ M_{theor}	[FeSO$_4$] (M)	[Secondary metal salt] (M)		TEM Size (nm)/PDI	DRX Size (nm)	$\%_{at}$ M_{exp}
FeBi5	5	$1 \cdot 10^{-2}$	Bi(NO$_3$)$_3$	$5 \cdot 10^{-4}$	14/0.33	18.1	7.3
FeBi10	10	$5 \cdot 10^{-3}$	Bi(NO$_3$)$_3$	$5 \cdot 10^{-4}$	9/0.29	9.3	13.3
FeBi20	20	$2.5 \cdot 10^{-3}$	Bi(NO$_3$)$_3$	$5 \cdot 10^{-4}$	6/0.29	6.3	19
FeGd2	2	$2.5 \cdot 10^{-2}$	Gd(NO$_3$)$_3$	$5 \cdot 10^{-4}$	43/0.29	41.1	1.9
FeGd5	5	$1 \cdot 10^{-2}$	Gd(NO$_3$)$_3$	$5 \cdot 10^{-4}$	59/0.35	55.6	4.6
FeGd10	10	$5 \cdot 10^{-3}$	Gd(NO$_3$)$_3$	$5 \cdot 10^{-4}$	107/0.32	104.3	9.0
FeGd20	20	$2.5 \cdot 10^{-3}$	Gd(NO$_3$)$_3$	$5 \cdot 10^{-4}$	112/0.33	122.7	18.6
FeCo2	2	$2.5 \cdot 10^{-2}$	Co(NO$_3$)$_2$	$5 \cdot 10^{-4}$	30/0.30	29.3	2.4
FeCo5	5	$1 \cdot 10^{-2}$	Co(NO$_3$)$_2$	$5 \cdot 10^{-4}$	47/0.40	63.2	5.6
FeCo10	10	$5 \cdot 10^{-3}$	Co(NO$_3$)$_2$	$5 \cdot 10^{-4}$	77/0.36	99.3	10.7

Table 5.1. Experimental conditions and basic data obtained for the synthesis of bimetallic nanocrystals by varying the iron concentration. %M$_{theor}$ is given in M/Fe atomic ratio ((M/Fe)$_{at}$ x 100) and %M$_{exp}$ is calculated by ICP results.

For this reason, we have carried out a systematic study keeping constant the iron concentration and varying the metal proportion. The experimental conditions that give rise to pure small and uniform magnetite nanocrystals (sample SN25 21 nm) have been chosen, that is: 0.2 M FeSO$_4$, 0.2 M NaNO$_3$, 0.02 M OH$^-$ excess and 25% ethanol.

Thus, the metal concentration was varied from 2 to 20 % in order to study how the secondary metal is incorporated as well as its effect on the size, shape and properties of the nanocrystals.

2.2. Synthesis of bimetallic nanocrystals by varying the metal concentration

Every sample was synthesized by the precipitation of an iron (II) salt ($FeSO_4$) dissolved in 10^{-2} M H_2SO_4 and metal salt ($CoNO_3$, $BiNO_3$, $HAuCl_4$, $GdNO_3$) in a basic media (NaOH) and in presence of a mild oxidant ($NaNO_3$) under stirring in an oxygen free atmosphere (glove box under nitrogen) (Andrés-Vergés, 2008). All reactions were carried out in a 500 ml double-walled reactor heated by means of a thermostated fluid set to 90ºC using a thermostat (figure 5.2).

In these cases, a new term corresponding to the secondary metal added should be included in the equation described by Sugimoto to calculate the base excess (equation 5.1).

$$[OH^-]_{excess} = [NaOH] - 2[Fe^{2+}] - m[metal] - n[Acid] - p[metal] \qquad (5.1)$$

where *n* is 1 or 2 depending on the monoprotic or diprotic character of the acid used to dissolve the iron salt, *m* is the oxidation state of the metal used and *p* is the number of acid protons of the precursor salt (*p* is equal to 1 for $HAuCl_4$ and 0 for all other precursors). For each case in order to maintain the excess of OH^- the concentration of [NaOH] is calculated using this expression.
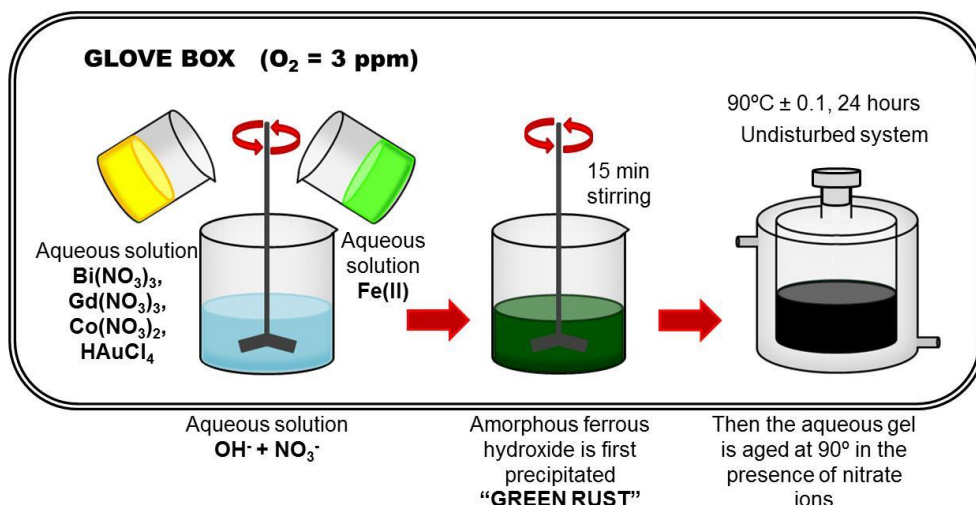

Figure 5.2. *Scheme of the experimental synthesis of bimetallic nanocrystals by oxidative precipitation.*

In all cases the precipitation is carried out under stirring, obtaining a final volume of 250 ml. When the precipitation was completed the green rust formed initially was overhead stirred for 15 min. After this time, this reaction intermediate was aged at 90 ºC for 24 h without agitation to obtain the bimetallic nanocrystals (figure 5.2). Ageing time was fixed at 24 h in order to reach conditions close to the equilibrium. At the end of the synthesis the system was left to cool down to room temperature and the nanocrystals were separated by magnetic decantation followed by several washings with distilled water outside the glove box.

Preparation of metal solutions and mixing procedure were adapted in each case to the different solubilities and reactivities of the metal salts.

- Bi salt was dissolved in 1.73 M HNO_3 and this solution was added quickly and simultaneously with the Fe (II) solution over the basic solution. Iron and bismuth cannot be mixed because the nitric acid necessary to dissolve the $Bi(NO_3)_3$ (is not easy to solubilize) oxidizes the Fe (II) prematurely. Bismuth salt can be added to the system either at the same time of the Fe salt or after the GR formation. A preliminary study was carried out to assess the optimal addition time, as shown in table 5.2.

Sample	%$_{at}$ M$_{theor}$	Addition time	TEM Size (nm)/PDI	DRX Size (nm)	%$_{at}$ M$_{exp}$
Bi2SN25	2	At the same time as Fe salt	29/0.36	28.6	2.2
Bi2SN25(2)	2	After the green rust formation	41/0.45	39.7	2.6

Table 5.2. *Experimental conditions and basic data obtained for the synthesis of bimetallic nanocrystals by varying the metal addition time. %M$_{theor}$ is given in M/Fe atomic ratio ((M/Fe)$_{at}$ × 100) and %M$_{exp}$ is calculated by ICP.*

Both size and polydispersity are smaller in the sample where Bi and Fe were added simultaneously, so we decided when possible to add the metal and iron salts simultaneously for the rest of the experiments that is the case of Co and Gd salts.

- In the case of Au salt, it was dissolved in water and added slowly after the green rust is formed (15 min after the addition of iron (II)). Given the oxidant character of Au^{3+} it will be immediately reduced to Au^0 in the presence of free Fe^{2+}. The above mixing procedure was devised in order to give chance to the Au^{+3} to hydrolyze by facing the green rust that is less reactive than Fe^{2+}.

3. SAMPLES CHARACTERIZATION

The structural and morphological characterization of the bimetallic nanocrystals synthesized by varying the iron concentration is included in Appendix III.

Table 5.3 shows a summary of the effect of M/Fe ratio on particle size for samples prepared keeping constant the iron concentration and varying the secondary metal concentration.

Sample	%$_{at}$ M_{theor}	[M] (M)	[NaOH] (M)	TEM Size (nm)/PDI	DRX Size (nm)	%$_{at}$ M_{exp}
Bi2SN25	2	$4 \cdot 10^{-3}$	0.607	29/0.36	28.6	2.2
Bi20SN25	20	$4 \cdot 10^{-2}$	0.715	19/0.60	19.8	19
Gd2SN25	2	$4 \cdot 10^{-3}$	0.436	42/0.31	40.9	1.6
Gd5SN25	5	$1 \cdot 10^{-2}$	0.454	51/0.40	50.6	4.0
Co2SN25	2	$4 \cdot 10^{-3}$	0.432	30/0.27	28.6	2.2
Co5SN25	5	$1 \cdot 10^{-2}$	0.444	26/0.24	25.4	5.0
Au2SN25	2	$4 \cdot 10^{-3}$	0.438	34/0.34	34.2	2.3
Au5SN25	5	$1 \cdot 10^{-2}$	0.462	31/0.39	29.0	4.3
Au20SN25	20	$4 \cdot 10^{-2}$	0.582	31/0.46	29.1	16.8

Table 5.3. *Experimental conditions for the synthesis of bimetallic nanocrystals by varying the secondary metal concentration. [M] is referred to $Bi(NO_3)_3$, $Gd(NO_3)_3$, $Co(NO_3)_3$ and $HAuCl_4$, respectively. %M_{theor} is given in M/Fe atomic ratio (($M/Fe)_{at}$ x 100) and %M_{exp} is calculated by ICP results.*

In all cases, the proportion of secondary metals determined by ICP in the samples closely follows the preexistent in the reactant mixture, indicating that both iron and secondary metal coprecipitate during the reaction process. The differences between the measured and the estimated values in the case of gold nanocrystals are probably due to the loss of Au during each washing step.

3.1. Bi-magnetite nanocrystals

Structural characterization of the powders was carried out from the X-ray patterns. The XRD diffractograms can be observed in Figure 5.3.
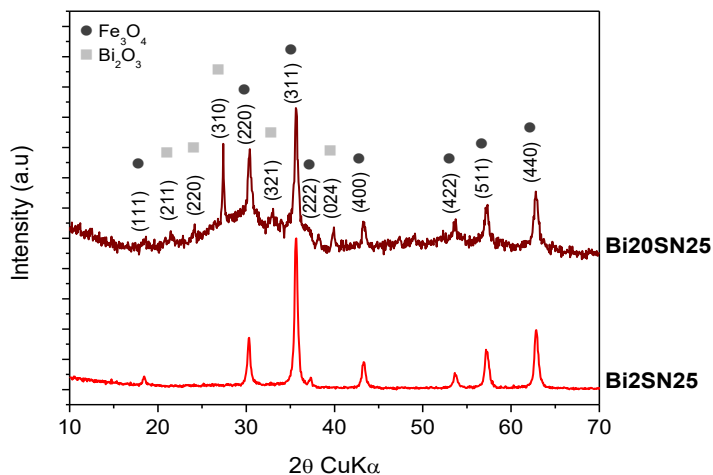
Figure 5.3 *X-ray diffraction patterns of magnetite/bismuth nanocrystals with two different bismuth content* *$((Bi/Fe)_{at} \times 100)$*

According to the diffraction pattern for the sample with 2% of Bi, all the peaks correspond to magnetite. However at higher Bi concentration, a new intense peak due to Bi_2O_3 appears at 27.3º (2θ) ((310) planes, (JCPDS 71-0467). Crystal size calculated from the width of the (311) peak agrees well with the TEM size, which strongly suggests that each particle is a single crystal as in the case of pure magnetite nanoparticles prepared by this method. The lattice constant (*a*) for samples Bi2SN25 and Bi20SN25 calculated from

311 peak is 0.8358 nm in both cases, so there is not significant evidence of substitution of Fe^{3+} for Bi^{3+} in the magnetite crystal structure. The broad band at around 30° (2θ) suggests the presence of amorphous material that can also be observed in the TEM pictures together with well-defined NC (Figure 5.3).

As the concentration of Bi increases from 2 to 20% nanoparticle size decreases from 29 nm to 19 nm (figure 5.4), as reported before in Andrés-Verges et al. (Andrés-Vergés, 2012). This reduction in size by introducing bismuth (III) cations in the reaction media is a clear indication of the interference of this element on the nanoparticle growth process. Sample with 2% of Bi is homogenous in size and shape, but sample with 20% of Bi presents a very high polydispersity. This represents a strong contrast with the sample FeBi20 with 20% of Bi but lower iron concentration, [Fe] = $2.5 \cdot 10^{-3}$ M instead of 0.2 M (presented in the previous section 2.1). In that case the average NC size was the same but the polydispersity was lower.
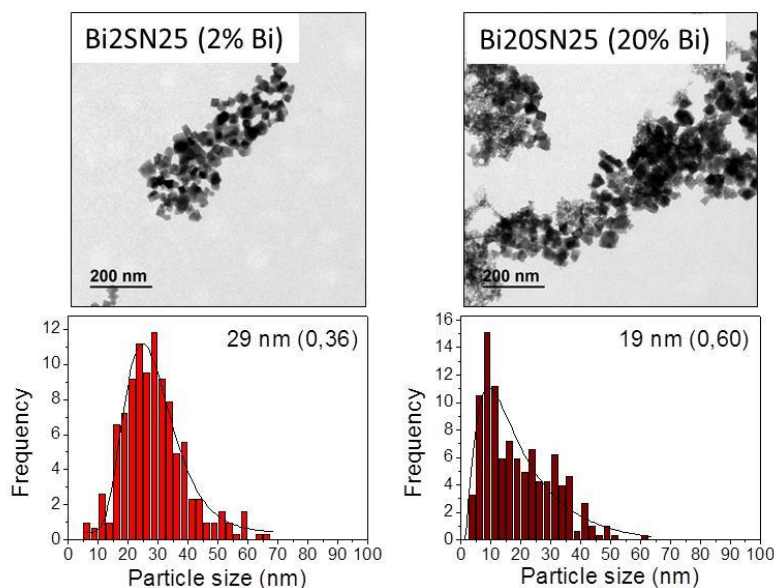
Figure 5.4. *TEM micrographs of magnetite/bismuth nanocrystals with two different bismuth content $((Bi/Fe)_{at}x100)$*

In order to gain more information on the microstructure of this material, we have chosen the 2% Bi (more homogeneous sample) to perform an electron microscopy study employing the HAADF technique (figure 5.5). In this figure the heavier Bi atoms (not distinguishable under ordinary TEM observation) appear brighter than the Fe atoms. The bismuth-bearing shell appears discontinuous with the Bi atoms distributed as isolated surface atoms or in small clusters of presumably bismuth oxide. In contrast to that, NC cores appear as well-ordered magnetite crystals.
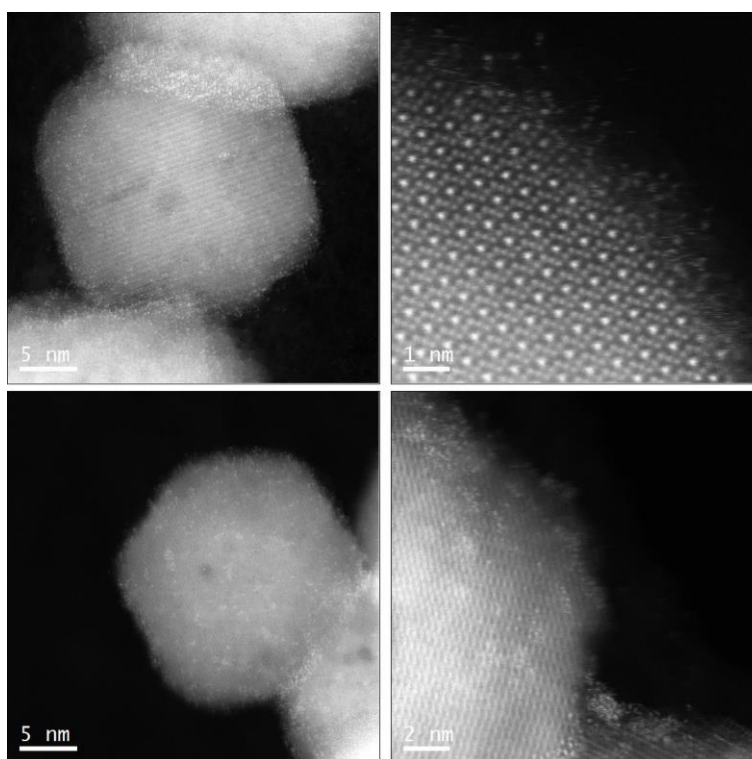
Figure 5.5. *HAADF images of 2% Bi nanocrystals (the bright points correspond to bismuth atoms).*

Magnetic properties of magnetite/bismuth oxide samples at 250 K are displayed in figure 5.6 and table 5.4.
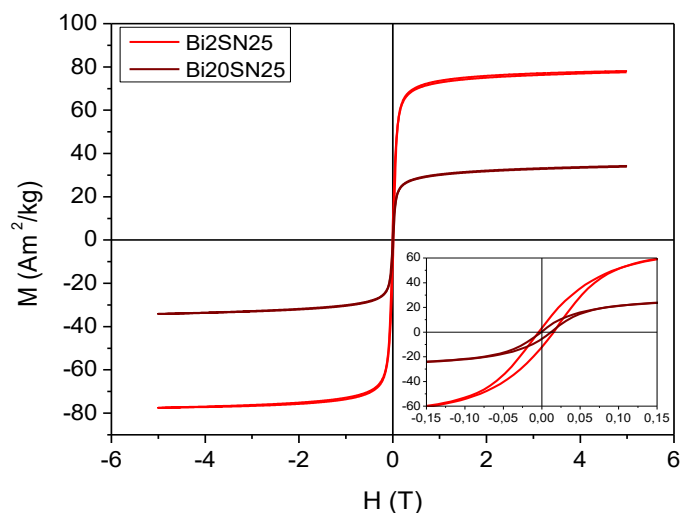
Figure 5.6. *Hysteresis loop at 250 K of magnetite/bismuth nanocrystals with two different bismuth content $((Bi/Fe)_{at} \times 100)$*

Saturation magnetization (Ms) for magnetite/bismuth NC was found to be 86 and 55 Am²/kg when curves are corrected for the 2% and 20% of bismuth, respectively. The first value is close to the saturation magnetization of bulk magnetite (Cullity, 2011), however when the concentration of Bi increases the saturation magnetization decreases considerably. The saturation magnetization depends strongly on the size of the nanoparticles (Demortiere, 2011), so the decrease in Ms value with particle sizes and crystallinity can be attributed to surface effects. In the case of sample Bi20SN25, the polydispersity accounts for an important reduction in Ms of nearly 40%.

Sample	$\%_{at}$ Bi	TEM size (nm)	Ms (Am^2/kg_{sample})	$Ms_{corrected}$ ($Am^2/kg_{Fe_3O_4}$)	Hc (kA/m)
Bi2SN25	2	29	80	86	8
Bi20SN25	20	19	36	55	2

Table 5.4. *Magnetic properties of magnetite/bismuth nanocrystals.*

If we represent M/Ms vs H (figure 5.7) it is observed that both loops are not identical, which could be due to internal spin frustrations. On the other hand, the squareness degree calculated as S = Mr/Ms for samples Bi2SN25 and Bi20SN25 is 0.095 and 0.081, respectively, which means that NCs are nearly at the superparamagnetic state.
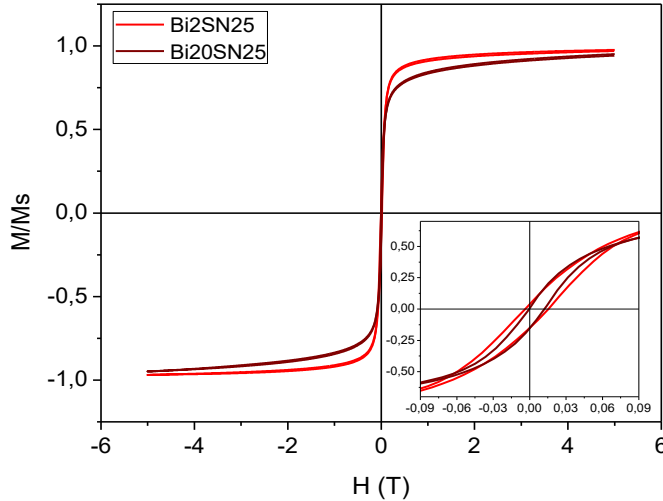
Figure 5.7. *Normalize magnetization curve at 250 K of magnetite/bismuth nanocrystals with different bismuth content ((Bi/Fe)$_{at}$ × 100).*

Coercivities at room temperature were low, decreasing from 8 kA/m down to 2 kA/m for the smallest particles. If we compare the Bi-magnetite samples with those of pure magnetite of the similar size (CN25 and SN25), it can be observed that in the case of pure magnetite the coertivity value is higher for the smaller sample (table 5.5).

	Bi2SN25	CN25	Bi20SN25	SN25
Size (nm)	29	30	19	21
Ms (Am²/kg$_{Fe_3O_4}$)	86	86	55	78
Hc (kA/m)	8	6	2	7

Table 5.5. *Comparison of the magnetic properties of Bi and pure magnetite nanocrystals with similar size.*

3.2. Gd-magnetite nanocrystals

Structural characterization of the powders was carried out from the X-ray patterns (Figure 5.8).
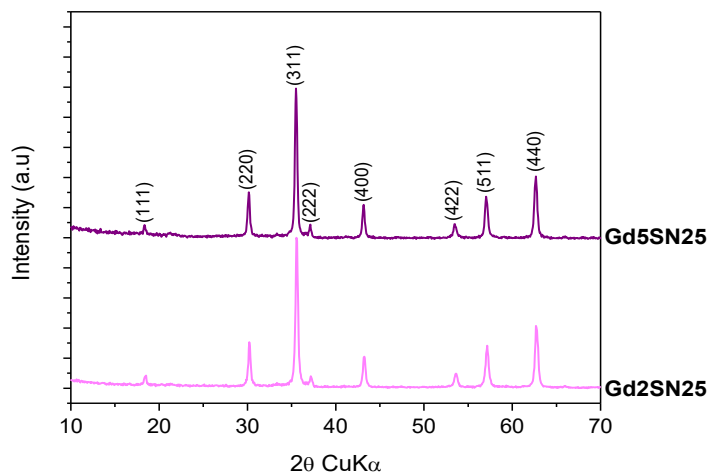
Figure 5.8. *X-ray diffraction patterns of magnetite/gadolinium nanocrystals with two different gadolinium content ((Gd/Fe)$_{at}$ x 100)*

According to the diffraction pattern for both samples, all the peak positions were consistent with a structure typical of magnetite. No significant structural changes were observed upon the incorporation of Gd ions to the Fe_3O_4 nanoparticles. Crystal size calculated from the width of the (311) peak agrees well with the TEM size, which strongly suggests that each particle is a single crystal as in the case of pure magnetite nanoparticles prepared by this method. The lattice constant (a) for samples Gd2SN25 and Gd5SN25 calculated from (311) peak is 0.8381 nm in both cases, so there is no significant evidence of substitution of Fe^{3+} for Gd^{3+} in the crystal structure of the magnetite.

As the concentration of Gd increases from 2 to 5% nanoparticles size increases from 42 nm to 51 nm (figure 5.9). This increase in size by introducing gadolinium (III) cations in the reaction media is a clear indication of the interference of this element during the synthesis process. The sample with 2% of Gd is more homogenous in size and shape

than the sample with 5% of Gd, but in both cases a secondary phase of iron oxide consisting of needle-shaped crystals (not observable by DRX, probably goethite) is formed. It seems that the presence of initial gadolinium hydroxide hinders the nucleation of magnetite (it is known that when less nuclei are formed, larger crystals are produced) in a similar way as high content of alcohol in the reaction media (50%) (Figure 3.7).
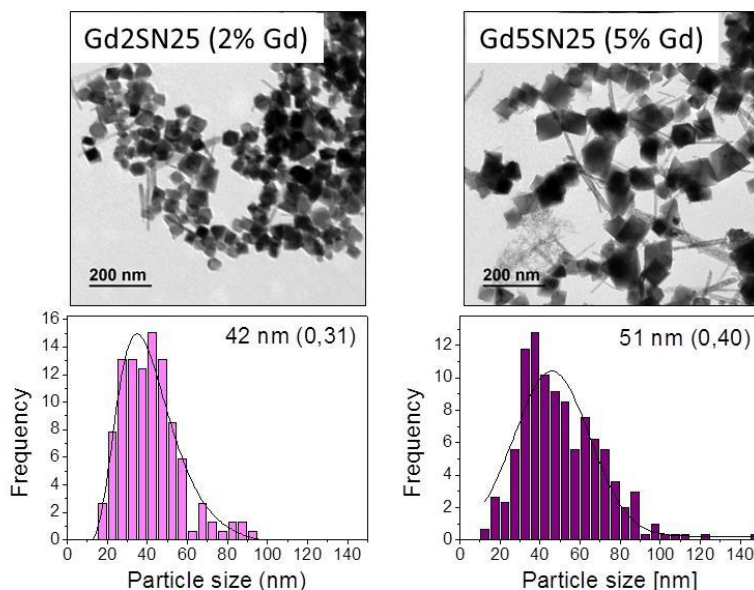
**Figure 5.9.** TEM *micrographs of magnetite/gadolinium nanocrystals with two different gadolinium content $((Gd/Fe)_{at} \times 100)$.*

In order to gain more information on the microstructure of this material, we have chosen the 2% Gd sample (more homogeneous in size) to perform an electron microscopy study employing the HAADF technique (figure 5.10). In this figure it can be seen that the distribution of Gd atoms is similar to the Bi atoms. The gadolinium-bearing shell appears discontinuous with the Gd atoms distributed as isolated surface atoms or in small clusters of presumably gadolinium oxide. The needle-shaped particles corresponding to the secondary goethite phase seems to be not associated to Gd (EDX analysis not shown).
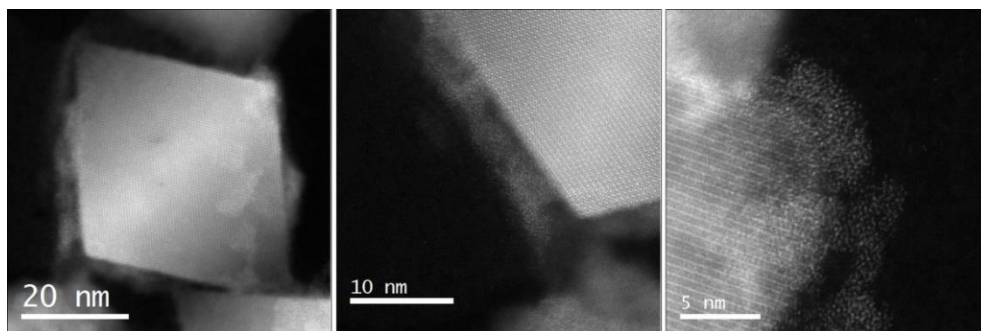
Figure 5.10. *HAADF images of 2% Gd nanocrystals (the bright points correspond to gadolinium atoms).*

STEM-EELS measurements were also performed and have the advantage that the obtained spectra provide an accurate representation of the chemical composition of the material at a given point without, for example, the secondary effects that produce the spurious Cu signal in EDX. This spatially-resolved compositional analysis is essential in determining the location of Gd in the nanocrystals.
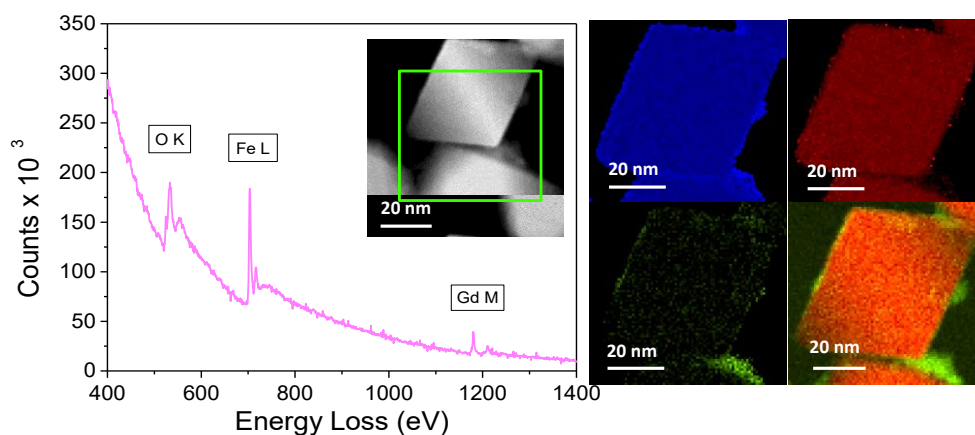
Figure 5.11. *EELS spectrum and relative composition of 2% Gd nanocrystals (O:blue, Fe: red, Gd: green).*

The EELS spectrum (figure 5.11) confirms the presence of Gd in the sample, specifically distributed on the surface of the particles as it can be observed in the relative composition images (practically no Gd is observed inside the nanocrystals, which directly confirms that these atoms are not incorporated into the magnetite structure).

Magnetic properties of magnetite/gadolinium samples at 250 K are displayed in figure 5.12 and table 5.6.
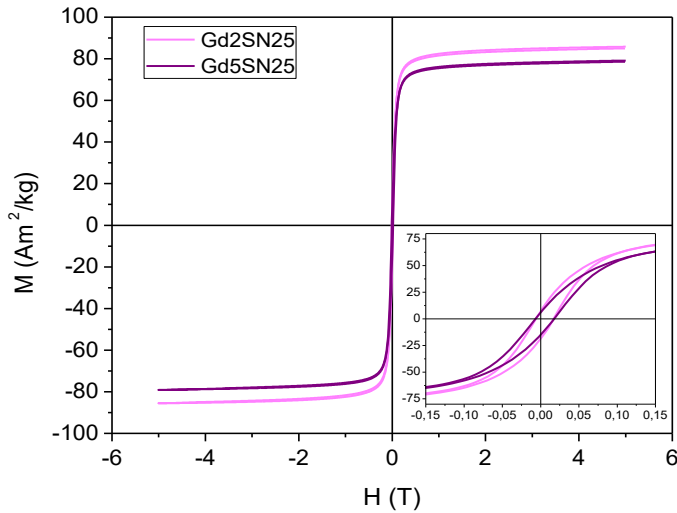
Figure 5.12. *Hysteresis loop at 250 K of magnetite/gadolinium nanocrystals with two different gadolinium content $((Gd/Fe)_{at} \times 100)$.*

Saturation magnetization (Ms) for magnetite/gadolinium NC was found to be 89 and 86 Am^2/kg when curves are corrected for the 2% and 5% of gadolinium, respectively. Both values are close to the saturation magnetization of bulk magnetite (Cullity, 2011). However when the concentration of Gd increases the saturation magnetization slightly decreases despite the fact that the particle size is larger. The most likely explanation for the observed decrease in magnetization upon doping is due to an increase in the sample polydispersity or in the secondary phase fraction.

Sample	%$_{at}$ Gd	TEM size (nm)	M_S (Am²/kg$_{sample}$)	$M_{Scorrected}$ (Am²/kg$_{Fe_3O_4}$)	Hc (kA/m)
Gd2SN25	2	42	86.6	89	9
Gd5SN25	5	51	80.4	86	10

Table 5.6. *Magnetic properties of magnetite/gadolinium nanocrystals.*

If we represent M/Ms vs H (figure 5.13) it is observed that both cycles are almost identical, which discards the internal spin frustrations. The squareness degree calculated as S = Mr/Ms for samples Gd2SN25 and Gd5SN25 is 0.15 and 0.13, respectively, much larger than for Bi samples and in good agreement with its larger NC size (42-51 nm for Gd and 29-19 for Bi). It means that a larger fraction of particles are blocked for Gd samples.
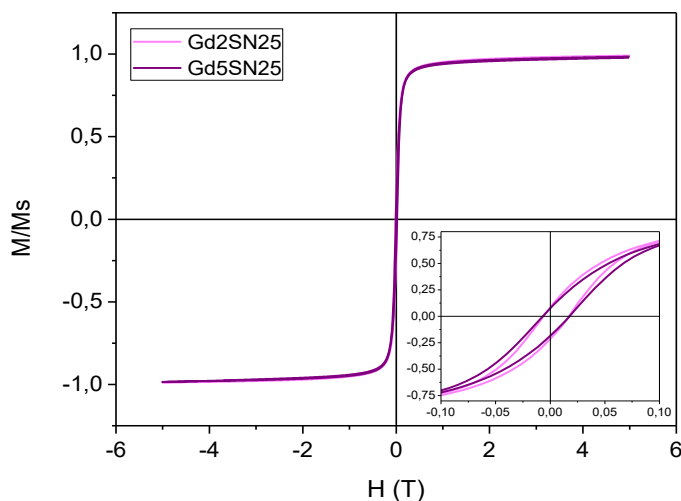
Figure 5.13. *Normalize magnetization curve at 250 K of magnetite/gadolinium nanocrystals with different gadolinium content ((Gd/Fe)$_{at}$ x 100).*

	Gd2SN25	CN0	Gd5SN25	CK0
Size (nm)	42	42	51	53
Ms (Am²/kg$_{Fe_3O_4}$)	89	87	87	96
Hc (kA/m)	9	8	10	9

Table 5.7. *Comparison of the magnetic properties of Gd and pure magnetite nanocrystals with similar size.*

Coercivities at room temperature increasing from 9 kA/m up to 10 kA/m for the biggest particles. If we compare the Gd-magnetite samples with those of pure magnetite

of the same size (CN0 and CK0), it can be observed that in both cases the coercivity is higher in samples containing gadolinium according to its larger crystal size (table 5.7).

3.3. Co-magnetite nanocrystals

The crystal structure, phases and purity of the as-synthesized Co doped magnetite nanocrystals were investigated through the X-Ray diffraction (XRD) (Figure 5.14).
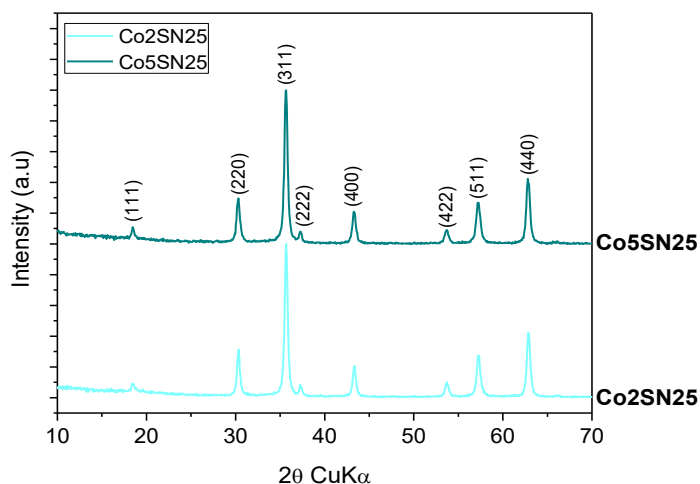
Figure 5.14. *X-ray diffraction patterns of magnetite/cobalt nanocrystals with two different cobalt content $((Co/Fe)_{ar}\times100)$.*

All of the diffraction peaks can be indexed to a cubic inverse spinel structure of $CoFe_2O_4$ nanocrystals (JCPDS 01-1121). Additionally, no other secondary phase was detected in the patterns, reflecting the high purity phase of the as-synthesized Co doped magnetite NCs under current mild experimental condition. Further, the crystallite particle size of the two samples was calculated from the width of the (311) peak using the Scherrer equation. Based on the calculation, we found a good agreement between the calculated crystallite particle size from XRD data and the estimated particles size from the TEM images. The lattice constant (a) for samples Co2SN25 and Co5SN25 calculated from peak

311 is 0.8339 nm in both cases, similar than the lattice constant for pure magnetite samples with similar size (0.8323 and 0.8368 for CN25 and CN50, respectively).

As the concentration of Co increases from 2 to 5% nanoparticles size decreases from 30 nm to 26 nm (figure 5.15), as reported before by Tamura and Matijević (Tamura, 1982). This size reduction by introducing cobalt (II) cations in the reaction media is related to the effect of doping on the stability of the green rust and the magnetite solubility product. Both samples consisted of cubic particles, very homogeneous in size and shape.
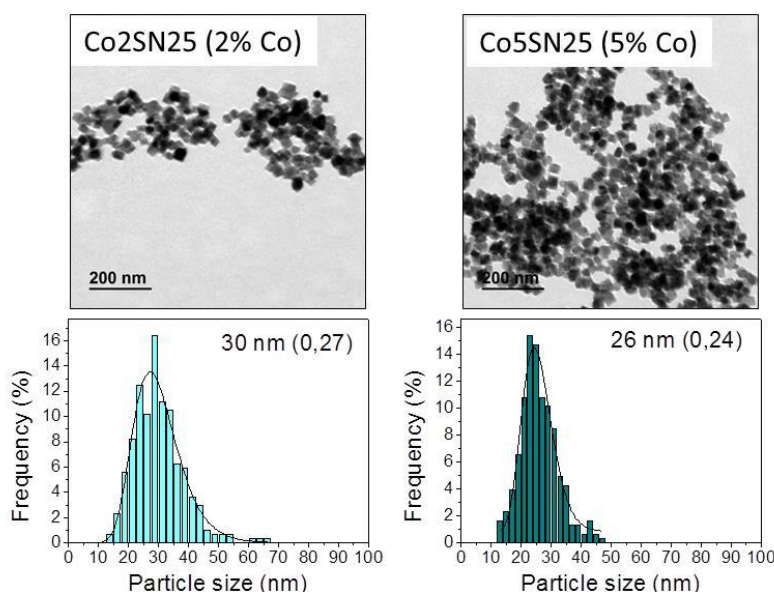
Figure 5.15. *TEM micrographs of magnetite/cobalt nanocrystals with two different cobalt content ((Co/Fe)$_{at}$x100).*

In order to gain more information on the microstructure of this material, we have chosen the 2% Co sample (more homogeneous) to perform an electron microscopy study employing the HAADF technique (figure 5.16). High-resolution micrographs clearly show the crystalline planes, which indicate that nanoparticles have high crystallinity. Likewise, the absence of defects is observed even on the surface of the nanocrystals, so crystal order is preserved.
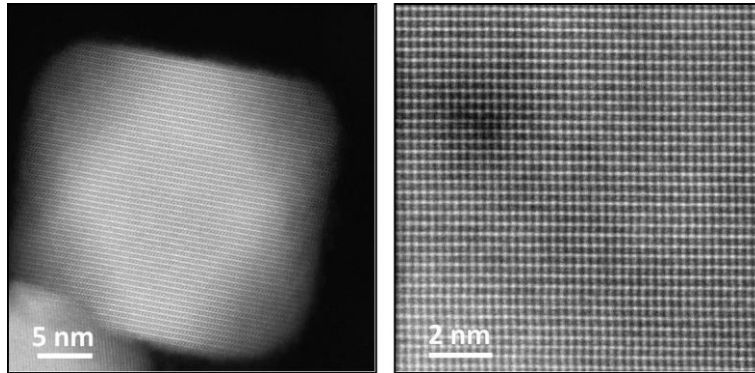
Figure 5.16. *HAADF images of 2% Co nanocrystals (crystalline planes are observed).*

The composition distributions in the as-synthesized nanocrystals were further characterized by the atomically resolved aberration-corrected scanning transmission electron microscopy-EELS (STEM-EELS). Figure 5.17 shows the elemental mappings of O (blue), Fe (red) and Co (cyan) in the nanocrystal. The color distribution within the nanocrystal indicates that all three elements have uniform distribution in the nanocrystal and the cobalt-substituted magnetite appears to be a perfect solid solution.
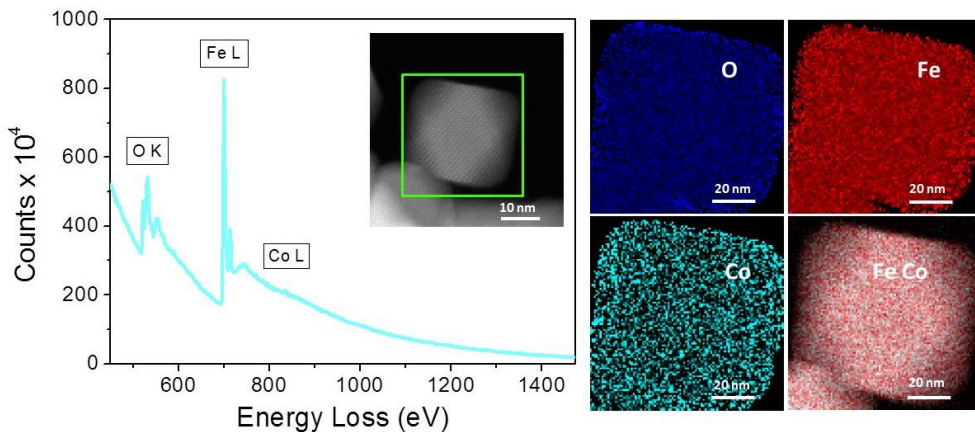
Figure 5.17. *EELS spectrum and relative composition of 2% Co nanocrystals (O:blue, Fe: red, Co: cyan).*

Magnetic properties of magnetite/cobalt samples at 250 K are displayed in figure 5.18 and table 5.8.
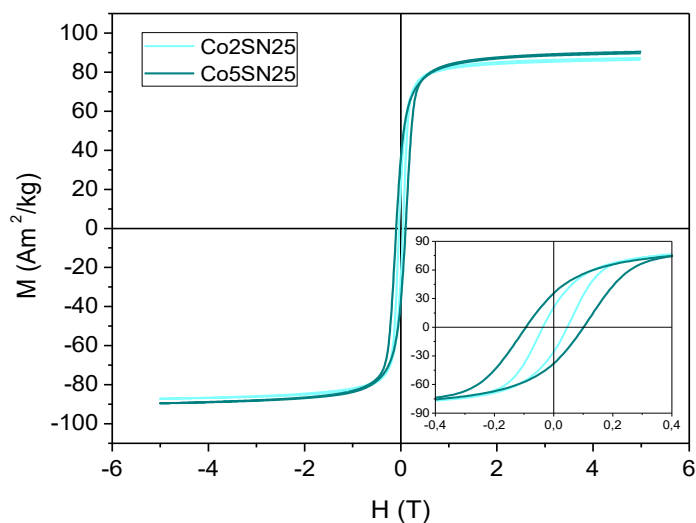
Figure 5.18. *Hysteresis loop at 250 K of magnetite/cobalt nanocrystals with two different cobalt content ((Co/Fe)$_{at}$ × 100).*

Saturation magnetization (Ms) for magnetite/cobalt samples was found to be 88 and 91 Am²/kg when curves are corrected for the 2% and 5% of cobalt, respectively. Both values are below the Ms value for magnetite bulk but above the saturation magnetization of bulk cobalt ferrite (Cullity, 2011).

SAMPLE	%$_{at}$ Co	TEM size (nm)	Ms (Am²/kg$_{sample}$)	Hc (kA/m)
Co2SN25	2	30	88	33
Co5SN25	5	26	92	78

Table 5.8. *Magnetic properties of magnetite/cobalt nanocrystals.*

Interestingly, Ms value increases with cobalt content even though the particle size is slightly smaller. This has been previously observed for Co doped magnetite nanoparticles

where Ms shows a maximum together with the magnetic anisotropy at x=0.6 for $Co_xFe_{3-x}O_4$ (Fantechi, 2015). However, Sathya and coworkers have been observed that as the cobalt stoichiometry increased from 0.1 to 1, the saturation magnetization Ms decreased systematically, due to the Co^{2+} ions, being smaller that the Fe^{2+} ions, tend to occupy both the octahedral sites and the smaller tetrahedral sites, breaking the antiferromagnetic ordering among the Fe^{3+} ions (Sathya, 2016).

At 250 K the magnetic loop of both samples exhibited a hysteresis, with finite coercivity increasing from 33 kA/m up to 78 kA/m for the particles with higher cobalt content. In the literature, an increase in the coercive field by increasing the cobalt stoichiometry from 0.1 to 0.5 has been observed, with a maximum Hc value for a composition around $Co_{0.5}Fe_{2.5}O_4$ (Yu, 2013; Fantechi, 2015; Sathya, 2016).
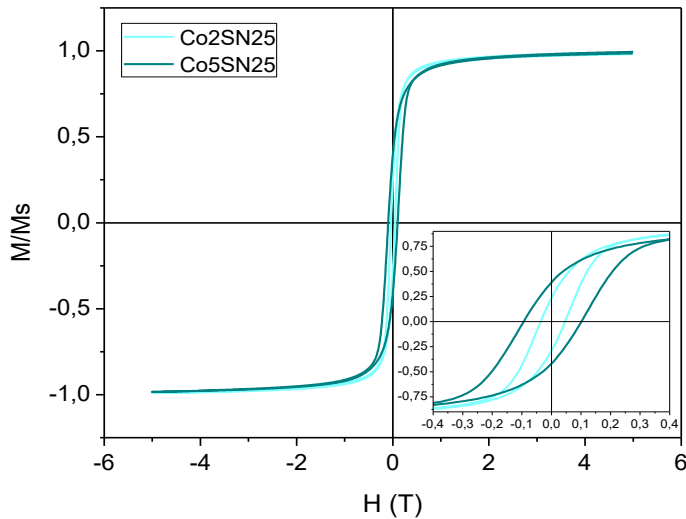
Figure 5.19. *Normalize magnetization curve at 250 K of magnetite/cobalt nanocrystals with different cobalt content ((Co/Fe)at x 100).*

If we represent M/Ms vs. H (figure 5.19) it is observed that saturation magnetization is almost identical in both cases, while coercivity increses as Co content increases, which discards internal spin frustrations. On the other hand, the squareness degree calculated as $S = Mr/Ms$ for samples Co2SN25 and Co5SN25 is 0.26 and 0.40,

respectively, much larger than those for Bi and Gd NCs. This clearly reflects the larger anisotropy of these Co-magnetite NCs in comparison to Bi-magnetite NCs of similar size, or even Gd-magnetite NCs with larger sizes.

If we compare the Co doped nanocrystals with those of pure magnetite of the same size (CN25 and CN50), it can be observed that in both cases the coercivity is much higher in samples containing cobalt (tabla 5.9).

	Co2SN25	CN25	Co5SN25	CN50
Size (nm)	30	30	26	26
Ms (Am²/kg$_{sample}$)	88	86	91	81
Hc (kA/m)	33.04	6.22	77.89	6.54

Table 5.9. *Comparison of the magnetic properties of Co doped and pure magnetite nanocrystals of similar size.*

3.4. Au-magnetite nanocrystals

Structural characterization of the powders was carried out from the X-ray patterns (Figure 5.20). According to the diffraction patterns, all samples show reflections corresponding to magnetite, and also other corresponding to gold, although in the case of the sample with 2% of Au it can only be seen the most intense peak at 38 ° (2θ) ((111) planes, (JCPDS 01-1172)). It can be observed that as the proportion of gold increases, peaks corresponding to this metal become more intense while those corresponding to magnetite appear less intense. This is caused by the heavy atom effect from Au (Teng, 2003; Robinson, 2010) and provides further evidence for the presence of Au in the NCs. Crystal size calculated from the width of the magnetite (311) peak varies between 34 and 29 nm and agrees well with the TEM size, which strongly suggests that each particle is a single crystal as in the case of pure magnetite NC prepared by this method. On the other hand, the crystal sizes calculated from the gold peak (111) are 14 nm, 18 nm and 27 nm for the samples Au2SN25, Au5SN25 and Au20SN25, respectively, increasing with the amount of gold.
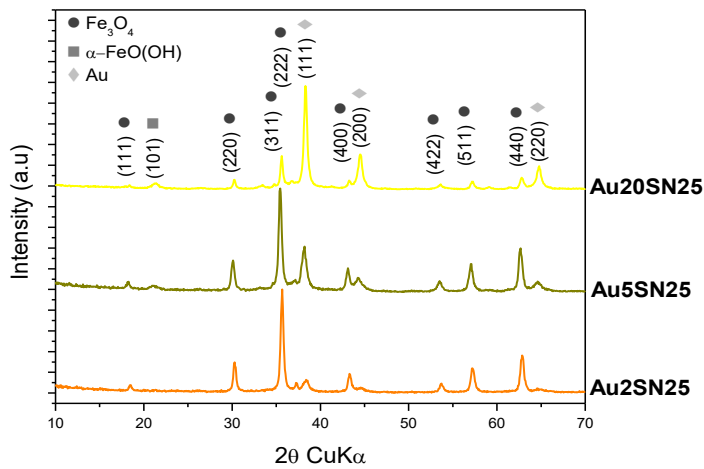
Figure 5.20. *X-ray diffraction patterns of magnetite/gold nanocrystals with two different gold content ((Au/Fe)$_{at}$×100).*
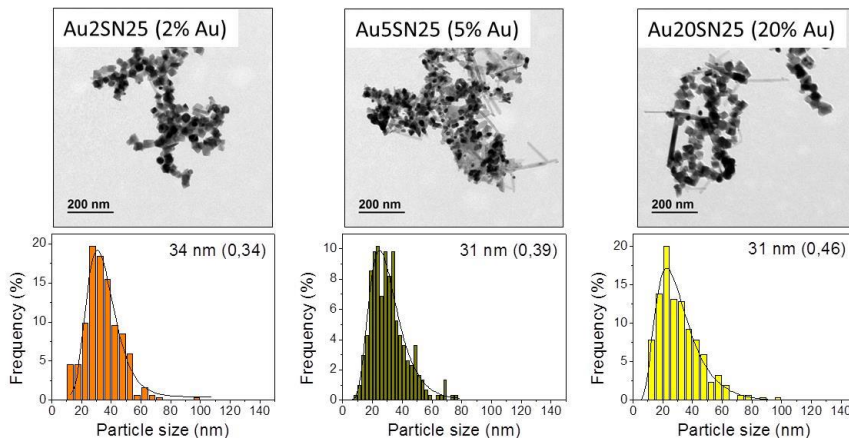
Figure 5.21. *TEM micrographs of magnetite/gold samples with two different gold content ((Au/Fe)$_{at}$ × 100)*

TEM images show that as the concentration of Au increases from 2 to 20% nanoparticles size slightly decreases from 34 nm to 31 nm (figure 5.21). This reduction in size by introducing gold in the reaction media could be an indication of the interference of this element on the nanoparticle growth process as well as on the reaction kinetics. The sample with 2% of Au is homogenous in size and shape, but as the amount of gold increases (5 to 20%) the polydispersity increases. Nanoparticles of gold appear in the

TEM images as highly electro dense objects, rather spherical and with a wide size distribution, together with the magnetite nanocrystals (figure 5.22). In conclusion, when the iron salt concentration is high (0.2 M) and increasing the amounts of gold salt concentration leads to not only a particle size reduction but also an increase in particle size distribution, and additionally, a second phase of iron oxide (the most intense peak of goethite is observed by DRX) is formed. The gold nanoparticle size increases as increases de gold content: 8 nm (0.46) for Au2SN25, 15 nm (0.34) for Au5SN25 and 17 nm (0.36) for Au20SN25.
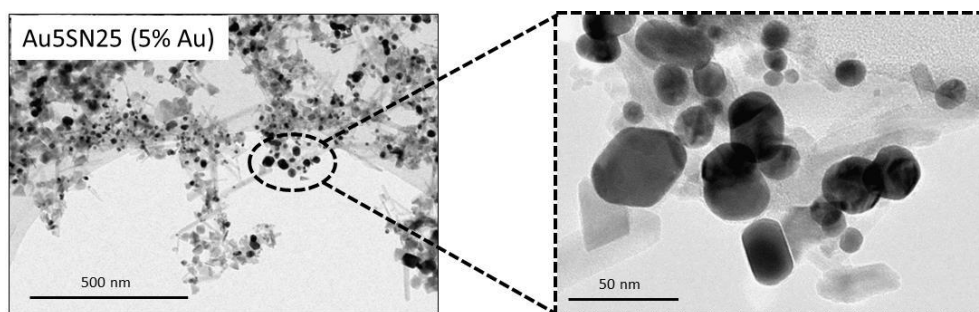
Figure 5.22. *TEM images of Au5SN25 sample at low and high magnification.*

In pure Au nanoparticles, the collective oscillations of free electrons, known as the surface plasmon (SP), cause an absorption peak to appear in the visible region of the electromagnetic spectrum (Creighton, 1991). Factors that affect the position of the SP peak have been investigated on the basis of Mie theory; for Au nanoparticles, the SP has been shown to shift as a function of particle size, stabilizing ligand and solvent dielectric (Jensen, 2000; Templeton, 2000; Lyon, 2004). Thus, the bimetallic Fe_3O_4/Au nanoparticles were further characterized by UV-Visible absorption spectroscopy (figure 5.23).

Samples with Au content above 5% showed a broad band corresponding to the SP of the gold particles at around 540 nm. This wavelength corresponds to pure gold particles of 60 nm, however since the gold particles present in our samples are much smaller it can be assumed that this red-shift is due to the interaction between gold particles

and magnetite NCs. Similar quenching effect has been previously observed for luminescent and magnetic NPs (Sun, 2010; Di Corato, 2014).
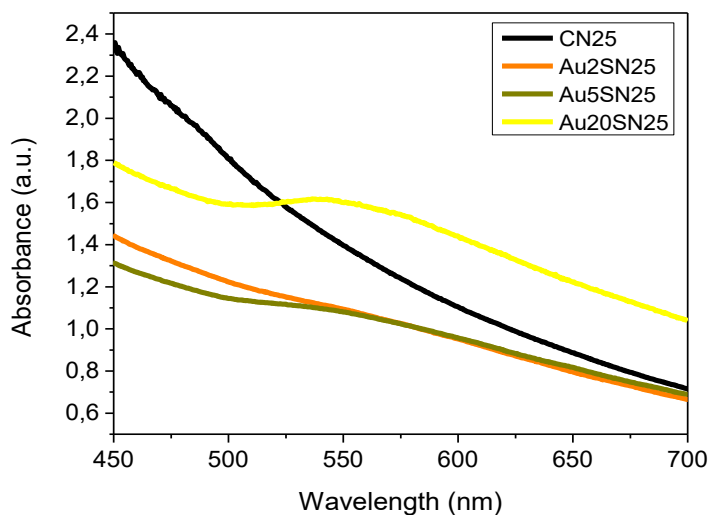
Figure 5.23. *UV-Vis absorption spectra comparing pure magnetite and samples containing different amount of gold.*

Magnetic properties of magnetite/gold samples at 250 K are displayed in figure 5.24 and table 5.10.

SAMPLE	$\%_{at}$ Au	TEM size (nm)	Ms (Am^2/kg_{sample})	Ms$_{corrected}$ ($Am^2/kg_{Fe_3O_4}$)	Hc (kA/m)
Au2SN25	2	34	78	82	8
Au5SN25	5	31	73	81	8
Au20SN25	20	31	30	42	9

Table 5.10. *Magnetic properties of magnetite/gold nanocrystals.*
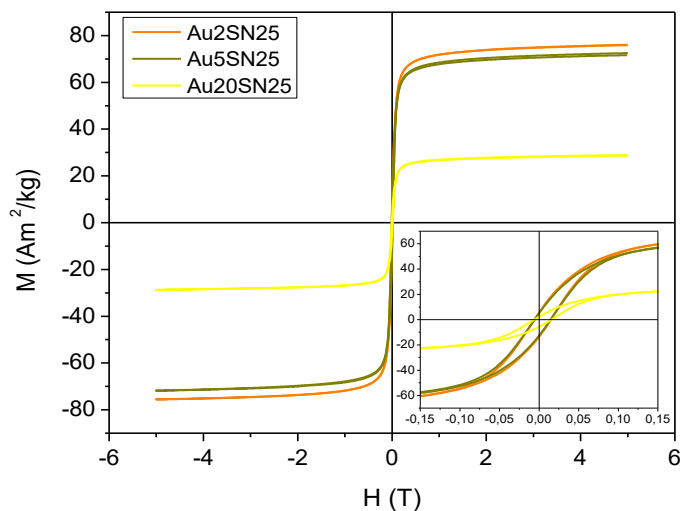
Figure 5.24. *Hysteresis loop at 250 K of magnetite/gold nanocrystals with three different gold content ((Au/Fe)$_{at}$x100).*

Saturation magnetization (Ms) for magnetite/gold samples was found to be 82, 81 and 42 Am²/kg when curves are corrected for the 2%, 5% and 20% of gold, respectively. The values for 2 and 5% of gold are close to the saturation magnetization of bulk magnetite (Cullity, 2011), however when the concentration of Au increases up to 20% the saturation magnetization decreases considerably. The difference in ionic radius of gold (r_{Au+3}=0.85Å) and iron (r_{Fe3+} = 0.64 A) (r_{Fe2+} = 0.74 A) (Lide, 1992) and the appearance of the peak of gold in the XRD excludes the possibility of gold being incorporated into the magnetite structure. The reduction of the magnetization of the sample with higher gold content is probably due to the dilution effect produced by the goethite.

If we represent M/Ms vs. H (figure 5.25) it is observed that the three loops are identical, which discards the internal spin frustrations. On the other hand, the degree of squareness calculated as S = Mr/Ms for samples Au2SN25, Au5SN25 and Au20SN25 is 0.12, 0.12 and 0.14, respectively, and similar to those for Bi-magnetite NCs as corresponds for similar NCs sizes (~30 nm).
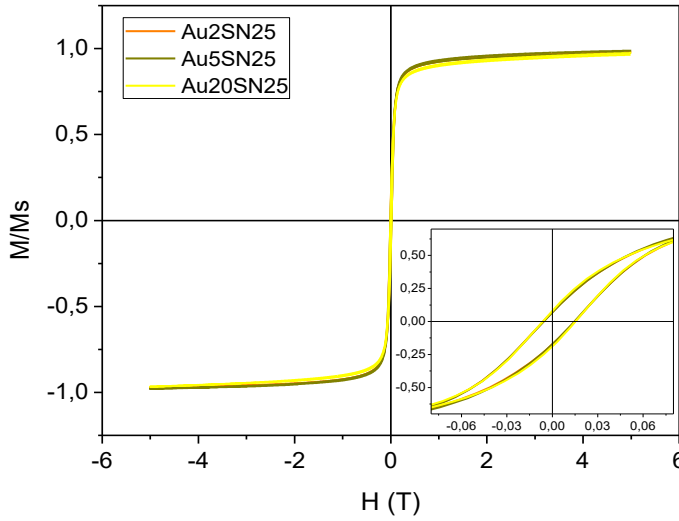
Figure 5.25. *Normalize magnetization curve at 250 K of magnetite/gold nanocrystals with three different gold content ((Au/Fe)$_{at}$ x 100).*

Coercivity values are similar for all samples (8-9 kA/m) independently on the amount of Au in good agreement with the fact that the magnetite NC size is kept constant (34-31 nm). It seems that there is not a close relation between the gold nanoparticles and the magnetite NC.

If we compare the Au-magnetite samples with those of pure magnetite of the similar size (BN50 and CN25), it can be observed that Au is not altering the magnetic behavior of the magnetite NCs (tabla 5.11). The reduction in Ms is mainly due to the presence of the secondary non-magnetic iron oxyhydroxide phase.

	Au2SN25	SN0	Au5SN25	Au20SN25	CN25
Size (nm)	34	37	31	31	30
Ms (Am²/kg$_{Fe_3O_4}$)	82	85	81	42	86
Hc (kA/m)	8	9	8	9	6

Table 5.11. *Comparison of the magnetic properties of Au bimetallic and pure magnetite nanocrystals of the same size.*

4. DISCUSSION

The co-crystallization of Bi, Gd, Co, and Au with magnetite under the conditions employed in the present work could result in: (1) Formation of a core-shell nanostructure as it is the case for bismuth and gadolinium, (2) Formation of a solid solution as in the case of cobalt, and (3) decoration of the surfaces or mixture of particles of different nature, that is the case of gold. In order to understand these differences, we consider the different ionic radius and reactivities of these ions. In the table 5.12 and figure 5.26 we compare the physicochemical characteristics of all the ions employed in this study.

	Fe	Bi	Gd	Co	Au
r_{M3+} (Å)	0.64	0.96	0.93	0.63	0.85
r_{M2+} (Å)	0.74			0.72	
Kps $M(OH)_3$	$6.3 \cdot 10^{-38}$	$3.2 \cdot 10^{-40}$	$8.9 \cdot 10^{-23}$	$4 \cdot 10^{-45}$	$1 \cdot 10^{-53}$
Kps $M(OH)_2$	$7.9 \cdot 10^{-15}$			$2.5 \cdot 10^{-16}$	
Reduction Potential (V)	0.77 (+3,+2)	0.308 (+3,0) 0.2 (+3,+1)	-2.28 (+3,0)	-0.28 (+2,0)	1.498 (+3,0)

$NO_3^- + H_2O + 2e^- = NO_2^- + 2OH^-$ E°=0.01 V

http://www.chemeddl.org/services/moodle/media/QBank/GenChem/Tables/KspTable.htm (solubility products)
L Garcia Rodenas and S J Liberman. Hydrolysis of Gadolinium(III) in light and heavy water. Talanta 38(1991)333-318
Handbook of Physical Chemistry 72ND Ed.1991-1992 Pag 8-17 for reduction potentials ansd Pag. 12-8 for crystal ionic radii

Table 5.12. *Ionic radius, solubility product of the hydroxide and reduction potential of the metal cations involved in the synthesis of bimetallic nanocrystals.*

The similitude of the ionic radius of Fe^{2+} and Co^{2+} justifies the formation of a solid solution. Other cations present much bigger ionic radius, like Gd^{3+} 0.93 Å, Bi^{3+} 0.96 Å and Au^{3+} 0.85 Å that limit the possibility of the formation of solid solutions. The high

positive reduction potential of Au^{3+} (much bigger than the nitrate) makes it the most powerful oxidant in the media with the immediate production of metal gold nanoparticles that due to its low reactivity could only decorate the surface of magnetite or form a particle apart.
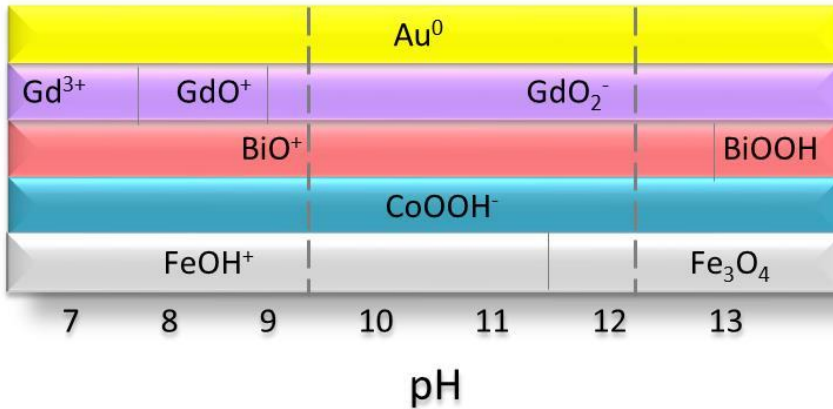
Figure 5.26. *Stable form of the metal ions in solution as a function of pH at 10^{-10} M and 298 K. The two vertical lines mark the pH range of the magnetite crystallization (Takeno, 2005).*

In the case of bismuth, gadolinium and cobalt ions they effectively co-precipitate as hydroxides with $Fe(OH)_2$ and evolve parallel with it towards the final product forming a core shell bimetallic nanoparticle or a solid solution in the case of $Co(II)$, that do not alter their oxidation state during the process. Differences in the quality of the coating seem to be related to the match of the solubility product of the metal hydroxide with the $Fe(III)$. In this sense the bismuth will form better coatings than gadolinium (as was effectively observed).

More subtle differences come from the hydrolysis behavior of the different metals represented in the figure 5.26. Again bismuth behaves differently than the rest of the ions in his unique ability to form positive specie (BiO^+) in the strong alkaline conditions of the synthesis. This could be relevant if we consider that all the colloidal forms of iron hydroxides present a negative charge at the same pH. Bismuth cation with positive charge will be attracted to the growing magnetite nuclei and altering their growth rate and the

final NC size as observed in this study and previously (Andrés-Vergés, 2012). Comparing our work with previous one, similar results were obtained in the case of the sample with 2% of Bi. However, when increasing the proportion of Bi up to 20% we get more polydispersity particles and we do not achieve such a drastic reduction in particle size. This is may be because we use higher concentrations of $FeSO_4$ (0.2 M) and the addition of 20% of Bi results in a total concentration of bismuth of 0.04 M close to the 0.046 M that was determined by Andres-Vergés for the segregation of iron and bismuth oxides (Andrés-Vergés, 2012). The strong hydrolysis and extremely low solubility of the hydroxides is reflected in the final nanostructure of a bismuth layer on the surface of the magnetite NC. From the HAADF micrographs it can be observed that bismuth atoms are not homogeneously distributed on the particle surface. Similar samples were studied by X-ray absorption spectroscopy (XAS) and revealed that the Bi atoms do not form a well-defined Bi oxide structure and that the bismuth shell consists in clusters $[BiO_{6-x}(OH)_x]$ bonded by multiple hydroxyl bridges to the magnetic core (Laguna-Marco, 2014).

In the case of gadolinium, it seems that this element has been left out the structure of magnetite, decorating the surface of the nanoparticles, which is in accordance with the results obtained by Li et al. (Li, 2015). However, it has been reported that the gadolinium may be incorporated into the structure of nanoparticles with no significant structural modifications but with decrease in magnetic moment (Orbaek, 2013; Nikoforov, 2014; Douglas, 2016; Park, 2016). According to our results we have not observed substantial changes in the saturation magnetization due to the presence of Gd.

Since Co^{2+} and Fe^{2+} have similar ionic radii and their corresponding hydroxides have similar solubility product constants, an exchange of Co^{2+} for Fe^{2+} in the green rust (intermediate reaction) took place (Tamura, 1982), and very homogeneous nanocrystals in size and shape were obtained. The high saturation magnetization obtained for both samples is attributed to their high crystallinity.

Gold decorated magnetite nanoparticles have up to our knowledge not prepared previously in one step. Most of the studies were focused in the obtaining of core-shell nanostructures of iron oxide/gold involving at least two steps (the synthesis of iron

nanoparticles and subsequent gold coating) which could adversely affect the yield and the reproducibility of the process (Lyon, 2004; Caruntu, 2005; Bao, 2007; Goon, 2009; Shah, 2013). The preparation of gold decorated nanocrystals in a single step reported here is simpler than previous studies but no new properties are expected arising from this association that could be viewed more as an intimate mixture than as a core-shell nanostructure.

In the case of magnetite samples prepared in the presence of Au^{3+} and Gd^{3+}, goethite (a pure Fe(III) phase) appears as secondary phase. It is commonly accepted that the presence of goethite in the synthesis of magnetite starting from a Fe(II) precursor is related to a fast oxidation, taking into account that prior oxidation, dehydroxylation of iron complexes should occur (Cornell, 2006). In the preparation of pure magnetite by oxidative precipitation the appearance of goethite as secondary phase is related to the presence of trace amounts of oxygen that accelerates the oxidation of Fe^{2+}. In the case of the bimetallic samples, the presence of goethite was due to the presence of the oxidant cation Au^{3+} substituting the oxygen. Gadolinium ion is not oxidant and its relation with the formation of goethite is unclear.

5. CONCLUSIONS

New bimetallic inorganic nanoparticles consisting of iron oxide and other metal integrated into the structure in different ways (forming a solid solution, forming structures core/shell decorating the surface or simply nano-intermixed) have been synthesized by a simple aqueous route which can be achieved in one step. The nanostructure formed in each case is controlled by the ionic radius of the secondary metal ion and the solubility of the metal hydroxide that controls the degree of simultaneity of the precipitation of both hydroxides in the initial steps of the reaction.

Important points that have been concluded from this work:

1) The introduction of an extra element is successful in all cases below $5\%_{at}$ reproducing the initial proportion of the mixture

2) Above 5%$_{at}$ good results have been obtained with bismuth and gold but with the appearance of a secondary phase of goethite.

3) The NC size generally decreases with doping, except for gadolinium.

4) Magnetic properties of the bimetallic systems are not damaged by the cocrystallization of any of the metal tested below the 5%$_{at}$ of doping. Moreover, Co produces an enhancement of the anisotropy.

5) The UV absorbance of nanocrystalline gold has been observed in gold decorated magnetite nanocrystals.

6

Coating process

1. INTRODUCTION

The application of iron oxide nanoparticles in biology, medical diagnosis, and therapy requires colloidal stability in physiological conditions (pH 7.4) to avoid aggregation in vivo that can lead to artery occlusion with subsequent thrombus occurrence (Krug, 2011; Sharifi, 2012; Ling, 2013).

Naked NPs normally show an isoelectric point around pH 7 that means that at physiological pH they tend to aggregate due to the lack of charges on the surface (Ling, 2013). An injection of these particles could cause an immediate threat to health, since they would clog up small blood vessels and obstruct free blood circulation (Schladt, 2011). As a consequence, a modification of the NPs' surface is essential to endow them with colloidal stability and hydrophilic properties for extensive biomedical applications (Dias, 2011; Ling, 2013; Marciello, 2016).

The stability of colloidal suspensions in the medium is determined by the balance of attractive and repulsive forces to which the particles are subjected (Myers, 1999). The most important forces that exist throughout colloidal system in aqueous media are van der Waals forces (attractive character) and electrostatic (repulsive character). Moreover, if the colloidal system consists of magnetic particles, magnetic dipolar interactions exist that possess attractive character. When attraction forces dominate, the particles will adhere with each other and finally the entire dispersion may coalesce. When repulsion forces dominate, the system will be stable and remain in a dispersed state.

Since there are always attractive forces between magnetic nanoparticles, it is necessary to provide repulsion between the particles to impart stability. This stability can be obtained by coating the colloidal particles (figure 6.1):

- With an electrical double layer (electrostatic or charge stabilization). This is achieved by adsorption of counterions or charged species on the nanoparticle surface once a surface electric charge is promoted by coating with a small molecule full ionized.

- With adsorbed or chemically attached polymeric molecules (steric stabilization). The presence of these polymer chains on the surface of the particles prevents the attraction and consequent aggregation of the nanoparticles.
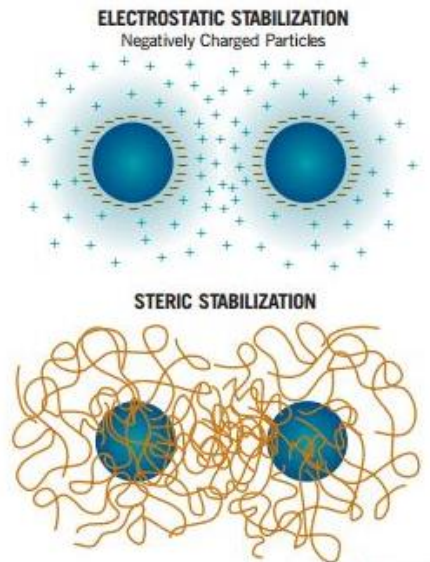
Figure 6.1. *Schematic representation of electrostatic and steric stabilization.*

A wide set of coatings have been studied including amphiphilic micelles (Laurent, 2014), polymers (Duguet, 2006; Thünemann, 2006), inorganic and organic compounds and surfactants (Tartaj, 2003; Duanmu, 2006; Srinivasan, 2008) which are becoming very popular due to its resistance to the ionic strength and pH of the physiological medium (the increase of ionic strength implies the narrowing of the electrical double layer). All these coating materials have the effect of prolonging nanoparticle permanence in blood, must be biocompatible and preferably biodegradable (to be eliminated spontaneously from the body through physiological processes). The coating often introduces on the surface some extra functional groups that offer a linkage point for further functionalization with a biomacromolecule or a specific ligand to provide special features (You, 2006; McCarthy, 2008).Various biological molecules such as antibodies, proteins,

DNA, enzymes, etc., may be bound to the primary coating onto the nanoparticles to make the particles target-specific (Gupta, 2005).

The coatings chosen in this work consist of molecules that provide positive, negative and a neutral charged coating, with active terminal groups (COOH, NH_2 and OH, respectively) that could be further functionalized. For comparison, samples were stabilized in organic media by coating with a surfactant.

As positive coating, the (3-aminopropyl)trietoxysilane (APS) was chosen as it has been proposed as an excellent material for modification of the surface of iron oxide magnetic nanoparticles directly, due to its capability to stabilize them in the pH range 3-9 and to provide positive charged groups at the NP surface ($-NH_3^+$) that can be used to attach other biomolecules (Gazeau, 2008). APS surface-functionalized NPs have found applications in many biological areas including cell separation (Sweetman, 2011) and enzyme separation, diagnosis as MRI contras agent (Yamaura, 2004; Feng, 2008), as magnetically controlled drug carriers (Neuberger, 2005) and hyperthermia treatment media as illustrated in many literature reports (Hong, 2011; Larsen, 2012; Rouhana, 2012). The mechanism of surface functionalization is the formation of Fe-O-Si bond between the nanoparticles and silane ligand, very similar to the siloxane layer formation on silica (Liu, 2013).
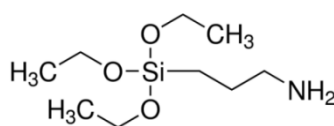
APS

For negative coating, dimercaptosuccinic acid (DMSA) was selected for being a molecule with two sulfhydryl and two carboxylic acid groups. It is a water-soluble non-toxic substance that presents two chiral centers and consequently has three stereoisomers, two diastereomers D and L and one optically inactive meso form (Miller, 1998). Due to its chemical properties as chelating agent, the Federal Drug Administration (FDA) has

approved the use of DMSA in its meso form for treatment of heavy metal poisoning in humans since 1989 (Aposhian, 1990). In part, this fact has been used to support its application as a biocompatible stabilizing coating for magnetic nanoparticles, once DMSA alone shows low-toxicity in various biological systems already studied (Pande, 2001; Flora, 2003). The DMSA binds to the iron oxide nanocrystal surface through its carboxylic bonding, and the intermolecular disulfide cross-linking between surface-bound DMSA ligands strengthens the nanocrystal stability. The remaining free carboxylic acid and thiol groups make the nanocrystals hydrophilic (with negative charge density of the particles at physiological pH) and can be used for further conjugation of target-specific biomolecules. The DMSA-coated Fe_3O_4 nanocrystals are stable in water in a large pH range (3-11), and in various buffers often used by biochemists, for example, acetate, citrate, phosphate and tris (Fauconnier, 1997; Huh, 2005).
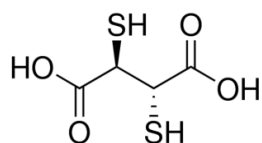
DMSA

Neutral coating was achieved with dextrans, consisting of polysaccharides formed by the union α-1,6 of glucose units. These form a linear long length chain (10 to 150 kDa), with small branches formed by additional α-1,3 bonds, which generally involve about 5% of the total. The versatility of the dextran is given by its properties: it is neutral and soluble in water, readily filterable, biocompatible, biodegradable and stable for more than five years (when stored as a dry powder in well-sealed containers at room temperature). Dextrans have traditionally been used in medicine as a component of intravenously injectable drugs. Dextran is currently the most widely used biopolymer for coating magnetic nanoparticles due to their low toxicity and biological compatibility, enhancement of blood circulation time, and suitability for suspension in cell culture media. These molecules have a large number of hydroxyl groups that foster multiple hydrogen-bonding

interactions with iron oxide surfaces as well as provide locations for subsequent surface modification (Laurent, 2008).
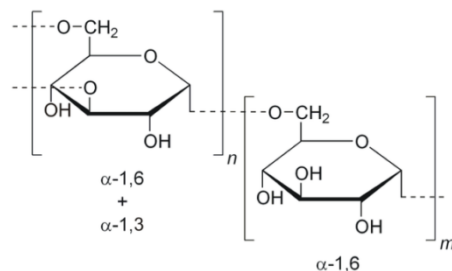
Dextran

Finally, oleic acid was used to gain stability in organic media. The OA is a monounsaturated fatty acid of the omega 9 series typical of vegetable oils such as olive oil, avocado oil, etc. It is the most abundant fatty acid in human, and second in abundance in human tissues after the palmitic acid (Oliveira, 2015). It has a beneficial effect on blood vessels reducing the risk of cardiovascular disease. OA is probably the most common small molecule used to stabilize magnetic nanoparticles acting as a capping agent (Bloemen, 2012; Patil, 2014).
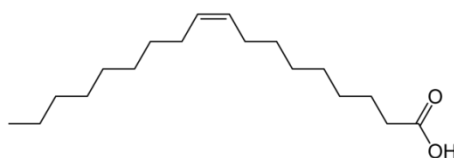
Oleic acid

OA possesses a non-polar hydrocarbon tail and a polar carboxylic acid head group. Carboxylate anions are known to coordinate with the surface of magnetite, presumably through a coordination of iron atoms with both carboxylate oxygens. The polar head group anchored on the magnetite surface, the non-polar tail extends into solution, causing

the magnetite to be hydrophobic and dispersible in organic solvents (Shete, 2015). The hydrocarbon tail presents a cis-double-bond in the middle, forming a kink which has been postulated to be necessary for effective stabilization (Gelbrich, 2006). Thus, OA forms a dense protective monolayer, strongly bonded to the nanoparticles surface, which lead to full particle disaggregation and colloids with long-term stability (Zhang, 2006a; Bronstein, 2007).

2. EXPERIMENTAL SECTION

2.1. Nanoparticles surface coating

NPs were coated with dimercaptosuccinic acid (DMSA), (3-aminopropyl)triethoxysilane (APS), dextran and oleic acid through the following procedures.

2.1.1. DMSA coating

5 mg (0.027 mol) of DMSA were added to a suspension of 10 ml of particles (4.3 g Fe_2O_3 per l) at pH 3 with gentle stirring. After adding DMSA, the pH of the mixture was raised to 11 and sonicated for 15 min (Fauconnier, 1997). After coating, NP suspensions were dialyzed and the pH was adjusted to 7 with diluted HNO_3 or KOH.

2.1.2. APS coating

Surface modification was performed by adding very slowly (10 µl s^{-1}) 1.22 ml (0.005 moles) of APS to a mixture of 10 ml of particles (28 g Fe_2O_3 per l) and 10 ml of methanol under strong stirring for 12 h (Mornet, 2005). After that, methanol was eliminated by using a rotary evaporator, and the rest of the APS was eliminated by dialysis.

2.1.3. Dextran coating

Surface modification was performed by adding dropwise the dispersion of particles (228 mg Fe_2O_3 per l) in 1.6 ml of NaOH (0.8 M) into a solution of 200 mg of dextran (40 kD) in 2.5 ml of NaOH (0.5 M) under sonication. The mixture was sonicated for 6 h

under refrigeration (Bautista, 2004). After coating, NP suspensions were dialyzed and the pH was adjusted to 7.

1.2.4. Oleic Acid coating

Surface modification is carried out by adding 640 mg of oleic acid to a colloid that contains 160 mg of Fe in 32 mL of water, keeping ultrasonic agitation at 70−80 °C for 1 h. After that, the sample is washed first with H_2O and then with ethanol and finally dried and redispersed in hexane.

2.2. Sample selection

We selected a representative group of magnetic NPs obtained by coprecipitation with 8, 11 and 13 nm thoroughly described in Chapter 2 and tested four different coatings. For pure NCs described in Chapter 3 and bimetallic NCs described in the previous Chapter 5 (table 6.1), APS coating has been tested and colloidal properties.

Sample	% M_{theor}	% M_{exp}	TEM Size (nm)/PDI	DRX Size (nm)
FeCo2	2	2.4	30/0.27	28.6
CN25	0	---	30/0.26	24.4
FeCo5	5	5.6	26/0.24	25.4
CN50	0	---	26/0.45	25.9
FeGd2	2	1.9	42/0.31	40.9
CN0	0	---	42/0.27	41.7
FeGd5	5	4.6	51/0.40	50.6
CK0	0	---	53/0.37	53.5

Table 6.1. *Magnetite and bimetallic nanocrystals selected for coating with APS.*

3. SAMPLE CHARACTERIZATION

3.1. Coated nanoparticles with different sizes and coatings

Three samples have been chosen (8, 11 and 13 nm) to be coated with APS and DMSA to study the influence of particle size with two different coatings on relaxometric and magnetothermal properties. Also, the smallest (8 nm) and the biggest (13 nm) samples were coated with oleic acid to study the influence of particle aggregation in the heat capacity. Finally, 11 nm particles are also coated with dextran (in addition to APS and DMSA) to study the influence of the coatings on the cell interaction and internalization.

The characterization of these samples was performed with techniques that allow determining qualitatively and quantitatively the surface modifications carried out (IR, TGA and colloidal properties). We performed a comparative study of samples with and without coating.

Figure 6.2 displays the FTIR spectra of the 8, 11, 13 nm samples before and after coating. In the case of the samples coated with APS the only difference observed in the spectra is the appearance of a broad band between 1100 and 800 cm^{-1} corresponding to silanol groups vibration bonded to the surface of the nanoparticles (figure 6.3). Also in the high frequency region it can also be seen a low intense band at 2930 cm^{-1} (seen in the spectrum of pure APS, not shown) that can be assigned to the vibrational mode of the protonated or deprotonated amino group, confirming the presence of APS.

In the case of the samples coated with DMSA absorption bands at 1640 cm^{-1} are displayed due to the vibration of the C=O bond of DMSA. The bands appearing at 1450 cm^{-1} are due to bending of CH bond. The presence of DMSA is evident in the spectrum with the appearance of an absorption band of low intensity at 2510 cm^{-1} because of the vibration of the SH bond. In addition, 1140 and 1000 cm^{-1} broad absorption bands appear owing to the vibration of the bond S-CH.
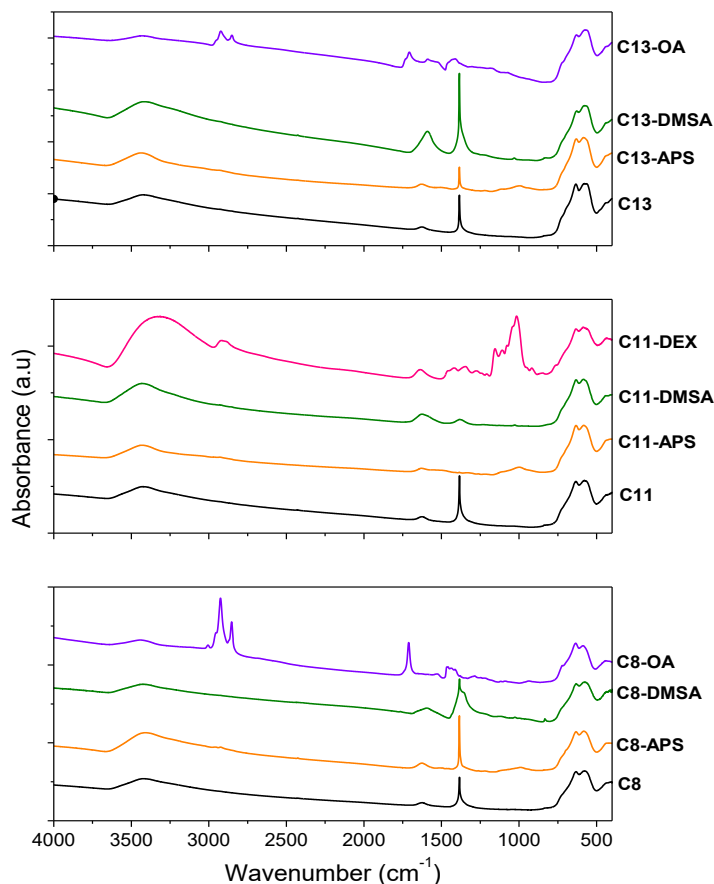
Figure 6.2. *FTIR spectra of 8, 11 and 13 nm iron oxide nanoparticles before and after coating with APS, DMSA and OA.*

The dextran coated sample spectrum shows absorption bands at 2930, 1420 and 1330 cm^{-1} assigned to the vibrations of stretching and deformation of the CH bonds. Besides there are bands appearing at 1157 and 1014 cm^{-1} due to the stretching vibration of C-O bonds in dextran molecules. The bands at 917, 850 and 760 cm^{-1} correspond to deformation modes α-glucopyranose ring (figures 6.2 and 6.3).

In the samples with oleic acid coated an absorption band at 1715 cm^{-1} corresponding to the vibration of C=O bond is observed. Also the band at 1443 cm^{-1} corresponds to the stretching vibration ν(CO) of the carboxyl group. Moreover two

intense absorption bands at 2930 and 2854 cm^{-1} corresponding to the stretching vibrations of CH$_2$ groups of oleic acid molecules appeared (figures 6.2 and 6.3).
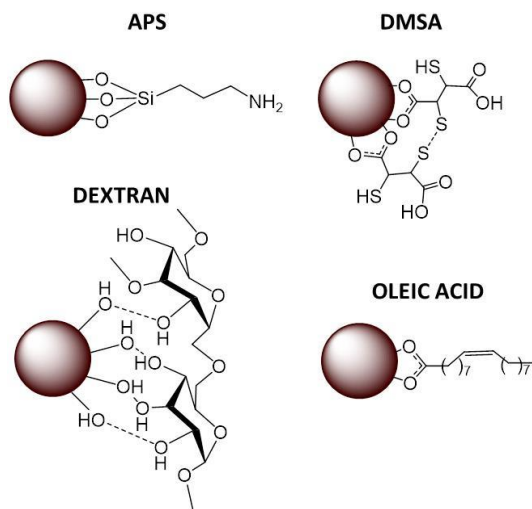
Figure 6.3. *Schematic representation of APS, DMSA, dextran and oleic acid coatings.*

TGA of the samples with different coatings were carried out from room temperature up to 900 °C (Figure 6.4) and the results are listed in table 6.2. In the case of the samples coated with APS and DMSA a small weight loss comparable with that of uncoated samples at temperatures around 290 and 220 °C respectively is observed. Furthermore, also it shows that the weight loss is smaller with increasing particle size.

However in the case of the samples coated with oleic acid double weight decay indicates that there are two types of coordinated oleic acid (Palchoudhury, 2011) with an average weight loss that occurs at 453 °C and total weight loss of 36.5% independent of particle size. Finally the sample coated with dextran has a greater weight loss (73%) due to the decomposition of dextran, which is a heavy and polymeric molecule (molecular weight 40 kD) (Table 6.2). In all cases weight losses at lower temperatures (as in the case of uncoated samples) are due to physically adsorbed water.
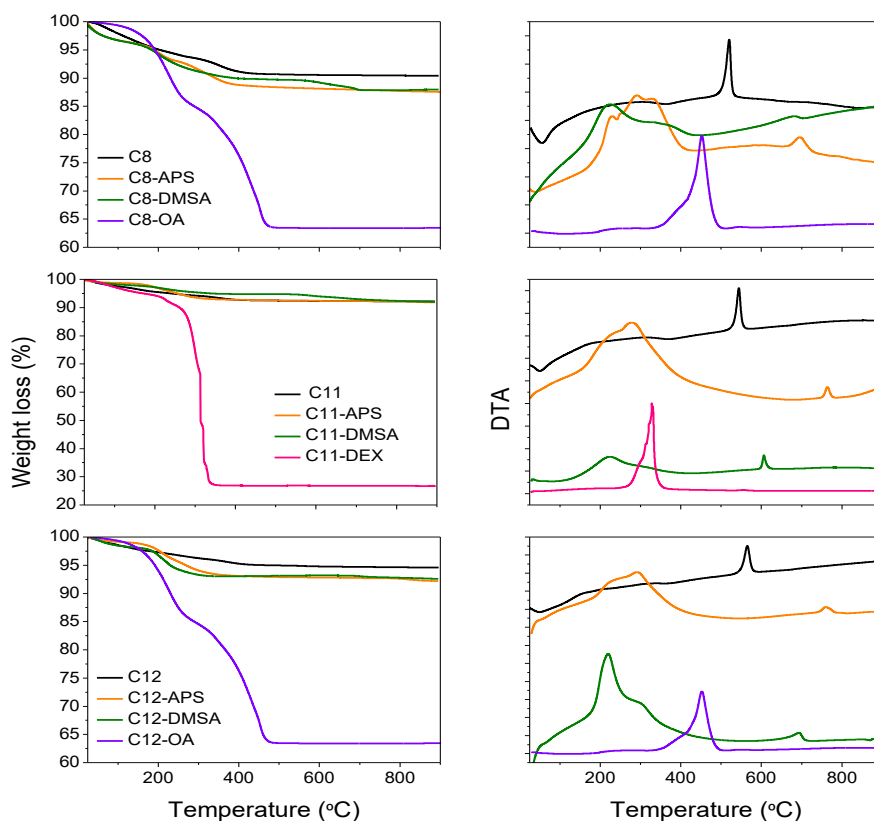
Figure 6.4. *Results of DTA-TGA of 8, 11 and 13 nm uncoated and coated nanoparticles.*

In the case of the samples coated with APS and DMSA it can be seen that the exothermic peak associated to the phase transition from maghemite to hematite occurs at higher temperatures than in the case of uncoated samples (from about 500 °C to 700 °C and 600 °C, respectively) indicating that both coatings are strongly bonded to the particle surface hindering the phase transformation. However, in the case of the samples coated with oleic acid and dextran this peak was not observed suggesting that this transformation occurs gradually over a wide temperatures range or well above 900 °C. We interpret that this is due to the high amount of carbon in the sample that could promote the intermediate formation of refractory carbides.

Sample	Weight loss (%)	Temperature of the main weight loss (ºC)	DTA transition to α-Fe$_2$O$_3$ (ºC)
C8	8.3	55	520
C8-APS	12.4	291	695
C8-DMSA	12.0	221	681
C8-OA	36.5	453	-
C11	7.8	51	544
C11-APS	8.2	277	764
C11-DMSA	8.0	224	607
C11-DEX	73.2	328	-
C13	5.4	49	565
C13-APS	7.8	290	760
C13-DMSA	7.4	219	694
C13-OA	36.5	453	-

Table 6.2. Results of the TGA for the uncoated and coated nanoparticles.

In addition to the particle size studied by XRD and TEM, we performed a study of the hydrodynamic aggregate size to verify the state of the particles in dispersion. To this purpose, we plotted in figure 6.5 the aggregate size distribution by intensity of every sample before and after coating. It can be seen that a mono-modal size distribution for each sample appears in all cases. In the case of uncoated samples it is clearly seen that increasing the particle size increases the hydrodynamic diameter, which is consequence of the unshielded interaction of the nanoparticles of maghemite.

Samples coated with APS, DMSA and dextran have a hydrodynamic size slightly higher than the corresponding uncoated samples, which is due to the presence of molecules of these coatings on the surface of the nanoparticles. The higher value corresponds to the dextran coating as expected due to the hydration of the polymer coating surrounding the magnetic core and the larger fraction of coating (73%). However, the hydrodynamic size of the samples coated with oleic acid dispersed in hexane is considerably lower than the rest dispersed in water, because acting as surfactant to both

disperse and coat the nanoparticles. In such a way that the nanoparticles were dispersed individually and hydrodynamic sizes in number for OA-coated samples (9.5 and 15 nm) fit the TEM mean particle size plus the oleic acid chain length (1-2 nm) within the experimental error.

It can be concluded that although APS, DMSA and dextran coated particles form aggregates of different sizes stable in water, OA-coating disaggregates the nanoparticles leading to nearly individually coated particles stable in organic media (hexane). Hydrodynamic sizes of samples C8-C12 coated with APS and DMSA are always smaller than 100 nm.
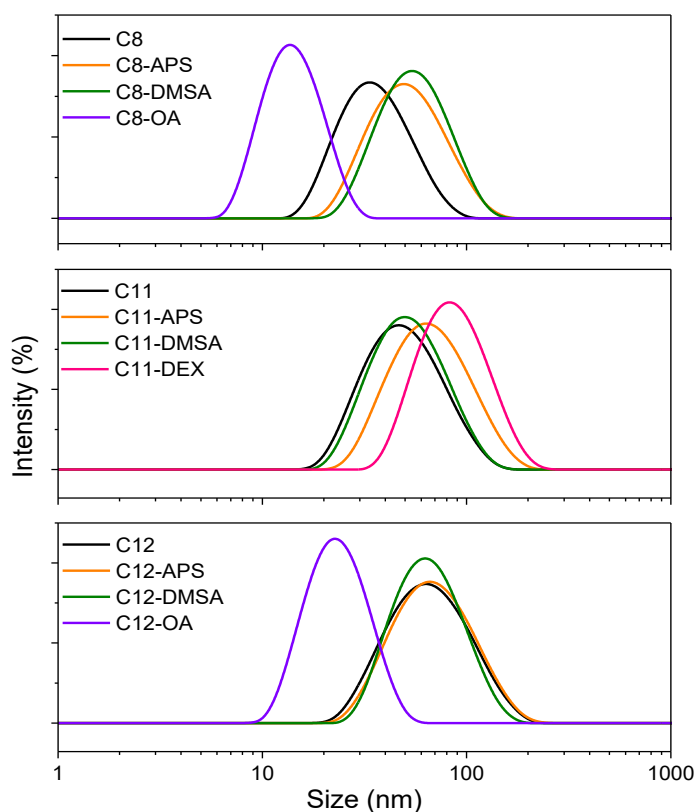
Figure 6.5. *Hydrodynamic size distribution of the uncoated and coated samples.*

For a complete characterization of the surface of the nanoparticles in aqueous dispersions it is important to determine their surface charge. In colloidal dispersions of metal oxides, it is generally assumed that the surface is covered with amphoteric hydroxyl groups: M-OH (where M is the metal, in this case Fe) (Jolivet, 2004; Cornell, 2006). Depending on the pH, the predominant species in the surface can be $M\text{-}O^-$ or $M\text{-}OH_2^+$, so it is necessary to determine the concentration of main surface species for each pH. For this purpose, an important concept is defined: the isoelectric point (IEP). This is the pH value at which the net electrical charge of an elementary entity is zero (McNaught, 1997). In this case, charge balance refers to the diffuse layer and is measured by electrokinetic measurements as the zeta potential.
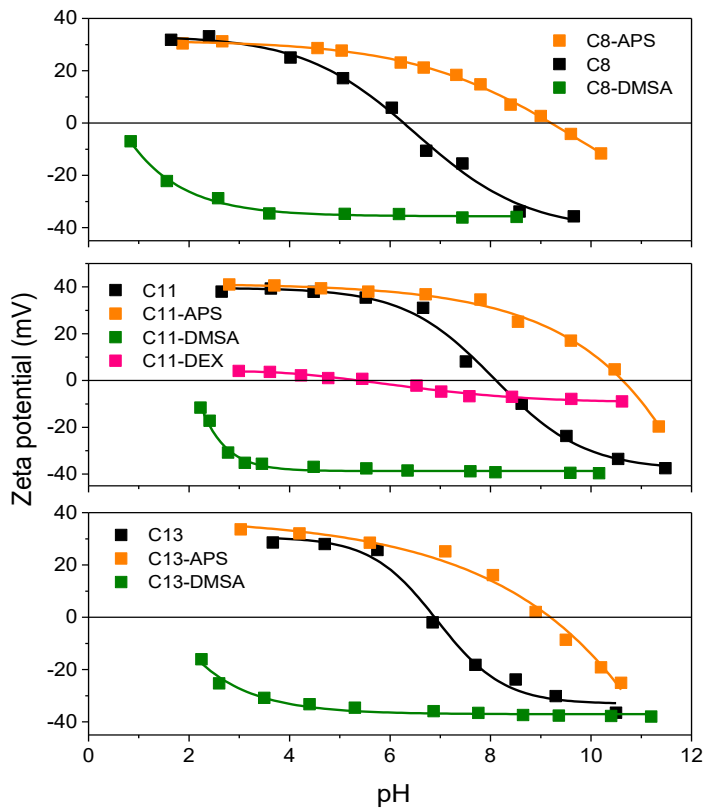
Figure 6.6. *Measurements of the IEP (Z potential as a function of pH) for uncoated and coated samples. The background electrolyte concentration was 10^{-2} M in all cases.*

Z-potential vs pH measurements were performed for the original and coated samples (figure 6.6) to determine the IEP, which for metal oxide can vary widely, depending on factors such as purity, temperature, nonstoichiometry, defect structures, etc. and on a great extent on the synthesis method (Parks, 1965). The isoelectric point at 6.7 is typical of maghemite (Parks, 1965; Kosmulski, 2002; Cornell, 2006), but uncoated particles exhibit an isoelectric point between 7 and 8 (Table 6.3). This change may be due to modifications in the particle surface, such as reorganization of the surface structure, changes in the hydration degree or changes in the type or quantities of impurities.

Sample	Z-Average (nm)	PDI	IEP	Z-Potential (mV) pH=7
C8	46.6	0.21	7.6	+15
C8-APS	54.0	0.15	10.1	+37
C8-DMSA	50.9	0.12	<2	-34
C8-OA	14	0.17	-	-
C11	47.6	0.23	7.9	+21
C11-APS	57.6	0.15	10.5	+36
C11-DMSA	49.1	0.15	<2	-39
C11-DEX	81.4	0.12	5.5	-5
C13	60.4	0.21	6.5	-3
C13-APS	75.5	0.13	9.2	+34
C13-DMSA	61.0	0.14	<2	-37
C13-OA	22	0.10	-	-

Table 6.3. *Experimental results of colloidal properties of nanoparticles before and after coating characterized by DLS.*

Therefore, as the acid treatment increases the surface hydration and also the surface density of acidic $-OH_2^+$ groups, i.e., more OH^- is needed in the aqueous media to equilibrate the charge and the isoelectric point of the samples is shifted to more basic values. Colloidal suspensions of uncoated maghemite nanoparticles are stable at pH 3 due

to the electrostatic repulsion among surface OH_2^+ groups but are unstable at physiological pH (7.4) due to its deprotonation. Surface modification adds positive charge with APS molecules (creating surface $-NH3^+$) or negative charge with DMSA molecules (creating surface $-COO^-$) with the result of shifting the IEP far from the neutrality. The resultant high positive or negative charge at physiological pH (>+30 mV) provides long-term stability of the dispersions. Dextran coated particles presented a low surface charge (~10 mV) changing from positive to negative at pH around 6. These polymer molecules generate steric repulsion to impart colloid stability. Table 6.3 summarizes the experimental results on hydrodynamic sizes, isoelectric point and surface charge at pH 7. The IEP for OA-coated nanoparticles was not measured because these samples were dispersed in hexane.

3.2. Coated pure and bimetallic nanocrystals with different sizes

In the case of nanocrystals we have chosen samples with two proportions of Co and Gd to coat them with APS and evaluate their magnetothermal and relaxometric properties, as well as bare nanocrystals of similar sizes to compare (CN0, CN25, CN50 and CK0).

The proportion of Co and Gd determined by ICP after coating (%at Co = 2.3 and 5.3, %at Gd = 1.8 and 3.5) closely follows the preexistent in uncoated samples (%at Co = 2.2 and 5.0, %at Gd = 1.6 and 4.0), which means that dopant losses during the coating process have not occurred.

The characterization of these samples was performed with the same techniques used for nanoparticles which allow determining qualitatively and quantitatively the surface modifications (IR, TGA and colloidal properties). We also performed a comparative study of samples with and without coating.

Figure 6.7 and figure 6.8 display the FTIR spectra of cobalt and gadolinium bimetallic samples and the corresponding pure samples with similar sizes, before and after the coating.
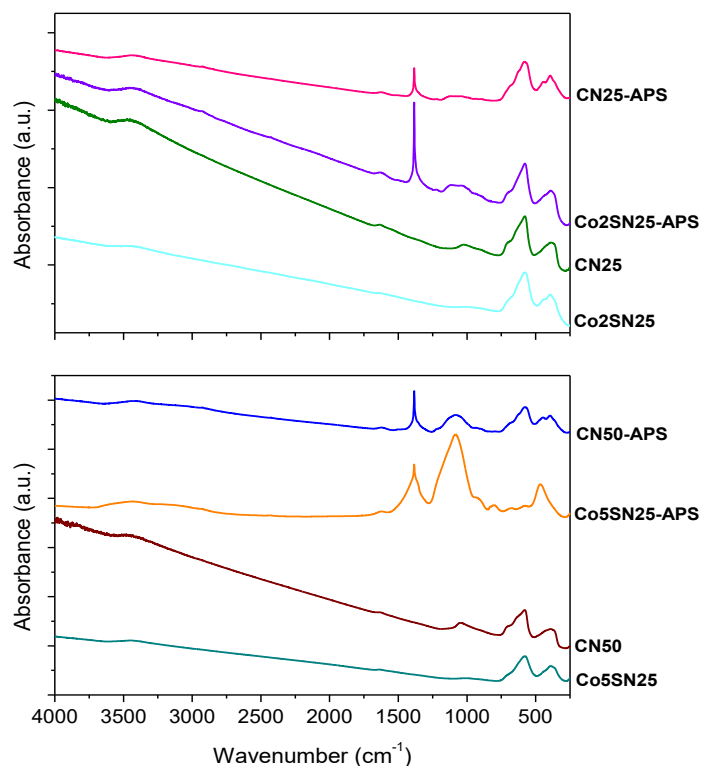
Figure 6.7. *FTIR spectra of pure and Co bimetallic nanocrystals before and after coating.*

As explained above, infrared spectra for magnetic nanocrystals (figure 3.5) show similar features: two main peaks at low frequency due to magnetite (around 400 and 600 cm^{-1}) (Cornell, 2006), a broad peak at around 1000 cm^{-1} due to surface impurities coming from the iron salts, and a broad band at 1630 cm^{-1} due to the bending HOH of water. The bands at 400-600 cm^{-1} are observed also in samples doped with Co, which is a common feature of the spinel ferrite (Patange, 2008).

In addition to the peaks described above, the gadolinium-magnetite bimetallic samples exhibit slightly weak signals at 800, 825, 1260 (only observed in the sample with 2% Gd) and 1385 cm^{-1}, which could be due to the secondary phase obtained during the synthesis (needle iron oxide nanoparticles).
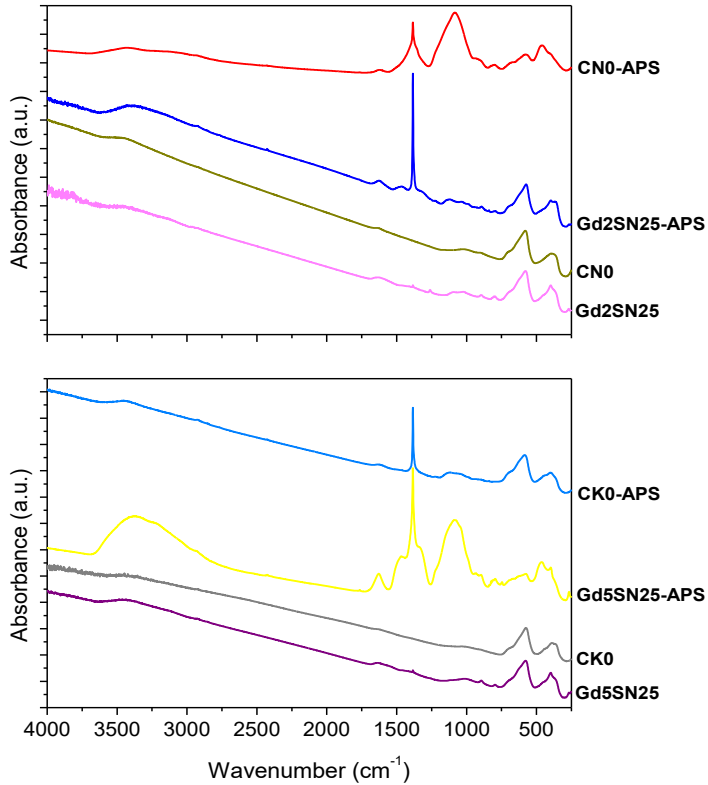
Figure 6.8. *FTIR spectra of the pure and Gd bimetallic nanocrystals before and after coating.*

In the case of the samples coated with APS the difference observed in the spectra is the appearance of an intense and narrow band around 1300 cm^{-1} and a wider band around 1000 cm^{-1} corresponding to silanol groups vibration bonded to the surface of the nanoparticles. In addition, in some cases it appears some less intense bands below 1000 cm^{-1}.

Thermogravimetric analyses of the samples before and after coating were carried out from room temperature up to 800 °C (Figures 6.9 and 6.10).
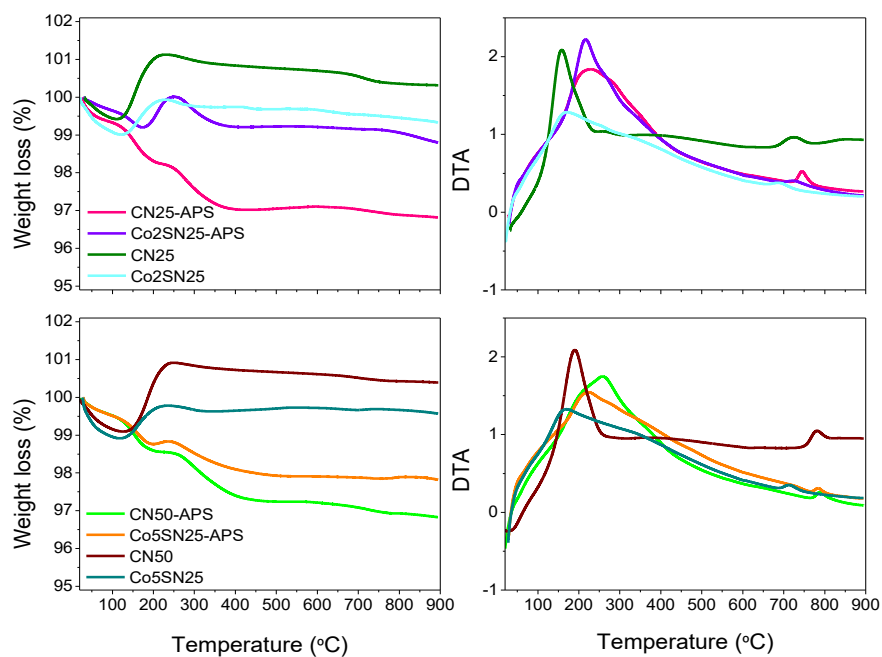
Figure 6.9. *Results of DTA-TGA of pure and Co bimetallic nanocrystals before and after coating.*
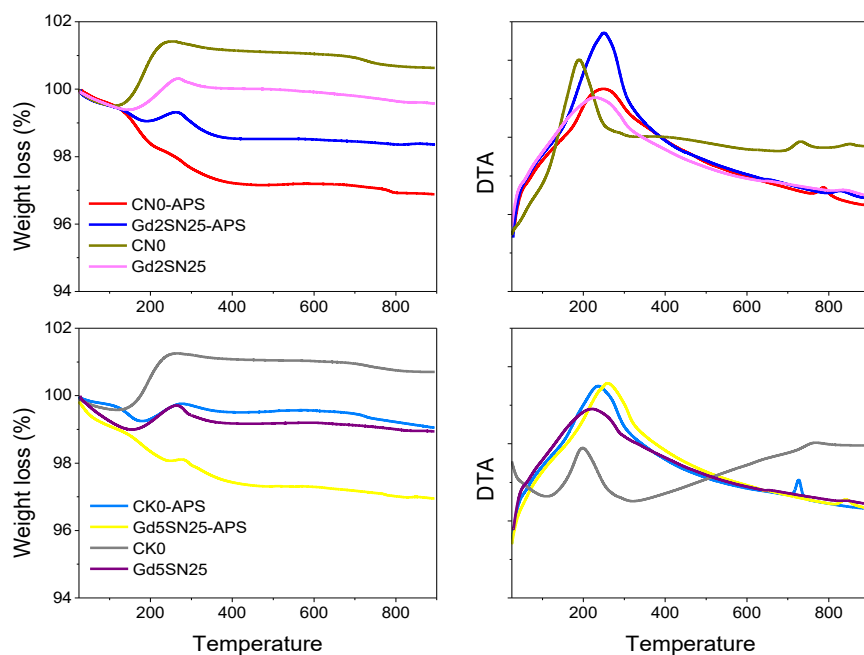
Figure 6.10. *Results of DTA-TGA of pure and Gd bimetallic nanocrystals before and after coating.*

All samples present an increase of weight and an exothermic peak at temperatures from the ambient to 300ºC due to the oxidation of the iron (II). Due to the partial oxidation during the coating in the case of coated samples this increase is lower than in the case of uncoated samples. In addition, the samples coated with APS present a greater weight loss that accounts for the APS molecules in addition to the physically adsorbed water molecules. The weight loss is much lower (1.5-3%) than for NPs (8-12%) (table 6.2) according to the reduction in surface area for NCs.

Sample	TEM size (nm)	Weight loss (%)	Weight increase (%)	DTA transition to α-Fe$_2$O$_3$ (ºC)
Co2SN25	30	0.7	0.9	688
Co2SN25-APS	30	1.2	0.8	783
Co5SN25	26	0.3	0.9	714
Co5SN25-APS	26	2.2	0.07	783
CN25	30	0.6	1.7	725
CN25-APS	30	3.2	0.09	745
CN50	26	0.9	1.8	780
CN50-APS	26	3.1	0	789
Gd2SN25	42	0.6	0.9	836
Gd2SN25-APS	42	1.5	0.3	827
Gd5SN25	51	1.0	0.7	864
Gd5SN25-APS	51	3	0.04	842
CN0	42	0.5	1.9	732
CN0-APS	42	3.1	0	787
CK0	53	0.4	1.7	769
CK0-APS	53	0.1	0.5	727

Table 6.4. *Results of the thermal analysis for uncoated and APS coated samples.*

For pure and Co doped samples coated with APS it can be seen that the phase transition of maghemite to hematite occurs at higher temperatures than in the case of

uncoated samples indicating that the silica coating persists at high temperatures hinders the phase transformation (this fact is not observed for sample CK0 since it presents no coating). For Gd samples, this effect is not observed. The Gd present at the surface of uncoated samples already shifts this transition to higher temperatures (>800 ºC) but when samples were coated with APS the transition temperature was somewhat reduced due probably to the partial loss of Gd. This temperature is in most of the cases similar to APS coating NPs.

In addition to the particle size studied by XRD and TEM, we performed a study of the hydrodynamic aggregate size to verify the state of the particles in dispersion. To this purpose, we plotted in figures 6.11 and 6.12 the aggregate size distribution by intensity of every sample before and after coating.
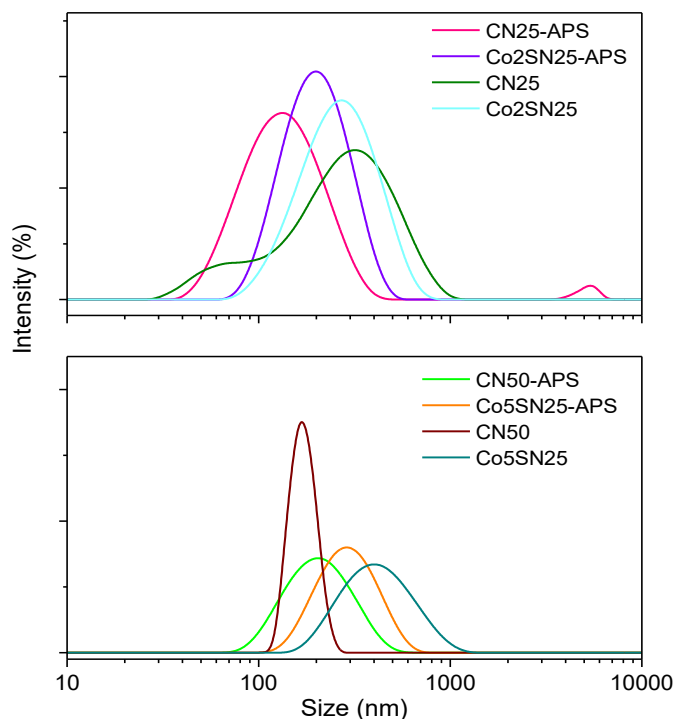
Figure 6.11. *Hydrodynamic size distribution of pure and Co bimetallic nanocrystals before and after coating.*

It can be seen that a mono-modal size distribution for each sample appears in almost all cases. In the case of uncoated samples it is clearly seen that increasing the particle size the hydrodynamic diameter increases (table 6.5), which is a consequence of the unshielded interaction of the nanoparticles of pure or bimetallic magnetite. Samples coated with APS have a hydrodynamic size lower than the corresponding uncoated samples, which mean that the coating reduces the aggregate size. Z-average values go from around 250-400 nm for uncoated samples down to 150 nm for APS coated NCs, always larger than those for NPs (50-70 nm).
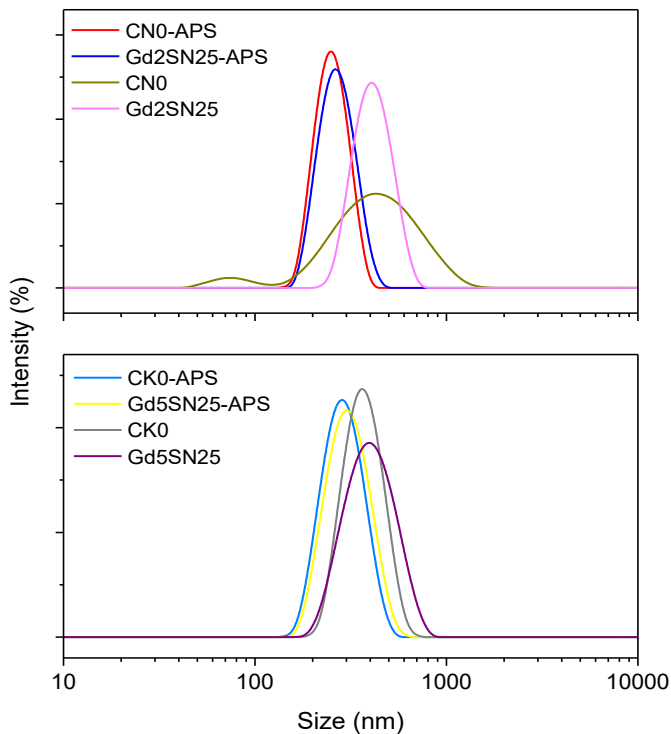
Figure 6.12. *Hydrodynamic size distribution of pure and Gd bimetallic nanocrystals before and after coating.*

Sample	Z-Average (nm)	PDI	IEP	Z-POT (mV) pH=7
Co2SN25	258	0.255	6.0	-14
Co2SN25-APS	161	0.231	7.3	+3
Co5SN25	328	0.279	5.7	-20
Co5SN25-APS	149	0.259	8.4	+13
CN25	198	0.344	2.9	-31
CN25-APS	122	0.248	8.5	+24
CN50	305	0.390	2.6	-34
CN50-APS	168	0.237	8.7	+22
Gd2SN25	379	0.208	6.8	-3
Gd2SN25-APS	306	0.222	8.1	+13
Gd5SN25	404	0.282	7.5	+3
Gd5SN25-APS	326	0.210	8.4	+14
CN0	348	0.267	3.1	-35
CN0-APS	293	0.211	8.6	+20
CK0	420	0.255	5.7	-25
CK0-APS	324	0.239	8.9	+20

Table 6.5. *Experimental results of colloidal properties for pure and bimetallic nanocrystals before and after coating characterized by DLS.*

Z-potential vs pH measurements were performed for the original and coated samples (figures 6.13 and 6.14) to determine the isoelectric point (IEP). For pure magnetite-maghemite particles, a value of 6.6 has been reported and small differences from this value were ascribed to the presence of impurities such as bromide or chloride anions. Bimetallic samples present an isoelectric point more similar to the value reported for magnetite. For the coated samples IEP shifting to higher pH values in all cases. The particle charge at pH 7 (and therefore the sample stability at that pHs) goes from negative or close to zero values for uncoated samples to positive values for coated samples.
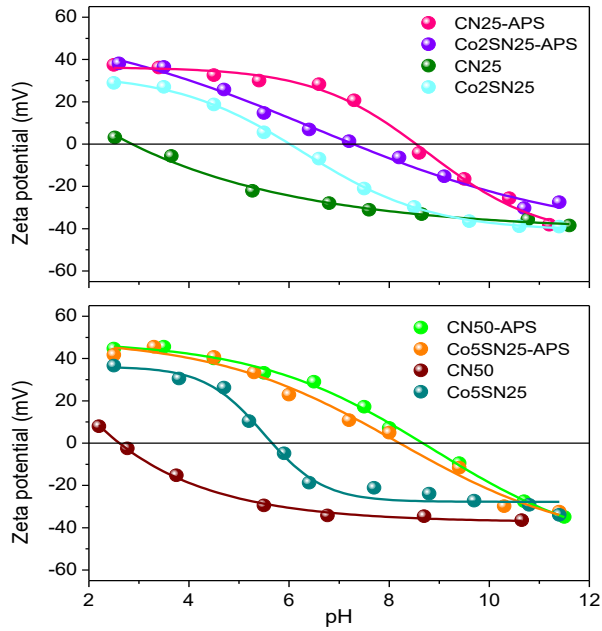
Figure 6.13. *Z potential as a function of pH for pure and Co bimetallic nanocrystals before and after coating. The background electrolyte concentration was 10^{-2} M in all cases.*
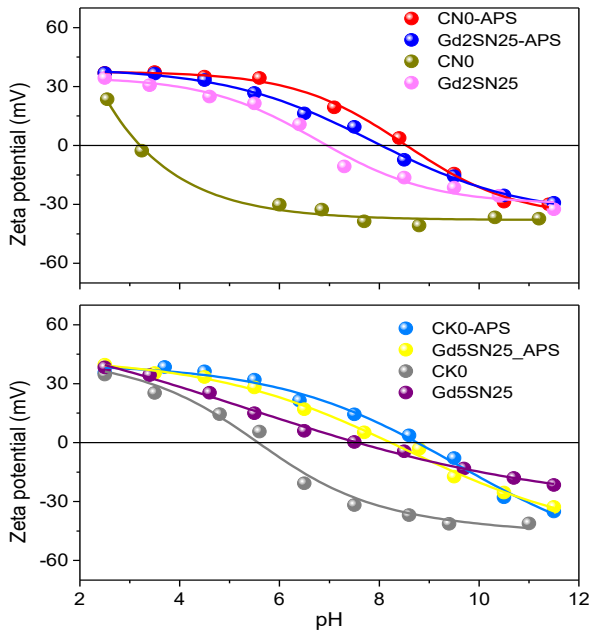
Figure 6.14. *Z potential as a function of pH for pure and Gd bimetallic nanocrystals before and after coating. The background electrolyte concentration was 10^{-2} M in all cases.*

4. DISCUSSION

Both nanoparticles and nanocrystals have been adequately coated with the compounds used in this work, however differences in the amount of coating present in each case are observed due to the large difference in size and, therefore, in the surface/volume ratio. This is evidenced in the weight loss obtained by TG, higher in the case of nanoparticles since the amount of coating is higher.

The smaller amount of coating present in the nanocrystals is also reflected in a lower isoelectric point shifts to around pH 8 when coating with APS, while in the case of nanoparticles is shifted to pH 10.

On the other hand, it has been verified that APS and DMSA coatings hinder the maghemite to hematite transformation both in nanoparticles and in pure and Co doped nanocrystals. However, in the case of Gd bimetallic NCs is the Gd present on the nanocrystal surface the responsible for hindering this transformation.

If we compare Co and Gd bimetallic magnetite nanocrystals with those of pure magnetite with the same size, it can be observed that the former are slightly worse coated, since they present smaller weight losses in TGA and less displacements in the isoelectric point.

To compare the efficiency of the coatings in the different samples, the amount of APS present on the surface of the NPs and the NCs (assuming spheres and cubes respectively) were calculated from the TGA data using equation 6.1 (Basti, 2016).

$$\frac{R}{NP} = \frac{100 - x}{x - 27.1} \qquad (6.1)$$

where R are the grams of APS, NP grams of uncoated nanoparticles/nanocrystals and x is the weight that is reached after removing the coating by heating to air. Factor 27.1 comes from the fact that APS is not completely removed when calcined but leaves the silica as residue.

Figure 6.15 shows the variation of APS molecules per nm² (calculated from the grams of coating per square meter of nanoparticles) with the particle size. In the overall this value is similar for NPs and NCs and the surfaces have similar reactivity. However it can be seen that 51 nm Gd bimetallic magnetite NCs presents the highest number of APS molecules per nm², in spite of its larger size, which indicates that it has a larger surface and/or that surface is more reactive, probably due to the presence of gadolinium.
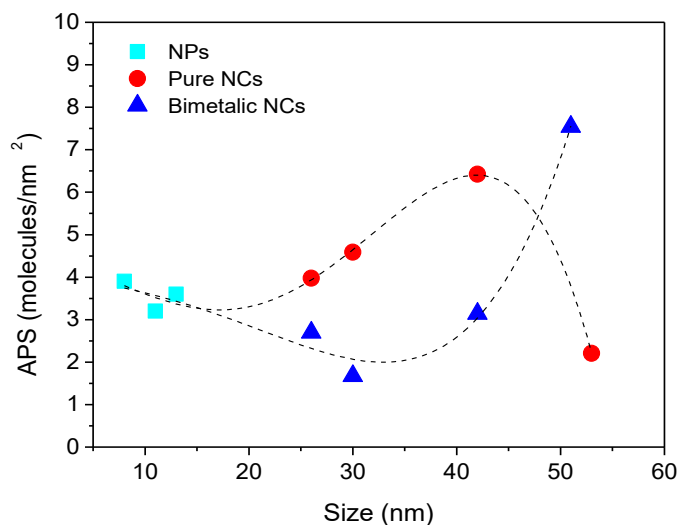
Figure 6.15. *Variation of APS molecules/nm² with the particle size.*

The value of the isoelectric point observed for the APS coated nanoparticles is greater than that observed in the case of nanocrystals (both pure and bimetallic) with the same coating. Likewise, both the surface charge at pH 7 and the maximum zeta potential attained are higher for nanoparticles than for nanocrystals. All of this corroborates the fact that the surface of the NPs is more reactive than the surface of the NCs, either by their nature or by acid treatment.

An interesting difference between the colloidal properties of NPs and NCs is that in the first case the coating increases the hydrodynamic size (14, 17 and 21% for the samples of 8, 11 and 13 nm, respectively) whereas in the case of the NCs the coating

decreases the hydrodynamic size (between 16 and 55%), i.e. the aggregates are smaller, are better dispersed and therefore the sample is more stable. This different behavior of NPs and NCs aggregates that enables the breaking of NCs aggregates and keeping the NPs aggregates during the coating is probably a consequence of the reduction of capillary forces with particle size.

5. CONCLUSIONS

Nanoparticles and nanocrystals have been coated with different molecules improving its colloidal properties due to electro-steric effect and providing different surface charge at pH 7. In the case of nanocrystals the coating process oxidizes the samples reducing the magnetite proportion. The coating of bimetallic samples does not alter the proportion of the secondary metal.

The amount of coating in APS coated pure and bimetallic nanocrystals is lower than in the case of nanoparticles, with the exception of 5% Gd bimetallic sample. This difference was interpreted considering the differences in specific surface of NPs and NCs. The results show that the coating density (g_{APS}/m^2) is different for NPs and NCs (especially in the case of bimetallic NCs) indicating different surface reactivities. The coating process induces an increase of the NPs hydrodynamic diameter (between 14 and 21%) and a reduction of NCs hydrodynamic diameter (between 16 and 55%). The isoelectric point shifts after APS coating to basic pHs giving electrically stabilization of the samples at pH 7, but NPs shift more than NCs.

7

Biomedical applications

1. INTRODUCTION

The combination of early diagnostic and early therapeutics is a very relevant aspect of the clinical treatments of cancer. One of this so called theranostic agents is the particulated T_2 contrast agent that has nanostructures to generate heat by magnetothermic effect. Recently a lot of attention has been attracted on development of these new theranostic agents (Muthu, 2014). Nanocrystals just below the superparamagnetic-ferrimagnetic limit (blocking temperatures close to the ambient) could in principle be the ideal candidates for such agents. Regarding their applications to hyperthermia, the important properties of magnetic particles are biocompatibility, non-toxicity, injectability, high-level accumulation in the target tumor and effective specific power absorption rate (SAR), which indicates the heat evolution rate in hyperthermia. Particles with sizes around the monodomain-multidomain transition, i.e. particles below 50 nm in diameter, have been pointed out as preferred since they are expected to produce the maximum SAR (Hergt, 1998; Jordan, 1999; Kawashita, 2005). Thus, it has been reported that the SAR of 35 nm magnetite particles is over twice as high as that of 10 nm particles. Furthermore, size distributions, as well as distributions of magnetic parameters, and, in particular, anisotropy fields must be taken into account (Andrés-Vergés, 2008). The problem is that the colloidal stability is limited by the particle size, and the optimization of relaxivity, specific absorption rate (SAR) at the available magnetic field and colloidal stability could be challenging for nanocrystals of such size.

The relaxometric properties of magnetic nanoparticles and thus its effectiveness as contrast agents are conditioned by parameters such as size, composition, crystallinity or surface coating characteristics (Singh, 2014). With respect to particle size, it has been suggested that relaxometric properties can be improved both by increasing the particle size and by obtaining magnetic nanoclusters formed by small nanoparticles (Shin, 2009). Furthermore, the coating characteristics of the nanoparticles also influence the relaxation times of water molecules. The final contrast in images obtained at a given Larmor frequency is a consequence of all these properties and can be evaluated in vitro by measurements of relaxivity using phantoms in a MRI scanner or a relaxometer.

In general terms, several parameters seem crucial for predicting cytotoxic responses mainly including nanoparticle chemical composition, surface charge and hydrodynamic size (Verma, 2010; Soenen, 2011b). The relevance of these parameters is such that toxic NP-induce responses can be reverted by selecting appropriate coatings, a reason why many different agents (including both synthetic and natural polymers) have already been tested (Soenen, 2011a). The extensive variability in these critical parameters, in addition to that originated by the experimental design itself, has generated a tremendous range of cell responses to NPs (Soenen, 2009). In this sense, iron oxide NPs have shown biocompatible responses when both uncoated (Heymer, 2008) and coated with specific molecules (Villanueva, 2009; Luengo, 2013; Calero, 2014).

1.1. Magnetothermal therapy

The heating efficiency of magnetic nanoparticles under an alternating magnetic field wakes up the interest of scientific community due to their applications in cancer treatments (Johannsen, 2010; Villanueva, 2010; Maier-Hauff, 2011; Hervault, 2014; Kolosnjaj-Tabi, 2014; Silvio, 2014). The aim of most research is to find biocompatible magnetic NPs with high specific absorption rate (SAR) (see below) values that can be synthesized in large quantities in an easy, cheap, and reproducible procedure. The present challenges are the optimization of both the exposure conditions and the magnetic NPs characteristics and the assessment of the limits of scalability of the treatment. However, maximizing the SAR values and interpreting experimental results is a complex task as the SAR of magnetic nanoparticles assemblies depends on (i) magnetic particle properties (size, composition, anisotropy, surface, etc.), (ii) dispersion media properties (dielectric constant, hydrophobicity and viscosity), (iii) the combination of both that determines finally the interactions between particles and (iv) measurement conditions (field amplitude and frequency).

The magnetothermal effect consists in the heating produced by the magnetic NP under a magnetic field that oscillates at a given frequency. The oscillation of the field induces the oscillation of the magnetic moment of the NP that dissipates heat. The

specific absorption power (SAR) given in W/g is the experimental parameter used to characterize the phenomenon. There exists a large amount of experimental data in the literature which are not directly comparable due to SAR dependence on instrumental parameters like field amplitude and frequency. A theoretical frame for understanding the physical mechanism involved in NPs heating efficiency is the linear response theory (LRT) described in Appendix IV.

Due to the strong SAR dependence on measurement parameters such as AC field amplitude H_0 and frequency f, the comparison of reported SAR values measured under different conditions does not give much information on the NPs heating efficiency. More recently, an intrinsic loss power parameter defined as ILP = $SAR/(fH_0^2)$ has been proposed in order to compare heating efficiencies obtained under different experimental conditions (Kallumadil, 2009). The definition of ILP parameter regards the magnetization losses (the imaginary component of the magnetic susceptibility, $\chi''(t)$ as frequency-independent (in the range of hyperthermia treatments (10−1000 kHz), allowing direct comparison of the particle-heating capabilities independently of the applied ac field strengths and frequencies. However, this approximation is not always satisfied by particles in suspensions; a nonlinear behavior of susceptibility imaginary part in magnetic NPs is reported by different authors (Fischer, 2005; Glöckl, 2006).

Additionally, the heating efficiency is expected to be influenced by any parameter affecting the magnetic interactions between particles and therefore the magnetic moment rotation. In fact, magnetic interactions have been observed to significantly diminish the dipolar magnetic field outside a capsule when particles are highly packed (Abbasi, 2011). In the same sense, SAR has been observed to increase with NPs size up to a certain value (Gonzales-Weimuller, 2009) but the dependence of this parameter on the media viscosity is not so clear (Glöckl, 2006; Hergt, 2006; Fortin, 2007; Levy, 2008). Other important issue limiting the application of the magnetic hyperthermia is the characteristics of the magnetic field required to produce the heating, which should be within the range approved for human use to avoid overcoming the discomfort factor limit $H_0 f < 5 \times 10^9$ $A \cdot m^{-1} \cdot s^{-1}$ (Hergt, 2007; Wust, 2009; Johannsen, 2010; Guardia, 2012).

Only for an assembly of single domain non-interacting particles, the heating mechanism is now well understood (equation IV-4, appendix IV) (Usov, 2010; Carrey, 2011). However, for an assembly of interacting particles, the role of dipolar interactions on the heating efficiency is still under investigation (Serantes, 2010; Mehdaoui, 2011; Piñeiro-Redondo, 2011; Mehdaoui, 2013; Landi, 2014; Garaio, 2015). Recently, the role of the dipolar interaction in the SARs has been analyzed by means of the mean-field model (Landi, 2014). The results point out that the strong influence of the dipolar interactions has an unpredictable effect; i.e., depending on system parameters like magnetic anisotropy or applied field, the SAR could increase as well as decrease. In particular, when nanoparticles are small enough to clearly have superparamagnetic behavior, the influence of magnetic interactions is to increase the effective anisotropy (Burrows, 2010). However, when the magnetic behavior is at the limit of the superparamagnetic to ferromagnetic regimen, the influence of the interactions is not so clear and apparently contradictory results are found (Serantes, 2010; Piñeiro-Redondo, 2011; de la Presa, 2012; Haase, 2012; Martinez-Boubeta, 2012; de la Presa, 2015).

To sum up: frequency and magnetic field amplitude strongly affect the heating efficiency of the magnetic NPs following different trends depending on the structural, colloidal, and magnetic properties of the material that makes difficult the understanding of the phenomenon behind.

1.2. Relaxometric properties

Other application of magnetic NPs and NCs is as contrast agents for Magnetic resonance Imaging (MRI). MRI images are mappings of relaxation times of the water protons presents in all tissues. Contrast agents for MRI are classified as T_1 or T_2 type based on its influence on the two proton relaxation processes (longitudinal for T_1 and transversal for T_2). The effect of the presence of a T_1 contrast agent is the increase of the signal intensity in the T_1 weighted MRI images that result in bright contrast while the presence of a T_2 contrast agents decreases the signal intensity in T_2-weighted images and generates dark contrast (Dias, 1986; Semelka, 2001; Corot, 2006). The FDA approved

application of T_2 contrast agents (ferumoxides) as in vivo tracers for liver metastasis is based on the fact that the liver is very effective in the uptake of the NPs and once in the liver they distribute among the healthy liver cells that can uptake the particles whereas are excluded from diseased or necrotic cells cannot do it. Thus, the healthy regions are darkened and the diseased regions remain bright (Mornet, 2004; Sosnovik, 2008; Geraldes, 2009). In practice, inorganic paramagnetic complexes based on Gd^{3+}, or less frequently Mn^{2+}, are used as T_1 contrast agent, it means that they are positive contrast agents and appear brighter in the MRI images (Caravan, 1999; Caravan, 2006). T_1 contrast agents based on paramagnetic inorganic ions have limitations (short blood half-lives and non-specific interaction with cells), thus particulated alternatives with a controlable biodistribution as superparamagnetic NPs materials similar than the bio-synthetic (ferrihydrite or the nanocrystals present in magnetosomes) or the hybrid oxides obtained by co-crystallization of iron oxide and oxides of Gd, Mn, Sb, Bi are worthy to be explored.

1.4. Cellular interaction and toxicity

When the magnetic nanoparticles come into contact with a biological system in vitro, the first interaction that occurs takes place with the cell membrane (Handgretinger, 1998). This union can occur by nonspecific electrostatic interactions between regions of the membrane with negative or positive charge and the particle surface (Wilhelm, 2002; Wilhelm, 2003; Holzapfel, 2006) or by binding to specific receptors when the nanoparticles are conjugated with biomolecules such as monoclonal antibodies, albumin, ferritin... (Schoepf, 1998; Gupta, 2005). The unspecific interactions are useful for drug delivery in the extracellular matrix, while the specific interactions are very useful to carry out a selective drug vectorization to tumor cells where certain biomolecule receptors are usually overexpressed (Lauffenburger, 1993; Qian, 2002). After the nanoparticle had positive interaction with the cell membrane their internalization can take place. Both nanomaterial interaction with cell membranes and its posterior cellular uptake efficiency is known to be dictated by chemical functionalities on its surface, along with its size and shape (Adler, 2010; Verma, 2010).

The cytotoxic effects of a treatment based on nanoparticles may be generally of two types: those which are independent of the cell-nanoparticle interaction or those associated with the process of internalization and intracellular transformation of nanoparticles. In the first case this type of cytotoxicity is secondary to the interaction of the nanoparticles with the culture medium. Due to the amount of surface available and their reactivity, nanoparticles they tend to form a "protein corona" (Cedervall, 2007) that captures proteins, nutrients and growth factors present in the environment to variable extent and the ensemble with hydrodynamic size and surface charge modified change their NP-cell interaction (Yen, 2009; Verma, 2010) increasing the toxicity of the ensemble (Lundqvist, 2011; Pelaz, 2015). Also adding particles to the culture medium can modify the pH or the osmotic pressure and indirectly cause cell death.

The cytotoxic effects associated with the internalization process at an early stage are usually studied by different microscopy techniques (TEM, optical) to see if there is full internalization or not. In the case of nanoparticles that only adhere to the cytoplasmic membrane but not internalized, it is more likely that these could be released during the cell division or cell migration processes due to shear forces (Soenen, 2009) and usually they do not cause damages of cell viability (Ruiz, 2013). The transmission electron microscopy allowed describing endocytosis, subcellular localization and degradation of magnetic nanoparticles (Lartigue, 2013). Nanoparticles are internalized by the cell via endocytosis (Appendix V) and they are initially added in early endosomes. Subsequently these endosomes fuse with heterolisosomes and a process of dispersion of nanoparticles gradually occurs and begins its degradation with variable degrees of toxicities.

2. EXPERIMENTAL SECTION

2.1. Measure of the heating efficiency

The SAR values of NPs prepared by coprecipitation (Chapter 2) and coated (Chapter 5) under an alternating magnetic field has been investigated as a function of size, concentration, coating, liquid carrier, and frequency and amplitude of the applied magnetic

field. Heating capacities of NPs have been measured with the commercial system Magnetherm 1.5 (Nanotherics).

The 8, 11, 13 nm NPs have been measured as a function of iron concentration (c_{Fe}) at H_0 = 7.5 kA/m and f = 522 kHz. The initial concentration was the highest (300 mg/ml), and the measurements were performed by diluting the concentration in half in consecutive steps with milli-Q water and indirect sonication (1 min). The effect of particle size on the SARs has been also investigated. Particles with diameter d = 6, 8, 11, 13, 14 nm have been measured at the same field and frequency. Since the SARs values were found to be independent of NPs concentration (as we will be discussed later), the concentration 50 mg/ml has been chosen because it is high enough to obtain heating curves that can be properly fitted and low enough to discard the influence of NPs on the specific heat capacities of the colloid. The magnetothermic effect has been measured as a function of field amplitude for particles dispersed in water or immobilized in agar in order to investigate the mechanism involved in the heating process. For this purpose, 50 mg/ml of the colloidal suspension in water or agar at 1 w % was measured at 522.7 kHz with the field amplitude varying from 2.4 to 7.5 kA/m for the 13 and 14 nm particle sizes and from 4 to 7.5 kA/m for the rest. The temperature of the agar suspension was not allowed to exceed 50 ºC to avoid the melting of agar. To check the effect of magnetic field 100 mg/ml of the 13 nm NPs aqueous colloid was used to get experimental data at very low fields ranging from 0.8 to 7.5 kA/m with a 0.4 kA/m step at 522.7 kHz. The SAR field frequency dependence was measured at H_0 = 4 kA/m amplitude field for the 8, 11, and 13 NPs sizes at frequencies 166.0, 330.9, 468.8, 522.8, 626.7, and 739.2 kHz, and the concentration was c_{Fe} = 50 mg/ml. The effect of coating was checked using APS-coated NPs of 8 and 13 nm measured at H_0 = 7.5 kA/m and f = 522.3 KHz at iron concentrations of c_{Fe} = 8 mg/ml. All the SAR values in this study were obtained under experimental condition $H_0 f < 5 \times 10^9$ A/m⁻¹s⁻¹, a limit at which an unwanted nonselective heating of both cancerous as well as healthy tissue due to generation of body eddy currents may occur (Hergt, 2007; Wust, 2009; Johannsen, 2010). Table 7.1 summarizes all the experimental conditions used for each experiment.

H₀ (kA/m)	f (kHz)	[Fe] mg/ml	Solution media	6 nm	8 nm	11 nm	13 nm	14 nm
7.5	522	300 150 75 37.5 18.7	Water		X			
7.5	522	100 50 25 12.5 6.25	Water			X		
7.5	522	166 83 41.5 20.75 8.5	Water				X	
7.5	522	50	Water	X	X	X	X	X
2.4-7.5* 4-7.5*	522	50	Water	X	X	X	X	X
2.4 - 7.5* 4.0 - 7.5*	522	50	Agar 1 w%	X	X	X	X	X
0.8 - 7.5	522	100	Water				X	
4.0	166.0 330.9 468.8 522.8 626.7 739.2	50	Water		X	X	X	
7.5	522.3	8	Water		X (APS)	X (APS)	X (APS)	

Table 7.1. *Summary of the experimental conditions used for each experiment (*with a 0.4 kA/m step).*

All the magnetic colloids formed by NP and NC are more or less aggregated. The influence of magnetic interactions in assemblies formed by either aggregated or disaggregated uniform maghemite nanoparticles are investigated as a function of particle size, concentration, and applied field. Hyperthermia measurements are performed in the liquid phase of colloids consisting of 8 and 13 nm uniform γ-Fe$_2$O$_3$ particles dispersed in

water and hexane. Although hexane allows obtaining the disagglomerated particle system, aggregation is observed in the case of water colloids. The SAR values of systems consisted of 8 and 13 nm particles coated with OA and APS are measured as a function of iron concentration at H = 15.9 kA/m and f = 110 kHz. By starting with the highest concentrated sample, we performed subsequent measurements by diluting the samples in consecutive steps with milli-Q water for aqueous colloid and hexane for organic colloid and sonicating for several minutes each step. The final concentrations used for hyperthermia measurements are c_{Fe} = 20, 10, 7.5, 5, and 2.5 mg/ml.

Heating efficiency of aqueous dispersions of APS coated pure and bimetallic (with Co and Gd) magnetic nanocrystals were measured using the commercial ac field applicator DM100 by nanoscale Biomagnetics© in the frequency range from 416 to 828 kHz and magnetic fields (H_0) of 20 to 24 kA/m at an iron concentration of 5 mg/ml.

2.2. Measure of relaxometric parameters

Additionally, in order to evaluate the efficiency of the suspensions as contrast agents for MRI measurements of the relaxation times of water protons in the presence of different NPs and pure and bimetallic NCs coated with APS were carried out in a time-domain NMR benchtop system MINISPEC MQ60 (Bruker) at 37 °C and 1.5 T. The preparation of the samples involves the gelification of the suspensions in agar solution (0.6%) with different iron concentrations below 1 mM Fe. The relaxivities r_1 and r_2 ($s^{-1}mMFe^{-1}$) were obtained from the measured longitudinal and transversal relaxation times T_1 and T_2 for each Fe concentration and blank solution from the linear plot of $1/T_1$ and $1/T_2$ in front of iron concentration . To measure the longitudinal relaxation t1_ir_mb pulse sequence was used at different inversion times according to the concentration of the sample. For transverse relaxation the sequence used was t2_ir_mb at different echo times depending on said concentration.

3.3. Evaluation of the toxicity

Finally, the influence of the different coatings attached on the nanoparticle surface (APS, DMSA and dextran) in the specific cell responses to their exposure. Prior to cell culture, Fe_2O_3 NP suspensions were sterilized under UV radiation for 20 min. Two different cell types were tested: murine L929 fibroblasts and human Saos-2 osteoblasts. Both cell types were seeded at the appropriate density that guaranteed subconfluence prior to NP addition, depending on their respective growth rates. Specifically, L929 fibroblasts were seeded at a density of ca. 4000 cells per well (5000 cells per cm²), whereas 5000 cells per well were seeded in the case of Saos-2 cells (ca. 6500 cells per cm²). Two days after cell seeding, cell cultures were exposed to three different types of NPs: DMSA, APS and dextran coated NPs. For both cell types, a range of NP concentrations was tested. Particularly, three different NP doses were evaluated: 0.25, 0.10 and 0.05 mg of iron per ml of solution (equivalent to 31, 12.5 and 6.25 applied pg of iron per cell for L929 fibroblasts and 25, 10 and 5 applied pg of iron per cell for Saos-2 cells, respectively, with respect to the initial cell seeding density). After exposure to NPs for 24 h, the excess NPs were eliminated and culture media were replaced. Culture media consisted of DMEM supplemented with fetal bovine serum (10%), streptomycin (100 UI ml⁻¹), penicillin (100 UI ml⁻¹), and L-glutamine (1 mM) (Lonza). Cultures were maintained at 37 ℃ in a sterile incubator under a CO_2 (5%) atmosphere for different times. Culture media were replaced every second day. Cell cultures were monitored over time by using an Axiovert CFL-40 optical microscope with an Axiocam ICC-1 digital camera coupled (Zeiss).

3. NANOPARTICLES RESULTS

3.1. Heating efficiency as a function of concentration, size and applied field

The small NPs size of magnetic nanoparticles and the value of the maximum applied field (<7.5 kA/m) allow the use of the linear response theory for the analysis of the experimental SARs values. The heating capacity was measured for the same samples as

the magnetic properties that is, for particles of 8, 11 and 13 nm in free flowing dispersion and in agar immobilized media.

3.1.1. Specific Absorption rate as a function of concentration and size

Among the large number of possible variations of the measurement parameters of SAR or ILP, most investigations are devoted on modification of particle concentration as an attempt for understanding how the magnetic interactions could affect particle heating efficiency. Nevertheless, controversial behaviors are found in the literature (Andrés-Vergés, 2008; Serantes, 2010; Piñeiro-Redondo, 2011; de la Presa, 2012; Haase, 2012; Martinez-Boubeta, 2012).

Figure 7.1 shows the experimental hyperthermia curves for different concentrations and sizes. By studying the heating function of the concentration of iron (figures A, B and C) it can be seen that the particles 13 nm reach 90 °C in less than one minute while the smaller particles need more time and concentration to achieve a similar temperature. Moreover studying heating dependence on the size (Figure D), keeping constant the concentration of iron (50 mg/ml), it is confirmed that the larger particles are reaching a higher temperature faster.

The results of SARs measured as a function of concentration for the 8, 11, and 13 nm NPs are shown in figure 7.2A. The uncoated NPs synthesized in this work can be concentrated up to 300 mg/ml at pH 3 with colloidal stability that can last for months. For each NP size, SAR is almost constant in the iron concentration range investigated here from ~6 to ~300 mg/ml. Previous works on iron oxide NPs have shown a SAR decrease when Fe concentration decreases below 5 mg/ml (Andrés-Vergés, 2008). As can be seen from figure 7.2A, there is a significant increase of a factor 4 in the SAR values for the 8 to the 11 nm size from ~10 to ~40 W/g, respectively, whereas for the 11 and 13 nm, the SAR increases only by a factor ~0.4 (from ~40 to ~55 W/g). In figure 7.2B, the SAR has a near cubic dependence on the NP radius, as expected from the LRT when Ms, H_0 and f are constant.
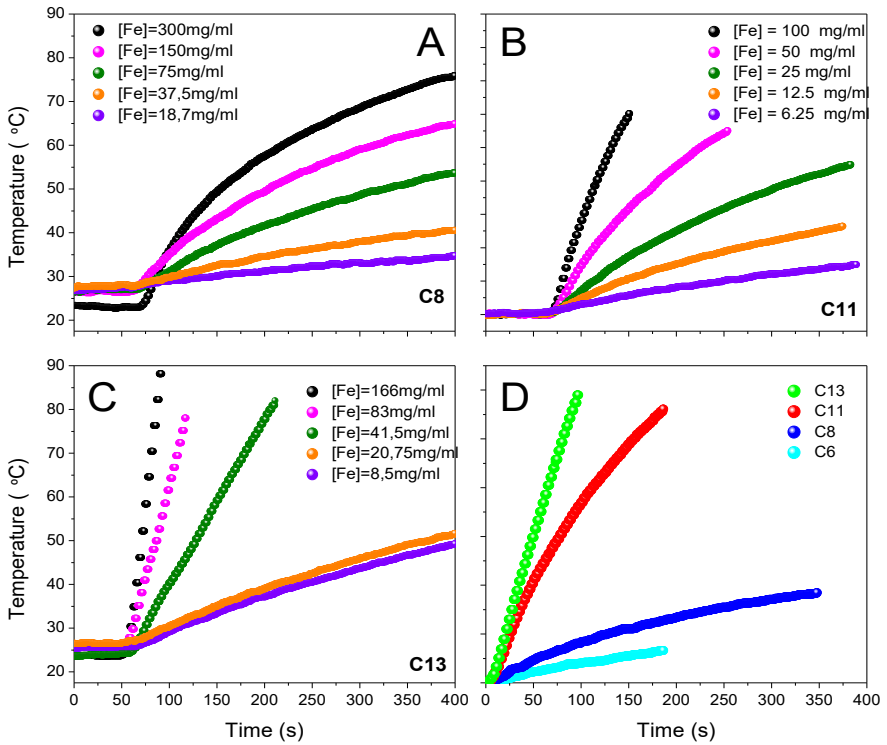
Figure 7.1. *Temperature increases of the magnetic colloidal suspensions for (A) 8 nm, (B) 11 nm, (C) 13 nm as a function of concentration, and (D) experimental heating curves for different sizes at 50 mg Fe/ml. All the experimental heating curves were performed at applied magnetic field H_0=7.5 kA/m and f=522.7 kHz.*
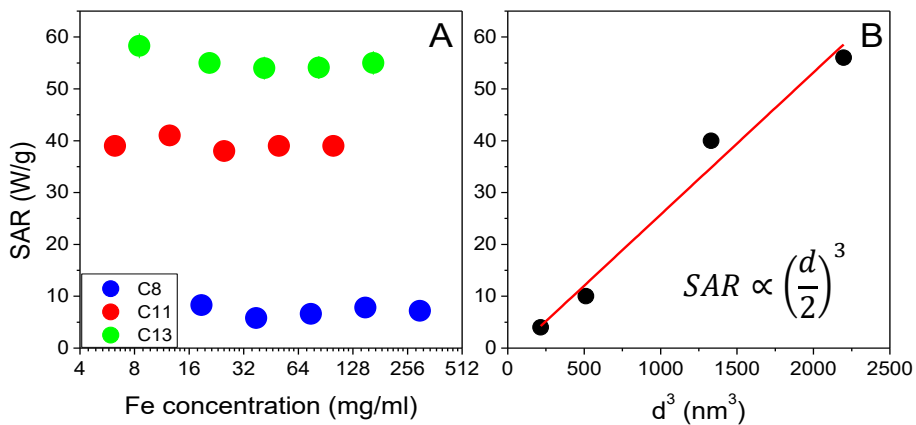
Figure 7.2. *(A) SAR vs Fe concentration for 8, 11 and 13 nm NPs. (B) SARs values as a function of nanoparticles size. The measurements have been performed at H_0=7.5 kA/m and f=522.7 kHz.*

NPs form aggregates by capillary forces. The effective field acting on a particle is the sum of the applied field and the field produced by the surrounding particles in the cluster. The average cluster sizes (number of NPs inside the aggregates) can be inferred from the hydrodynamic size as D_h^3/d_p^3 and depend on particle size and iron concentration (high NP concentration). The subsequent dilution and sonication cannot separate the particles inside the aggregates it merely separate the aggregates. Therefore, the magnetic interaction between NPs inside the clusters should remain unaffected by dilution whereas the magnetic interactions between aggregates would certainly change with dilution. The observed fact that SAR does not vary with NPs concentration strongly suggests either that interaction between clusters does not appreciably change for the studied concentration range or that is influence on the heating efficiency could be disregarded.

3.1.2. SARs as a function of field amplitude and frequency

Using the LRT model and SAR experimental values, relaxation times and effective anisotropy can be evaluated under $\mu_0 M_s V H_0 < kBT$ conditions. In figure 7.3, the gray area under the curve represents the maximum field amplitudes as NPs size function that allow the analysis of the results in the frame work of the LRT.
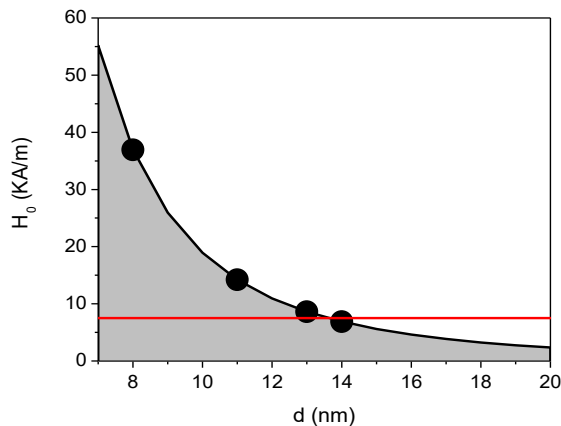
Figure 7.3. *Gray area under the curve representing the magnetic field amplitudes that satisfy the condition $\mu_0 M_s V H_0 < kBT$ of the LRT at room temperature for different particle sizes (the full black line represents $\mu_0 M_s V H_0 = kBT$). The maximum applied field in this work was 7.5 kA/m (red line).*

The maximum applied field in this work was 7.5 kA/m, which is well below the maximum for all NPs this justify the use of LRT in this work and also in biomedical applications of magnetothermic effect.

The frequency dependence of SAR has been fitted with a function presented in equation 7.1, obtained from equation IV-4 (Appendix IV).

$$SAR(f) = a \frac{\tau_R (2\pi f)^2}{1 + (2\pi f \tau_R)^2} \tag{7.1}$$

with $a = (\mu_0^2 M_s^2 V H_0^2)/(3 k_B T \rho_{Fe_2O_3})$.

Figure 7.4 shows the experimental results and fits and table 7.2 the fitted values. The advantage of the fitting is that it is possible to obtain the relaxations times directly form the fit.
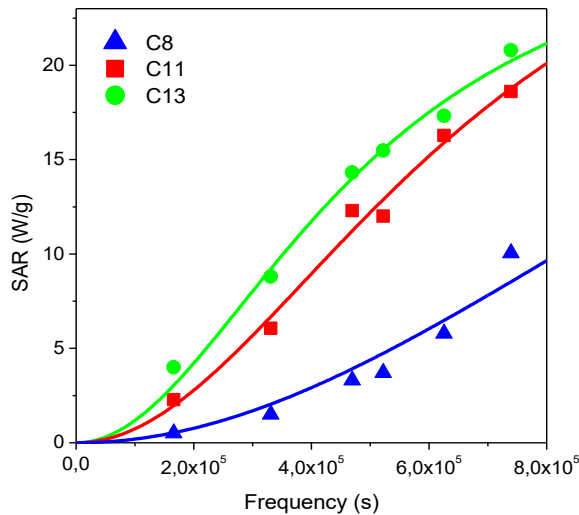
Figure 7.4. *Experimental SARs frequency dependence for 8, 11 and 13 nm NPs (triangles, circles and squares). The full lines represent the fits with equation 5. The measurements have been performed at $H_0 = 4 \ kA/m$ and $c_{Fe} = 50 \ mg/ml$.*

The parameter *a* depends only of the NPs volume if M_S, H_0 and T are the same for the three samples, as is the case. If we neglect the effect of the size distribution and

consider all NPs identical to the average size, then for the NP samples with sizes of 8, 11 and 13 nm the relationship $V_{C8}:V_{C11}:V_{C13}$ is 1:1.65:4.3. However, the relation between a's parameters $a_{C8}:a_{C11}:a_{C13}$ obtained from the fit is 1:1.25:3 and even that deviates slightly from that the evaluated from the average volume of the samples due to the distribution of sizes, as a first approximation, it could be considered that the a parameter depends on the nanoparticle volume.

	a (J/g)	τ_R (s)	τ_B (s)	K_{eff} (J/m^3)
13 nm	9.5(1) 10^{-6}	3.3(3) 10^{-7}	8.3·10^{-7}	2.1(2) 10^4
11 nm	8.1(1) 10^{-6}	2.4(2) 10^{-7}	5.0·10^{-7}	3.3(3) 10^4
8 nm	3.0(30) 10^{-6}	0.9(10) 10^{-7}	1.9·10^{-7}	6.7(10) 10^4

**Table 7.2.** *Fitted Parameters a (J/g) and τ_R (s) obtained by fitting SAR frequency dependence with equation 7.1. Brownian relaxation times τ_B are calculated with equation IV-2. Effective anisotropy K_{eff} is estimated considering $\tau_R = \tau_N$ and $\tau_0 = 10^{-9}$ s in equation IV-1.*

As can be observed from figure 7.4, the SARs dependence for the smaller NPs behaves nearly quadratically with frequency; therefore, the fitting of the parameters a and τ_R with equation 7.1 produces large uncertainties (from the fit we could only obtain with precision the product a·τ_R). In any case the quadratic approximation assures that the fitted value of τ_R correspondent to 8 nm NPs are in the regime $2\pi f \tau_R < 1$ even for the largest frequency used in this work $f = 739.2$ kHz. However, the trend of the a parameter looks quite similar to that observed for the larger NPs.

The fitted relaxation times τ_R obtained are about 10^{-7} s, which agrees well with relaxation times previously reported for γ-Fe$_2$O$_3$ in the frequency range investigated here (Fortin, 2007). The Brownian relaxation time τ_B was calculated with equation IV-2 (appendix IV) for NPs dispersed in water considering the water viscosity $\eta = 1$ cP and the hydrodynamic radius r_h as the particle radius (this will be the inferior limit of τ_B because we neglect further agglomeration under the measurement conditions). For NPs dispersed in water, Table 7.2 compares τ_B with the fitted τ_R. Although $\tau_R < \tau_B$, both relaxation times are of the same order of magnitude and both mechanism contribute to the heating.

The effective anisotropy, K_{eff}, can be estimated considering the fitted τ_R as a good approximation of the Neel relaxation time: $\tau_R = \tau_0 e^{(K_{eff}V)/(k_BT)}$, with $\tau_0 \approx 10^{-9}$ s (see table 7.2). Besides, K_{eff} can be independently estimated from ZFC-FC curves by considering that blocking temperature T_B, particle volume V, and K_{eff} satisfy the relation $K_{eff}V \approx 25k_BT_B$. Unfortunately ZFC-FC curves in figure 2.10 (Chapter 2) show a broad T_B distribution for the 11 and 13 nm NPs that makes difficult the determination of T_B for these samples. However, the 8 nm NPs show a T_B around 70 K giving an estimated K_{eff} around 9×10^4 J/m³, close to the value found by calculating K_{eff} by means of the relaxation time τ_R in equation 1, i.e., 6.7×10^4 J/m³ (see table 7.2). The similarity between both anisotropy values reinforces our hypothesis that the main mechanism contributing to the magnetization rotation for particles 8 nm in diameter is Neel relaxation. However, these anisotropy values are large compared to the bulk anisotropy at room temperature $K_1 = 4.64 \times 10^3$ J/m³ of γ-Fe_2O_3 (Bate, 1975) which means that surface or shape anisotropy effects are important in the NP of 8 nm.

3.1.3. SAR as a function of matrix and coating

The SAR was measured in different liquid carriers (water and agar) in order to elucidate the heating mechanism that takes place at different particle sizes. As can be seen from figure 7.5 and Table 7.3, the SAR values fall for the larger NPs when they are dispersed in agar, whereas for the smaller ones the heating efficiency seems to be independent of the media viscosity. Although the agar viscosity depends on average molecular weight, concentration, and type, its viscosity η can be more than 20 times larger than water viscosity (Suzuki, 1999), high enough to considerer the NPs are nearly immobilized.

The similar SAR values obtained for the smallest NPs dispersed in water and in agar evidence that the heating efficiency is not significantly affected by the media viscosity (see figure 7.5). If we assume that the NPs are quasi-immobilized in agar, the heat production mechanism is generated by the inversion of the magnetic moments inside the monodomain volume. On the other hand, the heating efficiency clearly diminishes when the larger NPs are dispersed in agar suggesting that a different mechanism is responsible

for the heat production. It is observed from table 7.3 that the maxima SARs for the larger NPs (13 and 14 nm) dispersed in agar are close to the maximum SAR value for the 11 nm NPs.
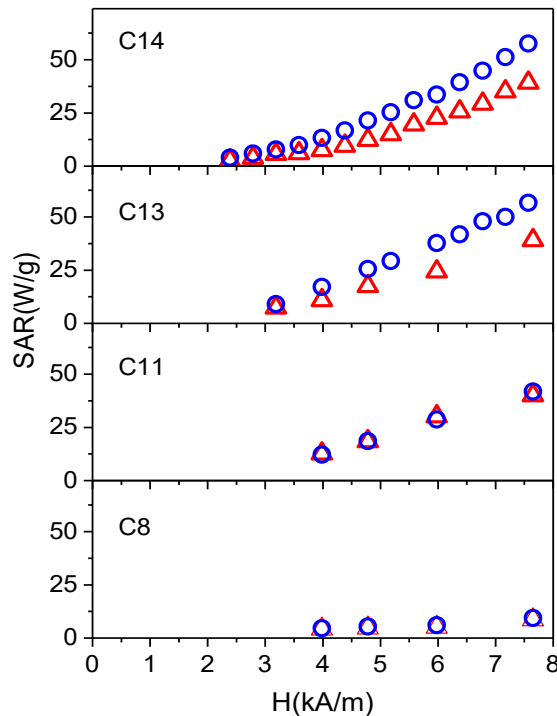
Figure 7.5. *Field amplitude dependence of the SARs values for 8, 11, 13 and 14 nm NPs dispersed in water (full circles) and in agar (full triangles). For the 8 and 11 NPs, the SARs values in water and agar overlap. The measurements have been performed at $c_{Fe} = 50$ mg/ml and $f = 522.3$ kHz.*

Actually, the average relaxation times calculated here do not take into account the NP size distribution. A simple calculation of the relaxation times as a function of size by means of equation IV-1 and IV-2 shows smaller NPs would relax by a Neel relaxation process whereas the Brown relaxation mechanism controls the relaxation process for the larger sizes (figure 7.6).

However, due to the size distribution and to the close values of the Brown and Neel relaxation times (table 2.4, chapter 2), both relaxation mechanisms are probably active in the larger mean NP sizes. As can be seen from the width of the size distribution

(figure 2.6, Chapter 2), sizes range from 8 to 16 nm when the mean particle size is 13 nm. For NPs suspended in agar, the Brownian relaxation time of the largest particles is increased about 20 times (see equation IV-3, appendix IV), slowing down the particle rotation and inhibiting them from heat production, whereas the smallest ones still relax by a Neel mechanism, contributing thus to the heating.
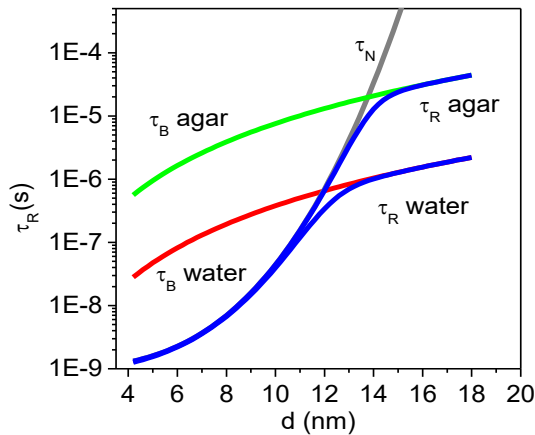
Figure 7.6. *Relaxation times for NPs dispersed in agar or water. The relaxation times τ_B, τ_N and τ_R have been calculated with equations IV-1, IV-2 and IV-3. We have considered a mean effective anisotropy $K_{eff} = 3x10^4 \, J/m^3$.*

The presence of both Neel and Brown relaxation mechanisms in the 13 and 14 nm particles accounts for SAR decrease in the higher media viscosity. The figure that emerges from all this is that in the range of NP produced by coprecipitation there is an optimal size (about 12 nm) at which heating production is a maximum regardless of media viscosity. Above this optimal size, the heating efficiency decrease with the increase of media viscosity, and below it decreases with particle volume. These facts are important for hyperthermia in cell culture media and tissues: large particle sizes with high SARs in aqueous colloid could not have the same heating efficiencies when the NPs are introduced in a more viscous media, as is the case for cell culture media and tissues.

Table 7.3 shows the SAR values obtained for uncoated and APS-coated NPs. The APS coating improves the colloidal properties and the biocompatibility, but it could affect

the heating efficiency since magnetic properties can be altered by the formation of the chemical bonds at the NP surface or the formation of different aggregates. However, the samples measured before and after APS coating show similar heating efficiency under the same applied magnetic field. It is worth to remain that the measurements were taken below the discomfort limit $H_0 f < 5 \times 10^9$ A/m^{-1} s^{-1}, a limit in the magnetic field conditions that is considered biomedically safe (Hergt, 2007). The calculated ILP value ILP = SAR/$f H_0^2$ for the 12 nm NPs is 1.78(1) nHm²/kg for field amplitudes higher than 2.4 kA/m and at field frequency 522.3 kHz, a value which is in the reported range 0.2−3.1 nHm²/kg (Kallumadil, 2009) of commercial thermal seeds for hyperthermia treatments.

	SAR (W/g$_{Fe}$)		
	Uncoated NPs (50 mg$_{Fe}$/ml)		APS-coated NPs (8 mg$_{Fe}$/ml)
Size (nm)	Water	Agar 1 wt %	Water
6	4(1)	-	-
8	10(1)	10(1)	8(1)
11	42(1)	40(1)	-
13	55(1)	41(1)	56(1)
14	58(1)	40(1)	-

Table 7.3. SAR values for uncoated and APS coated γ-Fe$_2$O$_3$ NPs dispersed in water or agar. The values were obtained at $H_0 = 7.5$ kA/m and $f = 522.3$ kHz. The product $H_0 f = 4 \times 10^9$ A/m$^{-1}\cdot$s^{-1} does not overcome the save limit for application of hyperthermia to patient.

Therefore, considering the heat capacity obtained under safe conditions and the possibility of preparing the material at low cost, we consider that the APS-coated γ-Fe$_2$O$_3$ NPs obtained by coprecipitation is a very promising magnetic colloid for hyperthermia therapy in human cancer treatments (de la Presa, 2012).

3.1.4. Effect of magnetic interactions on the heating efficiency

Once defined the optimal size of NP that could be used for magnetic hyperthermia treatments it is important to evaluate the effect of dipolar interactions among them on the heating efficiency. With this objective heating efficiency measurements were performed in assemblies formed by either aggregated or disaggregated uniform γ-Fe_2O_3 particles as a function of particle size, concentration, and applied field in the liquid phase of colloids consisting of nanoparticles of 8 and 13 nm uniform γ-Fe_2O_3 particles dispersed in water and hexane.

As can be seen from Figure 7.7, ΔT increases with increasing iron concentration (Figure 7.7A,B) and, additionally, for the same iron concentration, ΔT increases faster for hexane colloids than for aqueous colloids due to the smaller heat capacity of hexane (C_{hex} = 2.28 J/(g K), C_{water} = 4.18 J/(g K)) (compare panels A and B of Figure 7.7).

Table 7.4 shows the results of fitting the heating curves shown in figure 7.7, i.e., the slope $\Delta T/\Delta t$ and the calculated SAR values for each sample at a given concentration (for the linear fit we used the first ~30 s after turning the magnetic field on).

Particles	C_{liq} (J/gK)	Concentration (g Fe/L)	SAR (W/g)
C13-OA (in hexane)	2.28	20	61(3)
		10	78(3)
		5	95(5)
		2.5	96(7)
C13-APS (in water)	4.18	20	51(3)
		10	54(3)
		7.5	56(4)
		5	58(5)

Table 7.4. *Results of the fits of the heating curves: particles, liquid heating capacity (C_{liq}), iron concentration, average slope values $\Delta T/\Delta t$ and calculated SAR values. Average error is included in parentheses.*
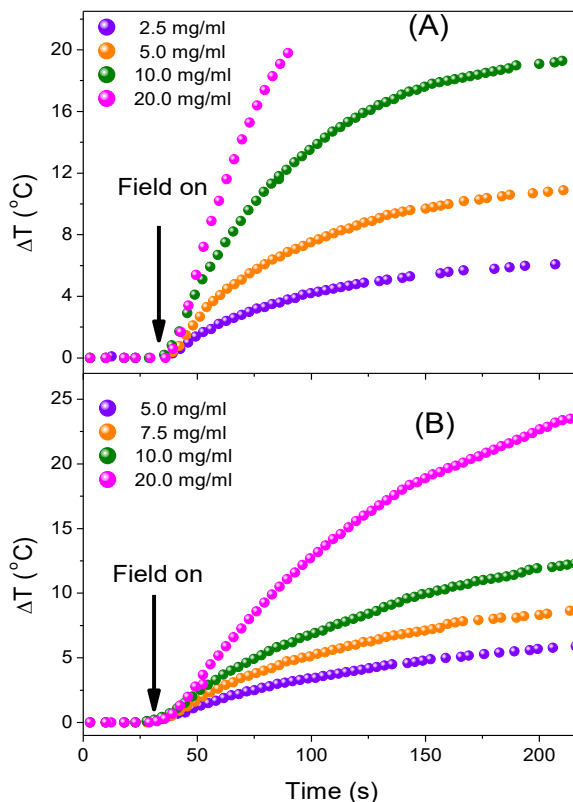
Figure 7.7. *Temperature increases for 13 nm nanoparticles at different concentration for (A) OA-coated dispersed in hexane and (B) APS-coated dispersed in water. The concentrations are 2.5, 5, 7.5, 10 and 20 mg/ml. The applied field is $f = 110$ kHz and $H_0 = 200$ Oe. The arrows indicate the instant the magnetic field is turned on.*

Given that the SAR is normalized to the different media heat capacities, it should be independent of the colloid media and could be used for the comparison among the different aggregation states of OA and APS coated nanoparticles. Notably, the SAR in aqueous colloids is almost concentration independent whereas the SAR in hexane is bigger and decreases noticeably as concentration increases and both values tend to approach each other with increasing concentration (see table 7.4 and figure 7.8).

As the particles in hexane and water are produced in the same batch and the coating does not alter significantly the magnetic properties, the interactions between particles appear to be responsible for the different heating efficiencies in OA- and APS-coated particles. In the case of multicore APS-coated nanoparticles, the magnetic

interactions between nanoparticles inside a cluster control the dynamic of the magnetization process and should not vary with particle concentration given that the SAR values are almost concentration independent (see figure 7.8). In the case of single core disaggregated OA-coated nanoparticles, the decrease of SAR as the concentration rises could be safely attributed to the increase of dipolar magnetic interactions. All points to the fact that the interactions make the effective field acting on a particle drop reducing the SAR and go to a minimum at high concentrations, leading in the limit of high concentration to similar low SAR values for both samples (de la Presa, 2015).
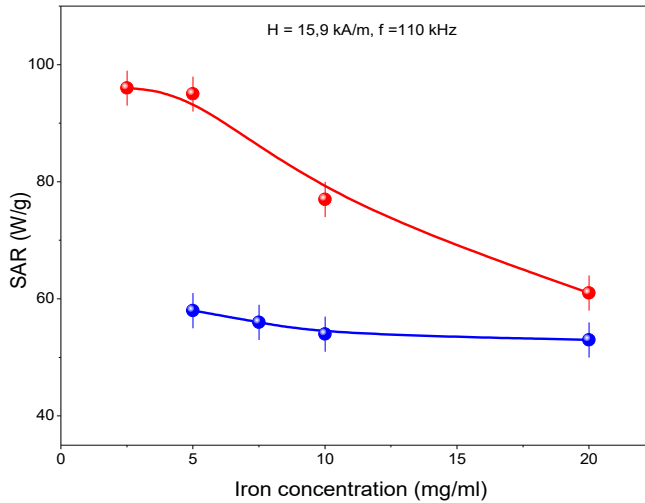
Figure 7.8. *SAR dependence on iron concentration at $H_0 = 15.9\ kA/m$ and $f = 110\ kHz$ for C13-APS (blue circles) and C13-OA (red circles) nanoparticles dispersed in water and hexane, respectively.*

3.2. Relaxometric measurements

Superparamagnetic magnetite nanoparticles with sizes of 8, 11 and 13 nm synthesized by co-precipitation and coated with APS, DMSA and dextran have been evaluated as contrast agents in vitro by measurements of T_1 and T_2 in aqueous dispersions and their performance will be related to the particle size and aggregate, and compared with standard of commercial contrast agents.

Study of the relaxometric properties was carried out by measuring the proton relaxation times (T_1 and T_2) at 37ºC and various concentrations of iron and calculating values relaxivity (r_1 and r_2). The results are collected in the figure 7.9.
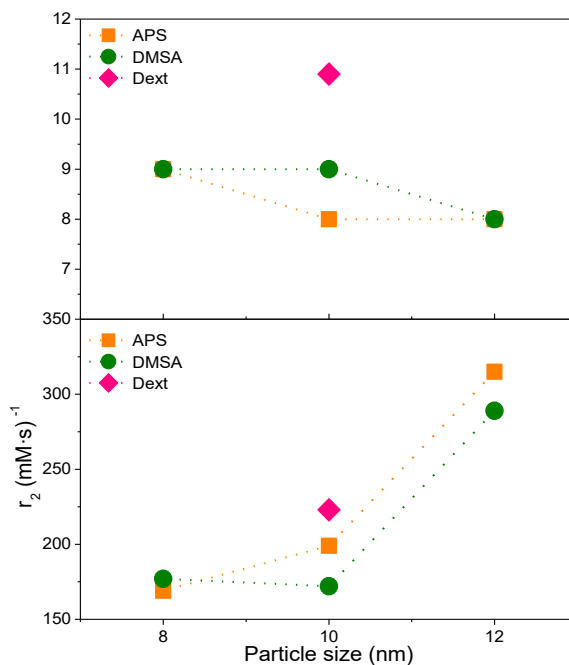
Figure 7.9. *r_1 and r_2 values vs. particle size for different coating samples.*

It can be observed that r_1 measured values remain constant (8-9 mM^{-1}·s^{-1}) with increasing size in the case of the samples coated with APS, while r_2 measured values increase with increasing particle size, from 169 to 315 mM^{-1}·s^{-1}. For the samples coated with DMSA the same behavior is observed: r_1 value is also keeping constant between 8 and 9 mM^{-1}·s^{-1}, and r_2 increase with particle size, however r_2 value for sample C11-DMSA is lower than expected probably due to the influence of its smaller hydrodynamic (aggregate) size. Polymeric coated C11-DEX sample show higher r_1 and r_2 values than the same size with APS and DMSA coatings, due to the bigger hydrodynamic size (Roch, 2005).

The effect of aggregation on the relaxometric properties (at difference than in magnetothermia) has been long time recognized. The fact that the particles are not evenly distributed in the medium but are forming small aggregates means that in certain areas local field gradients are created which accelerate the loss of phase coherence of the spins of protons contributing to the signal and produce an increase of r_2. The aggregate can be seen as a magnetized sphere where interactions between different nanocrystals produce high gradient of magnetic field and therefore a dominant effect in r_2 (Roch, 1999). Hence, an increase in the particle size (both crystalline and hydrodynamic) results in an increase in the relaxivity values (Huh, 2005). Even that r_1 values are similar to those shown by commercial agents approved for clinical use (Wang, 2011b) were of little use due in MRI for the generation of positive T1 weighed images due to the dominant r_2 effect. However r_2 values, which are responsible for the negative contrast of the nanoparticles are larger than those for the different contrast agents commercial and similar to those reported for other particles superparamagnetic iron synthesized by the decomposition method (Taboada, 2007; Roca, 2009) (Table 7.5).

Another important factor in the generation of T_2 weighed images is the value of r_2/r_1 used as an indicative of the effectiveness of the contrast agent. In all cases our samples show higher values than corresponding to those published for commercial contrast agents (Corot, 2006). The improvement of the performance of the contrast agent would allow the use of a reduced dose in clinical applications or gain in the imaging sensitivity. The main difference among the contrasts produced in this study and the commercial agents Endorem or Resovist, relies in that the contrast of these agents is determined by the high aggregation degree, and in our case the high crystallinity of our particles (enhanced by the acid treatment after synthesis) is the fundament of the relaxivities, so the contrasts obtained in this work were able to present high relaxivities with smaller aggregate sizes. The small aggregate size is considered a positive property in a contrast agent due to the reduction of side effects and the improvement of diffusion in tissues.

Samples	D_{TEM} (nm)	D_h (nm)	r_1 (mM^{-1}s^{-1})	r_2 (mM^{-1}s^{-1})	r_2/r_1
C8-APS	8	54	9	169	20
C11-APS	10	62	8	199	25
C13-APS	12	76	8	315	39
C8-DMSA	8	60	8	177	20
C11-DMSA	10	49	9	172	19
C13-DMSA	12	70	9	289	36
C11-DEX	10	81	11	223	21
Sinerem/Combidex	4-15	30	10	65	7
Resovist	4-15	45-60	10	189	19
Endorem/Feridex	4-15	120-180	10	120	12

Table 7.5. *Summary of the relaxometric properties for the samples prepared in this work and for various commercial agents (Wang, 2011b; Vuong, 2012).*

3.3. Cell response evaluation

We have investigated how controlled changes in the physicochemical properties of iron oxide NPs at their surface (i.e., surface charge and hydrodynamic size) affect, first, their interaction with cell media components and, subsequently, cell responses to NP exposure. For that purpose, we have used 11 nm iron oxide nanoparticles with the three different coatings (APS, DMSA and dextran). By doing so, we have obtained NPs varying in surface charge (negative, positive and neutral, respectively) and in hydrodynamic size. In this work, specific cell responses to their exposure were explored by using two different cell types, murine L929 fibroblasts and human Saos-2 osteoblasts, since the cell type has been described to significantly influence the toxicity of nanomaterials (Barua, 2009), including NPs (Lanone, 2009). Particularly, changes in cell adhesion, morphology, cell cycle, and viability were examined. Interestingly, different cell responses were found depending on the NP concentration, surface charge and cell type. Conclusions from these

studies are of crucial interest for future biomedical applications of iron oxide NPs (Luengo, 2013).

3.3.1. NPs interaction with culture medium

As the incubation of nanomaterials in cell culture media results in the adsorption of serum proteins on their surface (Khan, 2007), before the cells were cultured in presence of the NP's we investigated the behavior of the different coated NPs fabricated in Dulbecco's Modified Eagle's Medium (DMEM) and (endothelial growth media 2, (EGM-2, Lonza) and compared it to that obtained in distilled water. As illustrated in figure 7.10 and previously indicated, the NP hydrodynamic size in distilled water varied from 49 nm for DMSA, to 58 nm for APS and 81 nm for dextran.
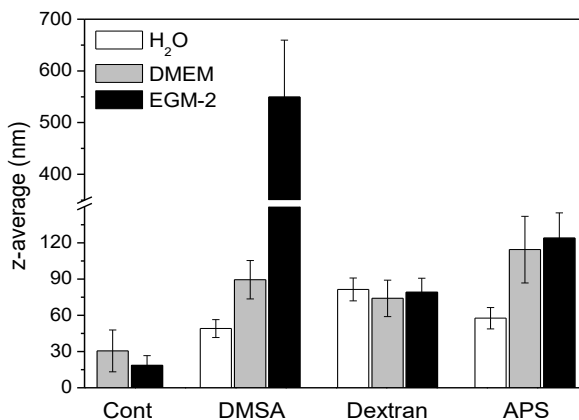
Figure 7.10. *Hydrodynamic size (Z-average, nm) variation for APS, DMSA and dextran coated NPs in distilled water and culture media (DMEM and EGM-2). The Cont bars represent the hydrodynamic size attributed by the DLS to the cell media (without NPs).*

Interestingly, when dispersed in DMEM, the hydrodynamic size almost duplicated for DMSA- and APS-coated NPs (90 and 114 nm, respectively), while NPs coated with dextran preserved their original size. The results were qualitatively similar in the two culture media essayed even that both DMEM and EGM-2 present different protein composition. These significant differences are related to the original surface charge of the different NPs, derived from their particular coating. In this sense, the original negative and

positive surface charges of DMSA- and APS-coated NPs, respectively, when dispersed in distilled water favored the adsorption of charged culture media components, such as proteins, and the subsequent increase in NP hydrodynamic size by the formation of a protein corona. Interestingly, the formation of this protein cover in DMSA- and APS-coated NPs resulted in NPs with a final negative net surface charge of very similar magnitude in both cases (-13 and -11 mV, respectively) (figure 7.11). In contrast, the absence of the surface charge in dextran-coated NPs prevented any adsorption of cell media components, so their hydrodynamic size in distilled water and DMEM did not vary significantly.
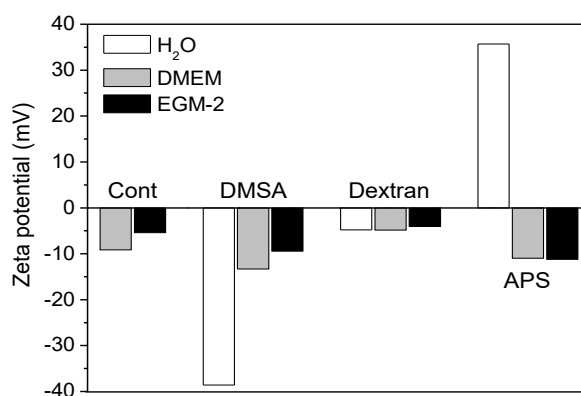
Figure 7.11. *Surface charge (Z potential, mV) variation for APS, DMSA and dextran coated NPs in distilled water and culture media (DMEM and EGM-2). The Cont bars represent the hydrodynamic size attributed by the DLS to the cell media (without NPs).*

3.3.2. NPs interaction with different cell lines

After physicochemical characterization in both distilled water and culture media, we next evaluated the interaction of the different types of NPs prepared with mammalian cells in vitro. For this purpose, we first explored the response of murine L929 fibroblasts, a reference cell line for cytocompatibility studies in vitro (Serrano, 2004).
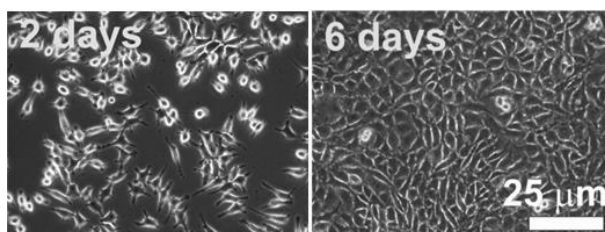
Figure 7.12. *Representative optical microcopy images of L929 fibroblast control cultures at 2 and 6 days without exposure to any NPs. Scale bars represent 25 μm in all images.*

Sub-confluent cell cultures were exposed for 1 day to either DMSA-, APS- or dextran-coated NPs at three different concentrations: 0.05, 0.10 and 0.25 mg mL^{-1}. When monitored by optical microscopy at 2 and 6 days, some significant differences in culture morphology were evidenced in comparison to control cells (Figure 7.12).

Particularly, DMSA-coated NPs seemed to affect cell adhesion when added to the culture media at the highest concentration (i.e., 0.25 mg ml^{-1}), as indicated by the significant amount of cells poorly attached to the substrate (i.e., more rounded and brighter cells) after 2 days of NP exposure (Figure 7.13).
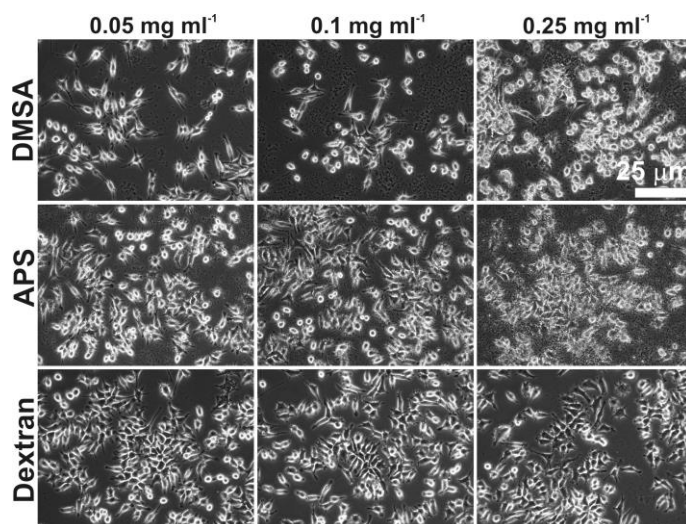
Figure 7.13. *Representative optical microscopy images of L929 fibroblast cultures after 2 days of exposure to DMSA-, APS- or dextran-coated NPs at different concentrations. Scale bars represent 25 μm in all images.*

Additionally, a slight tendency for cells to aggregate was observed. Cells exposed to a similar concentration of APS-coated NPs also experienced both phenomena, although less significantly. These alterations in cell adhesion and induction of cellular aggregation are a clear consequence of the interference of the cell attached NP's being this attachment controlled by the surface charge of the NP's (Verma, 2010). Interestingly, neither of these effects was observed in fibroblast cultures exposed to the lowest concentration (i.e., 0.05 mg ml-1), thus indicating concentration dependent effects. These effects mentioned above were more dramatically observed 6 days after NP exposure (Figure 7.14).
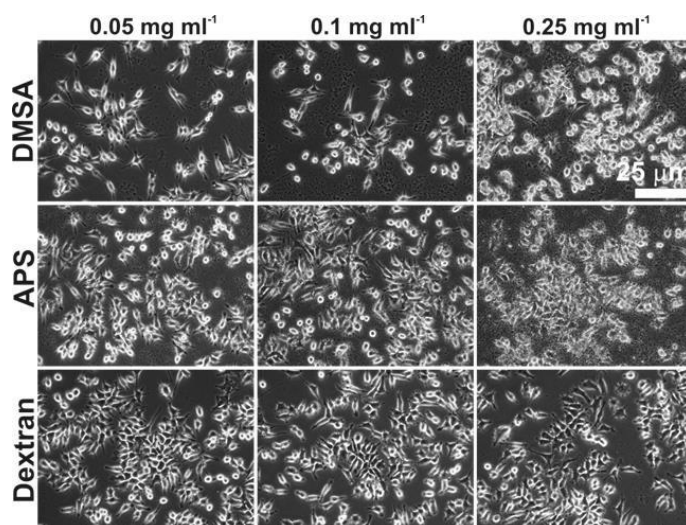
Figure 7.14. *Representative optical microscopy images of L929 fibroblast cultures after 6 days of exposure to DMSA-, APS- or dextran-coated NPs at different concentrations. Scale bars represent 25 µm in all images.*

Particularly, cultures in contact with higher concentrations of DMSA- and APS-coated NPs (i.e., 0.10 and 0.25 mg ml-1) showed more irregular plasmatic membrane limits and some cell aggregation. These alterations in cell morphology are likely related to NP effects on cellular cytoskeleton, which could be compromised by the intracellular volume occupied by NPs (Soenen, 2010) and their use in the cell endocytic machinery (Gupta, 2005). A reduced cellular attachment was also detected, which could be indicative of some deleterious effects on actin fibers and focal adhesion complexes, as previously reported

for other inorganic NPs (Wu, 2010). Finally, some inhibition of cell proliferation was observed, as indicated by a lower number of cells in comparison to the rest of cultures. It is important to mention that the excess NPs were removed 1 day after exposure, so only NPs either internalized or attached to the cell surface (i.e., those functionally relevant for biological interactions) (Soenen, 2011b) were retained. In this sense, we also hypothesize a relevant role in NP–cell interactions for those NPs somehow adhered to the extracellular matrix of the cell culture, as they are also retained after cell culture exchange and therefore remain available for later cellular uptake.

Optical microscopy studies also evidenced the intracellular uptake of both types of NPs at 2 days through a concentration dependent mechanism. To this regard, negatively charged iron oxide NPs have already demonstrated satisfactory cellular uptake (Shi, 2007; Villanueva, 2009) despite the unfavorable interaction between this type of NP and the negatively charged cell membrane (Verma, 2010), by binding and clustering on their cationic sites and posterior endocytosis. In contrast, positively charged NPs have shown superior efficiency of cellular uptake (Cho, 2009), entering the cell by binding to negatively charged groups at the cell membrane and being rapidly translocated across it via clathrin-mediated pathways (Harush-Frenkel, 2007). At this point, we must take into account that our results have indicated that both DMSA- and APS-coated NPs displayed a negative surface charge, very similar in magnitude, after dispersion in culture media and independent of their original surface charge. This fact is likely responsible for the comparable cell behavior found when in contact with both types of NPs. The formation of the protein corona in these NPs clearly facilitated their cellular internalization, probably by receptor mediated endocytosis (Verma, 2010), even when increasing their hydrodynamic size. The intrinsic capability of both types of NPs to be internalized by mammalian cells is indeed clearly advantageous, as it avoids the use of artificial methods for cell loading such as electroporation (Rojas-Chapana, 2004), direct microinjection (Wolff, 1990) or conjugation with cell penetrating or fusogenic molecules (Tkachenko, 2003). In contrast, dextran-coated NPs did not seem to induce any of these cellular effects, either at 2 or 6 days, likely due to a much reduced cellular uptake. Nevertheless, dextran-coated NPs have demonstrated high cytocompatibility, as some dextran-coated

formulations of NPs have been approved by the Food and Drug Administration of the USA for their medical use as contrast agents in magnetic resonance imaging of liver tumors (Colombo, 2012). These particles have also been suggested for cancer treatment by hyperthermia, in spite of their reduced cell internalization (Gordon, 1979).

Taking together, these results from studies on L929 fibroblasts indicate: (1) a concentration-dependent cytotoxicity mechanism, as previously found by other authors regarding NP exposure (Lehmann, 2010), (2) a critical role of NP surface charge in cell membrane interaction and posterior cell internalization, and (3) a significant influence of the original NP hydrodynamic size and surface charge on their cellular uptake. To this respect, those NPs charged at their surface (i.e., DMSA- and APS-coated NPs) were able to interact more actively first with charged culture media components (Verma, 2010), and then with the extracellular matrix, thus being retained longer times in the periphery of the cells and increasing their chances to be intracellularly loaded. This enhanced culture retention was indeed evidenced in the optical microscopy images, as a significant and concentration dependent amount of NPs were observed around cells at both 2 and 6 days for both types of surface-charged NPs. Additionally, their surface charge probably promoted interaction with cell membranes, also charged, thus contributing to their higher cellular internalization. These enhanced interactions are likely responsible for the phenomenon of cell aggregation illustrated under some culture conditions. The reduced cellular internalization of dextran-coated NPs is in agreement with that found for other iron oxide NPs coated with either dextran (Villanueva, 2009) or other neutral ligands such as poly(ethylene glycol) (Xie, 2007) or zwitterionic molecules (Agasti, 2009), in which a reduction of nonspecific interactions and binding to cell membranes was pursued for their satisfactory performance, for instance, as contrast agents. Last but not least, as the size has been found to greatly influence the NP cellular uptake and, therefore, their cytotoxicity (Verma, 2010; Soenen, 2011b), we also anticipated a significant contribution of NP size to the cell responses found. In this sense, the formation of the protein corona in DMSA- and APS-coated NPs seemed to promote their cellular uptake, despite their significant increase in hydrodynamic size. In an attempt to generate a more global overview of the interaction of these NPs with mammalian cells, we decided to investigate their cytocompatibility with

another cell type, e.g., human Saos-2 osteoblasts, as the cell type has also been evidenced as an important factor affecting NP cytotoxicity (Verma, 2010). These cells are obtained from a human osteosarcoma and, as tumor cells, they are more attractive for the future applicability of these NPs in cancer treatments by hyperthermia (Colombo, 2012). As previously performed for L929 fibroblasts, we first explored the induction of any morphological alterations by cell exposure to either DMSA-, APS- or dextran-coated NPs at similar concentrations used earlier (Figure 7.15). Importantly, no significant changes were observed for any condition, not even at the highest concentration of 0.25 mg ml^{-1}, other than a slight tendency to aggregate in Saos-2 cells exposed to APS-coated NPs at short culture times (1 day).
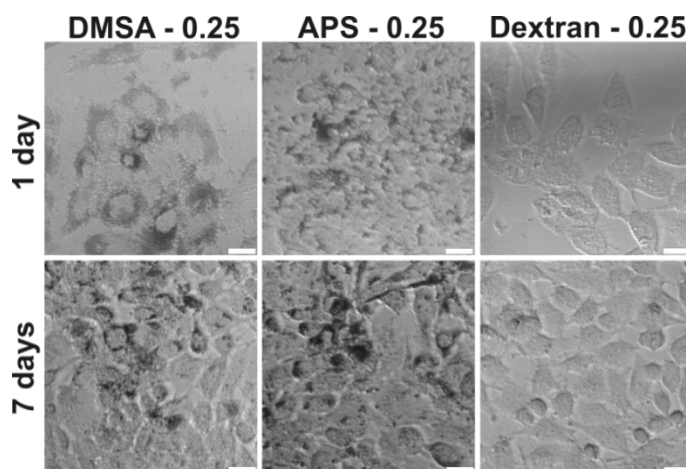
Figure 7.15. *Representative optical microscopy images illustrating differential intracellular uptake of NPs by Saos-2 osteoblasts depending on NP coating. Scale bars represent 25 μm in all images.*

A time-dependent NP intracellular uptake was also evidenced for all three NPs, thus indicating an active NP retention in the matrix around cells. Interestingly, a curious diversity in the degree of NP cellular uptake was appreciated within a particular culture condition. Specifically, some cells showed high NP loadings, preferentially concentrated in a perinuclear position, while others displayed almost negligible NP uptake. This intra-culture heterogeneity in NP cellular uptake has been already observed for other iron oxide NPs (Heymer, 2008). Previous studies have also revealed preferential localization of

inorganic NPs in lysosomal bodies arranged in a perinuclear fashion 24 h after internalization (Shukla, 2005; Soenen, 2010). This phenomenon of NP confinement in concrete subcellular areas at high concentrations is indeed an advantageous property of NPs for localized delivery applications over other systems such as free ions (Soenen, 2011b; Colombo, 2012). Nonetheless, some authors have related this favored perinuclear location to alterations in transcription and protein expression (Pisanic, 2007). According to the results with L929 fibroblasts, dextran-coated NPs were again significantly less internalized by cells than those coated with DMSA or APS.

Finally, to further confirm that the absence of morphological changes in Saos-2 osteoblasts after NP exposure correlated with no cell damage, we studied the viability of these cells over time by staining with calcein and EthD-1 (Figure 7.16).
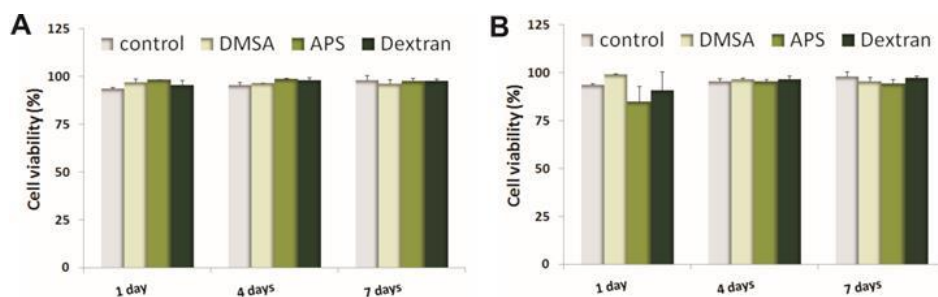
Figure 7.16. *Histograms illustrating cell viability percentages of Saos-2 osteoblast cultures after exposure to DMSA, APS or dextran coated NPs at two different concentrations: 0.05 mg/ml (A) and 0.25 mg/ml (B).*

We selected this procedure to test cell viability, rather than others such as MTT or Alamar blue, to avoid any interference of iron ions in the measurements. Cell viability in control Saos-2 cultures was evaluated in parallel for comparison (figure 7.17).
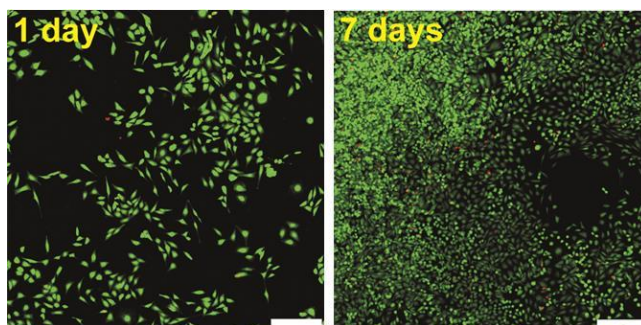
Figure 7.17. *Representative CLSM images of Saos-2 osteoblast control cultures at 1 and 7 days without exposure to any NPs. Cells were stained with the probes calcein and EthD-1 for monitoring cell viability over time. Scale bars represent 50 μm (left) and 250 μm (right).*

As it can be observed, highly viable cultures were obtained for all three NPs at 1, 4 and 7 days of culture, so no further cell cycle studies were considered necessary. Only the exposure to APS- and dextran coated NPs induced a slight and transitory reduction in cell viability at 1 day, no longer observed thereafter, which could be related to the transient generation of reactive oxygen species previously described for some inorganic NPs (Arbab, 2003). Careful inspection of these cultures further confirmed the concentration dependent NP uptake previously indicated (Figures 7.18, 7.19 and 7.20).

Interestingly, NPs internalized by cells were observed in these images as clear black circular dots intracellularly located (frequently in a perinuclear position as also evidenced by optical microscopy studies in L929 fibroblasts, Figure 7.14). In this sense, intracellular NP localization results are of great importance as they have been correlated with NP cytotoxicity (Brandenberger, 2010; Lehmann, 2010).

Dextran-coated NPs were again confirmed as those with lower cellular uptake. In contrast, DMSA- and APS-coated NPs seemed to show a very similar internalization, although further studies would be necessary to quantify this phenomenon. Nonetheless, the presence of some cells undergoing apoptosis 7 days after exposure to the highest concentration of DMSA-coated NPs (i.e., cell membranes carrying apoptotic bodies, see # symbols in Figure 7.18) may be indicative of a slightly inferior cytocompatibility of this type of NPs.
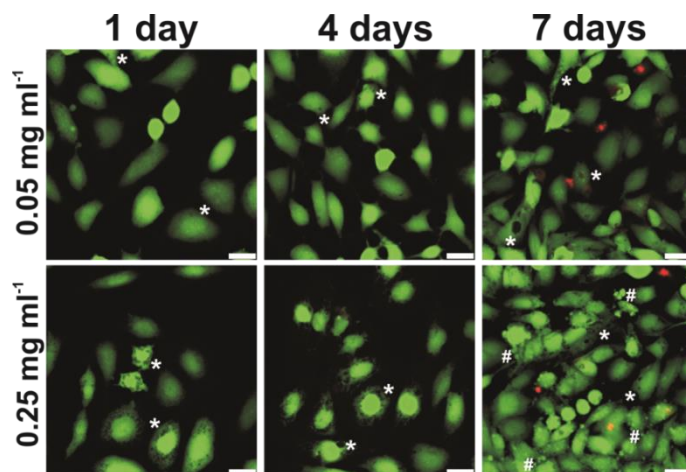
Figure 7.18. *Viability studies by CLSM of Saos-2 osteoblasts after exposure to 0.05 mg/ml or 0.25 mg/ml of DMSA-coated NPs. Evident intracellular uptake of NPs (*) was observed. Despite the high viability of the cultures, apoptotic cells were detected at high concentration of NPs and longer culture times (#). Scale bars represent 25 μm in all images.*
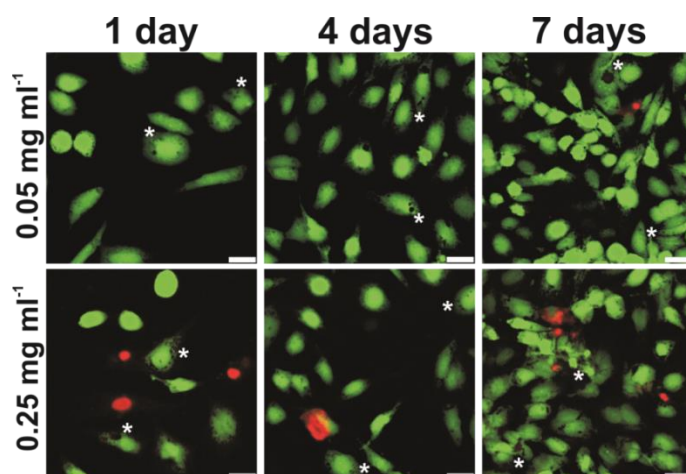
Figure 7.19. *Viability studies by CLSM of Saos-2 osteoblasts after exposure to 0.05 mg/ml or 0.25 mg/ml of APS-coated NPs. Evident intracellular uptake of NPs (*) was observed. Scale bars represent 25 μm in all images.*

Similarly, Pisanic et al. reported cytotoxic effects of DMSA-coated NPs on PC-12 cells (Pisanic, 2007). In general terms, the superior NP cytocompatibility found on Saos-2 cells in comparison to L929 fibroblasts is not surprising, as tumor cells present several characteristics that make them more resistant to NP-mediated cytotoxic effects (Soenen,

2011b), thus further supporting the relevance of differential and specific cell responses to nanomaterials.
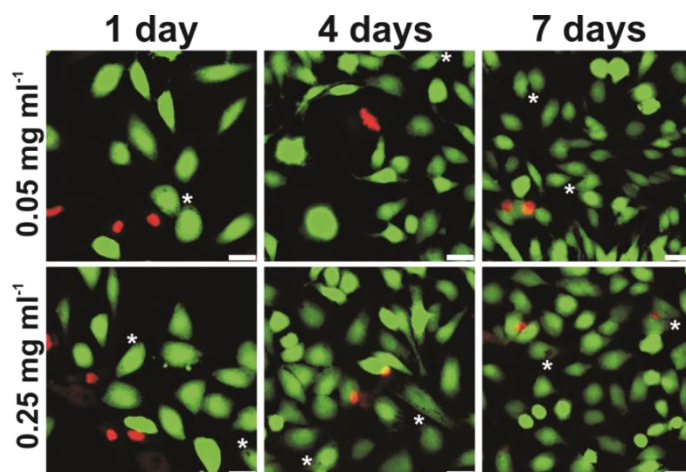
Figure 7.20. *Viability studies by CLSM of Saos-2 osteoblasts after exposure to 0.05 mg/ml or 0.25 mg/ml of dextran-coated NPs. Evident intracellular uptake of NPs (*) was observed. Scale bars represent 25 µm in all images.*

4. NANOCRYSTALS RESULTS

4.1. Magnetic properties of pure and bimetallic magnetite nanocrystals

The magnetic behavior of these nanocrystals before and after coating in powder form was investigated at room temperature (RT). Hysteresis parameters for magnetite nanocrystals of different samples are listed in table 7.6 and the corresponding curves are presented in figures 7.21 and 7.22.

All samples present a ferromagnetic behavior at room temperature, but this comportment is more pronounced for cobalt ferrite samples (ferromagnetism increases by increasing the proportion of Co). For pure magnetite nanocrystals, the saturation magnetization and coercivity values decrease as the particle size decreases. However, in the case of Co doped samples, these values increase by increasing the proportion of Co, in spite of the particle size decreases.
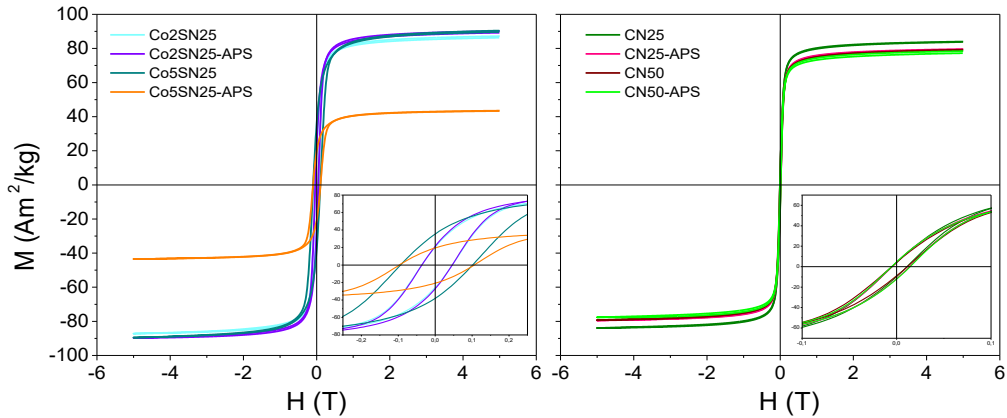
Figure 7.21. *Magnetization curves at room temperature for pure and Co bimetallic nanocrystals before and after APS coating.*
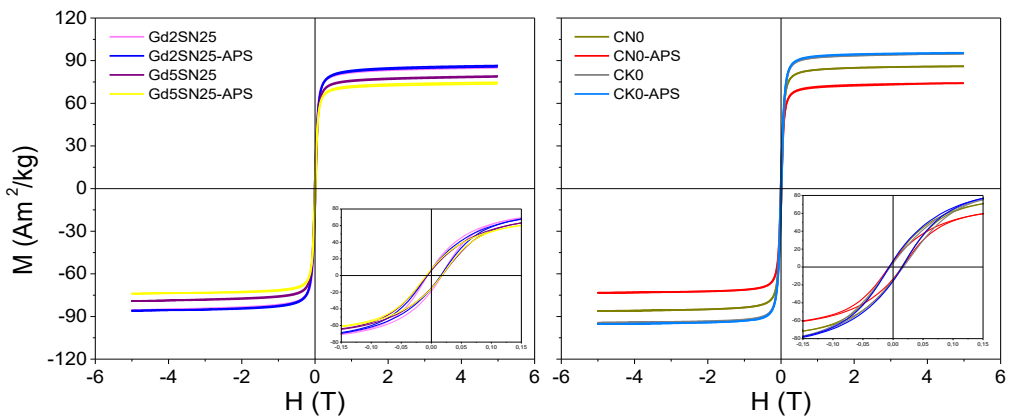
Figure 7.22. *Magnetization curves at room temperature for pure and Gd bimetallic nanocrystals before and after APS coating.*

The APS coating does not affect the value of saturation magnetization in any case except for the sample doped with 5% cobalt. The presence of the secondary metal affects the magnetic properties of the particles. In both Co and Gd samples, the coercivity and saturation magnetization increase (except in the sample Gd5SN25 saturation magnetization is slightly lower than its corresponding pure magnetite sample). On the other hand, the presence of the coating maintains or slightly reduces the values of Ms and Hc (Co5SN25-APS is the only case in which a dramatic decrease of Ms is observed).

Sample	TEM size (nm)	Ms (Am²/kg$_{sample}$)	Ms (Am²/kg$_{Fe3O4}$)	Hc (kA/m)
Co2SN25	30	88	88	33
Co2SN25-APS	30	91	92	33
Co5SN25	26	92	92	78
Co5SN25-APS	26	44	45	81
CN25	30	86	86	6
CN25-APS	30	81	84	7
CN50	26	81	81	7
CN50-APS	26	79	82	8
Gd2SN25	42	87	89	9
Gd2SN25-APS	42	87	91	9
Gd5SN25	51	80	86	10
Gd5SN25-APS	51	75	82	10
CN0	42	87	87	8
CN0-APS	42	76	78	9
CK0	53	96	96	9
CK0-APS	53	96	96	9

Table 7.6. *Hysteric parameters at room temperature for nanocrystals before and after coating process.*

4.1. Heating efficiency of pure and bimetallic nanocrystals

The heating power of selected pure and Co doped nanocrystals coated with APS is presented in figures 7.23. SAR values are obtained by fitting the experimental heating curves and normalizing to the iron mass (W per g Fe) as explain above. From these results it can be observed that in all cases, the highest SAR value is obtained when the samples are measured at 710 kHz and 24 kA/m $H_0 \cdot f = 1.7 \cdot 10^{10}$ Am^{-1}s^{-1} close to the recommended value $5 \cdot 10^9$ Am^{-1}s^{-1}. There is a dramatic reduction of the SAR values in all measured conditions when the samples are doped with Co, which could be related to the larger anisotropy of these samples (Hc = 40 mT). This reduction is more pronounced in the case

of 5% at Co, probably because this sample has a much more low saturation magnetization value.
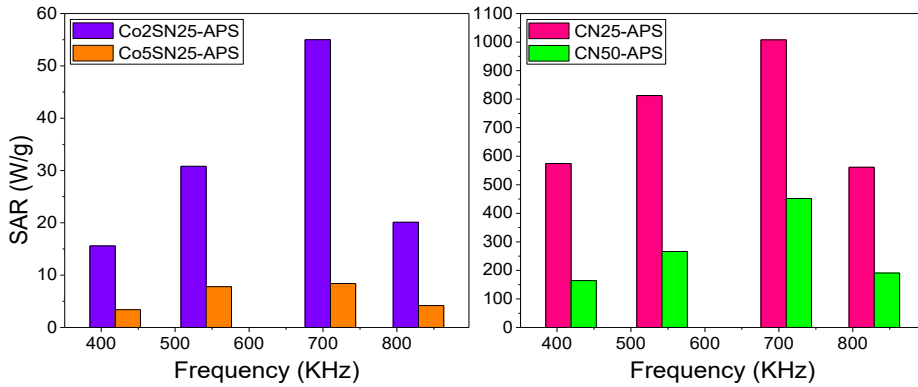
Figure 7.23. *SAR values of aqueous dispersions of selected pure and 2% at and 5%at Co doped samples coated with APS measured at 24 kA/m (419, 542 and 710 kHz) and at 20 kA/m (829 kHz).*
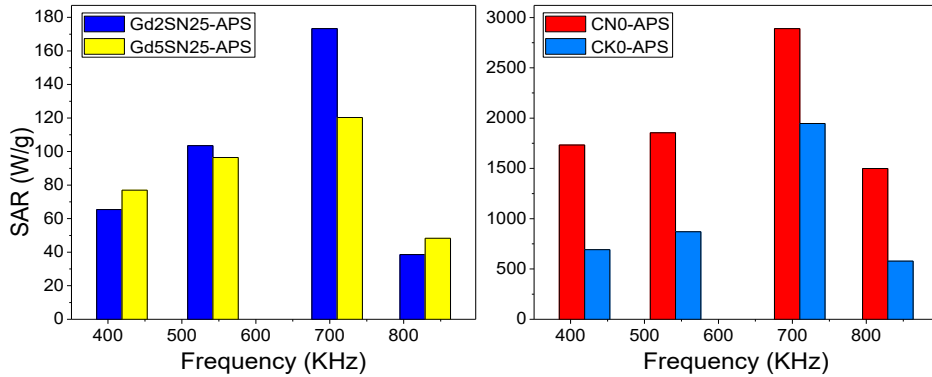
Figure 7.24. *SAR values of aqueous dispersions of selected pure and 2%at and 5%at Gd bimetallic samples coated with APS measured at 24 kA/m (419, 542 and 710 kHz) and at 20 kA/m (829 kHz).*

Figure 7.24 shows the heating power of selected pure and 2%at and 5%at Gd bimetallic nanocrystals coated with APS. In these cases, there is also a reduction of the SAR values for the samples with Gd, but not as accused as in the previous case. Samples with 5% Gd present lower SAR values than samples with 2% Gd, probably due to its bigger particle size (above 50 nm) and smaller Ms.

Both bimetallic samples with 2% Co and 2% Gd present a higher saturation magnetization value than the corresponding pure samples of the same size (from 80.8 to 90.9 Am^2/kg and from 75.5 to 87.2 Am^2/kg, respectively). In spite of this, the SARs values measured in all different conditions tested are lower for the bimetallic samples. These values are reduced by approximately 96% for the sample with 2% Co and 95% for the sample with 2% Gd. In the case of samples with 5% Co and 5% Gd saturation magnetization is reduced with respect to pure samples of the same size from 79 to 44 Am^2/kg and from 96 to 75 Am^2/kg, respectively. Likewise, the SAR values are also reduced by 98% for the sample with Co and 91% for the sample with Gd. The high heating capacity of the reference nanocrystals is due to the high crystallinity of the particles and their size and the magnetic field conditions that seems to be the best for these materials.

4.2. Relaxometric measurements

Pure and bimetallic nanocrystals (containing Co and Gd) with sizes of 26, 30, 42, 51 and 53 nm synthesized by oxidative precipitation and coated with APS have been evaluated as contrast agents in vitro by measurements of T_1 and T_2.

Study of the relaxometric properties was carried out by measuring the proton relaxation times (T_1 and T_2) at various concentrations of iron and calculating relaxivity values (r_1 and r_2). In the figure 7.25, it can be observed that both pure and bimetallic nanocrystals present maximum r_1 and r_2 measured values in the 26-30 nm core size range. Larger nanocrystals showed a decrease of both r_1 and r_2 values. Co2SN25-APS and Gd5SN25-APS samples show r_1 and r_2 values higher than pure magnetite samples of the same size. In all samples r_2 values, which are responsible for the negative contrast of the nanoparticles, are of the same order or greater than the than those for the different commercial contrast agents and to those reported for other superparamagnetic iron oxide nanocrystals synthesized by the decomposition method (Taboada, 2007; Roca, 2009) (Table 7.7).
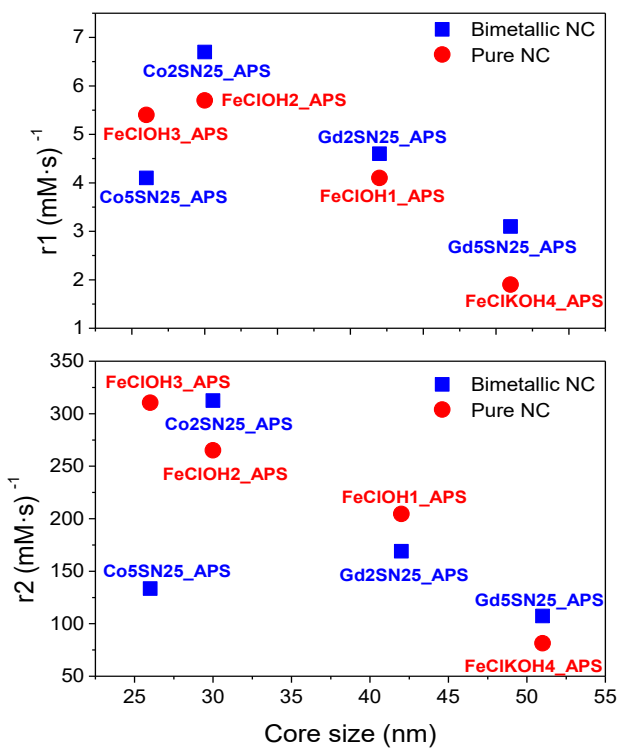
Figure 7.25. *r_1 and r_2 values vs. particle size for different APS coating samples.*

Samples	D_{TEM} (nm)	D_h (nm)	r_1 (mM^{-1}s^{-1})	r_2 (mM^{-1}s^{-1})	r_2/r_1
Co2SN25-APS	30	161.2	6.7	312.5	46.6
Co5SN25-APS	26	148.6	4.1	133.4	32.5
CN25-APS	30	121.8	5.7	265.2	46.5
CN50-APS	26	167.7	5.4	310.4	57.5
Gd2SN25-APS	42	306.4	4.6	168.9	36.7
Gd5SN25-APS	51	325.8	3.1	107.4	34.6
CN0-APS	42	293.0	4.1	204.6	49.9
CK0-APS	53	324.3	1.9	81.4	42.9

Table 7.7 *Summary of the relaxometric properties for pure and bimetallic nanocrystals prepared by oxidative precipitation.*

Another important factor is the value of r_2/r_1 effectiveness indicative of the contrast agent. In all cases our samples show higher values than corresponding to those published for commercial contrast agents (Corot, 2006).
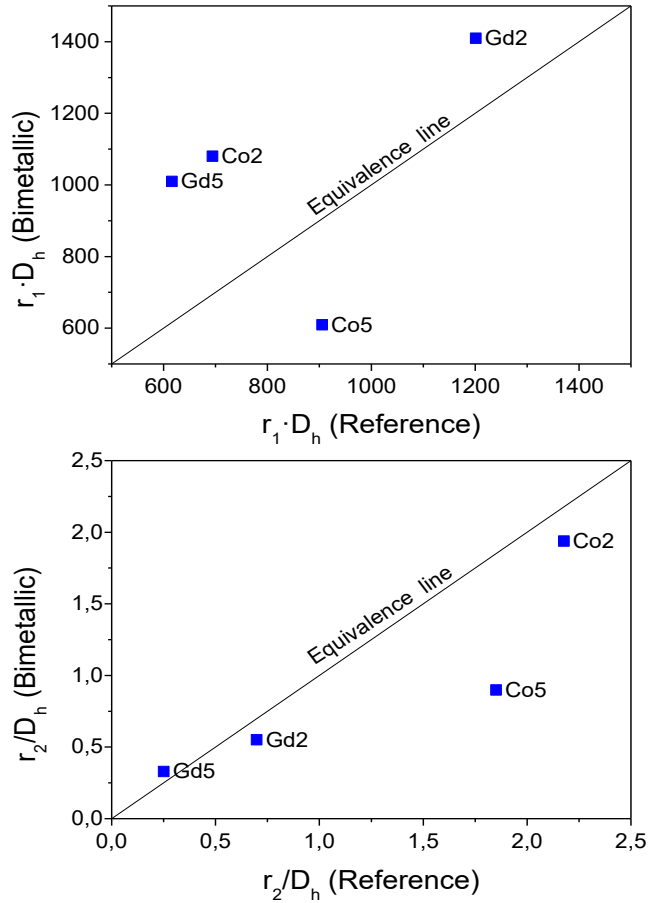
Figure 7.26. *Comparison of the relaxivities of bimetallic nanocrystals with their reference counterparts of the same crystallite size taking into account the aggregation.*

5. DISCUSSION

Once the separate study of the nanoparticles and the nanocrystals, we will compare both nanostructures coated with APS. Figure 7.27 shows the variation of the magnetic properties (Ms and Hc) with the size.
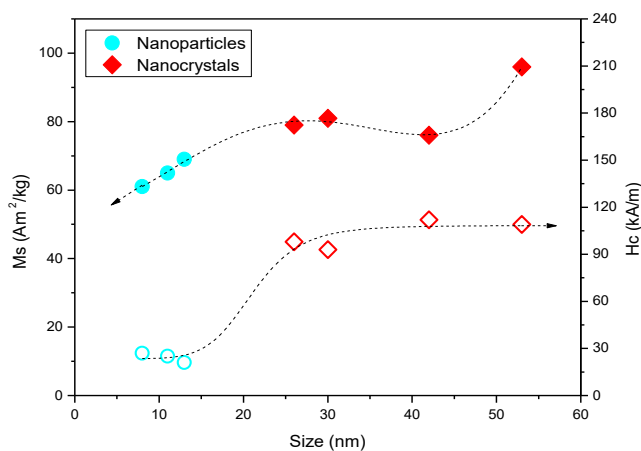
Figure 7.27. *Variation of saturation magnetization and coercivity values at room temperature with the particle size.*

It can be observed that the saturation magnetization increases as the particle size increases to reach a value close to that of the bulk material. However, the behavior of the coercivity is different in the case of nanoparticles and nanocrystals. The coercivity values decrease with increasing size for nanoparticles, while they increase slightly with increasing size in the case of nanocrystals. The deviating point (at around 40 nm) corresponds to the CN0 sample since the saturation magnetization after APS coating passes from 87 Am²/kg to 76 Am²/kg because it has been completely oxidized.

There is no difference in the average agglomeration number (AAN) of nanocrystals and nanoparticles being 250 magnetic cores per aggregate in average (Powers, 2006; Leconte, 2007). We understand then that this parameter is more dependent on the

dispersant and dispersion conditions than the magnetic properties of the material dispersed or the particle size.

Figure 7.28 shows the variation of the SAR values with the particle size for the nanoparticles and nanocrystals coated with APS. It is a comparison of NPs and NCs yields with respect to their biomedical applications and therefore we have chosen the optimal conditions for each material satisfying $H_0f < 5 \cdot 10^9$ A/m^{-1}s^{-1} for nanoparticles and $H_0f < 1.7 \cdot 10^{10}$ A/m^{-1}s^{-1} for nanocrystals. It can be seen that the SAR values increase with the particle size up to a maximum value (corresponding to particles of 42 nm) and from there it begins to decrease.
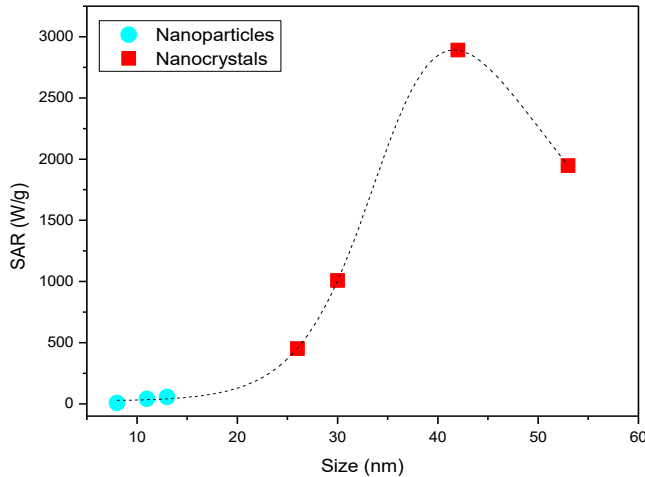
Figure 7.28. *Variation of SAR values with the particle size. Measures were carried out satisfying $H_0f < 5 \cdot 10^9$ A/$m^{-1}s^{-1}$ for nanoparticles and $H_0f < 1.7 \cdot 10^{10}$ A/$m^{-1}s^{-1}$ for nanocrystals.*

Finally, in figure 7.29 relaxometric values as a function of the particle size for nanoparticles and nanocrystals are represented. It can be clearly seen that r_1 values decrease linearly as the particle size increases. However, r_2 values increase with increasing size up to a maximum (corresponds to 20-25 nm approximately) and for larger sizes begins to decrease due to the increasing proportion of non superparamagnetic fraction in the NCs in the samples of bigger sizes.
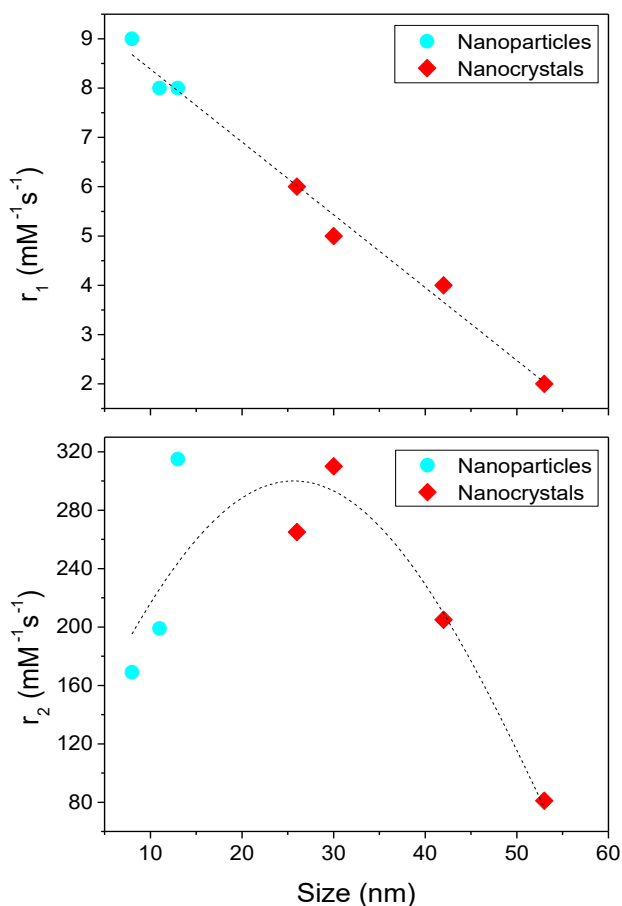
Figure 7.29. *Variation of relaxometric values with the particle size.*

6. CONCLUSIONS

When the NPs are dispersed in water, the SAR values are independent of NPs concentration in the range 6−300 mg/ml. The experimental SAR values as a function of field amplitude have a quadratic dependence, as expected from the model, for H_0 higher than 2.4 kA/m. The fitting of the SARs as function of field frequency allows obtaining the relaxation times τ_R which are about 10^{-7} s, close to the calculated Brown relaxation times τ_B. There exists an optimal particle size for NPs at which heating efficiency is maximal and

independent of media viscosity that in the case of these γ-Fe_2O_3 NPs is around 12 nm. Additionally, it is observed that SAR values decrease when going from a noninteracting to an interacting system by increasing concentration.

Pure magnetite nanocrystals coated with APS have much larger SAR values than nanoparticles with the same coating under the measurement conditions used. The number of magnetic cores per aggregate (AAN) is approximately constant for NPs and NCs independently of their magnetic properties or particle size.

Bimetallic Co and Gd NCs did not show improved SAR values with respect to their iron equivalents, and they present similar relaxometric properties than their iron pure equivalents except in the case of samples with 2% Co and 5% Gd behave better than their iron references.

L929 fibroblasts evidenced a higher sensitivity to surface-charged NPs. In contrast, on Saos-2 osteoblast cultures, only DMSA-coated NPs were able to induce some detectable cellular damage by activation of apoptotic cascades. Neutral NPs, as those coated with dextran, induced negligible cell damage, as their cellular internalization was also significantly reduced when compared to DMSA- and APS-coated NPs. Previous studies with NCs and Bi-NCs show similar results.

8

Conclusions

Different inorganic multifunctional nanostructures based on iron oxide have been successfully prepared by two synthesis methods in aqueous media: coprecipitation and oxidative precipitation. The nanoparticles prepared by coprecipitation are smaller and less crystalline than the nanocrystals obtained by oxidative precipitation. The experimental conditions have been tuned to obtain samples with a narrow size distribution in a range of sizes between 6 and 100 nm. Likewise, the effect of particle size on the magnetic and colloidal properties, the heating efficiency and the relaxometric properties has been studied for both nanoparticles and nanocrystals.

The study of the oxidative precipitation reaction kinetics allowed us to determine that the main factors that influence the final particle size of the magnetic nanocrystals are: dehydration of hydroxylated iron species, stability of the intermediate green rust and oxidation rates of iron (II). The differential stabilities of green rust as well as the dehydration and the Fe(II) oxidation processes are strongly influenced by cosmotropic environments and, finally, are responsible for the differences in magnetite particle sizes.

New bimetallic inorganic nanocrystals consisting of iron oxide (magnetite) and other metal integrated into the structure in different ways have been synthesized by oxidative precipitation maintaining the proportion of the second metal during the synthesis. The nanostructure formed in each case depends on the ionic radius and the solubility of hydroxide for the different metals. In particular, Bi and Gd formed core/shell NCs, Co formed a solid solution with magnetite and Au formed pudding-like NCs.

Both nanoparticles and nanocrystals were successfully coated with different types of ligands (APS, DMSA, dextran and oleic acid in the case of nanoparticles and APS in the case of nanocrystals). The coating process was in all cases very effective being the amount of coating lower for NCs than for NPs, due to the reduction on surface/volume rate. The coating process leads to a reduction in hydrodynamic size in the case of NPs below 100 nm and in the case of NCs bellow 200 nm. In addition, the coating increases the colloidal stability of the samples since IEP is shifted (which increases the pH stability range) and surface charge at pH 7 is provided (which would allow a later functionalization). It has

been found that the number of magnetic cores per aggregate (AAN) is approximately constant for NPs and NCs independently of their magnetic properties or particle size.

When the NPs are dispersed in water, the SAR values are independent of NPs concentration in the range 6−300 mg/ml. Due to dilution procedure, the magnetic interactions remain almost unchanged inside the cluster, whereas the interaction between clusters seems to make a negligible contribution to NPs heating capacity. The experimental SAR values as a function of field amplitude have a quadratic dependence, as expected from the model, for H_0 higher than 2.4 kA/m. The fitting of the SARs as function of field frequency allows obtaining the relaxation times τ_R which are about 10^{-7} s, close to the calculated Brown relaxation times τ_B. Larger NPs (13 and 14 nm) dispersed in agar show a decrease in the SARs when compared with NPs aqueous colloid of the same size, whereas the smaller particles (6, 8 and 11 nm) keep their heating efficiencies regardless of the media viscosity. There exists an optimal particle size for NPs at which heating efficiency is maximal and independent of media viscosity that in the case of these γ-Fe_2O_3 NPs is around 12 nm. Additionally, it is observed that SAR values decrease when going from a noninteracting to an interacting system by increasing concentration.

Pure magnetite nanocrystals coated with APS have much larger SAR values than nanoparticles with the same coating under the measurement conditions used. Bimetallic nanocrystals did not presented improved magnetic properties in general over pure NCs, only Co bimetallic NCs present an increase of the anisotropy. Regarding relaxometric properties, a linear variation of r_1 with the particle size can be observed, while the variation of r_2 presents a maximum for ~30 nm particle size. Only showed better properties as contrast agents 2% Co and 5% Gd samples and 20% Au sample showed a plasmon absorbance at 540 nm (close to the 532 nm of the common medical green laser), in spite of the quenching effect of magnetite.

Finally, it has been observed that changes in the physicochemical properties of magnetic NPs at their surface induced differential cell responses to NP exposure. L929 fibroblasts evidenced a higher sensitivity to surface charged NPs, with significant compromise of cellular integrity after exposure to DMSA and APS coated NPs. In

contrast, on Saos-2 osteoblast culture only DMSA coated NPs were able to induce some detectable cellular damage. Neutral NPs, as those coated with dextran, induced negligible cell damage, as their cellular internalization was also significantly reduced when compared to DMSA and APS coated NPs. On the other hand, these results reveal certain cell ability to detect and remember the original physicochemical properties of the NPs (hydrodynamic size and surface charge), as significantly different cell responses have been found for these three types of NPs (APS, DMSA and dextran coatings) even when dispersion in culture media made their physicochemical properties more comparable.

Se han obtenido diferentes nanoestructuras multifuncionales inorgánicas basadas en óxido de hierro mediante dos métodos de síntesis en medio acuoso: la coprecipitación y la precipitación oxidativa. Las nanopartículas preparadas por coprecipitación presentan un tamaño y una cristalinidad menores que los nanocristales obtenidos por precipitación oxidativa. Se han variado los parámetros experimentales para conseguir sintetizar muestras con distribuciones de tamaños estrechas en un rango de tamaños entre 6 y 100 nm. Así mismo, se ha evaluado el efecto del tamaño de partícula en las propiedades magnéticas y coloidales, en la efectividad de calentamiento y en las propiedades relaxométricas, tanto para nanopartículas como para nanocristales.

En el caso de la precipitación oxidativa, el estudio de la cinética de reacción nos ha permitido determinar que los principales factores que influyen en el tamaño final de partícula de los nanocristales magnéticos son: la deshidratación de las especies de hierro hidroxiladas, la estabilidad del "Green Rust" (intermedio de la reacción) y la velocidad de oxidación del hierro (II). Las diferencias en la estabilidad del GR, así como en los procesos de deshidratación y oxidación del Fe(II) están fuertemente influenciados por la cosmotropicidad del medio, y es el responsable final de los diferentes tamaños de partícula.

Se han sintetizado mediante precipitación oxidativa nuevos nanocristales bimetálicos inorgánicos constituidos por óxido de hierro (magnetita) y otro metal que se integra de diferentes formas en la estructura. Las nanoestructuras obtenidas en cada caso dependen tanto del radio iónico como de la solubilidad del hidróxido de cada uno de los diferentes metales. En concreto, el Bi y el Gd forman estructura tipo "core/shell", el Co se integra en la estructura formando una solución sólida y el oro forma estructuras tipo "pudding".

Tanto las nanoparticulas como los nanocristales se han recubierto satisfactoriamente con diferentes ligandos (APS, DMSA, dextrano y ácido oleico en el caso de las nanopartículas y APS en el caso de los nanocristales). El proceso de recubrimiento ha sido muy efectivo en todos los casos aunque la cantidad de

recubrimiento es menor para los NCs que para las NPs debido a que su relación superficie/volumen es menor. El proceso de recubrimiento conlleva una reducción en el tamaño hidrodinámico por debajo de 100 nm en el caso de las NPs y por debajo de 200 nm en el caso de los NCs. Además, el recubrimiento aumenta la estabilidad coloidal de las muestras ya que produce un desplazamiento del punto isoeléctrico (lo que aumenta el intervalo de pH en el que son estables las muestras) y aporta carga superficial a pH 7 (lo que permitiría posteriores funcionalizaciones). Por último, se ha comprobado que el número de núcleos magnéticos por agregado (NNA) es aproximadamente constante para NPs y NCs, independientemente de las propiedades magnéticas y del tamaño de partícula.

Cuando los NP se dispersan en agua, los valores de SAR son independientes de la concentración de NPs en el rango de 6-300 mg/ml. Debido al proceso de dilución, las interacciones magnéticas permanecen casi sin cambios dentro de los agregados, mientras que las interacciones entre los agregados parecen tener una contribución insignificante en la capacidad de calentamiento de las NPs. Los valores de SAR obtenidos en función de la amplitud del campo presentan una dependencia cuadrática, como se esperaba del modelo, para H_0 mayores que 2.4 kA/m. El ajuste de los valores de SAR en función de la frecuencia de campo permite obtener los tiempos de relajación τ_R que son de aproximadamente 10-7 s, próximos a los tiempos de relajación browniana calculados τ_B. Cuando se dispersan las NPs más grandes (13 y 14 nm) en agar se observa una disminución en los valores de SAR en comparación con los valores obtenidos para las muestras del mismo tamaño dispersas en agua. Sin embargo las partículas más pequeñas (6, 8 y 11 nm) mantienen su eficiencia de calentamiento independientemente de la viscosidad del medio. Por lo tanto, en el caso de NPs de γ-Fe_2O_3 existe un tamaño de partícula óptimo (aproximadamente 12 nm) para el cual la eficiencia de calentamiento es máxima e independiente de la viscosidad del medio. Adicionalmente, se observa que los valores de SAR disminuyen al pasar de un sistema que no interacciona a un sistema que interacciona por aumento de la concentración.

Por otra parte, los nanocristales de magnetita recubiertos con APS presentan valores de SAR mucho mayores que las NPs con el mismo recubrimiento en las condiciones de medida utilizadas. En general, los NCs bimetálicos no presentan mejores

propiedades magnéticas que los NCs puros, solamente las muestras con Co presentan un aumento de la anisotropía. En cuanto a las propiedades relaxométricas se observa una variación lineal de r1 con el tamaño de partícula, mientras que la variación de r_2 presenta un máximo para un tamaño de partícula de aproximadamente 30 nm. Únicamente las muestras con 2% de Co y 5% de Gd muestran mejores propiedades como agentes de contraste. Además, la muestra con 20% de Au presenta una banda de absorción a 540 nm correspondiente al plasmón superficial del Au (próxima a 532 nm correspondiente al máximo de absorción del láser verde de uso común en medicina), a pesar de la interferencia con la magnetita.

Finalmente, se ha observado que los cambios en las propiedades fisicoquímicas de la superficie de las NPs inducen diferentes respuestas celulares. Los fibroblastos L929 evidenciaron una mayor sensibilidad a la carga superficial de las NPs, con compromiso significativo de la integridad celular después de la exposición a NPs recubiertas con APS y DMSA. Por el contrario, en el cultivo de osteoblastos Saos-2, sólo las NP recubiertas con DMSA fueron capaces de inducir un daño celular detectable. Las NPs neutras recubiertas con dextrano, indujeron un daño celular insignificante, debido a que su internalización celular también se redujo significativamente en comparación con las NPs recubiertas con APS y DMSA. Por otra parte, estos resultados revelan cierta capacidad celular para detectar y recordar las propiedades fisicoquímicas originales de las NPs (tamaño hidrodinámico y carga superficial), ya que se han encontrado respuestas celulares significativamente diferentes para estos tres tipos de recubrimientos (APS, DMSA y dextrano) incluso cuando la dispersión en el medio de cultivo confiere a las NPs propiedades fisicoquímicas más comparables.

Appendix

I

Characterization methods

1. X-RAY DIFFRACTION (XRD)

The crystal structure of the samples was identified by X-ray power diffraction performed in a Bruker D8 Advance diffractometer with an energy discriminator detector (SolX) using CuKα radiation (λ = 1.5406 Å).

To carry out the measurement about 50 mg of the powder sample was taken and deposited on a square glass slide. The patterns were collected within 10º and 70º in 2θ. The XRD spectra were indexed to an inverse spinel structure. The average particle size was calculated by Scherrer's formula (equation I-1) using the full width at half maximum (FWHM) of the more intense X-ray diffraction peak.

$$D_{XRD} = \frac{k\lambda}{B_C \cdot cos\theta} \qquad \text{(I-1)}$$

where k is a constant depending on the experimental conditions and whose value is 0.89 for isometric crystallites , λ is the wavelength of the X-ray source, which in this case is the CuKα line (1.5406 Å), B_C is the corrected half width and θ is the angle at which the diffraction occurs in degrees. D_{XRD} is the average dimension of the crystal, normal to the reflection planes, that is, with this parameter the number of cells coherently diffracting is measured. In this way, only the crystalline part of the particles is taken into account.

The calculations were made using the APD (Phillips) computer program, the error in the crystallite sizes obtained by use of the Scherrer's equation is estimated to be ±0.1 nm, which is related to the small broadening produced for our samples in comparison to the instrumental line width (Δ2θ = 0.11º).

2. TRANSMISSION ELECTRON MICROSCOPY (TEM)

Transmission electron microscopy has allowed the structural and morphological characterization of the samples by acquiring images of the nanoparticles and nanocrystals

prepared. From these images it was possible to calculate the size and size distribution, in addition to displaying its shape and aggregation state.

Particles size and shape were studied using a JEOL JEM-2000 FX microscope operated at 200 keV and a JEOL JEM-1010 microscope operated at 100 keV and equipped with a Gatan Orius 200 SC digital camera. TEM samples were prepared by placing one drop of a dilute particle suspension in water or ethanol on an amorphous carbon-coated copper grid and evaporating the solvent at room temperature and pressure.

The mean particle size and distributions were evaluated by measuring the largest internal dimension of, at least, 300 particles. Afterwards, the data were fitted to a log-normal distribution (equation I-2) obtaining the mean size (D_{TEM}) and the standard deviation (σ).

$$f(D) = \frac{1}{\sigma D \sqrt{2\pi}} exp\left[-\frac{(lnD - D_{TEM})^2}{2\sigma^2}\right] \qquad \text{(I-2)}$$

Atomic resolution scanning TEM images and HAADF images were acquired in a Nion UltraSTEM200 equipped with a spherical aberration fifth-order corrector and a Gatan Enfinium EEL spectrometer. A Nion UltraSTEM100 operated at 60 kV and equipped with a Nion aberration corrector and a Gatan Enfina spectrometer was also used (Electron Microscopy Group of Materials Science and Technology Division of Oak Ridge National Laboratory, Dr. Matthew F. Chisholm and Dra. Maria Varela). In STEM mode, the electron beam is converged into a point which scans over the sample in a raster. The advantage of STEM is that the user has far greater control over the placement of the electron beam, allowing for nanometer scale precision. It provides elemental composition and crystal information at atomic scale. For nanoparticle characterization, STEM mode allows for the simultaneous imaging and collection of data from a series of points across an individual particle, which allows the user to map elemental distributions for an individual particle.

Annular dark-field imaging is a method of mapping samples in a scanning transmission electron microscope (STEM). These images are formed by collecting

scattered electrons with an annular dark-field detector. In traditional dark-field imaging (in a parallel beam mode, not STEM), an objective aperture is placed in the diffraction plane so as to only collect electrons scattering through that aperture, avoiding the main beam. By contrast, in STEM mode the optics distinguishing between dark and bright field modes is positioned further downstream, after the converged beam has interacted with the specimen. Consequently, the contrast mechanisms are different between conventional dark field imaging and STEM dark field. An annular dark field detector collects electrons from an annulus around the beam, sampling far more scattered electrons than can pass through an objective aperture. This gives an advantage in terms of signal collection efficiency and allows the main beam to pass to an EELS detector, allowing both types of measurement to be performed simultaneously. Annular dark field imaging is also commonly performed in parallel with Energy-dispersive X-ray spectroscopy acquisition, and can be also done in parallel to bright-field (STEM) imaging. An annular dark field image formed only by very high angle, incoherently scattered electrons — as opposed to Bragg scattered electrons — is highly sensitive to variations in the atomic number of atoms in the sample (Z-contrast images). This technique is also known as high-angle annular dark-field imaging (HAADF) (Jesson, 1995; Pennycook, 2009).

Electron energy loss spectroscopy (EELS) is the analysis of the energy distributions of electrons that have passed through the sample, these are electrons that will have loss no energy (ie, have passed straight through) or have suffered inelastic collisions. Energy losses like these can reveal aspects of the chemistry of the sample atoms, which can give us information on their valence states and bonding modes. In EELS, an electron that has ionized an atom within the sample will have lost the energy associated with that ionization. As the energy required to ionize an electron from an element is unique to that element and also to the shell that the electron was ionized from, analysis of the distribution of energy losses of the electrons that pass through a sample provides key information on the elements that are present in a sample. An ionization event will be represented by a feature known as an 'edge' in the EELS spectrum, and comparison to literature values allows the identification of the elements present in a sample. In our cases,

we compared the spectrum edges with O K (532 eV), Fe L (708 eV), Co L (779 eV) and Gd M (1185 eV) bibliography edges.

The electron diffraction pattern of the nanoparticles was obtained in a FEI Tecnai T20 microscope. Diffraction patterns arise when electrons are scattered from crystallographic planes within the specimen, which are subsequently transmitted at a variety of angles. These scattered electrons are focused by the objective lens, resulting in a diffraction pattern in the back focal plane of the objective lens. When operated in diffraction mode, a selected area aperture can be inserted into the image plane of the objective lens. This has the effect of excluding all the electrons apart from those which pass through the area defined by the selected area aperture. The advantage of selected area electron diffraction (SAED) is that diffraction patterns can be collected from specific regions (or even specific nanoparticles) within the sample, meaning that the diffraction data can unambiguously be ascribed to the images that we see. Information on phase purity, crystalline orientation and crystallite size can be obtained from diffraction.

3. INFRARED SPECTROSCOPY (FTIR)

Infrared spectroscopy has been used in the characterization of the coating present on the nanoparticle surface through the identification of the functional groups.

Fourier transform infrared spectra of the samples were recorded in the range of $4000 - 250$ cm^{-1} in a Bruker IFS 66V-S. The resolution of the spectrometer measurements is 2 cm^{-1}. Samples were prepared by diluting the dried powders in KBr at 2% by weight and pressing into a pellet. Static pressure was applied to the powder sample until the pellet made a clear disc.

4. THERMAL ANALYSIS (TG)

Thermogravimetric analysis allows quantification of the amount of coating present on the particle surface.

212

Simultaneous TG and DTA analysis were performed in a Seiko TG/DTA 320U thermobalance, whose temperature scanning range is from room temperature to 1100ºC. For this work, 10-20 mg of sample were heated from room temperature to 900ºC at 10ºC/min under an air flow of 100 ml/min. Platinum pans were used and α-Al_2O_3 was used as reference.

5. CHEMICAL ANALYSIS

Iron, bismuth, gadolinium, cobalt and gold determination were carried out on an Inductively Coupled Plasma – Optical Emission Spectrometry (ICP-OES) apparatus from Perkin Elmer, model OPTIME 2100DV. The wavelengths used for iron, bismuth, gadolinium, cobalt and gold determination were 238.204, 190.171, 376.839, 228.616 and 190.171 nm respectively. For the iron determination an extra wavelength was used (239.562 nm) to control the interferences from other elements at the standard wavelength. For an appropriate determination is necessary to digest the nanoparticle dispersion prior to analysis. These digestions were carried out as follows: an aliquot of sample (typically 20 µl) was mixed with 1 ml of HCl 15 M under stirring at room temperature until complete digestion is obtained. Then, distilled water is added until the iron concentration is around 10 ppm. For the different elements determination, the samples were compared with a calibration curve plotted from a set of standards of known concentration.

6. DINAMIC LIGHT SCATTERING (DLS)

This technique has allowed the colloidal characterization of suspensions, it means, the size of the colloidal entities formed by the nanoparticles in the dispersion (the hydrodynamic diameter D_H) and their surface charge (Z potential) as a function of pH, which provides information about the forces involved in stabilizing colloids.

A ZETASIZER nano ZS by Malvern Instruments was used to determine both, the hydrodynamic diameter and the Z potential. This device is equipped with a He-Ne laser (4

mW, 633 nm), an automatic laser attenuator (transmission from 100% to 0.0003%) and an avalanche photodiode detector. The mean hydrodynamic diameter of the aggregates was measured thanks to non-invasive back scatter (NIBS) technology and dynamic light scattering (DLS) which allow measure sizes from 0.6 nm to 6 µm.

For measurement of hydrodynamic diameter it is necessary to have a stable suspension of particles in water. To minimize the effect of scattering multiple, each sample was measured at three different concentrations from 0.5 mgFe/ml to 0.1 mgFe/ml. Hydrodynamic diameter measurements were presented in intensity mode.

The Z potential of the aqueous dispersions was measured by combination of laser Doppler velocimetry and Phase Analysis Light Scattering (PALS) techniques which provide enough resolution to measure samples from 5 nm to 10 µm. The ZETASIZER nano ZS of Malvern Instruments calculates the zeta potential by determining the electrophoretic mobility and then applying the Smoluchowski approximation of the Henry equation. All measurements were carried out at room temperature, using 0.01 M KNO_3 as background electrolyte (which allows maintaining a constant ionic strength) and HNO_3 and KOH to change the pH of the suspensions.

7. UV-VIS SPECTROSCOPY

Optical properties of the gold bimetallic nanoparticles were measured with a Varian Cary Bio UV- Visible spectrophotometer over the wavelength range from 450 to 700 nm. The samples were dispersed in water at 0.1 mgFe/ml and placed on a 1 mm wide quartz cuvette.

The spectral range of the apparatus is 190-1100 nm. The scanning rate can be controlled between 0.01 nm/min and 2400 nm/min. The resolution of the equipment is ≤ 1.5 nm and the precision is ± 0.5 to 541.94 nm. The computer is connected to a computer with software (cary WinUV) that allows to control and process the data.

8. MAGNETIC MEASUREMENTS

Magnetic characterization of the samples was carried out in a Quantum Design MPMS-5S SQUID magnetometer (smaller nanoparticles) (Instituto de Magnetismo Aplicado, Dra. Patricia de la Presa) or in a vibrating sample magnetometer MagLabVSM by Oxford Instruments (larger nanocrystals).

In the first case, the magnetic characterization of 50 μL iron oxide suspensions at 2.5, 5 10, 20, 50 and 80 mg Fe/ml or 75 μl iron oxide suspensions at 70 mg Fe/ml was carried out in special closed nylon holders. Magnetization curves with a maximum applied field of 50 kOe have been measured at 5, 10 and 250 K. Thermal dependence of the magnetization under zero field cooled (ZFC) and field cooled (FC) conditions, from 5 to 300 K, has been measured by applying 50, 100 and 150 Oe magnetic fields. In some cases the maximum temperature was 250 K in order to maintain the colloid frozen during the magnetic characterization. Diamagnetic contribution from water/hexane is subtracted from the experimental data (in the samples with larger iron oxide content, the diamagnetic contribution from water at high fields can be discarded). In the case of ZFC-FC curves, the blocking temperature T_B was determined from the maximum of the ZFC curve.

In the second case, samples were measured in solid state. For the measurement of powders, the samples were dried in an inox-coated oven at 50º C 24 h. Afterwards samples were accurately weighed and fitted into the gelatin sample holder. Hysteresis loops of the powder samples were measured at RT at a rate of 5 kOe·min^{-1}. The saturation magnetization was evaluated by extrapolating to infinite field the experimental data obtained in the field range where magnetization increases and it can be approximated to a 1/H law.

9. HEATING EFFICIENCY

Heating capacities of nanoparticles in colloidal form have been measured with the commercial system Magnetherm® 1.5 (Nanotherics) (Instituto de Magnetismo Aplicado, Dra. Patricia de la Presa). The system (figure I-1) is provided with 2 coils of different turns

and length and 5 different capacitors arrays that constitute 10 circuits with different resonant frequency, which allows studying the effect of magnetic field frequency on the heating response of the NPs. The resonance frequency of the equipment has been tuned for each measurement. Mean magnetic field inside the coil has been measured with a secondary two turns coil with a cross-sectional value close to that of the sample holder (6.2 mm diameter). A half-length of the sample holder was made to coincide with the maximum value of the magnetic field. The volume sample suspension was 1 mL. The temperatures of the coils have been controlled through a close circuit of water maintained at 16 °C with a cryostat bath. In these conditions, a water sample has been measured under the experimental conditions, and it has been checked that water temperature does not increase in the sample space.

Figure I-1. *Magnetherm 1.5 (Nanotherics) device.*

The temperature of NPs suspension has been measured with a fiber optical thermometer and registered with a computer. The temperature sample has been controlled and stabilized to room temperature before each measurement. Prior to turning the magnetic field on, the sample temperature was recorded for about 30 s in order to ensure thermal stability and to have a baseline for the calculation of the SARs values. As the field is turned on, the temperature increase is measured either during 300 s or up to 80 °C for aqueous colloids and 40 °C for hexane colloids, well below the corresponding boiling temperatures 100 and 69 °C, respectively.

As the Fe concentrations are in the range 1−10 wt %, the SAR values can be calculated using equation I-3.

$$SAR = \left(\frac{C_{liq}}{c_{Fe}}\right)\left(\frac{\Delta T}{\Delta t}\right) \tag{I-3}$$

where C_{liq} is the specific heat capacity of water (4.185 J/(g K)) or hexane (2.28 J/(gK)) and c_{Fe} is the Fe weight concentration in the colloid (Gonzalez-Fernandez, 2009). By performing a linear fit of data (temperature versus time) in the initial time interval, the slope $\Delta T/\Delta t$ can be obtained. As the measurements are performed in nonadiabatic conditions, the curve slopes $\Delta T/\Delta t$ are fitted only in the first few seconds after turning the magnetic field on. The time range is selected such as the slope is maximum, typically during the first 30 s (Natividad, 2009). Then, the SARs values were obtained by fitting the experimental heating curves which were normalized to the iron mass (W/gFe).

The 8, 11, and 13 nm NPs have been measured as a function of iron concentration (c_{Fe}) at H = 7.5 kA/m and f = 522 kHz. The SAR values of systems consisted of 8 and 13 nm particles coated with OA and APS are measured as a function of iron concentration (c_{Fe}) at H = 200 Oe and f = 110 kHz. By starting with the highest concentrated sample, we performed subsequent measurements by diluting the samples in consecutive steps with milli-Q water for aqueous colloid and hexane for organic colloid and sonicating for several minutes.

The effect of size on the SARs has been also investigated. Particles with diameter d= 6, 8, 11, 13, and 14 nm have been measured at H_0 = 7.5 kA/m and f = 522.7 kHz. The concentration 50 mg/mL has been chosen for this part of the experiment because it is high enough to obtain heating curves that can be properly fitted and low enough to discard the influence of the NPs specific heat capacities on the solvent.

The magnetic colloid has been also characterized as a function of field amplitude for particles dispersed in water or immobilized in an agar gel in order to investigate the mechanism involved in the heating process. For this purpose, 50 mg/mL of the colloidal suspension in water or agar at 1 wt % was measured at 522.7 kHz with the field amplitude

varying from 2.4 to 7.5 kA/m for the 13 and 14 nm particle sizes and from 4 to 7.5 kA/m for the rest. The temperature of the agar suspension was not allowed to exceed 50 °C to avoid the melting of agar. Due to temperature increase in the colloid depends on NPs concentration, a concentration of 100 mg/mL of the 13 nm NPs aqueous colloid was used to get experimental data at very low fields (lower than 2.4 kA/m).

The measurements were performed at 522.7 kHz with the field amplitude ranging from 0.8 to 7.5 kA/m with a 0.4 kA/m step. The SAR field frequency dependence was measured at $H_0 = 4$ kA/m amplitude field for the 8, 11, and 13 NPs sizes at frequencies 166.0, 330.9, 468.8, 522.8, 626.7, and 739.2 kHz, and the concentration was $c_{Fe} = 50$ mg/mL.

APS-coated NPs were measured at $H_0 = 7.5$ kA/m and f = 522.3 kHz. The concentrations was $c_{Fe} = 8$ mg/mL for the 8 and 13 nm NPs sizes.

All the SAR values were obtained under experimental condition $H_0 f < 5 \times 10^9$ A m^{-1} s^{-1}, a limit at which an unwanted nonselective heating of both cancerous as well as healthy tissue due to generation of body eddy currents may occur (Hergt, 2007).

The concentrations used for hyperthermia measurements of APS and OA coated nanoparticles in the study of particle interactions were $c_{Fe} = 20$, 10, 7.5, 5, and 2.5 mg/mL. It should be mentioned that in the case of APS-coated nanoparticles, it has not been possible to obtain long time stable aqueous colloid for concentration larger than 20 mg/mL. For the maximum iron concentration, 20 mg/mL, the weight concentration is 2% wt; then, it is assumed that the heat capacity of the colloid is close to the heat capacity of the liquid carrier for all measurements.

Heating capacities of aqueous dispersions of APS coated magnetic nanocrystals were measured using the commercial ac field applicator DM100 by nanoscale Biomagnetics© (Instituto de Nanociencia de Aragon, grupo de Nanotecnologia y Apoptosis, Dr. Jesús Martínez de la Fuente) in the frequency range from 416 to 828 kHz and magnetic fields (H_0) of 25.2 mT to 30 mT at an iron concentration of 5 mg mL^{-1}. Experiments were carried within a thermally-insulated working space of about 1 cm^3, using a closed container of 0.5 mL volume conditioned for measurements in the liquid

phase. The temperature of the colloids is measured using an optic fiber sensor incorporated in the equipment and registered using a computer (figure I-2). Prior to turning the magnetic field on, the sample temperature is recorded for about 30 s to ensure thermal stability and to have a baseline for the calculation of the specific absorption rate (SAR). As the field is turned on, the temperature increase is measured during 300 s. By performing a linear fit of the data (temperature versus time) in the initial time interval, we can obtain the slope $\Delta T/\Delta t$ in the first few seconds after turning the magnetic field on. The time range is selected such as when the slope is maximum, typically during the first 30 s. Then, SAR values (W per g_{Fe}) can be calculated using equation 3 where C_{liq} is the specific heat capacity of water (4.185 J g^{-1} K^{-1}) and c_{Fe} is the Fe weight concentration in the colloid.

Figure I-2. *Commercial ac field applicator DM100 by nanoscale Biomagnetics©.*

The intrinsic loss power parameter (ILP), defined by equation I-4, has been proposed in order to compare heating efficiencies obtained under different experimental conditions of field and frequency.

$$ILP = \frac{SAR}{f \cdot H_0^2} \tag{I-4}$$

10. RELAXOMETRIC MEASUREMENTS

In order to evaluate the efficiency of the suspensions as contrast agents for MRI measurements of the relaxation times of water protons (both T_1 and T_2) in the presence of magnetic nanoparticles were carried out in a time-domain NMR benchtop system MINISPEC MQ60 (Bruker) (Unidad de Imagen Avanzada CNIC Prof. Dr. Jesus Ruiz Cabello and Dr. Fernando Herranz Rabanal) at 37 °C and 1.5 T using standard methods.

The relaxivities r_1 and r_2 (s^{-1} $mMFe^{-1}$) were obtained from the measured longitudinal and transversal relaxation times T_1 and T_2 of gelified (agar 0.5%) dispersions of samples at concentrations below 1 mM Fe from the linear plot of $1/T_1$ and $1/T_2$ as a function of the concentration.

For the measurement of T_1 a pulse sequence called "Inversion Recovery" has been used. In this sequence, after applying the constant magnetic field of 1.5 T, a 90 ° pulse is emitted in the z direction followed by another 180º pulse in the same axis and the magnetic moment of the nuclei is measured in the z axis. These pulses are separated by a time τ.

For the measurement of T_2 a pulse sequence called "Carr-Purcell-Maiboom-Gill (CPMG)" has been used. After application of the 1.5 T magnetic field a 90º pulse is applied on the on the x axis which is followed, after a time τ, of a 180 ° pulse in the y axis. This pulse is followed by another 180º pulse on the same axis after passed twice the time τ. Finally the signal of the magnetic moment of the nuclei is recorded on the x and y axis which decreases with time. During the measurements separation of the 90º and 180º pulses (τ) is optimized whose value can be obtained from equation I-5.

$$\tau = \frac{10 \cdot T_{2_{estimated}}}{dp \cdot 2(dm + 1)} \tag{I-5}$$

where *dp* is the number of points to adjust the curve (depending on the relaxation time of each sample were used 30 points for low T_2 and 100 points for high T_2) and *dm* is the number of unadjusted "echoes" (whose value has fixed constant for all measurements).

11. CELL CULTURES

Experiments were performed in the Instituto de Ciencia de Materiales de Madrid under the supervision of Dr. María C. Serrano.

Prior to cell culture, Fe_2O_3 NP suspensions were sterilized under UV radiation for 20 min. Two different cell types were tested: murine L929 fibroblasts and human Saos-2 osteoblasts. Both cell types were seeded at the appropriate density that guaranteed subconfluence prior to NP addition, depending on their respective growth rates. Specifically, L929 fibroblasts were seeded at a density of *ca.* 4000 cells per well (5000 cells per cm²), whereas 5000 cells per well were seeded in the case of Saos-2 cells (*ca.* 6500 cells per cm²). 48-well tissue culture polystyrene plates (TCP) were used in all experiments.

The working volumes of 500 ml and 2 ml were used for 48-well and 6-well plates, respectively. Two days after cell seeding, cell cultures were exposed to three different types of NPs: DMSA-, APS- and dextran-coated NPs. For both cell types, a range of NP concentrations was tested. Particularly, three different NP doses were evaluated: 0.25, 0.10 and 0.05 mg of iron per ml of solution (equivalent to 31, 12.5 and 6.25 applied pg of iron per cell for L929 fibroblasts and 25, 10 and 5 applied pg of iron per cell for Saos-2 cells, respectively, with respect to the initial cell seeding density). After exposure to NPs for 24 h, the excess NPs were eliminated and culture media were replaced. Culture media consisted of DMEM supplemented with fetal bovine serum (10%), streptomycin (100 UI ml⁻¹), penicillin (100 UI ml⁻¹), and L-glutamine (1 mM) (Lonza).

Cultures were maintained at 37 °C in a sterile incubator under a CO_2 (5%) atmosphere for different times. Culture media were replaced every other day. Cell cultures were monitored over time by using an Axiovert CFL-40 optical microscope with an Axiocam ICC-1 digital camera coupled (Zeiss).

12. CELL VIABILITY STUDIES

Experiments performed in the Instituto de Ciencia de Materiales de Madrid under the supervision of Dr. María C. Serrano.

To test cell viability, cell cultures were analyzed by using a Live/Dead® kit according to manufacturer's instructions (Life Sciences). This kit is based on the use of calcein and ethidium homodimer-1 (EthD-1). Calcein is a non-fluorescent cell permeable dye that gets converted into a strong green light emitting compound after contact with intracellular esterases and so retained inside live cells. In contrast, EthD-1 is a DNA intercalating agent that penetrates cell membranes in dead cells and emits orange/red fluorescence when inserted into the DNA double helix. After staining, samples were visualized by using a Leica SP5 confocal laser scanning microscope (CLSM). The fluorescence of both probes was excited by an argon laser tuned to 488 nm. After excitation, emitted fluorescence was separated by using a triple dichroic filter 488/561/633 and measured in the range 505–570 nm for green fluorescence (calcein) and 630–750 nm for red fluorescence (EthD-1). To quantify cell viability, the number of live (green) and dead (red) cells was counted and averaged from the confocal images acquired.

II

Weight increase by oxidation

The oxidation of the magnetite takes place according to the equation:

$$Fe_3O_4 + \frac{1}{4}O_2 = \frac{3}{2}Fe_2O_3$$
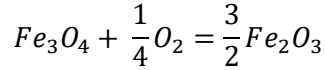
This implies that 1 mol of magnetite (231.5 g) gives 3/2 mol of maghemite (239.5 g), which represents a weight increase of 0.0345 g per gram of magnetite (3.45%).

The problem to be solved is what weight gain occurs when there is a surface layer thickness of $d_{magnetite}$ (nm) that is already oxidized in the nanocrystal of D initial size. We will consider densities of magnetite and maghemite 5.2 and 4.9 g/cm³, respectively.
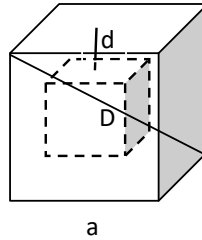
$$D = a\sqrt{2}$$

$$V_{total} = a^3$$

$$V_{magnetite} = (a - 2d)^3$$

$$V_{maghemite} = a^3 - (a - 2d)^3$$

$$\% \, magnetite = \frac{(a - 2d)^3 \times 5.2}{(a - 2d)^3 \times 5.2 + [a^3 - (a - 2d)^3] \times 4.9} \times 100$$

Substituting *a* for its value:

$$\% \, magnetite = \frac{(\frac{D}{\sqrt{2}} - 2d)^3 \times 5.2}{(\frac{D}{\sqrt{2}} - 2d)^3 \times 5.2 + \left[\left(\frac{D}{\sqrt{2}}\right)^3 - (\frac{D}{\sqrt{2}} - 2d)^3\right] \times 4.9} \times 100$$

The weight gain will be obtained by multiplying this value by 0.0345:

$$Weight \, increase \, (\%) = \frac{\left(\frac{D}{\sqrt{2}} - 2d\right)^3 \times 5.2}{\left(\frac{D}{\sqrt{2}} - 2d\right)^3 \times 5.2 + \left[\left(\frac{D}{\sqrt{2}}\right)^3 - \left(\frac{D}{\sqrt{2}} - 2d\right)^3\right] \times 4.9} \times 3.45$$

Expression that can be written in terms of d/D

$$Weight \, increase \, (\%) = \frac{\left(\frac{1}{\sqrt{2}} - 2\frac{d}{D}\right)^3 \times 5.2}{\left(\frac{1}{\sqrt{2}} - 2\frac{d}{D}\right)^3 \times 5.2 + \left[\left(\frac{1}{\sqrt{2}}\right)^3 - \left(\frac{1}{\sqrt{2}} - 2\frac{d}{D}\right)^3\right] \times 4.9} \times 3.45$$

As the value of d/D decreases with increasing size, the increase in weight tends to a constant value of 3.45%, which is the case of pure magnetite, because for large sizes it is irrelevant if there is an oxidation layer.

III

Preliminary bimetallic samples

We carried out a preliminary study of bimetallic nanocrystals by varying the secondary metal concentration (M/Fe atomic ratio from 5 to 20%) to evaluate the effect of these secondary metals.

1. Bi SAMPLES

Figure III-1 shows TEM micrographs for samples with different Bi amount (from 5% to 20%). It can be observed that as the concentration of Bi increases nanoparticle size decreases from 14 to 6 nm, as reported before in Andres-Verges et al. (Andrés-Vergés, 2012).
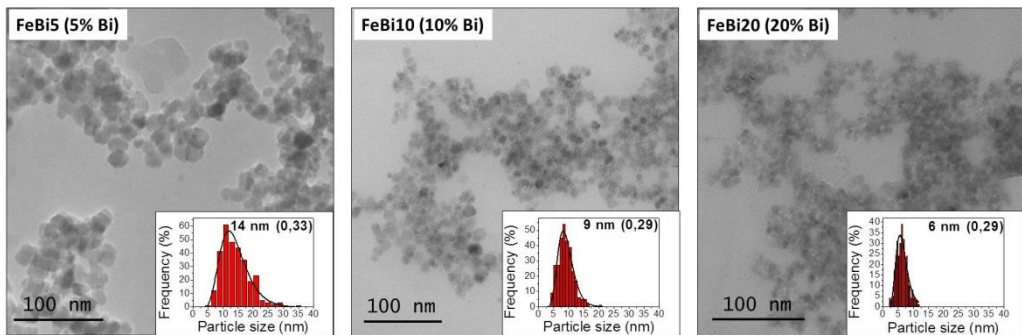
Figure III-1. *TEM micrographs of magnetite/bismuth nanocrystals with different bismuth content ((Bi/Fe)at x100).*

This reduction in size by introducing bismuth (III) cations in the reaction media is a clear indication of the interference of this element on the nanoparticle growth process as well as on the reaction kinetics. All samples are homogenous in size and shape with near spherical morphology.

2. Gd SAMPLES

Figure III-2 shows TEM micrographs for samples with different Gd amount (from 2% to 20%). It can be observed that as the concentration of Gd increases nanoparticle size increases from 43 to 112 nm. This trend could be due to the effect of the Gd present during the synthesis or due to the reduction of the amount of Fe (II) in the reaction vessel. All samples are homogenous in size and shape with near cubic morphology. In these conditions secondary phases are not obtained during the synthesis, however, for Gd quantities greater than 5% a separation of the Gd oxide and the magnetite nanoparticles is observed.
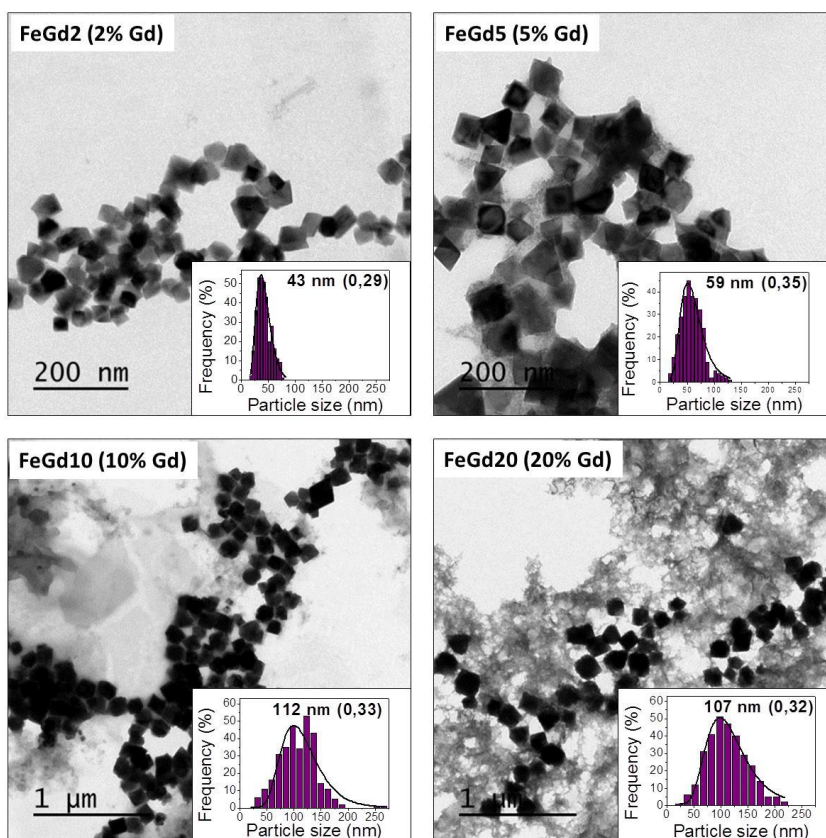
Figure III-2. *TEM micrographs of magnetite/gadolinium nanocrystals with different gadolinium content ((Gd/Fe)at x 100).*

3. Co SAMPLES

Figure III-3 shows TEM micrographs for samples with different Co amount (from 2% to 10%). It can be observed that as the concentration of Co increases nanoparticle size increases from 30 to 77 nm.
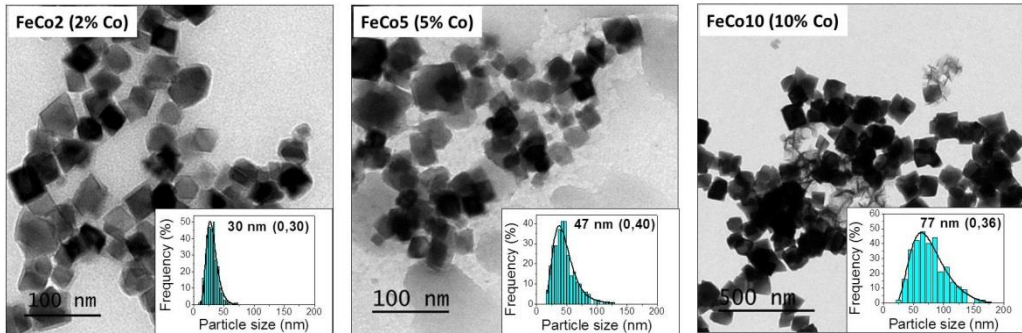
Figure III-3. *TEM micrographs of magnetite/cobalt nanocrystals with different cobalt content ((Co/Fe)at x 100).*

This trend could be due to the effect of the Co present during the synthesis or due to the reduction of the amount of Fe (II) in the reaction vessel. All samples are homogenous in size and shape with near cubic morphology. All samples are homogenous in size and shape with near cubic morphology. In these conditions secondary phases are not obtained during the synthesis, however, for Co quantities greater than 5% a separation of the Co oxide and the magnetite nanoparticles is observed.

IV

The linear response theory model

The linear response theory (LRT) aims to calculate the hysteresis loop area and shape when the magnetic response is linear with the applied magnetic field, which is satisfied under the condition $\mu_0 M_S V H_0 < k_B T$, where μ_0 is the vacuum permeability, Ms the saturation magnetization, V the particle volume, H_0 the field amplitude, k_B the Boltzmann constant, and T the absolute temperature (Carrey, 2011). The magnetic moment of a particle suspended in a fluid can relax after magnetic field removal by two different mechanisms: the Neel (oscillation of the magnetic moment of the NP) and Brown (physical rotation of the NP) relaxations (Glöckl, 2006; Hergt, 2006; Laurent, 2011). The relaxation times can be then described by Neel relaxation time τ_N (equation IV-1) or by Brown relaxation time τ_B (equation IV-2).

$$\tau_N = \tau_0 e^{K_{eff} V / k_B T} \tag{IV-1}$$

$$\tau_B = \frac{4\pi \eta r_h^3}{k_B T} = \frac{3\eta V_h}{k_B T} \tag{IV-2}$$

where η is the viscosity of the fluid and r_h the hydrodynamic radius of the particle.

In a general case, both mechanisms are present, but the faster relaxation mechanism is dominant and an effective relaxation time may be defined by equation IV-3.

$$\frac{1}{\tau_R} = \frac{1}{\tau_B} + \frac{1}{\tau_N} \tag{IV-3}$$

The crossover between Neel and Brown relaxation regimes depends, for a given size, on effective anisotropy K_{eff} and media viscosity η. The Neel relaxation time depends exponentially on volume whereas the Brownian relaxation varies linearly with it.

Finally, within the validity of LRT, the loss power density P for randomly oriented magnetic NPs is given by equation IV-4 (Carrey, 2011).

$$P = \frac{\mu_0^2 M_s^2 V H_0^2}{3 k_B T \tau_R} \frac{(2\pi f \tau_R)^2}{1 + (2\pi f \tau_R)^2} \tag{IV-4}$$

The loss power density P ($W \cdot m^{-3}$) is related to the specific absorption rate SAR ($W \cdot g^{-1}$) by the mean mass density of the particles ($SAR = P/\rho_{Fe_2O_3}$).

Therefore, in the LRT the SARs depend on several parameters: it increases linearly with the NPs volume and quadratically with the field amplitude. Furthermore, the frequency dependence has three different regimens: i) for low frequencies such as $2\pi f \tau_R < 1$, the loss power increases quadratically with the frequency, ii) at very high frequencies $2\pi f \tau_R \gg 1$, the loss power saturates to the value $P = (\mu_0 \chi_0 H_0^2)/\tau_R$, and (iii) for intermediate values of the frequency, the loss power varies with the expression given in equation IV-4.

V

Endocytosis process

Endocytosis defined as physical crossing through cellular membranes are challenging due to their strength needed to their barrier function of maintaining cellular integrity. Although there are differences on the definition of endocytosis, it could be said that it is the process by which cells are able to incorporate in their inner space molecules of different sizes, which in general terms include initially an invagination of the plasmatic membrane around the object to be endocyted finishing with the object contained within a vesicle floating into the cytoplasm (Bareford, 2007). This vesicle follows different routes once inside the cell depending on the endocytic mechanism. It can head towards the degradative pathway of lysosomes, or it can avoid it and go to the Golgi apparatus, the endoplasmic reticulum and even the nucleus.

Endocytosis comprises two different mechanisms: phagocytosis and pinocytosis. Phagocytosis is involved in the internalization of large particles (more than 200 nm) as well as bacteria and other microorganisms. Pinocytosis is involved in the entry of fluid and solute in the cell. Within each of them there are different variants which can be divided into two categories: receptor independent (macropinocytosis) and receptor dependent (clathrin-mediated endocytosis, caveolin-mediated endocytosis or both independent endocytosis) (Figure V-1).
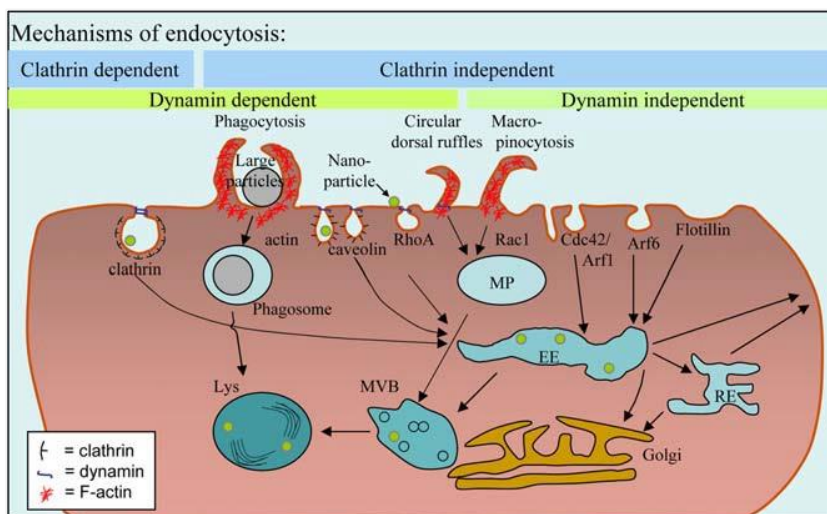
Figure V-1. *Scheme of principal endocytosis mechanisms.*

As shown in Figure V-1, difference between different mechanisms consists, among other things on the size of endocytic vesicle forming (Verma, 2010). Internalization of large particles is favored through phagocytosis processes. Non-specific internalization of 1 µm particles takes place through pinocytosis mechanisms and particles smaller than 100 nm enter into the cell via clathrin- or caveolin-mediated endocytosis (Petros, 2010). Non-specific internalization processes are useful in applications such as hyperthermia where having the tumor cell loaded with the most possible particles to produce the resulting increase in temperature and cause cell death is pursued.

References

- Abbasi, A. Z., Gutiérrez, L. a., del Mercato, L. L., Herranz, F., Chubykalo-Fesenko, O., Veintemillas-Verdaguer, S., Parak, W. J., Morales, M. P., González, J. s. M., Hernando, A. and de la Presa, P. (**2011**). "Magnetic Capsules for NMR Imaging: Effect of Magnetic Nanoparticles Spatial Distribution and Aggregation." *The Journal of Physical Chemistry C* 115(14): 6257-6264.

- Adler, A. F. and Leong, K. W. (**2010**). "Emerging links between surface nanotechnology and endocytosis: impact on nonviral gene delivery." *Nano Today* 5(6): 553-569.

- Agasti, S. S., Chompoosor, A., You, C. C., Ghosh, P., Kim, C. K. and Rotello, V. M. (**2009**). "Photoregulated release of caged anticancer drugs from gold nanoparticles." *J Am Chem Soc* 131(16): 5728-5729.

- Ali, Z., Abbasi, A. Z., Zhang, F., Arosio, P., Lascialfari, A., Casula, M. F., Wenk, A., Kreyling, W., Plapper, R., Seidel, M., Niessner, R., Knoll, J., Seubert, A. and Parak, W. J. (**2011**). "Multifunctional nanoparticles for dual imaging." *Anal Chem* 83(8): 2877-2882.

- Alphandery, E., Faure, S., Seksek, O., Guyot, F. and Chebbi, I. (**2011**). "Chains of magnetosomes extracted from AMB-1 magnetotactic bacteria for application in alternative magnetic field cancer therapy." *ACS Nano* 5(8): 6279-6296.

- Andrés-Vergés, M., Costo, R., Roca, A. G., Marco, J. F., Goya, G. F., Serna, C. J. and Morales, M. P. (**2008**). "Uniform and water stable magnetite nanoparticles with diameters around the monodomain–multidomain limit." *Journal of Physics D: Applied Physics* 41(13): 134003.

- Andrés-Vergés, M., Morales, M. P., Veintemillas-Verdaguer, S., Palomares, F. J. and Serna, C. J. (**2012**). "Core/Shell Magnetite/Bismuth Oxide Nanocrystals with Tunable Size, Colloidal, and Magnetic Properties." *Chemistry of Materials* 24(2): 319-324.

- Aphesteguy, J. C., Kurlyandskaya, G. V., de Celis, J. P., Safronov, A. P. and Schegoleva, N. N. (**2015**). "Magnetite nanoparticles prepared by co-precipitation method in different conditions." *Materials Chemistry and Physics* 161: 243-249.

- Aposhian, H. V. and Aposhian, M. M. (**1990**). "meso-2,3-Dimercaptosuccinic acid: chemical, pharmacological and toxicological properties of an orally effective metal chelating agent." *Annual Review of Pharmacology and Toxicology* 30: 279-306.

- Arbab, A. S., Bashaw, L. A., Miller, B. R., Jordan, E. K., Lewis, B. K., Kalish, H. and Frank, J. A. (**2003**). "Characterization of biophysical and metabolic properties of cells labeled with superparamagnetic iron oxide nanoparticles and transfection agent for cellular MR imaging 1." *Radiology* 229(3): 838-846.

- Avazpour, L., Zandi khajeh, M. A., Toroghinejad, M. R. and Shokrollahi, H. (**2015**). "Synthesis of single-phase cobalt ferrite nanoparticles via a novel EDTA/EG precursor-based route and their magnetic properties." *Journal of Alloys and Compounds* 637: 497-503.

- Bae, K. H., Kim, Y. B., Lee, Y., Hwang, J., Park, H. and Park, T. G. (**2010**). "Bioinspired synthesis and characterization of gadolinium-labeled magnetite nanoparticles for dual contrast t1- and T2-weighted magnetic resonance imaging." *Bioconjug Chem* 21(3): 505-512.

- Bao, J., Chen, W., Liu, T., Zhu, Y., Jin, P., Wang, L., Liu, J., Wei, Y. and Li, Y. (**2007**). "Bifunctional Au-Fe3O4 nanoparticles for protein separation." *ACS Nano* 1(4): 293-298.

- Bareford, L. M. and Swaan, P. W. (**2007**). "Endocytic mechanisms for targeted drug delivery." *Adv Drug Deliv Rev* 59(8): 748-758.

- Barua, S. and Rege, K. (**2009**). "Cancer-cell-phenotype-dependent differential intracellular trafficking of unconjugated quantum dots." *Small* 5(3): 370-376.

- Basti, H., Ben Tahar, L., Smiri, L.S., Herbst, F., Nowak, S., Mangeney, C., Ammar, S. (**2016**). "Surface modification of γ-Fe2O3 nanoparticles by grafting from poly-(hydroxyethylmethacrylate) and poly-(methacrylic acid): Qualitative and quantitative analysis of the polymeric coating." *Colloids and Surfaces A: Physicochemical and Engineering Aspects* 490: 222-231.

- Bate, G. (**1975**). *Magnetic Oxides.*

- Batlle, X. and Labarta, A. (**2002**). "Finite-size effects in fine particles: magnetic and transport properties." *Journal of Physics D: Applied Physics* 35(6): R15-R42.

- Bautista, M. C., Bomati-Miguel, O., Zhao, X., Morales, M. P., González-Carreño, T., Alejo, R. P. d., Ruiz-Cabello, J. and Veintemillas-Verdaguer, S. (**2004**). "Comparative study of ferrofluids based on dextran-coated iron oxide and metal nanoparticles for contrast agents in magnetic resonance imaging." *Nanotechnology* 15(4): S154-S159.

- Bee, A., Massart, R. and Neveu, S. (**1995**). "Synthesis of very fine maghemite particles." *Journal of Magnetism and Magnetic Materials* 149(1-2): 6-9.

- Bernal, J. D. (**1959**). "The Oxides and Hydroxides of Iron and Their Structural Inter-Relationships." *Clay Minerals* 4(21): 15-30.

- Bishop, K. J., Kowalczyk, B. and Grzybowski, B. A. (**2009**). "Precipitation of oppositely charged nanoparticles by dilution and/or temperature increase." *J Phys Chem B* 113(5): 1413-1417.

- Blanco-Mantecón, M. and O'Grady, K. (**1999**). "Grain size and blocking distributions in fine particle iron oxide nanoparticles." *Journal of Magnetism and Magnetic Materials* 203(1-3): 50-53.

- Bloemen, M., Brullot, W., Luong, T., Geukens, N., Gils, A. and Verbiest, T. (**2012**). "Improved functionalization of oleic acid-coated iron oxide nanoparticles for biomedical applications." *Journal of Nanoparticle Research* 14(9).

- Bomatí-Miguel, O., Mazeina, L., Navrotsky, A. Veintemillas-Verdaguer, S. (**2008**). "Calorimetric study of maghemite nanoparticles synthesized by laser induced pyrolysis." *Chem. Mater* 20, 591-598.

- Bottrill, M., Kwok, L. and Long, N. J. (**2006**). "Lanthanides in magnetic resonance imaging." *Chem Soc Rev* 35(6): 557-571.

- Brandenberger, C., Muhlfeld, C., Ali, Z., Lenz, A. G., Schmid, O., Parak, W. J., Gehr, P. and Rothen-Rutishauser, B. (**2010**). "Quantitative evaluation of cellular uptake and trafficking of plain and polyethylene glycol-coated gold nanoparticles." *Small* 6(15): 1669-1678.

- Bronstein, L. M., Huang, X., Retrum, J., Schmucker, A., Pink, M., Stein, B. D. and Dragnea, B. (**2007**). "Influence of Iron Oleate Complex Structure on Iron Oxide Nanoparticle Formation." *Chemistry of Materials* 19(15): 3624-3632.

- Bulte, J. W., Douglas, T., Witwer, B., Zhang, S. C., Strable, E., Lewis, B. K., Zywicke, H., Miller, B., van Gelderen, P., Moskowitz, B. M., Duncan, I. D. and Frank, J. A. (**2001**). "Magnetodendrimers allow endosomal magnetic labeling and in vivo tracking of stem cells." *Nat Biotechnol* 19(12): 1141-1147.

- Burrows, F., Parker, C., Evans, R. F. L., Hancock, Y., Hovorka, O. and Chantrell, R. W. (**2010**). "Energy losses in interacting fine-particle magnetic composites." *Journal of Physics D: Applied Physics* 43(47): 474010.

- Calero, M., Gutierrez, L., Salas, G., Luengo, Y., Lazaro, A., Acedo, P., Morales, M. P., Miranda, R. and Villanueva, A. (**2014**). "Efficient and safe internalization of magnetic iron oxide nanoparticles: two fundamental requirements for biomedical applications." *Nanomedicine* 10(4): 733-743.

- Caravan, P. (**2006**). "Strategies for increasing the sensitivity of gadolinium based MRI contrast agents." *Chem Soc Rev* 35(6): 512-523.

- Caravan, P., Ellison, J. J., McMurry, T. J. and Lauffer, R. B. (**1999**). "Gadolinium(III) Chelates as MRI Contrast Agents: Structure, Dynamics, and Applications." *Chemical Reviews* 99(9): 2293-2352.

- Carrey, J., Mehdaoui, B. and Respaud, M. (**2011**). "Simple models for dynamic hysteresis loop calculations of magnetic single-domain nanoparticles: Application to magnetic hyperthermia optimization." *Journal of Applied Physics* 109(8): 083921.

- Caruntu, D., Cushing, B. L., Caruntu, G. and O'Connor, C. J. (**2005**). "Attachment of Gold Nanograins onto Colloidal Magnetite Nanocrystals." *Chemistry of Materials* 17(13): 3398-3402.

- Cedervall, T., Lynch, I., Lindman, S., Berggard, T., Thulin, E., Nilsson, H., Dawson, K. A. and Linse, S. (**2007**). "Understanding the nanoparticle-protein corona using methods to quantify exchange rates and affinities of proteins for nanoparticles." *Proc Natl Acad Sci U S A* 104(7): 2050-2055.

- Coey, J. M. (**2010**). *Magnetism and magnetic materials*, Cambridge University Press.

- Cole, A. J., Yang, V. C. and David, A. E. (**2011**). "Cancer theranostics: the rise of targeted magnetic nanoparticles." *Trends Biotechnol* 29(7): 323-332.

- Colombo, M., Carregal-Romero, S., Casula, M. F., Gutierrez, L., Morales, M. P., Bohm, I. B., Heverhagen, J. T., Prosperi, D. and Parak, W. J. (**2012**). "Biological applications of magnetic nanoparticles." *Chem Soc Rev* 41(11): 4306-4334.

- Collins, K. D. (**2006**). "Ion hydration: Implications for cellular function, polyelectrolytes, and protein crystallization." *Biophys Chem* 119(3): 271-281.

- Cornell, R. M. and Schwertmann, U. (**2006**). *The Iron Oxides: Structure, Properties, Reactions, Occurrences and Uses*, Wiley.

- Corot, C., Robert, P., Idee, J. M. and Port, M. (**2006**). "Recent advances in iron oxide nanocrystal technology for medical imaging." *Adv Drug Deliv Rev* 58(14): 1471-1504.

- Costo, R., Bello, V., Robic, C., Port, M., Marco, J. F., Morales, M. P. and Veintemillas-Verdaguer, S. (**2012**). "Ultrasmall iron oxide nanoparticles for biomedical applications: improving the colloidal and magnetic properties." *Langmuir* 28(1): 178-185.

- Creighton, J. A. and Eadon, D. G. (**1991**). "Ultraviolet-visible absorption spectra of the colloidal metallic elements." *Journal of the Chemical Society, Faraday Transactions* 87(24): 3881-3891.

- Cui, L., Guo, P., Zhang, G., Li, Q., Wang, R., Zhou, M., Ran, L. and Zhao, X. S. (**2013**). "Facile synthesis of cobalt ferrite submicrospheres with tunable magnetic and electrocatalytic properties." *Colloids and Surfaces A: Physicochemical and Engineering Aspects* 423: 170-177.

- Cullity, B. D. and Graham, C. D. (**2011**). *Introduction to Magnetic Materials*, Wiley.

- Chen, Z., Wu, Y., Hu, J. and Bretos, I. (**2013**). "Ethanol-Assisted Hydrothermal Synthesis and Characterization of BiFeO3Nanopowders." *Journal of the American Ceramic Society* 96(5): 1345-1348.

- Cheon, J. and Lee, J. H. (**2008**). "Synergistically integrated nanoparticles as multimodal probes for nanobiotechnology." *Acc Chem Res* 41(12): 1630-1640.

- Cho, E. C., Xie, J., Wurm, P. A. and Xia, Y. (**2009**). "Understanding the role of surface charges in cellular adsorption versus internalization by selectively removing gold nanoparticles on the cell surface with a I2/KI etchant." *Nano Lett* 9(3): 1080-1084.

- Choi, J. S., Lee, J. H., Shin, T. H., Song, H. T., Kim, E. Y. and Cheon, J. (**2010**). "Self-confirming "AND" logic nanoparticles for fault-free MRI." *J Am Chem Soc* 132(32): 11015-11017.

- Christiansen, B. C., Balic-Zunic, T., Petit, P. O., Frandsen, C., Mørup, S., Geckeis, H., Katerinopoulou, A. and Stipp, S. L. S. (**2009**). "Composition and structure of an iron-bearing, layered double hydroxide (LDH) – Green rust sodium sulphate." *Geochimica et Cosmochimica Acta* 73(12): 3579-3592.

- de la Presa, P., Luengo, Y., Multigner, M., Costo, R., Morales, M. P., Rivero, G. and Hernando, A. (**2012**). "Study of Heating Efficiency as a Function of Concentration, Size, and Applied Field in γ-Fe2O3Nanoparticles." *The Journal of Physical Chemistry C* 116(48): 25602-25610.

- de la Presa, P., Luengo, Y., Velasco, V., Morales, M. P., Iglesias, M., Veintemillas-Verdaguer, S., Crespo, P. and Hernando, A. (**2015**). "Particle Interactions in Liquid Magnetic Colloids by Zero Field Cooled Measurements: Effects on Heating Efficiency." *The Journal of Physical Chemistry C* 119(20): 11022-11030.

- de la Presa, P., Rueda, T., Hernando, A., Ramallo-López, J. M., Giovanetti, L. J. and Requejo, F. G. (**2008**). "Spontaneous oxidation of disordered fcc FePt nanoparticles." *Journal of Applied Physics* 103(10): 103909.

- De Stasio, G., Casalbore, P., Pallini, R., Gilbert, B., Sanita, F., Ciotti, M. T., Rosi, G., Festinesi, A., Larocca, L. M., Rinelli, A., Perret, D., Mogk, D. W., Perfetti, P., Mehta, M. P. and Mercanti, D. (**2001**). "Gadolinium in human glioblastoma cells for gadolinium neutron capture therapy." *Cancer Res* 61(10): 4272-4277.

- Deepak, F. L., Bañobre-López, M., Carbó-Argibay, E., Cerqueira, M. F., Piñeiro-Redondo, Y., Rivas, J., Thompson, C. M., Kamali, S., Rodríguez-Abreu, C., Kovnir, K. and Kolen'ko, Y. V. (**2015**). "A Systematic Study of the Structural and Magnetic Properties of Mn-, Co-, and Ni-Doped Colloidal Magnetite Nanoparticles." *The Journal of Physical Chemistry C* 119(21): 11947-11957.

- Del Bianco, L., Hernando, A., Multigner, M., Prados, C., Sánchez-López, J. C., Fernández, A., Conde, C. F. and Conde, A. (**1998**). "Evidence of spin disorder at the surface–core interface of oxygen passivated Fe nanoparticles." *Journal of Applied Physics* 84(4): 2189-2192.

- Demortiere, A., Panissod, P., Pichon, B. P., Pourroy, G., Guillon, D., Donnio, B. and Begin-Colin, S. (**2011**). "Size-dependent properties of magnetic iron oxide nanocrystals." *Nanoscale* 3(1): 225-232.

- Di Corato, R., Espinosa, A., Lartigue, L., Tharaud, M., Chat, S., Pellegrino, T., Menager, C., Gazeau, F. and Wilhelm, C. (**2014**). "Magnetic hyperthermia efficiency in the cellular environment for different nanoparticle designs." *Biomaterials* 35(24): 6400-6411.

- Dias, A. M., Hussain, A., Marcos, A. S. and Roque, A. C. (**2011**). "A biotechnological perspective on the application of iron oxide magnetic colloids modified with polysaccharides." *Biotechnol Adv* 29(1): 142-155.

- Dias, M. and Lauterbur, P. C. (**1986**). "Ferromagnetic particles as contrast agents for magnetic resonance imaging of liver and spleen." *Magnetic resonance in medicine* 3(2): 328-330.

- Ding, H. L., Zhang, Y. X., Wang, S., Xu, J. M., Xu, S. C. and Li, G. H. (**2012**). "Fe3O4@SiO2Core/Shell Nanoparticles: The Silica Coating Regulations with a Single Core for Different Core Sizes and Shell Thicknesses." *Chemistry of Materials* 24(23): 4572-4580.

- Ding, Z., Wang, W., Zhang, Y., Li, F. and Liu, J. P. (**2015**). "Synthesis, characterization and adsorption capability for Congo red of CoFe2O4 ferrite nanoparticles." *Journal of Alloys and Compounds* 640: 362-370.

- Domingo, C., Rodríguez-Clemente, R. and Blesa, M. (**1994**). "Morphological properties of α-FeOOH, γ-FeOOH and Fe3O4 obtained by oxidation of aqueous Fe (II) solutions." *Journal of Colloid and Interface Science* 165(1): 244-252.

- Domingo, C., Rodríguez-Clemente, R. and Blesa, M. A. (**1991**). "The pathways to spinel iron oxides by oxidation of iron (II) in basic media." *Materials Research Bulletin* 26(1): 47-55.

- Douglas, F. J., MacLaren, D. A., Maclean, N., Andreu, I., Kettles, F. J., Tuna, F., Berry, C. C., Castro, M. and Murrie, M. (**2016**). "Gadolinium-doped magnetite nanoparticles from a single-source precursor." *RSC Adv.* 6(78): 74500-74505.

- Drake, P., Cho, H.-J., Shih, P.-S., Kao, C.-H., Lee, K.-F., Kuo, C.-H., Lin, X.-Z. and Lin, Y.-J. (**2007**). "Gd-doped iron-oxide nanoparticles for tumour therapy via magnetic field hyperthermia." *Journal of Materials Chemistry* 17(46): 4914.

- Duanmu, C., Saha, I., Zheng, Y., Goodson, B. M. and Gao, Y. (**2006**). "Dendron-Functionalized Superparamagnetic Nanoparticles with Switchable Solubility in Organic and Aqueous Media: Matrices for Homogeneous Catalysis and Potential MRI Contrast Agents." *Chemistry of Materials* 18(25): 5973-5981.

- Duguet, E., Vasseur, S., Mornet, S., Goglio, G., Demourgues, A., Portier, J., Grasset, F., Veverka, P. and Pollert, E. (**2006**). "Towards a versatile platform based on magnetic nanoparticles for in vivo applications." *Bulletin of Materials Science* 29(6): 581-586.

- Fantechi, E., Innocenti, C., Albino, M., Lottini, E. and Sangregorio, C. (**2015**). "Influence of cobalt doping on the hyperthermic efficiency of magnetite nanoparticles." *Journal of Magnetism and Magnetic Materials* 380: 365-371.

- Faraudo, J., Andreu, J. S. and Camacho, J. (**2013**). "Understanding diluted dispersions of superparamagnetic particles under strong magnetic fields: a review of concepts, theory and simulations." *Soft Matter* 9(29): 6654.

- Fauconnier, N., Pons, J. N., Roger, J. and Bee, A. (**1997**). "Thiolation of Maghemite Nanoparticles by Dimercaptosuccinic Acid." *J Colloid Interface Sci* 194(2): 427-433.

- Feitknecht, W. and Mannweiler, U. (**1967**). "Der Mechanismus der Umwandlung von γ-zu α-Eisensesquioxid [1]." *Helvetica Chimica Acta* 50(2): 570-581.

- Feng, B., Hong, R. Y., Wang, L. S., Guo, L., Li, H. Z., Ding, J., Zheng, Y. and Wei, D. G. (**2008**). "Synthesis of Fe3O4/APTES/PEG diacid functionalized magnetic nanoparticles for MR imaging." *Colloids and Surfaces A: Physicochemical and Engineering Aspects* 328(1-3): 52-59.

- Figuerola, A., Di Corato, R., Manna, L. and Pellegrino, T. (**2010**). "From iron oxide nanoparticles towards advanced iron-based inorganic materials designed for biomedical applications." *Pharmacol Res* 62(2): 126-143.

- Fischer, B., Huke, B., Lücke, M. and Hempelmann, R. (**2005**). "Brownian relaxation of magnetic colloids." *Journal of Magnetism and Magnetic Materials* 289: 74-77.

- Flora, S. J. S., Pande, M. and Mehta, A. (**2003**). "Beneficial effect of combined administration of some naturally occurring antioxidants (vitamins) and thiol chelators in the treatment of chronic lead intoxication." *Chemico-Biological Interactions* 145(3): 267-280.

- Fortin, J. P., Wilhelm, C., Servais, J., Menager, C., Bacri, J. C. and Gazeau, F. (**2007**). "Size-sorted anionic iron oxide nanomagnets as colloidal mediators for magnetic hyperthermia." *J Am Chem Soc* 129(9): 2628-2635.

- Gao, J., Gu, H. and Xu, B. (**2009**). "Multifunctional magnetic nanoparticles: design, synthesis, and biomedical applications." *Acc Chem Res* 42(8): 1097-1107.

- Garaio, E., Sandre, O., Collantes, J. M., Garcia, J. A., Mornet, S. and Plazaola, F. (**2015**). "Specific absorption rate dependence on temperature in magnetic field hyperthermia measured by dynamic hysteresis losses (ac magnetometry)." *Nanotechnology* 26(1): 015704.

- Garcell, L., Morales, M. P., Andres-Verges, M., Tartaj, P. and Serna, C. J. (**1998**). "Interfacial and Rheological Characteristics of Maghemite Aqueous Suspensions." *J Colloid Interface Sci* 205(2): 470-475.

- Gazeau, F., Levy, M. and Wilhelm, C. (**2008**). "Optimizing magnetic nanoparticle design for nanothermotherapy." *Nanomedicine (Lond)* 3(6): 831-844.

- Gelbrich, T., Feyen, M. and Schmidt, A. M. (**2006**). "Magnetic Thermoresponsive Core−Shell Nanoparticles." *Macromolecules* 39(9): 3469-3472.

- Génin, J.-M. R., Refait, P., Simon, L. and Drissi, S. H. (**1998**). "Preparation and Eh–pH diagrams of Fe(II)--Fe(III) green rust compounds; hyperfine interaction characteristics and stoichiometry of hydroxy-chloride, -sulphate and -carbonate." *Hyperfine Interactions* 111(1): 313-318.

- Geraldes, C. F. and Laurent, S. (**2009**). "Classification and basic properties of contrast agents for magnetic resonance imaging." *Contrast Media Mol Imaging* 4(1): 1-23.

- Giorgi, R., Bozzi, C., Dei, L., Gabbiani, C., Ninham, B. W. and Baglioni, P. (**2005**). "Nanoparticles of Mg(OH)2: synthesis and application to paper conservation." *Langmuir* 21(18): 8495-8501.

- Glöckl, G., Hergt, R., Zeisberger, M., Dutz, S., Nagel, S. and Weitschies, W. (**2006**). "The effect of field parameters, nanoparticle properties and immobilization on the specific heating power in magnetic particle hyperthermia." *Journal of Physics: Condensed Matter* 18(38): S2935-S2949.

- Glotzer, S. C. and Solomon, M. J. (**2007**). "Anisotropy of building blocks and their assembly into complex structures." *Nature materials* 6(8): 557-562.

- Gnanaprakash, G., Ayyappan, S., Jayakumar, T., Philip, J. and Raj, B. (**2006**). "Magnetic nanoparticles with enhanced γ-Fe2O3 to α-Fe2O3 phase transition temperature." *Nanotechnology* 17(23): 5851-5857.

- Gomes, J. d. A., Sousa, M. H., Tourinho, F. A., Aquino, R., da Silva, G. J., Depeyrot, J., Dubois, E. and Perzynski, R. (**2008**). "Synthesis of Core−Shell Ferrite Nanoparticles for Ferrofluids: Chemical and Magnetic Analysis." *The Journal of Physical Chemistry C* 112(16): 6220-6227.

- Gonzales-Weimuller, M., Zeisberger, M. and Krishnan, K. M. (**2009**). "Size-dependant heating rates of iron oxide nanoparticles for magnetic fluid hyperthermia." *J Magn Magn Mater* 321(13): 1947-1950.

- Gonzalez-Fernandez, M. A., Torres, T. E., Andrés-Vergés, M., Costo, R., de la Presa, P., Serna, C. J., Morales, M. P., Marquina, C., Ibarra, M. R. and Goya, G. F. (**2009**). "Magnetic nanoparticles for power absorption: Optimizing size, shape and magnetic properties." *Journal of Solid State Chemistry* 182(10): 2779-2784.

- Goon, I. Y., Lai, L. M. H., Lim, M., Munroe, P., Gooding, J. J. and Amal, R. (**2009**). "Fabrication and Dispersion of Gold-Shell-Protected Magnetite Nanoparticles: Systematic Control Using Polyethyleneimine." *Chemistry of Materials* 21(4): 673-681.

- Gordon, R., Hines, J. and Gordon, D. (**1979**). "Intracellular hyperthermia a biophysical approach to cancer treatment via intracellular temperature and biophysical alterations." *Medical Hypotheses* 5(1): 83-102.

- Goya, G. F., Berquó, T. S., Fonseca, F. C. and Morales, M. P. (**2003**). "Static and dynamic magnetic properties of spherical magnetite nanoparticles." *Journal of Applied Physics* 94(5): 3520-3528.

- Grigorova, M., Blythe, H., Blaskov, V., Rusanov, V., Petkov, V., Masheva, V., Nihtianova, D., Martinez, L. M., Munoz, J. and Mikhov, M. (**1998**). "Magnetic properties and Mössbauer spectra of nanosized CoFe 2 O 4 powders." *Journal of Magnetism and Magnetic Materials* 183(1): 163-172.

- Guardia, P., Di Corato, R., Lartigue, L., Wilhelm, C., Espinosa, A., Garcia-Hernandez, M., Gazeau, F., Manna, L. and Pellegrino, T. (**2012**). "Water-soluble iron oxide nanocubes with high values of specific absorption rate for cancer cell hyperthermia treatment." *ACS Nano* 6(4): 3080-3091.

- Guilbaud, R., White, M. L. and Poulton, S. W. (**2013**). "Surface charge and growth of sulphate and carbonate green rust in aqueous media." *Geochimica et Cosmochimica Acta* 108: 141-153.

- Guo, R., Wang, H., Peng, C., Shen, M., Pan, M., Cao, X., Zhang, G. and Shi, X. (**2010**). "X-ray Attenuation Property of Dendrimer-Entrapped Gold Nanoparticles." *The Journal of Physical Chemistry C* 114(1): 50-56.

- Gupta, A. K. and Gupta, M. (**2005**). "Synthesis and surface engineering of iron oxide nanoparticles for biomedical applications." *Biomaterials* 26(18): 3995-4021.

- Haase, C. and Nowak, U. (**2012**). "Role of dipole-dipole interactions for hyperthermia heating of magnetic nanoparticle ensembles." *Physical Review B* 85(4).

- Hamada, S. and Matijević, E. (**1981**). "Ferric hydrous oxide sols. IV. Preparation of uniform cubic hematite particles by hydrolysis of ferric chloride in alcohol—water solutions." *Journal of Colloid and Interface Science* 84(1): 274-277.

- Hamada, S. and Matijević, E. (**1982**). "Formation of monodispersed colloidal cubic haematite particles in ethanol+ water solutions." *Journal of the Chemical Society, Faraday Transactions 1: Physical Chemistry in Condensed Phases* 78(7): 2147-2156.

- Handgretinger, R., Lang, P., Schumm, M., Taylor, G., Neu, S., Koscielnak, E., Niethammer, D. and Klingebiel, T. (**1998**). "Isolation and transplantation of autologous peripheral CD34+ progenitor cells highly purified by magnetic-activated cell sorting." *Bone Marrow Transplant* 21(10): 987-993.

- Harush-Frenkel, O., Debotton, N., Benita, S. and Altschuler, Y. (**2007**). "Targeting of nanoparticles to the clathrin-mediated endocytic pathway." *Biochem Biophys Res Commun* 353(1): 26-32.

- Hergt, R., Andra, W., d'Ambly, C. G., Hilger, I., Kaiser, W. A., Richter, U. and Schmidt, H.-G. (**1998**). "Physical limits of hyperthermia using magnetite fine particles." *IEEE Transactions on Magnetics* 34(5): 3745-3754.

- Hergt, R. and Dutz, S. (**2007**). "Magnetic particle hyperthermia—biophysical limitations of a visionary tumour therapy." *Journal of Magnetism and Magnetic Materials* 311(1): 187-192.

- Hergt, R., Dutz, S., Müller, R. and Zeisberger, M. (**2006**). "Magnetic particle hyperthermia: nanoparticle magnetism and materials development for cancer therapy." *Journal of Physics: Condensed Matter* 18(38): S2919-S2934.

- Hernandez-Minguez, A., Hernandez, J. M., Macia, F., Garcia-Santiago, A., Tejada, J. and Santos, P. V. (**2005**). "Quantum magnetic deflagration in acetate." *Phys Rev Lett* 95(21): 217205.

- Hernando, A., Vázquez, M., Kulik, T. and Prados, C. (**1995**). "Analysis of the dependence of spin-spin correlations on the thermal treatment of nanocrystalline materials." *Physical Review B* 51(6): 3581-3586.

- Hervault, A. and Thanh, N. T. K. (**2014**). "Magnetic nanoparticle-based therapeutic agents for thermo-chemotherapy treatment of cancer." *Nanoscale* 6(20): 11553-11573.

- Heymer, A., Haddad, D., Weber, M., Gbureck, U., Jakob, P. M., Eulert, J. and Noth, U. (**2008**). "Iron oxide labelling of human mesenchymal stem cells in collagen hydrogels for articular cartilage repair." *Biomaterials* 29(10): 1473-1483.

- Hirsch, L. R., Stafford, R. J., Bankson, J. A., Sershen, S. R., Rivera, B., Price, R. E., Hazle, J. D., Halas, N. J. and West, J. L. (**2003**). "Nanoshell-mediated near-infrared thermal therapy of tumors under magnetic resonance guidance." *Proc Natl Acad Sci U S A* 100(23): 13549-13554.

- Hofmeister, F. (**1891**). "Zur Lehre von der Wirkung der Salze." *Archiv für experimentelle Pathologie und Pharmakologie* 28(3-4): 210-238.

- Holzapfel, V., Lorenz, M., Weiss, C. K., Schrezenmeier, H., Landfester, K. and Mailänder, V. (**2006**). "Synthesis and biomedical applications of functionalized fluorescent and magnetic dual reporter nanoparticles as obtained in the miniemulsion process." *Journal of Physics: Condensed Matter* 18(38): S2581-S2594.

- Hong, S., Lee, J., Kim, H., Park, J., Cho, J. and Han, D.-W. (**2011**). "Subtle cytotoxicity and genotoxicity differences in superparamagnetic iron oxide nanoparticles coated with various functional groups." *International journal of nanomedicine* 6: 3219-3231.

- Houshiar, M., Zebhi, F., Razi, Z. J., Alidoust, A. and Askari, Z. (**2014**). "Synthesis of cobalt ferrite (CoFe2O4) nanoparticles using combustion, coprecipitation, and precipitation methods: A comparison study of size, structural, and magnetic properties." *Journal of Magnetism and Magnetic Materials* 371: 43-48.

- Hu, Z., Oskam, G., Penn, R. L., Pesika, N. and Searson, P. C. (**2003**). "The Influence of Anion on the Coarsening Kinetics of ZnO Nanoparticles." *The Journal of Physical Chemistry B* 107(14): 3124-3130.

- Huh, Y. M., Jun, Y. W., Song, H. T., Kim, S., Choi, J. S., Lee, J. H., Yoon, S., Kim, K. S., Shin, J. S., Suh, J. S. and Cheon, J. (**2005**). "In vivo magnetic resonance detection of cancer by using multifunctional magnetic nanocrystals." *J Am Chem Soc* 127(35): 12387-12391.

- Ivanov, E. V. (**2012**). "Volumetric properties of dilute solutions of water in ethanol and water-d2 in ethanol-d1 between T=(278.15 and 318.15)K." *The Journal of Chemical Thermodynamics* 47: 162-170.

- Jensen, T. R., Malinsky, M. D., Haynes, C. L. and Van Duyne, R. P. (**2000**). "Nanosphere Lithography: Tunable Localized Surface Plasmon Resonance Spectra of Silver Nanoparticles." *The Journal of Physical Chemistry B* 104(45): 10549-10556.

- Jeong, J.-R., Shin, S.-C., Lee, S.-J. and Kim, J.-D. (**2005**). "Magnetic properties of superparamagnetic γ-Fe2O3 nanoparticles prepared by coprecipitation technique." *Journal of Magnetism and Magnetic Materials* 286: 5-9.

- Jeong, U., Teng, X., Wang, Y., Yang, H. and Xia, Y. (**2007**). "Superparamagnetic Colloids: Controlled Synthesis and Niche Applications." *Advanced Materials* 19(1): 33-60.

- Jesson, D. E. and Pennycook, S. J. (**1995**). "Incoherent Imaging of Crystals Using Thermally Scattered Electrons." *Proceedings of the Royal Society of London. Series A: Mathematical and Physical Sciences* 449(1936): 273-293.

- Jin, Y. and Gao, X. (**2009**). "Plasmonic fluorescent quantum dots." *Nat Nanotechnol* 4(9): 571-576.

- Jing, L., Ding, K., Kershaw, S. V., Kempson, I. M., Rogach, A. L. and Gao, M. (**2014**). "Magnetically engineered semiconductor quantum dots as multimodal imaging probes." *Adv Mater* 26(37): 6367-6386.

- Johannsen, M., Thiesen, B., Wust, P. and Jordan, A. (**2010**). "Magnetic nanoparticle hyperthermia for prostate cancer." *Int J Hyperthermia* 26(8): 790-795.

- Jolivet, J. P., Chaneac, C. and Tronc, E. (**2004**). "Iron oxide chemistry. From molecular clusters to extended solid networks." *Chem Commun (Camb)*(5): 481-487.

- Jordan, A., Scholz, R., Wust, P., Fähling, H. and Felix, R. (**1999**). "Magnetic fluid hyperthermia (MFH): Cancer treatment with AC magnetic field induced excitation of biocompatible superparamagnetic nanoparticles." *Journal of Magnetism and Magnetic Materials* 201(1): 413-419.

- Jun, Y. W., Huh, Y. M., Choi, J. S., Lee, J. H., Song, H. T., Kim, S., Yoon, S., Kim, K. S., Shin, J. S., Suh, J. S. and Cheon, J. (**2005**). "Nanoscale size effect of magnetic nanocrystals and their utilization for cancer diagnosis via magnetic resonance imaging." *J Am Chem Soc* 127(16): 5732-5733.

- Kalender, W. A. (**2006**). "X-ray computed tomography." *Phys Med Biol* 51(13): R29-43.

- Kallumadil, M., Tada, M., Nakagawa, T., Abe, M., Southern, P. and Pankhurst, Q. A. (**2009**). "Suitability of commercial colloids for magnetic hyperthermia." *Journal of Magnetism and Magnetic Materials* 321(10): 1509-1513.

- Kawashita, M., Tanaka, M., Kokubo, T., Inoue, Y., Yao, T., Hamada, S. and Shinjo, T. (**2005**). "Preparation of ferrimagnetic magnetite microspheres for in situ hyperthermic treatment of cancer." *Biomaterials* 26(15): 2231-2238.

- Ke, H., Wang, J., Dai, Z., Jin, Y., Qu, E., Xing, Z., Guo, C., Yue, X. and Liu, J. (**2011**). "Gold-nanoshelled microcapsules: a theranostic agent for ultrasound contrast imaging and photothermal therapy." *Angew Chem Int Ed Engl* 50(13): 3017-3021.

- Khan, J. A., Pillai, B., Das, T. K., Singh, Y. and Maiti, S. (**2007**). "Molecular effects of uptake of gold nanoparticles in HeLa cells." *Chembiochem* 8(11): 1237-1240.

- Khan, U., Li, W. J., Adeela, N., Irfan, M., Javed, K., Wan, C. H., Riaz, S. and Han, X. F. (**2016**). "Magnetic response of hybrid ferromagnetic and antiferromagnetic core-shell nanostructures." *Nanoscale* 8(11): 6064-6070.

- Kiyama, M. (**1974**). "Conditions for the Formation of Fe3O4by the Air Oxidation of Fe(OH)2Suspensions." *Bulletin of the Chemical Society of Japan* 47(7): 1646-1650.

- Kolosnjaj-Tabi, J., Di Corato, R., Lartigue, L., Marangon, I., Guardia, P., Silva, A. K. A., Luciani, N., Clément, O., Flaud, P., Singh, J. V., Decuzzi, P., Pellegrino, T., Wilhelm, C. and Gazeau, F. (**2014**). "Heat-Generating Iron Oxide Nanocubes: Subtle "Destructurators" of the Tumoral Microenvironment." *ACS Nano* 8(5): 4268-4283.

- Kosmulski, M. (**2002**). "The pH-dependent surface charging and the points of zero charge." *J Colloid Interface Sci* 253(1): 77-87.

- Kovalenko, M. V., Manna, L., Cabot, A., Hens, Z., Talapin, D. V., Kagan, C. R., Klimov, V. I., Rogach, A. L., Reiss, P., Milliron, D. J., Guyot-Sionnnest, P., Konstantatos, G., Parak, W. J., Hyeon, T., Korgel, B. A., Murray, C. B. and Heiss, W. (**2015**). "Prospects of nanoscience with nanocrystals." *ACS Nano* 9(2): 1012-1057.

- Krug, H. F. and Wick, P. (**2011**). "Nanotoxicology: an interdisciplinary challenge." *Angew Chem Int Ed Engl* 50(6): 1260-1278.

- Kumar, C. S. and Mohammad, F. (**2011**). "Magnetic nanomaterials for hyperthermia-based therapy and controlled drug delivery." *Adv Drug Deliv Rev* 63(9): 789-808.

- Kumbhar, V. S., Jagadale, A. D., Shinde, N. M. and Lokhande, C. D. (**2012**). "Chemical synthesis of spinel cobalt ferrite (CoFe2O4) nano-flakes for supercapacitor application." *Applied Surface Science* 259: 39-43.

- Laguna-Marco, M. A., Piquer, C., Roca, A. G., Boada, R., Andres-Verges, M., Veintemillas-Verdaguer, S., Serna, C. J., Iadecola, A. and Chaboy, J. (**2014**). "Structural determination of Bi-doped magnetite multifunctional nanoparticles for contrast imaging." *Phys Chem Chem Phys* 16(34): 18301-18310.

- LaMer, V. K. and Dinegar, R. H. (**1950**). "Theory, production and mechanism of formation of monodispersed hydrosols." *Journal of the American Chemical Society* 72(11): 4847-4854.

- Landi, G. T. (**2014**). "Role of dipolar interaction in magnetic hyperthermia." *Physical Review B* 89(1).

- Lanone, S., Rogerieux, F., Geys, J., Dupont, A., Maillot-Marechal, E., Boczkowski, J., Lacroix, G. and Hoet, P. (**2009**). "Comparative toxicity of 24 manufactured nanoparticles in human alveolar epithelial and macrophage cell lines." *Part Fibre Toxicol* 6: 14.

- Larsen, B., Hurst, K., Ashurst, W. R., Serkova, N. and Stoldt, C. (**2012**). "Mono and dialkoxysilane surface modification of superparamagnetic iron oxide nanoparticles for application as magnetic resonance imaging contrast agents." *Journal of Materials Research* 27(14): 1846-1852.

- Lartigue, L., Alloyeau, D., Kolosnjaj-Tabi, J., Javed, Y., Guardia, P., Riedinger, A., Pechoux, C., Pellegrino, T., Wilhelm, C. and Gazeau, F. (**2013**). "Biodegradation of iron oxide nanocubes: high-resolution in situ monitoring." *ACS Nano* 7(5): 3939-3952.

- Lartigue, L., Hugounenq, P., Alloyeau, D., Clarke, S. P., Levy, M., Bacri, J. C., Bazzi, R., Brougham, D. F., Wilhelm, C. and Gazeau, F. (**2012**). "Cooperative organization in iron oxide multi-core nanoparticles potentiates their efficiency as heating mediators and MRI contrast agents." *ACS Nano* 6(12): 10935-10949.

- Lauffenburger, D. A. and Linderman, J. (**1993**). *Receptors: Models for Binding, Trafficking, and Signaling*, Oxford University Press.

- Laurent, S., Dutz, S., Hafeli, U. O. and Mahmoudi, M. (**2011**). "Magnetic fluid hyperthermia: focus on superparamagnetic iron oxide nanoparticles." *Adv Colloid Interface Sci* 166(1-2): 8-23.

- Laurent, S., Forge, D., Port, M., Roch, A., Robic, C., Vander Elst, L. and Muller, R. N. (**2008**). "Magnetic Iron Oxide Nanoparticles: Synthesis, Stabilization, Vectorization, Physicochemical Characterizations, and Biological Applications." *Chemical Reviews* 108(6): 2064-2110.

- Laurent, S., Saei, A., Behzadi, S., Panahifar, A. and Mahmoudi, M. (**2014**). "Superparamagnetic iron oxide nanoparticles for delivery of therapeutic agents: opportunities and challenges." *Expert opinion on drug delivery* 11(9): 1449-1470.

- Leconte, Y., Veintemillas-Verdaguer, S., Morales, M. P., Costo, R., Rodríguez, I., Bonville, P., Bouchet-Fabre, B., Herlin-Boime, N. (**2007**). "Continuous production of water dispersible carbon-iron nanocomposites by laser pyrolysis: application as MRI contrast." *Journal of Colloid and Interface Science* 313, 511-518.

- Lee, D. C., Smith, D. K., Heitsch, A. T. and Korgel, B. A. (**2007a**). "Colloidal magnetic nanocrystals: synthesis, properties and applications." *Annual Reports Section" C"(Physical Chemistry)* 103: 351-402.

- Lee, J. H., Huh, Y. M., Jun, Y. W., Seo, J. W., Jang, J. T., Song, H. T., Kim, S., Cho, E. J., Yoon, H. G., Suh, J. S. and Cheon, J. (**2007b**). "Artificially engineered magnetic nanoparticles for ultra-sensitive molecular imaging." *Nat Med* 13(1): 95-99.

- Lee, J. H., Jang, J. T., Choi, J. S., Moon, S. H., Noh, S. H., Kim, J. W., Kim, J. G., Kim, I. S., Park, K. I. and Cheon, J. (**2011**). "Exchange-coupled magnetic nanoparticles for efficient heat induction." *Nat Nanotechnol* 6(7): 418-422.

- Lee, N., Choi, S. H. and Hyeon, T. (**2013**). "Nano-sized CT contrast agents." *Adv Mater* 25(19): 2641-2660.

- Lehmann, A. D., Parak, W. J., Zhang, F., Ali, Z., Rocker, C., Nienhaus, G. U., Gehr, P. and Rothen-Rutishauser, B. (**2010**). "Fluorescent-magnetic hybrid nanoparticles induce a dose-dependent increase in proinflammatory response in lung cells in vitro correlated with intracellular localization." *Small* 6(6): 753-762.

- Levy, M., Wilhelm, C., Siaugue, J. M., Horner, O., Bacri, J. C. and Gazeau, F. (**2008**). "Magnetically induced hyperthermia: size-dependent heating power of gamma-Fe(2)O(3) nanoparticles." *J Phys Condens Matter* 20(20): 204133.

- Levy, P. M. and Fert, A. (**2006**). "Spin transfer in magnetic tunnel junctions with hot electrons." *Phys Rev Lett* 97(9): 097205.

- Li, Y., Li, C. H. and Talham, D. R. (**2015**). "One-step synthesis of gradient gadolinium ironhexacyanoferrate nanoparticles: a new particle design easily combining MRI contrast and photothermal therapy." *Nanoscale* 7(12): 5209-5216.

- Lide, D. R. (**1992**). *CRC handbook of chemistry and physics : a ready-reference book of chemical and physical data.* Boca Raton [etc.], CRC Press.

- Lim, J., Eggeman, A., Lanni, F., Tilton, R. D. and Majetich, S. A. (**2008**). "Synthesis and Single-Particle Optical Detection of Low-Polydispersity Plasmonic-Superparamagnetic Nanoparticles." *Advanced Materials* 20(9): 1721-1726.

- Ling, D. and Hyeon, T. (**2013**). "Chemical design of biocompatible iron oxide nanoparticles for medical applications." *Small* 9(9-10): 1450-1466.

- Ling, D., Lee, N. and Hyeon, T. (**2015**). "Chemical synthesis and assembly of uniformly sized iron oxide nanoparticles for medical applications." *Acc Chem Res* 48(5): 1276-1285.

- Liu, Y., Li, Y., Li, X.-M. and He, T. (**2013**). "Kinetics of (3-Aminopropyl)triethoxylsilane (APTES) Silanization of Superparamagnetic Iron Oxide Nanoparticles." *Langmuir* 29(49): 15275-15282.

- Lo, C. K., Xiao, D. and Choi, M. M. F. (**2007**). "Homocysteine-protected gold-coated magnetic nanoparticles: synthesis and characterisation." *Journal of Materials Chemistry* 17(23): 2418.

- Lo Nostro, P. and Ninham, B. W. (**2012**). "Hofmeister phenomena: an update on ion specificity in biology." *Chem Rev* 112(4): 2286-2322.

- Lopes-Moriyama, A. L., Madigou, V., Souza, C. P. d. and Leroux, C. (**2014**). "Controlled synthesis of CoFe2O4 nano-octahedra." *Powder Technology* 256: 482-489.

- Luengo, Y., Morales, M. P., Gutiérrez, L. and Veintemillas-Verdaguer, S. (**2016**). "Counterion and solvent effects on the size of magnetite nanocrystals obtained by oxidative precipitation." *J. Mater. Chem. C* 4(40): 9482-9488.

- Luengo, Y., Nardecchia, S., Morales, M. P. and Serrano, M. C. (**2013**). "Different cell responses induced by exposure to maghemite nanoparticles." *Nanoscale* 5(23): 11428-11437.

- Lundqvist, M., Stigler, J., Cedervall, T., Berggard, T., Flanagan, M. B., Lynch, I., Elia, G. and Dawson, K. (**2011**). "The evolution of the protein corona around nanoparticles: a test study." *ACS Nano* 5(9): 7503-7509.

- Lyklema, J. (**2009**). "Simple Hofmeister series." *Chemical Physics Letters* 467(4-6): 217-222.

- Lyon, J. L., Fleming, D. A., Stone, M. B., Schiffer, P. and Williams, M. E. (**2004**). "Synthesis of Fe Oxide Core/Au Shell Nanoparticles by Iterative Hydroxylamine Seeding." *Nano Letters* 4(4): 719-723.

- Ma, M., Wu, Y., Zhou, J., Sun, Y., Zhang, Y. and Gu, N. (**2004**). "Size dependence of specific power absorption of Fe3O4 particles in AC magnetic field." *Journal of Magnetism and Magnetic Materials* 268(1-2): 33-39.

- Mahmoudi, M., Sant, S., Wang, B., Laurent, S. and Sen, T. (**2011**). "Superparamagnetic iron oxide nanoparticles (SPIONs): development, surface modification and applications in chemotherapy." *Adv Drug Deliv Rev* 63(1-2): 24-46.

- Maier-Hauff, K., Ulrich, F., Nestler, D., Niehoff, H., Wust, P., Thiesen, B., Orawa, H., Budach, V. and Jordan, A. (**2011**). "Efficacy and safety of intratumoral thermotherapy using

magnetic iron-oxide nanoparticles combined with external beam radiotherapy on patients with recurrent glioblastoma multiforme." *J Neurooncol* 103(2): 317-324.

- Mandal, M., Kundu, S., Ghosh, S. K., Panigrahi, S., Sau, T. K., Yusuf, S. M. and Pal, T. (**2005**). "Magnetite nanoparticles with tunable gold or silver shell." *J Colloid Interface Sci* 286(1): 187-194.

- Marciello, M., Connord, V., Veintemillas-Verdaguer, S., Vergés, M. A., Carrey, J., Respaud, M., Serna, C. J. and Morales, M. P. (**2013**). "Large scale production of biocompatible magnetite nanocrystals with high saturation magnetization values through green aqueous synthesis." *Journal of Materials Chemistry B* 1(43): 5995.

- Marciello, M., Luengo, Y. and Morales, M. P (**2016**). Iron Oxide Nanoparticles for Cancer Diagnosis and Therapy. *Nanoarchitectonics for Smart Delivery and Drug Targeting*. A. M. Holban and A. M. Grumezescu, Elsevier 667-694.

- Martinez-Boubeta, C., Simeonidis, K., Serantes, D., Conde-Leborán, I., Kazakis, I., Stefanou, G., Peña, L., Galceran, R., Balcells, L., Monty, C., Baldomir, D., Mitrakas, M. and Angelakeris, M. (**2012**). "Adjustable Hyperthermia Response of Self-Assembled Ferromagnetic Fe-MgO Core-Shell Nanoparticles by Tuning Dipole-Dipole Interactions." *Advanced Functional Materials* 22(17): 3737-3744.

- Massart, R. (**1981**). "Preparation of aqueous magnetic liquids in alkaline and acidic media." *IEEE Transactions on Magnetics* 17(2): 1247-1248.

- Matijević, E. and Cimaš, Š. (**1987**). "Formation of uniform colloidal iron (III) oxides in ethylene glycol-water solutions." *Colloid and Polymer Science* 265(2): 155-163.

- McCarthy, J. R. and Weissleder, R. (**2008**). "Multifunctional magnetic nanoparticles for targeted imaging and therapy." *Advanced Drug Delivery Reviews* 60(11): 1241-1251.

- McNaught, A. D. and Wilkinson, A. (**1997**). *IUPAC. Compendium of Chemical Terminology, 2nd ed. (the "Gold Book")*, Blackwell Scientific Publications, Oxford 2nd Revised Edition

- Mehdaoui, B., Meffre, A., Carrey, J., Lachaize, S., Lacroix, L.-M., Gougeon, M., Chaudret, B. and Respaud, M. (**2011**). "Optimal Size of Nanoparticles for Magnetic Hyperthermia: A Combined Theoretical and Experimental Study." *Advanced Functional Materials* 21(23): 4573-4581.

- Mehdaoui, B., Tan, R. P., Meffre, A., Carrey, J., Lachaize, S., Chaudret, B. and Respaud, M. (**2013**). "Increase of magnetic hyperthermia efficiency due to dipolar interactions in low-anisotropy magnetic nanoparticles: Theoretical and experimental results." *Physical Review B* 87(17).

- Merk, V., Rehbock, C., Becker, F., Hagemann, U., Nienhaus, H. and Barcikowski, S. (**2014**). "In situ non-DLVO stabilization of surfactant-free, plasmonic gold nanoparticles: effect of Hofmeister's anions." *Langmuir* 30(15): 4213-4222.

- Mikhaylova, M., Kim, D. K., Bobrysheva, N., Osmolowsky, M., Semenov, V., Tsakalakos, T. and Muhammed, M. (**2004**). "Superparamagnetism of magnetite nanoparticles: dependence on surface modification." *Langmuir* 20(6): 2472-2477.

- Miller, A. L. (**1998**). "Dimercaptosuccinic acid (DMSA), a non-toxic, water-soluble treatment for heavy metal toxicity." *Alternative medicine review* 3(3): 199-207.

- Mokari, T., Rothenberg, E., Popov, I., Costi, R. and Banin, U. (**2004**). "Selective growth of metal tips onto semiconductor quantum rods and tetrapods." *Science* 304(5678): 1787-1790.

- Morales, M. P., Gonzalez-Carreno, T. and Serna, C. (**1992**). "The formation of a–Fe 2 O 3 monodispersed particles in solution." *Journal of Materials Research* 7(09): 2538-2545.

- Morales, M. P., Pecharroman, C., Carreñ, T. G. and Serna, C. (**1994**). "Structural characteristics of uniform γ-Fe 2 O 3 particles with different axial (length/width) ratios." *Journal of Solid State Chemistry* 108(1): 158-163.

- Morales, M. P., Veintemillas-Verdaguer, S. and Serna, C. J. (**1999**). "Magnetic properties of uniform γ–Fe2O3 nanoparticles smaller than 5 nm prepared by laser pyrolysis." *Journal of Materials Research* 14(07): 3066-3072.

- Mornet, S., Portier, J. and Duguet, E. (**2005**). "A method for synthesis and functionalization of ultrasmall superparamagnetic covalent carriers based on maghemite and dextran." *Journal of Magnetism and Magnetic Materials* 293(1): 127-134.

- Mornet, S., Vasseur, S., Grasset, F. and Duguet, E. (**2004**). "Magnetic nanoparticle design for medical diagnosis and therapy." *Journal of Materials Chemistry* 14(14): 2161.

- Moser, A., Takano, K., Margulies, D. T., Albrecht, M., Sonobe, Y., Ikeda, Y., Sun, S. and Fullerton, E. E. (**2002**). "Magnetic recording: advancing into the future." *Journal of Physics D: Applied Physics* 35(19): R157.

- Mukh-Qasem, R. A. and Gedanken, A. (**2005**). "Sonochemical synthesis of stable hydrosol of Fe 3 O 4 nanoparticles." *Journal of Colloid and Interface Science* 284(2): 489-494.

- Muthu, M. S., Leong, D. T., Mei, L. and Feng, S. S. (**2014**). "Nanotheranostics - application and further development of nanomedicine strategies for advanced theranostics." *Theranostics* 4(6): 660-677.

- Myers, D. (**1999**). *Surfaces, interfaces, and colloids: principles and applications*, Wiley-VCH.

- Na, H. B., Song, I. C. and Hyeon, T. (**2009**). "Inorganic Nanoparticles for MRI Contrast Agents." *Advanced Materials* 21(21): 2133-2148.

- Nairan, A., Khan, U., Iqbal, M., Khan, M., Javed, K., Riaz, S., Naseem, S. and Han, X. (**2016**). "Structural and Magnetic Response in Bimetallic Core/Shell Magnetic Nanoparticles." *Nanomaterials* 6(4): 72.

- Narayanan, S., Sathy, B. N., Mony, U., Koyakutty, M., Nair, S. V. and Menon, D. (**2012**). "Biocompatible magnetite/gold nanohybrid contrast agents via green chemistry for MRI and CT bioimaging." *ACS Appl Mater Interfaces* 4(1): 251-260.

- Natividad, E., Castro, M. and Mediano, A. (**2009**). "Adiabatic vs. non-adiabatic determination of specific absorption rate of ferrofluids." *Journal of Magnetism and Magnetic Materials* 321(10): 1497-1500.

- Neuberger, T., Schöpf, B., Hofmann, H., Hofmann, M. and von Rechenberg, B. (**2005**). "Superparamagnetic nanoparticles for biomedical applications: Possibilities and limitations of a new drug delivery system." *Journal of Magnetism and Magnetic Materials* 293(1): 483-496.

- Nikoforov, V. N. and Oksengendler, B. L. (**2014**). "Magnetometric study of gadolinium solubility in magnetite nanocrystals." *Inorganic Materials* 50(12): 1222-1225.

- Nishio, K., Ikeda, M., Gokon, N., Tsubouchi, S., Narimatsu, H., Mochizuki, Y., Sakamoto, S., Sandhu, A., Abe, M. and Handa, H. (**2007**). "Preparation of size-controlled (30–100nm) magnetite nanoparticles for biomedical applications." *Journal of Magnetism and Magnetic Materials* 310(2): 2408-2410.

- O'Grady, K. and Bradbury, A. (**1983**). "Particle size analysis in ferrofluids." *Journal of Magnetism and Magnetic Materials* 39(1-2): 91-94.

- Oliveira, A., Cunha, D., Ladriere, L., Igoillo Esteve, M., Bugliani, M., Marchetti, P. and Cnop, M. (**2015**). "In vitro use of free fatty acids bound to albumin: A comparison of protocols." *BioTechniques* 58(5): 228-233.

- Orbaek, A. W., Morrow, L., Maguire-Boyle, S. J. and Barron, A. R. (**2013**). "Reagent control over the composition of mixed metal oxide nanoparticles." *Journal of Experimental Nanoscience* 10(5): 324-349.

- Palchoudhury, S., An, W., Xu, Y., Qin, Y., Zhang, Z., Chopra, N., Holler, R. A., Turner, C. H. and Bao, Y. (**2011**). "Synthesis and growth mechanism of iron oxide nanowhiskers." *Nano Lett* 11(3): 1141-1146.

- Pan, X., Siewerdsen, J., La Riviere, P. J. and Kalender, W. A. (**2008**). "Anniversary paper. Development of x-ray computed tomography: the role of medical physics and AAPM from the 1970s to present." *Med Phys* 35(8): 3728-3739.

- Pande, M., Mehta, A., Pant, B. P. and Flora, S. J. S. (**2001**). "Combined administration of a chelating agent and an antioxidant in the prevention and treatment of acute lead intoxication in rats." *Environmental Toxicology and Pharmacology* 9(4): 173-184.

- Pankhurst, Q. A., Connolly, J., Jones, S. K. and Dobson, J. (**2003**). "Applications of magnetic nanoparticles in biomedicine." *Journal of Physics D: Applied Physics* 36(13): R167.

- Park, J. C., Yeo, S., Kim, M., Lee, G. T. and Seo, J. H. (**2016**). "Synthesis and characterization of novel lanthanide-doped magnetite@Au core@shell nanoparticles." *Materials Letters* 181: 272-277.

- Parks, G. A. (**1965**). "The isoelectric points of solid oxides, solid hydroxides, and aqueous hydroxo complex systems." *Chemical Reviews* 65(2): 177-198.

- Parsons, D. F., Bostrom, M., Lo Nostro, P. and Ninham, B. W. (**2011**). "Hofmeister effects: interplay of hydration, nonelectrostatic potentials, and ion size." *Phys Chem Chem Phys* 13(27): 12352-12367.

- Patange, S. M., Shirsath, S. E., Toksha, B. G., Jadhav, S. S., Shukla, S. J. and Jadhav, K. M. (**2008**). "Cation distribution by Rietveld, spectral and magnetic studies of chromium-substituted nickel ferrites." *Applied Physics A* 95(2): 429-434.

- Patil, R. M., Shete, P. B., Thorat, N. D., Otari, S. V., Barick, K. C., Prasad, A., Ningthoujam, R. S., Tiwale, B. M. and Pawar, S. H. (**2014**). "Non-aqueous to aqueous phase transfer of oleic acid coated iron oxide nanoparticles for hyperthermia application." *RSC Advances* 4(9): 4515-4522.

- Pelaz, B., del Pino, P., Maffre, P., Hartmann, R., Gallego, M., Rivera-Fernandez, S., de la Fuente, J. M., Nienhaus, G. U. and Parak, W. J. (**2015**). "Surface Functionalization of Nanoparticles with Polyethylene Glycol: Effects on Protein Adsorption and Cellular Uptake." *ACS Nano* 9(7): 6996-7008.

- Pennycook, S. J., Chisholm, M. F., Lupini, A. R., Varela, M., Borisevich, A. Y., Oxley, M. P., Luo, W. D., van Benthem, K., Oh, S.-H., Sales, D. L., Molina, S. I., García-Barriocanal, J., Leon, C., Santamaría, J., Rashkeev, S. N. and Pantelides, S. T. (**2009**). "Aberration-corrected scanning transmission electron microscopy: from atomic imaging and analysis to solving energy problems."

Philosophical Transactions of the Royal Society A: Mathematical, Physical and Engineering Sciences 367(1903): 3709-3733.

- Petros, R. A. and DeSimone, J. M. (**2010**). "Strategies in the design of nanoparticles for therapeutic applications." *Nat Rev Drug Discov* 9(8): 615-627.

- Piñeiro-Redondo, Y., Banobre-Lopez, M., Pardinas-Blanco, I., Goya, G., Lopez-Quintela, M. A. and Rivas, J. (**2011**). "The influence of colloidal parameters on the specific power absorption of PAA-coated magnetite nanoparticles." *Nanoscale Res Lett* 6(1): 383.

- Pisanic, T. R., 2nd, Blackwell, J. D., Shubayev, V. I., Finones, R. R. and Jin, S. (**2007**). "Nanotoxicity of iron oxide nanoparticle internalization in growing neurons." *Biomaterials* 28(16): 2572-2581.

- Pissuwan, D., Valenzuela, S. M. and Cortie, M. B. (**2006**). "Therapeutic possibilities of plasmonically heated gold nanoparticles." *Trends Biotechnol* 24(2): 62-67.

- Port, M., Corot, C., Raynal, I. and Rousseaux, O. (**2009**). Nouvelles compositions de particules magnetiques recouvertes de derives gem-bisphosphonates, Google Patents.

- Powers, K.W., Brown, S.C., Krishna, V.B., Wasdo, S.C., Moudgil, B.M., Roberts, S.M. (**2006**). "Research stragegies for safety evaluation of nanomaterials. Part VI. Characterization of nanoscale particles for toxicological evaluation". *Toxicological Sciences* 90(2): 296-303.

- Prodi, L., Rampazzo, E., Rastrelli, F., Speghini, A. and Zaccheroni, N. (**2015**). "Imaging agents based on lanthanide doped nanoparticles." *Chem Soc Rev* 44(14): 4922-4952.

- Qian, Z. M., Li, H., Sun, H. and Ho, K. (**2002**). "Targeted drug delivery via the transferrin receptor-mediated endocytosis pathway." *Pharmacol Rev* 54(4): 561-587.

- Raju, G. S. R., Benton, L., Pavitra, E. and Yu, J. S. (**2015**). "Multifunctional nanoparticles: Recent progress in cancer therapeutics." *Chemical Communications* 51(68): 13248-13259.

- Rao, C. N. R., Thomas, P. J. and Kulkarni, G. U. (**2007**). Basics of Nanocrystals. *Nanocrystals: Synthesis, Properties and Applications*. Berlin, Heidelberg, Springer Berlin Heidelberg**:** 1-23.

- Reddy, L. H., Arias, J. L., Nicolas, J. and Couvreur, P. (**2012**). "Magnetic nanoparticles: design and characterization, toxicity and biocompatibility, pharmaceutical and biomedical applications." *Chem Rev* 112(11): 5818-5878.

- Regazzoni, A. E. and Matijević, E. (**1983**). "Formation of uniform colloidal mixed cobalt—nickel ferrite particles." *Colloids and Surfaces* 6(2): 189-201.

- Rickard, D. and Luther, G. W., III (**2007**). "Chemistry of iron sulfides." *Chem Rev* 107(2): 514-562.

- Rivera-Gil, P., Jimenez de Aberasturi, D., Wulf, V., Pelaz, B., del Pino, P., Zhao, Y., de la Fuente, J. M., Ruiz de Larramendi, I., Rojo, T., Liang, X. J. and Parak, W. J. (**2013**). "The challenge to relate the physicochemical properties of colloidal nanoparticles to their cytotoxicity." *Acc Chem Res* 46(3): 743-749.

- Robinson, I., Tung le, D., Maenosono, S., Walti, C. and Thanh, N. T. (**2010**). "Synthesis of core-shell gold coated magnetic nanoparticles and their interaction with thiolated DNA." *Nanoscale* 2(12): 2624-2630.

- Roca, A. G., Veintemillas-Verdaguer, S., Port, M., Robic, C., Serna, C. J. and Morales, M. P. (**2009**). "Effect of nanoparticle and aggregate size on the relaxometric properties of MR contrast agents based on high quality magnetite nanoparticles." *J Phys Chem B* 113(19): 7033-7039.

- Roch, A., Gossuin, Y., Muller, R. N. and Gillis, P. (**2005**). "Superparamagnetic colloid suspensions: Water magnetic relaxation and clustering." *Journal of Magnetism and Magnetic Materials* 293(1): 532-539.

- Roch, A., Muller, R. N. and Gillis, P. (**1999**). "Theory of proton relaxation induced by superparamagnetic particles." *The Journal of Chemical Physics* 110(11): 5403-5411.

- Rojas-Chapana, J. A., Correa-Duarte, M. A., Ren, Z., Kempa, K. and Giersig, M. (**2004**). "Enhanced Introduction of Gold Nanoparticles into VitalAcidothiobacillus ferrooxidansby Carbon Nanotube-based Microwave Electroporation." *Nano Letters* 4(5): 985-988.

- Ross, C. A. (**2001**). "Patterned magnetic recording media." *Annual Review of Materials Research* 31(1): 203-235.

- Rouhana, L. and Schlenoff, J. (**2012**). "Aggregation resistant zwitterated superparamagnetic nanoparticles." *Journal of Nanoparticle Research* 14(5).

- Roux, S., Faure, A.-C., Mandon, C., Dufort, S., Rivière, C., Bridot, J.-L., Mutelet, B., Marquette, C. A., Josserand, V., Le Duc, G., Le Pape, A., Billotey, C., Janier, M., Coll, J.-L., Perriat, P. and Tillement, O. (**2010**). "Multifunctional gadolinium oxide nanoparticles: towards image-guided therapy." *Imaging in Medicine* 2(2): 211-223.

- Ruiz, A., Salas, G., Calero, M., Hernandez, Y., Villanueva, A., Herranz, F., Veintemillas-Verdaguer, S., Martinez, E., Barber, D. F. and Morales, M. P. (**2013**). "Short-chain PEG molecules strongly bound to magnetic nanoparticle for MRI long circulating agents." *Acta Biomater* 9(5): 6421-6430.

- Sadeghi, O., Zakharov, L. N. and Nyman, M. (**2015**). "Crystal growth. Aqueous formation and manipulation of the iron-oxo Keggin ion." *Science* 347(6228): 1359-1362.

- Salas, G., Casado, C., Teran, F. J., Miranda, R., Serna, C. J. and Morales, M. P. (**2012**). "Controlled synthesis of uniform magnetite nanocrystals with high-quality properties for biomedical applications." *Journal of Materials Chemistry* 22(39): 21065.

- Salas, G., Veintemillas-Verdaguer, S. and Morales, M. P. (**2013**). "Relationship between physico-chemical properties of magnetic fluids and their heating capacity." *International Journal of Hyperthermia* 29(8): 768-776.

- Salis, A. and Ninham, B. W. (**2014**). "Models and mechanisms of Hofmeister effects in electrolyte solutions, and colloid and protein systems revisited." *Chem Soc Rev* 43(21): 7358-7377.

- Santra, S., Yang, H., Holloway, P. H., Stanley, J. T. and Mericle, R. A. (**2005**). "Synthesis of water-dispersible fluorescent, radio-opaque, and paramagnetic CdS:Mn/ZnS quantum dots: a multifunctional probe for bioimaging." *J Am Chem Soc* 127(6): 1656-1657.

- Sathya, A., Guardia, P., Brescia, R., Silvestri, N., Pugliese, G., Nitti, S., Manna, L. and Pellegrino, T. (**2016**). "CoxFe3–xO4Nanocubes for Theranostic Applications: Effect of Cobalt Content and Particle Size." *Chemistry of Materials* 28(6): 1769-1780.

- Schartl, W. (**2010**). "Current directions in core-shell nanoparticle design." *Nanoscale* 2(6): 829-843.

- Schladt, T. D., Schneider, K., Schild, H. and Tremel, W. (**2011**). "Synthesis and bio-functionalization of magnetic nanoparticles for medical diagnosis and treatment." *Dalton Trans* 40(24): 6315-6343.

- Schoepf, U., Marecos, E. M., Melder, R. J., Jain, R. K. and Weissleder, R. (**1998**). "Intracellular magnetic labeling of lymphocytes for in vivo trafficking studies." *Biotechniques* 24(4): 642-646, 648-651.

- Schultz-Sikma, E. A., Joshi, H. M., Ma, Q., Macrenaris, K. W., Eckermann, A. L., Dravid, V. P. and Meade, T. J. (**2011**). "Probing the Chemical Stability of Mixed Ferrites: Implications for MR Contrast Agent Design." *Chem Mater* 23(10): 2657-2664.

- Schwertmann, U. and Cornell, R. M. (**2008**). *Iron oxides in the laboratory: preparation and characterization*, John Wiley & Sons.

- Schwertmann, U. and Taylor, R. M. (**1989**). Iron Oxides. *Minerals in Soil Environments*. J. B. Dixon and S. B. Weed. Madison, WI, Soil Science Society of America**:** 379-438.

- Semelka, R. C. and Helmberger, T. K. (**2001**). "Contrast agents for MR imaging of the liver." *Radiology* 218(1): 27-38.

- Serantes, D., Baldomir, D., Martinez-Boubeta, C., Simeonidis, K., Angelakeris, M., Natividad, E., Castro, M., Mediano, A., Chen, D. X., Sanchez, A., Balcells, L. I. and Martínez, B. (**2010**). "Influence of dipolar interactions on hyperthermia properties of ferromagnetic particles." *Journal of Applied Physics* 108(7): 073918.

- Serrano, M. C., Pagani, R., Vallet-Regi, M., Pena, J., Ramila, A., Izquierdo, I. and Portoles, M. T. (**2004**). "In vitro biocompatibility assessment of poly(epsilon-caprolactone) films using L929 mouse fibroblasts." *Biomaterials* 25(25): 5603-5611.

- Shah, B., Yin, P. T., Ghoshal, S. and Lee, K. B. (**2013**). "Multimodal magnetic core-shell nanoparticles for effective stem-cell differentiation and imaging." *Angew Chem Int Ed Engl* 52(24): 6190-6195.

- Sharifi, S., Behzadi, S., Laurent, S., Forrest, M. L., Stroeve, P. and Mahmoudi, M. (**2012**). "Toxicity of nanomaterials." *Chem Soc Rev* 41(6): 2323-2343.

- Shete, P. B., Patil, R. M., Tiwale, B. M. and Pawar, S. H. (**2015**). "Water dispersible oleic acid-coated Fe3O4 nanoparticles for biomedical applications." *Journal of Magnetism and Magnetic Materials* 377: 406-410.

- Shi, X., Thomas, T. P., Myc, L. A., Kotlyar, A. and Baker, J. R., Jr. (**2007**). "Synthesis, characterization, and intracellular uptake of carboxyl-terminated poly(amidoamine) dendrimer-stabilized iron oxide nanoparticles." *Phys Chem Chem Phys* 9(42): 5712-5720.

- Shih, J.-L. A. and Brugger, R. M. (**1992**). "Gadolinium as a neutron capture therapy agent." *Medical Physics* 19(3): 733-744.

- Shin, J., Anisur, R. M., Ko, M. K., Im, G. H., Lee, J. H. and Lee, I. S. (**2009**). "Hollow manganese oxide nanoparticles as multifunctional agents for magnetic resonance imaging and drug delivery." *Angew Chem Int Ed Engl* 48(2): 321-324.

- Shin, T. H., Choi, Y., Kim, S. and Cheon, J. (**2015**). "Recent advances in magnetic nanoparticle-based multi-modal imaging." *Chem Soc Rev* 44(14): 4501-4516.

- Shukla, R., Bansal, V., Chaudhary, M., Basu, A., Bhonde, R. R. and Sastry, M. (**2005**). "Biocompatibility of gold nanoparticles and their endocytotic fate inside the cellular compartment: a microscopic overview." *Langmuir* 21(23): 10644-10654.

- Si, S., Kotal, A., Mandal, T. K., Giri, S., Nakamura, H. and Kohara, T. (**2004**). "Size-Controlled Synthesis of Magnetite Nanoparticles in the Presence of Polyelectrolytes." *Chemistry of Materials* 16(18): 3489-3496.

- Silvio, D. and Rudolf, H. (**2014**). "Magnetic particle hyperthermia—a promising tumour therapy?" *Nanotechnology* 25(45): 452001.

- Singh, A. and Sahoo, S. K. (**2014**). "Magnetic nanoparticles: a novel platform for cancer theranostics." *Drug Discov Today* 19(4): 474-481.

- Soenen, S. J. and De Cuyper, M. (**2009**). "Assessing cytotoxicity of (iron oxide-based) nanoparticles: an overview of different methods exemplified with cationic magnetoliposomes." *Contrast Media Mol Imaging* 4(5): 207-219.

- Soenen, S. J., De Meyer, S. F., Dresselaers, T., Vande Velde, G., Pareyn, I. M., Braeckmans, K., De Cuyper, M., Himmelreich, U. and Vanhoorelbeke, K. I. (**2011a**). "MRI assessment of blood outgrowth endothelial cell homing using cationic magnetoliposomes." *Biomaterials* 32(17): 4140-4150.

- Soenen, S. J., Nuytten, N., De Meyer, S. F., De Smedt, S. C. and De Cuyper, M. (**2010**). "High intracellular iron oxide nanoparticle concentrations affect cellular cytoskeleton and focal adhesion kinase-mediated signaling." *Small* 6(7): 832-842.

- Soenen, S. J., Rivera-Gil, P., Montenegro, J.-M., Parak, W. J., De Smedt, S. C. and Braeckmans, K. (**2011b**). "Cellular toxity of inorganic nanoparticles: Common aspects and guidelines for improved nanotoxicity evaluation." *Nano Today* 6(5): 446-465.

- Sood, A., Arora, V., Shah, J., Kotnala, R. K. and Jain, T. K. (**2016**). "Ascorbic acid-mediated synthesis and characterisation of iron oxide/gold core–shell nanoparticles." *Journal of Experimental Nanoscience* 11(5): 370-382.

- Sosnovik, D. E., Nahrendorf, M. and Weissleder, R. (**2008**). "Magnetic nanoparticles for MR imaging: agents, techniques and cardiovascular applications." *Basic Res Cardiol* 103(2): 122-130.

- Spaldin, N. A. (**2003**). *Magnetic Materials: Fundamentals and Device Applications*, Cambridge University Press.

- Srinivasan, B. and Huang, X. (**2008**). "Functionalization of magnetic nanoparticles with organic molecules: Loading level determination and evaluation of linker length effect on immobilization." *Chirality* 20(3-4): 265-277.

- Starowicz, M., Starowicz, P., Zukrowski, J., Przewoznik, J., Lemanski, A., Kapusta, C. and Banas, J. (**2011**). "Electrochemical synthesis of magnetic iron oxide nanoparticles with controlled size." *J Nanopart Res* 13(12): 7167-7176.

- Sugimoto, T. and Matijević, E. (**1980**). "Formation of uniform spherical magnetite particles by crystallization from ferrous hydroxide gels." *Journal of Colloid and Interface Science* 74(1): 227-243.

- Sun, C., Lee, J. S. and Zhang, M. (**2008**). "Magnetic nanoparticles in MR imaging and drug delivery." *Adv Drug Deliv Rev* 60(11): 1252-1265.

- Sun, L., Zang, Y., Sun, M., Wang, H., Zhu, X., Xu, S., Yang, Q., Li, Y. and Shan, Y. (**2010**). "Synthesis of magnetic and fluorescent multifunctional hollow silica nanocomposites for live cell imaging." *J Colloid Interface Sci* 350(1): 90-98.

- Sun, S., Zeng, H., Robinson, D. B., Raoux, S., Rice, P. M., Wang, S. X. and Li, G. (**2004**). "Monodisperse MFe2O4 (M = Fe, Co, Mn) nanoparticles." *J Am Chem Soc* 126(1): 273-279.

- Suzuki, H., Sawai, Y. and Takada, M. (**1999**). "Molecular weight of agar by high temperature type gel permeation chromatography and physical properties." *Journal-Japanese Society Of Food Science And Technology* 46(12): 821-826.

- Sweetman, M. J., Shearer, C. J., Shapter, J. G. and Voelcker, N. H. (**2011**). "Dual Silane Surface Functionalization for the Selective Attachment of Human Neuronal Cells to Porous Silicon." *Langmuir* 27(15): 9497-9503.

- Sytnyk, M., Kirchschlager, R., Bodnarchuk, M. I., Primetzhofer, D., Kriegner, D., Enser, H., Stangl, J., Bauer, P., Voith, M., Hassel, A. W., Krumeich, F., Ludwig, F., Meingast, A., Kothleitner, G., Kovalenko, M. V. and Heiss, W. (**2013**). "Tuning the magnetic properties of metal oxide nanocrystal heterostructures by cation exchange." *Nano Lett* 13(2): 586-593.

- Taboada, E., Rodriguez, E., Roig, A., Oro, J., Roch, A. and Muller, R. N. (**2007**). "Relaxometric and magnetic characterization of ultrasmall iron oxide nanoparticles with high magnetization. Evaluation as potential T1 magnetic resonance imaging contrast agents for molecular imaging." *Langmuir* 23(8): 4583-4588.

- Takeno, N. (**2005**). Atlas of Eh-pH diagrams: Intercomparison of thermodynamics databases *National Institute of Advanced Industrial Science and Technology*. G. S. o. J. o. f. r. N. 419, Research Center for deep Geological Environments.

- Tamaura, Y., Buduan, P. V. and Katsura, T. (**1981**). "Studies on the oxidation of iron(II) ion during the formation of Fe3O4 and [small alpha]-FeO(OH) by air oxidation of Fe[OH]2 suspensions." *Journal of the Chemical Society, Dalton Transactions*(9): 1807-1811.

- Tamura, H., Goto, K. and Nagayama, M. (**1976**). "Effect of anions on the oxygenation of ferrous ion in neutral solutions." *Journal of Inorganic and Nuclear Chemistry* 38(1): 113-117.

- Tamura, H. and Matijevic, E. (**1982**). "Precipitation of cobalt ferrites." *Journal of Colloid and Interface Science* 90(1): 100-109.

- Tan, R. L., Song, X., Chen, B., Chong, W. H., Fang, Y., Zhang, H., Wei, J. and Chen, H. (**2016**). "Levelling the playing field: screening for synergistic effects in coalesced bimetallic nanoparticles." *Nanoscale* 8(6): 3447-3453.

- Tartaj, P. (**2006**). "Nanomagnets-from fundamental physics to biomedicine." *Current Nanoscience* 2(1): 43-53.

- Tartaj, P. and Serna, C. J. (**2003**). "Synthesis of Monodisperse Superparamagnetic Fe/Silica Nanospherical Composites." *Journal of the American Chemical Society* 125(51): 15754-15755.

- Taylor, R. and McKenzie, R. (**1980**). "The influence of aluminum on iron oxides. VI. The formation of Fe (II)-AI (III) hydroxychlorides,-sulfates, and-carbonates as new members of the pyroaurite group and their significance in soils." *Clays Clay Miner* 28: 179-187.

- Templeton, A. C., Pietron, J. J., Murray, R. W. and Mulvaney, P. (**2000**). "Solvent Refractive Index and Core Charge Influences on the Surface Plasmon Absorbance of

Alkanethiolate Monolayer-Protected Gold Clusters." *The Journal of Physical Chemistry B* 104(3): 564-570.

- Teng, X., Black, D., Watkins, N. J., Gao, Y. and Yang, H. (**2003**). "Platinum-Maghemite Core−Shell Nanoparticles Using a Sequential Synthesis." *Nano Letters* 3(2): 261-264.

- Thünemann, A. F., Schütt, D., Kaufner, L., Pison, U. and Möhwald, H. (**2006**). "Maghemite Nanoparticles Protectively Coated with Poly(ethylene imine) and Poly(ethylene oxide)-block-poly(glutamic acid)." *Langmuir* 22(5): 2351-2357.

- Tkachenko, A. G., Xie, H., Coleman, D., Glomm, W., Ryan, J., Anderson, M. F., Franzen, S. and Feldheim, D. L. (**2003**). "Multifunctional gold nanoparticle-peptide complexes for nuclear targeting." *J Am Chem Soc* 125(16): 4700-4701.

- Tourinho, F. A., Franck, R. and Massart, R. (**1990**). "Aqueous ferrofluids based on manganese and cobalt ferrites." *Journal of Materials Science* 25(7): 3249-3254.

- Usov, N. A. (**2010**). "Low frequency hysteresis loops of superparamagnetic nanoparticles with uniaxial anisotropy." *Journal of Applied Physics* 107(12): 123909.

- van der Linden, M., Conchuir, B. O., Spigone, E., Niranjan, A., Zaccone, A. and Cicuta, P. (**2015**). "Microscopic Origin of the Hofmeister Effect in Gelation Kinetics of Colloidal Silica." *J Phys Chem Lett* 6(15): 2881-2887.

- van Ewijk, G. A., Vroege, G. J. and Philipse, A. P. (**1999**). "Convenient preparation methods for magnetic colloids." *Journal of Magnetism and Magnetic Materials* 201(1–3): 31-33.

- Veintemillas-Verdaguer, S., Luengo, Y., Serna, C. J., Andres-Verges, M., Varela, M., Calero, M., Lazaro-Carrillo, A., Villanueva, A., Sisniega, A., Montesinos, P. and Morales, M. P. (**2015**). "Bismuth labeling for the CT assessment of local administration of magnetic nanoparticles." *Nanotechnology* 26(13): 135101.

- Veintemillas-Verdaguer, S., Marciello, M., Morales, M. P., Serna, C. J. and Andrés-Vergés, M. (**2014**). "Magnetic nanocrystals for biomedical applications." *Progress in Crystal Growth and Characterization of Materials* 60(3-4): 80-86.

- Vereda, F., de Vicente, J., Morales, M. P., Rull, F. and Hidalgo-Álvarez, R. (**2008**). "Synthesis and Characterization of Single-Domain Monocrystalline Magnetite Particles by Oxidative Aging of Fe(OH)2." *The Journal of Physical Chemistry C* 112(15): 5843-5849.

- Vereda, F., Martin-Molina, A., Hidalgo-Alvarez, R. and Quesada-Perez, M. (**2015**). "Specific ion effects on the electrokinetic properties of iron oxide nanoparticles: experiments and simulations." *Phys Chem Chem Phys* 17(26): 17069-17078.

- Verma, A. and Stellacci, F. (**2010**). "Effect of surface properties on nanoparticle-cell interactions." *Small* 6(1): 12-21.

- Villanueva, A., Canete, M., Roca, A. G., Calero, M., Veintemillas-Verdaguer, S., Serna, C. J., Morales M. P. and Miranda, R. (**2009**). "The influence of surface functionalization on the enhanced internalization of magnetic nanoparticles in cancer cells." *Nanotechnology* 20(11): 115103.

- Villanueva, A., de la Presa, P., Alonso, J. M., Rueda, T., Martínez, A., Crespo, P., Morales, M. P., Gonzalez-Fernandez, M. A., Valdés, J. and Rivero, G. (**2010**). "Hyperthermia HeLa Cell Treatment with Silica-Coated Manganese Oxide Nanoparticles." *The Journal of Physical Chemistry C* 114(5): 1976-1981.

- Vuong, Q. L., Berret, J. F., Fresnais, J., Gossuin, Y. and Sandre, O. (**2012**). "A universal scaling law to predict the efficiency of magnetic nanoparticles as MRI T(2)-contrast agents." *Adv Healthc Mater* 1(4): 502-512.

- Wahajuddin, M. and Arora, S. (**2012**). "Superparamagnetic iron oxide nanoparticles: magnetic nanoplatforms as drug carriers." *Int J Nanomedicine* 7: 3445-3471.

- Waldron, R. D. (**1955**). "Infrared Spectra of Ferrites." *Physical Review* 99(6): 1727-1735.

- Wang, D., He, J., Rosenzweig, N. and Rosenzweig, Z. (**2004**). "Superparamagnetic Fe2O3Beads−CdSe/ZnS Quantum Dots Core−Shell Nanocomposite Particles for Cell Separation." *Nano Letters* 4(3): 409-413.

- Wang, G., Peng, Q. and Li, Y. (**2011a**). "Lanthanide-doped nanocrystals: synthesis, optical-magnetic properties, and applications." *Acc Chem Res* 44(5): 322-332.

- Wang, J., Deng, T. and Dai, Y. (**2005a**). "Study on the processes and mechanism of the formation of Fe3O4 at low temperature." *Journal of Alloys and Compounds* 390(1-2): 127-132.

- Wang, L., Bai, J., Li, Y. and Huang, Y. (**2008**). "Multifunctional nanoparticles displaying magnetization and near-IR absorption." *Angew Chem Int Ed Engl* 47(13): 2439-2442.

- Wang, L., Luo, J., Fan, Q., Suzuki, M., Suzuki, I. S., Engelhard, M. H., Lin, Y., Kim, N., Wang, J. Q. and Zhong, C. J. (**2005b**). "Monodispersed core-shell Fe3O4@Au nanoparticles." *J Phys Chem B* 109(46): 21593-21601.

- Wang, X., Zhou, Z., Wang, Z., Xue, Y., Zeng, Y., Gao, J., Zhu, L., Zhang, X., Liu, G. and Chen, X. (**2013**). "Gadolinium embedded iron oxide nanoclusters as T1-T2 dual-modal MRI-visible vectors for safe and efficient siRNA delivery." *Nanoscale* 5(17): 8098-8104.

- Wang, Y. and Gu, H. (**2015**). "Core-shell-type magnetic mesoporous silica nanocomposites for bioimaging and therapeutic agent delivery." *Adv Mater* 27(3): 576-585.

- Wang, Y. X. (**2011b**). "Superparamagnetic iron oxide based MRI contrast agents: Current status of clinical application." *Quant Imaging Med Surg* 1(1): 35-40.

- Wilhelm, C., Billotey, C., Roger, J., Pons, J., Bacri, J.-C. and Gazeau, F. (**2003**). "Intracellular uptake of anionic superparamagnetic nanoparticles as a function of their surface coating." *Biomaterials* 24(6): 1001-1011.

- Wilhelm, C., Gazeau, F., Roger, J., Pons, J. N. and Bacri, J. C. (**2002**). "Interaction of Anionic Superparamagnetic Nanoparticles with Cells: Kinetic Analyses of Membrane Adsorption and Subsequent Internalization." *Langmuir* 18(21): 8148-8155.

- Williams, H., O'Grady, K., El Hilo, M. and Chantrell, R. (**1993**). "Superparamagnetism in fine particle dispersions." *Journal of Magnetism and Magnetic Materials* 122(1): 129-133.

- Wolff, J. A., Malone, R. W., Williams, P., Chong, W., Acsadi, G., Jani, A. and Felgner, P. L. (**1990**). "Direct gene transfer into mouse muscle in vivo." *Science* 247(4949): 1465-1468.

- Wu, B., Zhang, H., Chen, C., Lin, S. and Zheng, N. (**2009**). "Interfacial activation of catalytically inert Au (6.7 nm)-Fe3O4 dumbbell nanoparticles for CO oxidation." *Nano Research* 2(12): 975-983.

- Wu, X., Tan, Y., Mao, H. and Zhang, M. (**2010**). "Toxic effects of iron oxide nanoparticles on human umbilical vein endothelial cells." *Int J Nanomedicine* 5: 385-399.

- Wust, P., Gneveckow, U., Wust, P., Gneveckow, U., Johannsen, M., Böhmer, D., Henkel, T., Kahmann, F., Sehouli, J., Felix, R., Ricke, J. and Jordan, A. (**2009**). "Magnetic nanoparticles for interstitial thermotherapy – feasibility, tolerance and achieved temperatures." *International Journal of Hyperthermia* 22(8): 673-685.

- Xiao, N., Gu, W., Wang, H., Deng, Y., Shi, X. and Ye, L. (**2014**). "T1-T2 dual-modal MRI of brain gliomas using PEGylated Gd-doped iron oxide nanoparticles." *J Colloid Interface Sci* 417: 159-165.

- Xie, J., Xu, C., Kohler, N., Hou, Y. and Sun, S. (**2007**). "Controlled PEGylation of Monodisperse Fe3O4 Nanoparticles for Reduced Non-Specific Uptake by Macrophage Cells." *Advanced Materials* 19(20): 3163-3166.

- Xu, Y. and Liu, G. (**2014**). "Amplification of hofmeister effect by alcohols." *J Phys Chem B* 118(26): 7450-7456.

- Xu, Z., Hou, Y. and Sun, S. (**2007**). "Magnetic core/shell Fe3O4/Au and Fe3O4/Au/Ag nanoparticles with tunable plasmonic properties." *J Am Chem Soc* 129(28): 8698-8699.

- Xuan, S., Wang, Y. X., Yu, J. C. and Leung, K. C. (**2009**). "Preparation, characterization, and catalytic activity of core/shell Fe3O4@polyaniline@au nanocomposites." *Langmuir* 25(19): 11835-11843.

- Yamaura, M., Macedo, M. A., Nakamura, M., Camilo, R. L., Sampaio, L. C., Macêdo, M. A. and Toma, H. E. (**2004**). "Preparation and characterization of (3-aminopropyl)triethoxysilane-coated magnetite nanoparticles." *Journal of Magnetism and Magnetic Materials* 279(2-3): 210-217.

- Yang, J. B., Zhou, X. D., Yelon, W. B., James, W. J., Cai, Q., Gopalakrishnan, K. V., Malik, S. K., Sun, X. C. and Nikles, D. E. (**2004**). "Magnetic and structural studies of the Verwey transition in Fe3−δO4 nanoparticles." *Journal of Applied Physics* 95(11): 7540-7542.

- Yao, Q., Yu, Y., Yuan, X., Yu, Y., Zhao, D., Xie, J. and Lee, J. Y. (**2015**). "Counterion-assisted shaping of nanocluster supracrystals." *Angew Chem Int Ed Engl* 54(1): 184-189.

- Yardımcı, F. S., Şenel, M. and Baykal, A. (**2012**). "Amperometric hydrogen peroxide biosensor based on cobalt ferrite–chitosan nanocomposite." *Materials Science and Engineering: C* 32(2): 269-275.

- Ye, X., Lin, D., Jiao, Z. and Zhang, L. (**1998**). "The thermal stability of nanocrystalline maghemite." *Journal of Physics D: Applied Physics* 31(20): 2739.

- Yen, H. J., Hsu, S. H. and Tsai, C. L. (**2009**). "Cytotoxicity and immunological response of gold and silver nanoparticles of different sizes." *Small* 5(13): 1553-1561.

- You, C.-C., Verma, A. and Rotello, V. M. (**2006**). "Engineering the nanoparticle-biomacromolecule interface." *Soft Matter* 2(3): 190-204.

- Yu, M. K., Kim, D., Lee, I. H., So, J. S., Jeong, Y. Y. and Jon, S. (**2011**). "Image-guided prostate cancer therapy using aptamer-functionalized thermally cross-linked superparamagnetic iron oxide nanoparticles." *Small* 7(15): 2241-2249.

- Yu, Y., Mendoza-Garcia, A., Ning, B. and Sun, S. (**2013**). "Cobalt-substituted magnetite nanoparticles and their assembly into ferrimagnetic nanoparticle arrays." *Adv Mater* 25(22): 3090-3094.

- Yue, J., Jiang, X. and Yu, A. (**2011**). "Experimental and theoretical study on the β-FeOOH nanorods: growth and conversion." *Journal of Nanoparticle Research* 13(9): 3961-3974.

- Zavitsas, A. A. (**2001**). "Properties of Water Solutions of Electrolytes and Nonelectrolytes." *The Journal of Physical Chemistry B* 105(32): 7805-7817.

- Zhang, L.-Y., Gu, H.-C. and Wang, X.-M. (**2007**). "Magnetite ferrofluid with high specific absorption rate for application in hyperthermia." *Journal of Magnetism and Magnetic Materials* 311(1): 228-233.

- Zhang, L., Dong, W. F. and Sun, H. B. (**2013a**). "Multifunctional superparamagnetic iron oxide nanoparticles: design, synthesis and biomedical photonic applications." *Nanoscale* 5(17): 7664-7684.

- Zhang, L., He, R. and Gu, H.-C. (**2006a**). "Oleic acid coating on the monodisperse magnetite nanoparticles." *Applied Surface Science* 253(5): 2611-2617.

- Zhang, L., Wang, Y. S., Yang, Y., Zhang, F., Dong, W. F., Zhou, S. Y., Pei, W. H., Chen, H. D. and Sun, H. B. (**2012**). "Magnetic/upconversion luminescent mesoparticles of Fe3O4@LaF3:Yb3+, Er3+ for dual-modal bioimaging." *Chem Commun (Camb)* 48(91): 11238-11240.

- Zhang, S., Qi, Y., Yang, H., Gong, M., Zhang, D. and Zou, L. (**2013b**). "Optimization of the composition of bimetallic core/shell Fe2O3/Au nanoparticles for MRI/CT dual-mode imaging." *Journal of Nanoparticle Research* 15(11).

- Zhang, Y. and Cremer, P. S. (**2006b**). "Interactions between macromolecules and ions: The Hofmeister series." *Curr Opin Chem Biol* 10(6): 658-663.

- Zhou, Z., Huang, D., Bao, J., Chen, Q., Liu, G., Chen, Z., Chen, X. and Gao, J. (**2012**). "A synergistically enhanced T(1) -T(2) dual-modal contrast agent." *Adv Mater* 24(46): 6223-6228.

- Zhou, Z., Wang, L., Chi, X., Bao, J., Yang, L., Zhao, W., Chen, Z., Wang, X., Chen, X. and Gao, J. (**2013**). "Engineered iron-oxide-based nanoparticles as enhanced T1 contrast agents for efficient tumor imaging." *ACS Nano* 7(4): 3287-3296.

List of publications

- P. de la Presa, Y. Luengo, M. Multigner, R. Costo, M.P. Morales, G. Rivero and A. Hernando. Study of heating efficiency as function of concentration, size and applied field in γ-Fe_2O_3 nanoparticle. The Journal of Physical Chemistry C (2012).

- Y. Luengo, S. Nardecchia, M.P. Morales and M.C. Serrano. Different cell response induced by exposure to maghemite nanoparticles. Nanoscale (2013).

- S. Chamorro, A. Brenes, A. Viveros, C. Romero, L. Gutierrez, G. Salas, Y. Luengo, M.P. Morales, F.J. Teran. Iron bioavailability from ingested iron oxide nanoparticles. American Journal of Hematology (2013).

- M. Calero, L. Gutiérrez, G. Salas, Y. Luengo, A. Lázaro, P. Acedo, M. P. Morales, R. Miranda and A. Villanueva. Efficient and safe internalization of magnetic iron oxide nanoparticles: Two fundamental requirements for biomedical applications. Nanomedicine: Nanotechnology, Biology, and Medicine (2013).

- S. Veintemillas-Verdaguer, Y. Luengo, C.J. Serna, M. Andres-Vergés, M. Varela, M. Calero, A. Lazaro-Carrillo, A. Villanueva, A. Sisniega, P. Montesinos and M.P. Morales. Bismuth labeling for the CT assessment of local administration of magnetic nanoparticles. Nanotechnology (2015).

- P. de la Presa, Y. Luengo, V. Velasco, M. P. Morales, M. Iglesias, S. Veintemillas-Verdaguer, P. Crespo and A. Hernando. Particle Interactions in Liquid Magnetic Colloids by Zero Field Cooled Measurements: Effects on Heating Efficiency. The Journal of Physical Chemistry C (2015).

- S. Chamorro, L. Gutiérrez, M.P. Vaquero, D. Verdoy, G. Salas, Y. Luengo, A. Brenes and F.J. Teran. Safety assessment of chronic oral exposure to iron oxide nanoparticles. Nanotechnology (2015).

- M. Marciello, Y. Luengo, M. P. Morales. Iron Oxide Nanoparticles for Cancer Diagnosis and Therapy. Nanoarchitectonics for smart delivery and drug targeting. Ed. Elservier (2016).

- Y. Luengo, M. P. Morales, L. Gutierrez and S. Veintemillas-Verdaguer. Counterion and solvent effects on the size of magnetite nanocrystals obtained by oxidative precipitation. Journal of Materials Chemistry C (2016).

- I. Acebron, A.G. Ruiz-Estrada, Y. Luengo, M.P. Morales, J.M. Guisan, J.M. Mancheño. Oriented attachment of recombinant proteins to agarose-coated magnetic nanoparticles by means of abeta-trefoil lectin domain. Bioconjugate Chemistry (2016).